

Université du Québec  
Institut National de la Recherche Scientifique  
Énergie, Matériaux et Télécommunications

# **INVESTIGATION OF HETEROSTRUCTURE PHOTOANODES FOR SOLAR ENERGY CONVERSION**

Par  
Kaustubh Basu

THÈSE PRÉSENTÉE POUR L'OBTENTION DU GRADE DE  
PHILOSOPHIAE DOCTOR (Ph.D.)  
EN SCIENCES DE L'ÉNERGIE ET DES MATÉRIAUX

## **Jury d'évaluation**

Président du jury et examineur interne	Prof. Shuhui Sun INRS-EMT
Examineur externe	Prof. Fabio Cicoira École Polytechnique, Montreal
Examineur externe	Prof. Mohamed Sijaj Université du Québec à Montréal
Directeur de recherche	Prof. Fiorenzo Vetrone INRS-EMT
Codirecteur de recherche	Prof. Federico Rosei INRS-EMT

Université du Québec  
Institut National de la Recherche Scientifique  
Énergie, Matériaux et Télécommunications

**INVESTIGATION OF HETEROSTRUCTURE PHOTOANODES FOR  
SOLAR ENERGY CONVERSION**

By  
Kaustubh Basu

A DISSERTATION SUBMITTED  
IN PARTIAL FULFILLMENT OF THE REQUIREMENTS  
FOR THE DEGREE OF DOCTOR OF PHILOSOPHY  
TO THE CENTER OF ENERGY AND MATERIAL SCIENCE.

**Jury of Evaluation**

President of the Jury and Internal Examiner	Prof. Prof. Shuhui Sun INRS-EMT
External Examiner	Prof. Fabio Cicoira École Polytechnique, Montreal
External Examiner	Prof. Mohamed Sijaj Université du Québec à Montréal
Research Director	Prof. Fiorenzo Vetrone INRS-EMT
Research Co-Director	Prof. Federico Rosei INRS-EMT

*I dedicate this thesis to my family.*

# Abstract

Given the continuous escalation in the rate of energy consumption, fossil fuels, which presently meet ~86% of the global energy demand, are anticipated to run out by the end of 21<sup>st</sup> century. Moreover, increasing concern of global warming from greenhouse gases emitted by fossil fuels, drives us to explore viable alternatives, such as renewable energy sources. Solar energy, the cleanest form of renewable energy, strikes the earth annually with a staggering  $3 \times 10^{24}$  joules which is ~10,000 times more than our global energy consumption. Abundance of solar energy, can be exploited by converting and storing them into forms like electricity and H<sub>2</sub> by means of photovoltaics and photoelectrochemical H<sub>2</sub> generation, respectively. Ever since the discovery of the photoelectric effect by Edmond Becquerel, there has been extensive research on converting light into electric power or chemical fuels. Here, our research is focused mainly on two types of PEC cells, firstly DSSCs, which is the regenerative cell that converts sunlight into electric power leaving no net chemical change behind. Secondly, a photoelectrochemical cell where there are two redox systems: one reacting with the holes at the surface of the n-type semiconductor photoanode producing oxygen, and the other, reacting with the electrons entering the counter-electrode yielding hydrogen.

The quest for efficient and stable PEC cells has led to extensive research on photoanode materials, which play a key role in the charge dynamics of the overall photoelectrochemical device. Nanoparticle based photoanodes, have received significant attention mainly due to their high surface area and facile fabrication methods. Anatase TiO<sub>2</sub> has been widely used as a photoanode to fabricate photoelectrochemical cells, because of the ultra-fast electron injection rates from the excited sensitizer into the TiO<sub>2</sub> nanoparticles. But high electron recombination rates due to low

electron mobility in  $\text{TiO}_2$  limits its use.  $\text{SnO}_2$  on the other hand is a promising photoanode material because of its higher electronic mobility and large band gap. Mobility reported in both single crystal  $\text{SnO}_2$  as well as nanostructures are orders of magnitude higher than  $\text{TiO}_2$ . In addition,  $\text{SnO}_2$  has a low sensitivity to UV degradation due to its larger band gap, and hence has better long term stability. Our goal is to fabricate  $\text{SnO}_2$ - $\text{TiO}_2$  heterostructure photoanodes by a straight forward chemical post treatment approach, to combine the advantages of higher conduction band edge of  $\text{TiO}_2$ , and the high stability and exceptional electronic mobility of  $\text{SnO}_2$ . Moreover,  $\text{SnO}_2$ - $\text{TiO}_2$  heterojunction has a type-II band alignment, which facilitates charge separation and transport.

In the first part of this thesis, we report the fabrication and characterization of DSSCs based on  $\text{SnO}_2$ - $\text{TiO}_2$  photoanodes. Firstly, FTO coated conducting glass substrates were treated with  $\text{TiO}_x$  or  $\text{TiCl}_4$  precursor solutions to create a blocking layer before tape casting the  $\text{SnO}_2$  mesoporous anode. In addition,  $\text{SnO}_2$  photoanodes were treated with the same precursor solutions to deposit a  $\text{TiO}_2$  passivating layer covering the  $\text{SnO}_2$  particles. We found that the modification enhances the short circuit current, open-circuit voltage and fill factor, leading to nearly 2-fold increase in power conversion efficiency, from 1.48% without any treatment, to 2.85% achieved with  $\text{TiCl}_4$  treatment. The superior photovoltaic performance of the DSSCs assembled with modified photoanode is attributed to enhanced electron lifetime and suppression of electron recombination to the electrolyte, as confirmed by EIS carried out under dark condition. These results indicate that modification of the FTO and  $\text{SnO}_2$  anode by  $\text{TiO}_2$  can play a major role in maximizing the photo conversion efficiency.

Although, nanoparticle-based photoanodes exhibit high surface to volume ratio, the main drawback in using nanoparticles, is that mesoporous networks experience high density of grain

boundaries, which facilitate charge recombination. Carbon-based nanostructures such as graphene and carbon nanotubes possess exceptional mechanical and electronic properties, can be used as charge directing structures in mesoporous nanoparticle networks. In the next part of this thesis, we report the effect of incorporation of graphene microplatelets into SnO<sub>2</sub>-TiO<sub>2</sub> mesoporous anode to boost the performance and long-term stability of DSSCs. DSSCs were fabricated by incorporating different concentrations of graphene microplatelets (up to 0.50 wt.%) into the SnO<sub>2</sub>-TiO<sub>2</sub> mesoporous network utilizing a fast and large area-scalable technique. At optimized concentration of graphene (0.03 wt.%), highest PCE of 3.37% was achieved, which is ~16% higher than for SnO<sub>2</sub>-TiO<sub>2</sub> photoanodes based DSSC. This enhancement of PCE can be attributed to higher electron lifetime and reduced charge recombination in SnO<sub>2</sub>-TiO<sub>2</sub>/graphene photoanodes as confirmed by transient photovoltage decay and impedance spectroscopy. Furthermore, the performance of the solar cells was recorded for 200 hours of continuous illumination under simulated sunlight (AM 1.5G) for long-term stability measurements. Our results demonstrated that the addition of graphene microplatelets results in superior stability of DSSCs, where the drop in PCE was a mere 8%, while a sharp plummet of 30% in PCE was observed in case of SnO<sub>2</sub>-TiO<sub>2</sub> photoanodes. These findings are encouraging, and establish SnO<sub>2</sub>-TiO<sub>2</sub>/graphene architecture as a promising photoanode towards efficient and stable DSSC.

In the final part of our thesis, we introduce our novel SnO<sub>2</sub>-TiO<sub>2</sub>/graphene photoanodes for fabrication of PEC cells for H<sub>2</sub> generation. H<sub>2</sub>, being a zero emission fuel, is expected to be a major player in the future energy scenario especially in the automobile fuel sector. However, presently large scale industrial production of H<sub>2</sub> relies on utilization of fossil fuels, resulting in greenhouse gas emissions. PEC water splitting, exploiting solar energy as a clean energy source and implementing colloidal QDs as sensitizers is a promising approach for H<sub>2</sub> generation due to the

QD's size-tunable optical properties. However, the challenge of long term stability of the QDs is still unresolved. Here, we introduce a highly stable QD-based PEC device for H<sub>2</sub> generation using a photoanode based on a SnO<sub>2</sub>-TiO<sub>2</sub> heterostructure, sensitized by CdSe/CdS core/thick-shell QDs. This hybrid photoanode architecture leads to an appreciable saturated photocurrent density of ~4.7 mA/cm<sup>2</sup>, retaining an unprecedented ~96% of its initial current density after two hours, and sustaining ~93% after five hours of continuous irradiation under AM 1.5G (100 mW/cm<sup>2</sup>) simulated solar spectrum. Transient PL measurements demonstrate that the heterostructured SnO<sub>2</sub>-TiO<sub>2</sub> photoanode exhibits faster electron transfer compared with the bare TiO<sub>2</sub> photoanode. The lower electron transfer rate in the TiO<sub>2</sub> photoanode can be attributed to slow electron kinetics in the ultraviolet regime, revealed by ultrafast transient absorption spectroscopy. Graphene microplatelets were further introduced into the heterostructured photoanode, which boosted the photocurrent density to ~5.6 mA/cm<sup>2</sup>. Our results clearly demonstrate that SnO<sub>2</sub>-TiO<sub>2</sub> heterostructured photoanode holds significant potential for developing highly stable PEC cells.

# Acknowledgements

First and foremost, I would like to convey my gratitude and appreciation to my supervisors, Professor Fiorenzo Vetrone and Professor Federico Rosei, for their invaluable support and guidance at every stage of my PhD study. Their professionalism and dedication has always inspired me, and it has been a truly rewarding experience, getting the opportunity to work with them. I am also indebted to my group leaders Professor Alberto Vomiero from Luleå University of Technology, Sweden and Professor Haiguang Zhao from Qingdao University, China and Dr. Gurpreet Singh Selopal from INRS-EMT for their relentless efforts in mentoring and motivating me. They have always been there for me, with their priceless inputs and invaluable suggestions which helped me advance and reach my research goals. I am also grateful to Professor Ana Tavares for allowing me to work in her laboratory and to use her facilities.

I would like to convey my deepest gratitude to the following members of my PhD committee for their invaluable comments and inputs: Professor Fabio Cicoira from École Polytechnique, Montreal, Professor Mohamed Siaj from the Université du Québec à Montréal Professor Shuhui Sun from INRS-EMT, Varennes.

I am grateful to all the group members from nano-femto lab and advanced materials lab for their continuous help and support throughout my PhD work. I am thankful to be a part of such a supportive, hardworking, and inspiring group of graduate students and postdoctoral fellows. These people include: Dr. Gurpreet Singh Selopal, as well as other collaborators. I also thank our institute technical staff for training me on different scientific equipment. I would like to thank the INRS-EMT administrative staff Ms. H  l  ne Sabourin, Ms. Nathalie M  tras, Ms. Michelle Marcotte, Mr. Sylvain Gingras for administrative support.

I extend my heartfelt gratitude to my beloved parents for their unconditional love, support, and encouragement. Finally, I owe my loving thanks to my wife Suchismita, for being there with me during all the ups and downs, and for the many sacrifices that she has made to support me in undertaking my doctoral studies. Thank you my dear for building my inner strength with your endless love and encouragement.

# Contents

<b>Abstract .....</b>	<b>II</b>
<b>Acknowledgements.....</b>	<b>VI</b>
<b>List of figures .....</b>	<b>XI</b>
<b>List of abbreviations, chemical compounds and symbols .....</b>	<b>XIV</b>
Abbreviations .....	xiv
Chemical compounds.....	xvi
Symbols .....	xvii
<b>Chapter 1: Introduction .....</b>	<b>1</b>
<b>1.1 Fossil fuel and adverse effects.....</b>	<b>1</b>
<b>1.2 Renewable energy .....</b>	<b>2</b>
<b>1.3 Solar- The centre stage of renewable energy.....</b>	<b>3</b>
<b>1.4 Solar spectrum and solar energy conversion.....</b>	<b>4</b>
1.4.1 Solar cell .....	5
1.4.1.1 Dye Sensitized Solar Cells.....	7
1.4.1.1.1 Key components of a DSSC .....	8
1.4.1.1.1.1. Transparent conducting substrate .....	9
1.4.1.1.1.2. Nanocrystalline photoanode.....	9
1.4.1.1.1.3. Dye sensitizer.....	11
1.4.1.1.1.4. Redox Electrolyte.....	12
1.4.1.1.1.5. Counter electrode .....	13
1.4.1.1.2. Working Mechanism of a DSSC.....	13
1.4.1.1.3. Dynamic competition in a DSSC.....	15
1.4.1.1.4. Role of the photoanode of a DSSC .....	17
1.4.1.1.5. DSSC photoanode material.....	18
1.4.1.1.6. Various photoanode architectures in DSSCs .....	20
1.4.1.1.7. SnO <sub>2</sub> as a photoanode of DSSCs .....	23
1.4.2 Hydrogen Production from solar energy.....	25

1.4.2.1 Hydrogen generation using PEC cells .....	26
1.4.2.1.1 Semiconductor photoanodes for PEC cells.....	29
1.4.2.1.1.1 Quantum Dot based PEC cells.....	30
<b>Chapter 2.....</b>	<b>32</b>
<b>2.1 Research objectives.....</b>	<b>32</b>
2.1.1. Part I: Fabrication and characterization of DSSCs with novel heterostructure photoanode.....	32
2.1.2 Part II: Investigation of novel heterostructure photoanode for PEC based H <sub>2</sub> generation .....	34
<b>2.2 Thesis organization.....</b>	<b>35</b>
<b>Chapter 3: Materials and methods.....</b>	<b>38</b>
<b>3.1 Materials.....</b>	<b>38</b>
<b>3.2 Methods.....</b>	<b>39</b>
3.2.1 Experimental details relevant to DSSC fabrication with SnO <sub>2</sub> photoanodes with different post treatment routes .....	39
3.2.1.1 Preparation of SnO <sub>2</sub> paste.....	39
3.2.1.2 Pre- and post-treatment of the SnO <sub>2</sub> photoanode.....	39
3.2.1.3 DSSC fabrication .....	40
3.2.1.4 Dye sensitization and DSSC assembly .....	40
3.2.2 Experimental details relevant to DSSC fabrication with SnO <sub>2</sub> -TiO <sub>2</sub> photoanodes with graphene.....	41
3.2.2.1 Fabrication of the SnO <sub>2</sub> -TiO <sub>2</sub> /graphene photoanodes and DSSCs .....	41
3.2.3 Experimental details relevant to colloidal QD based PEC H <sub>2</sub> generation .....	41
3.2.3.1 Synthesis of CdSe QDs.....	41
3.2.3.2 Synthesis of CdSe/CdS “giant” QDs .....	42
3.2.3.3 Sensitization of the SnO <sub>2</sub> film with CdSe/CdS “giant” QDs.....	43
3.2.3.4 ZnS capping layer .....	43
<b>3.3 Characterization techniques.....</b>	<b>43</b>
3.3.1 SEM and TEM characterizations .....	43
3.3.2 XRD characterizations .....	44

3.3.3	DRS measurements .....	44
3.3.4	UPS measurements .....	45
3.3.5	PL measurements .....	45
3.3.6	Ultrafast TAS measurements .....	46
3.3.7	PV measurements.....	47
3.3.8	Electrochemical impedance spectroscopy measurements .....	48
3.3.9	PEC performance analysis .....	48
<b>Chapter 4: Results .....</b>		<b>50</b>
4.1	Enhanced photovoltaic properties in dye sensitized solar cells by surface treatment of SnO <sub>2</sub> photoanodes .....	50
4.2	Hybrid graphene/metal oxide photoanodes for efficient and stable dye sensitized solar cell.....	81
4.3	Highly stable photoelectrochemical cells for hydrogen production using SnO <sub>2</sub> TiO <sub>2</sub> / quantum dot heterostructured photoanode.....	111
<b>Chapter 5: Conclusion .....</b>		<b>153</b>
<b>References .....</b>		<b>157</b>
<b>Appendix: Résumé .....</b>		<b>179</b>

# List of figures

<b>Figure 1.1:</b> (a) Contribution of fossil fuels and cement manufacture in global CO <sub>2</sub> annual emissions.[2] (b) Global CO <sub>2</sub> emission in parts per million (ppm) of air molecules since 1980.[5]	1
<b>Figure 1.2:</b> (a) Trend in global energy consumption (1900-2015).[2] (b) Global energy consumption statistics.[10]	2
<b>Figure 1.3:</b> Comparison of spectral irradiance: black body radiation (black) at 5800 K, AM0 irradiation in space (blue), AM1.5 irradiation in central Europe and north American latitudes (red).[22] The path length in Air Mass unit as a function of the zenith angle.[23]	4
<b>Figure 1.4:</b> Evolution of power conversion efficiency records of solar cells over time since 1976.[38]	6
<b>Figure 1.5:</b> DSSC façade at SwissTech convention center at École polytechnique fédérale de Lausanne.[51]	7
<b>Figure 1.6:</b> Schematic diagram[59] of a typical DSSC, individual components are shown in details on the right	8
<b>Figure 1.7:</b> The effect of using a mesoporous photoanode in DSSCs: IPCE as a function of the excitation wavelength; (a) Single-crystal anatase TiO <sub>2</sub> cut along (101) plane, (b) Mesoporous anatase TiO <sub>2</sub> film. In both cases, TiO <sub>2</sub> photoanodes were sensitized by the same dye and same electrolyte was used.[16]	10
<b>Figure 1.8:</b> Examples of few Ruthenium polypyridyl dyes used in DSSCs.[65]	11

**Figure 1.9:** A schematic representation of a typical DSSC illustrating the different charge transfer mechanisms;[59] The structure of a classical DSSC is shown in the inset.....**14**

**Figure 1.10:** Different charge transport and recombination mechanisms in a typical DSSC.<sup>84</sup> Time scale of different processes in a DSSC.[83].....**16**

**Figure 1.11:** Evolution of the number of research publications in DSSC. Inset shows the distribution of publications for each DSSC component in 2012.[67].....**17**

**Figure 1.12:** Energy band positions[16] of different semiconductors with reference to normal hydrogen electrode (NHE) or the vacuum level.....**19**

**Figure 1.13:** (a) Typical photoanode structure consisting of small nanoparticles presenting random electron transport pathways; (b) bi-layer photoanode structure where light is scattered by the top layer of bigger nanoparticles; (c) directional electron transport in 1D nanowires and (d) hierarchical 1D nanowire architectures.[105].....**20**

**Figure 1.14:** (a) Schematic representation of a hierarchical ZnO sphere consisting of densely packed ZnO nanoparticles;[112] (b) Enhanced light-scattering effect in a photoanode based on SnO<sub>2</sub> octahedra, the structure of a SnO<sub>2</sub> octahedra is shown on the bottom right.[113].....**21**

**Figure 1.15:** Schematic illustration of a TiO<sub>2</sub> nanoparticle/ZnO nanowire composite photoanode.[120].....**22**

**Figure 1.16:** Schematic representation of improved charge collection mechanism in a photoanode based on a graphene network embedded in a TiO<sub>2</sub> nanoparticle network.[121] .....**22**

**Figure 1.17:** Schematic diagram of tetragonal rutile crystal structure of SnO<sub>2</sub>,[132] the (110) crystal plane shown in green. ....**24**

**Figure 1.18:** Schematic diagram of the PEC cell used by Fujishima and Honda.[155].....**26**

<b>Figure 1.19:</b> Fundamental mechanism of semiconductor-based photocatalytic water splitting for hydrogen generation.[156].....	<b>27</b>
<b>Figure 1.20:</b> The main processes for charge transport and recombination in photocatalytic water splitting.[156].....	<b>28</b>
<b>Figure 1.21:</b> PEC based water splitting systems implementing (a) n-type semiconductor photoanode, and (b) p-type semiconductor photocathode.[158].....	<b>29</b>
<b>Figure 1.22:</b> Band structure of different semiconductors w.r.t. the redox potentials of water splitting.[18].....	<b>30</b>

# List of abbreviations, chemical compounds and symbols

## Abbreviations

<b>1D</b>	One dimension
<b>2D</b>	Two dimension
<b>3D</b>	Three dimension
<b>AFM</b>	Atomic force microscopy
<b>AM</b>	Air mass
<b>APS</b>	Average particle size
<b>AOI</b>	Angle of incidence
<b>BL</b>	Blocking layer
<b>CB</b>	Conduction band
<b>CE</b>	Counter electrode
<b>CNT</b>	Carbon nanotube
<b>CT</b>	Charge transfer
<b>CV</b>	Cyclic voltammetry
<b>DRS</b>	Diffuse reflectance spectroscopy
<b>DSSC</b>	Dye sensitized solar cell
<b>EDS</b>	Energy dispersive x-ray spectroscopy
<b>EPD</b>	Electrophoretic deposition
<b>EQE</b>	External quantum efficiency
<b>EIS</b>	Electrochemical impedance spectroscopy
<b>EPFL</b>	École polytechnique fédérale de Lausanne
<b>FESEM</b>	Field emission scanning electron microscope
<b>FF</b>	Fill factor
<b>FTO</b>	Fluorine doped tin oxide
<b>FWHM</b>	Full width at half maximum
<b>HER</b>	Hydrogen evolution reaction

<b>HOMO</b>	Highest occupied molecular orbital
<b>HRTEM</b>	High resolution transmission electron microscope
<b>IEP</b>	Isoelectric point
<b>INRS</b>	Institut national de la recherche scientifique
<b>IPCE</b>	Incident photon-to-current conversion efficiency
<b>IR</b>	Infrared
<b>KM</b>	Kubelka Munk
<b>LH</b>	Light harvesting
<b>LUMO</b>	Lowest unoccupied molecular orbital
<b>MWCNT</b>	Multi walled carbon nanotube
<b>NBs</b>	Nanobeads
<b>NHE</b>	Normal hydrogen electrode
<b>NFs</b>	Nanoflowers
<b>NMR</b>	Nuclear magnetic resonance
<b>NPs</b>	Nanoparticles
<b>NREL</b>	National renewable energy laboratory
<b>OER</b>	Oxygen evolution reaction
<b>PCE</b>	Power/photo conversion efficiency
<b>PEC</b>	Photoelectrochemical
<b>PL</b>	Photo-luminescence
<b>PV</b>	Photovoltaic
<b>QD</b>	Quantum dot
<b>RF</b>	Radio frequency
<b>RHE</b>	Reversible hydrogen electrode
<b>RPM</b>	Revolutions per minute
<b>SAED</b>	Selected area electron diffraction
<b>SEM</b>	Scanning electron microscopy
<b>SILAR</b>	Successive ionic layer adsorption and reaction
<b>STM</b>	Scanning tunneling microscope
<b>SWCNT</b>	Single walled carbon nanotube
<b>TAS</b>	Transient absorption spectroscopy

<b>TCSPC</b>	Time correlated single photon counting
<b>TCO</b>	Transparent conducting oxide
<b>TEM</b>	Transmission electron microscope
<b>UPS</b>	Ultraviolet photoelectron spectroscopy
<b>UV-VIS-NIR</b>	Ultraviolet-visible-near infrared
<b>UV</b>	Ultraviolet
<b>VB</b>	Valence band
<b>WLC</b>	White light continuum
<b>XRD</b>	X-ray diffraction
<b>XPS</b>	X-ray photoelectron spectroscopy

## **Chemical compounds**

<b>CaF<sub>2</sub></b>	Calcium fluoride
<b>CH<sub>4</sub></b>	Methane
<b>CIGS</b>	Copper indium gallium selenide
<b>CuInSe<sub>2</sub></b>	Copper indium selenide
<b>CO<sub>2</sub></b>	Carbon dioxide
<b>CdS</b>	Cadmium sulfide
<b>CdSe</b>	Cadmium selenide
<b>CdTe</b>	Cadmium telluride
<b>IPA</b>	Isopropanol
<b>ITO</b>	Indium doped tin oxide
<b>H<sub>2</sub></b>	Hydrogen
<b>HAD</b>	Hexadecylamine
<b>HCl</b>	Hydrochloric acid
<b>He</b>	Helium
<b>N<sub>2</sub></b>	Nitrogen
<b>NaOH</b>	Sodium hydroxide
<b>Na<sub>2</sub>SO<sub>3</sub></b>	Sodium sulphite

<b>OA</b>	Oleic acid
<b>ODE</b>	Octadecene
<b>OLA</b>	Oleylamine
<b>Pt</b>	Platinum
<b>PET</b>	Poly ethylene terphthalate
<b>SnO<sub>2</sub></b>	Tin dioxide
<b>TiCl<sub>4</sub></b>	Titanium tetrachloride
<b>TiO<sub>2</sub></b>	Titanium dioxide
<b>Zn(CH<sub>3</sub>COO)<sub>2</sub></b>	Zinc acetate
<b>ZnO</b>	Zinc oxide
<b>ZnS</b>	Zinc sulphide

## Symbols

<b>h</b>	Hour
<b>min</b>	Minute
<b>μs</b>	Microsecond
<b>ms</b>	Millisecond
<b>ns</b>	Nanosecond
<b>fs</b>	Femtosecond
<b>ps</b>	Picosecond
<b>M</b>	Molar
<b>mM</b>	Millimolar
<b>E<sub>g</sub></b>	Bandgap
<b>I<sub>sc</sub></b>	Short circuit current
<b>I<sub>max</sub></b>	Current at maximum power output
<b>J<sub>sc</sub></b>	Short circuit current density
<b>P<sub>in</sub></b>	Input light power
<b>P<sub>max</sub></b>	Maximum power output
<b>V<sub>oc</sub></b>	Open circuit voltage

<b>V<sub>max</sub></b>	Voltage at maximum power output
<b>J<sub>max</sub></b>	Current density at maximum power output
<b>η</b>	Power conversion efficiency
<b>Ω/□</b>	Ohm per square
<b>eV</b>	Electron volt
<b>kV</b>	Kilovolt
<b>c</b>	Speed of light in vacuum
<b>k</b>	Boltzmann constant
<b>h</b>	Planck constant
<b>km</b>	Kilometer
<b>m</b>	Meter
<b>cm</b>	Centimeter
<b>mm</b>	Millimeter
<b>μm</b>	Micrometer
<b>nm</b>	Nanometer
<b>W</b>	Watt
<b>kW</b>	Kilowatt
<b>l</b>	Liter
<b>ml</b>	Milliliter
<b>g</b>	Gram
<b>mg</b>	Milligram
<b>λ</b>	Lambda
<b>°C</b>	Degree celcius
<b>K</b>	Kelvin
<b>J</b>	Joule
<b>Ppm</b>	Parts per million
<b>MPa</b>	Megapascal



# Chapter 1: Introduction

## 1.1 Fossil fuel and adverse effects

The awareness for renewable energy sources has increased gravely around the world due to immense concern over environmental pollution, increasing energy demand and limited availability of the traditional sources of energy such as coal, oil, and natural gas i.e. fossil fuels. In the past five decades, demand of energy around the globe has accelerated world energy consumption by more than double.[1] Presently, fossil fuels provide more than 85% of the world's energy[2], combustion of fossil fuels during electricity generation release CO<sub>2</sub> and other harmful pollutants to the atmosphere causing significant health and environmental impacts.[3]

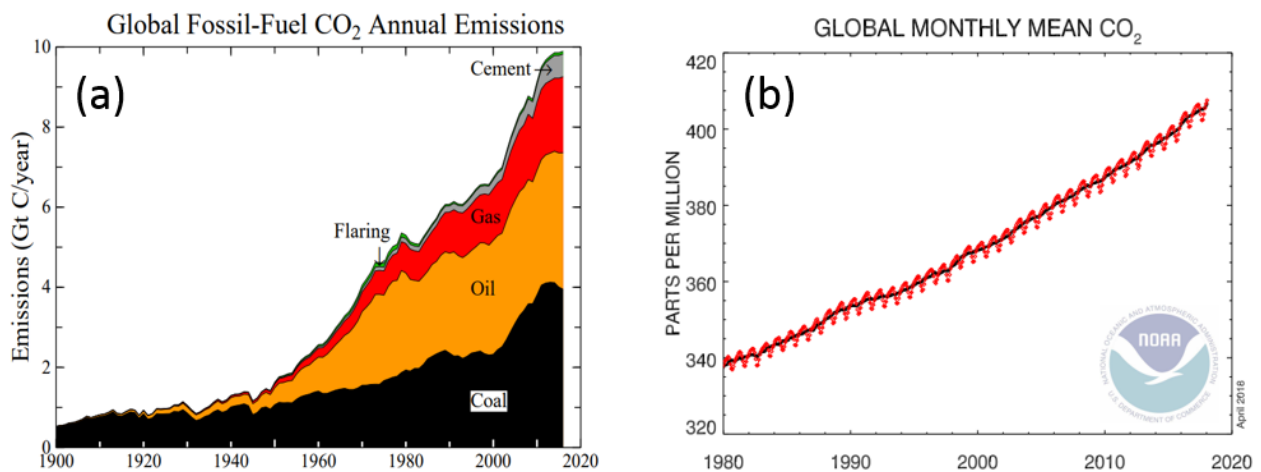


Figure 1.1: (a) Contribution of fossil fuels and cement manufacture in global CO<sub>2</sub> annual emissions.[2] (b) Global CO<sub>2</sub> emission in parts per million (ppm) of air molecules since 1980.[5]

CO<sub>2</sub> being the main candidate responsible for global warming based on human activity, pose serious threat and have long-standing negative impacts on public health.[4] With the advent of the industrial revolution, human activities has been mainly responsible for the increase in the atmospheric concentration of CO<sub>2</sub> (~45% in the period of 1750-2018).[5] CO<sub>2</sub> emissions

continue to grow at an accelerated rate, shown in figure 1.1(b), even though a decline of carbon emissions was projected following the 1997 Kyoto Protocol.[5,6]

## 1.2 Renewable energy

To meet increasing energy demand, while minimising damage to the environment, we need to utilize clean, sustainable, and renewable energy sources.[7] Renewable energy is a form of energy that is derived from resources, which can be naturally replenished on a human timescale.[8] There are many forms of renewable energy, such as solar, wind, geothermal, hydropower and ocean resources amongst others, which are attractive primarily because they have minimal effect on the environment.[9]

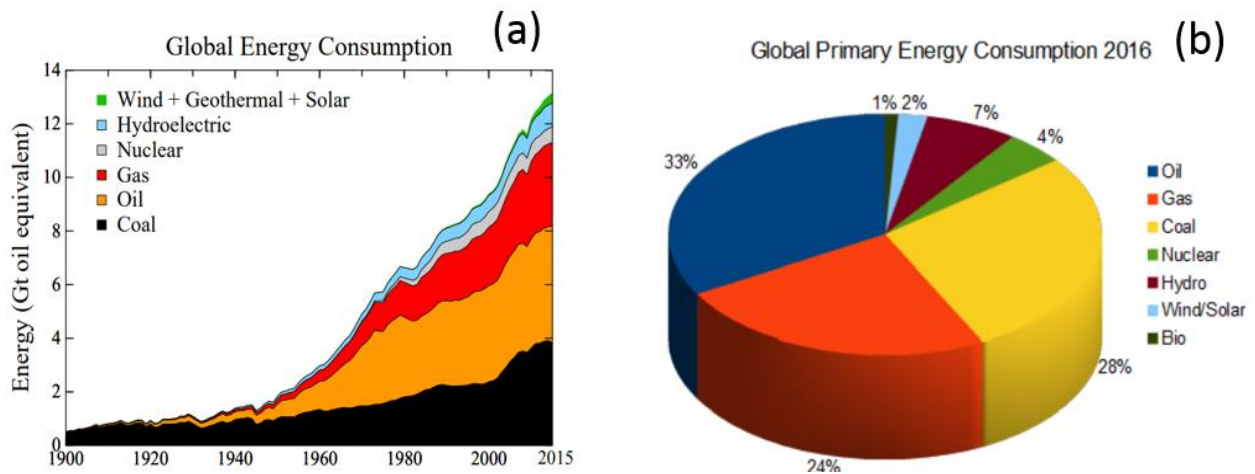


Figure 1.2: (a) Trend in global energy consumption (1900-2015).[2] (b) Global energy consumption statistics.[10]

The majority of the renewable energy sources yield little or no CO<sub>2</sub> emissions, even after taking into account the CO<sub>2</sub> emissions from each stage of its life cycle i.e. manufacturing, installation, operation and decommissioning.[11,12] To reduce CO<sub>2</sub> emissions, renewable based energy generation should emerge as a frontrunner, however it constitutes only around 10% of the global energy consumption shown in Figure 1.2(b).

### 1.3 Solar- The centre stage of renewable energy

Amongst all the renewable energy sources available, solar energy is the most abundant one. The sun emits energy at a colossal rate of  $3.8 \times 10^{23}$  kW[13] among which, the earth being located ~150 million km away from the sun, intercepts, approximately, energy at the rate of  $1.8 \times 10^{14}$  kW.[13] Around 60% of this amount reaches the earth's surface while the rest is absorbed by the atmosphere and radiated back into space.[13] Considering the abundance of solar irradiance, and the present demand for a clean and renewable energy resource, it is essential to explore a safe way to harness and utilize the environmentally benign and renewable solar energy.[14] Among several ways of utilizing solar energy, two very appealing and promising technologies are solar cells and H<sub>2</sub> generation using PEC cells. After the discovery of photoelectric effect, by the French scientist Edmond Becquerel,[15] there has been immense effort from scientists all around the globe to convert light into electric power or chemical fuels such as H<sub>2</sub>. [16] Solar cells are mainly attractive because they can convert sunlight into electric power. Since the annual solar irradiation reaching the earth's surface is about  $3 \times 10^{24}$  J/year, which is ~ 10,000 times the present energy consumed by the entire world's population,[16] the global energy demand can be satisfied by covering ~ 0.1% of the earth's surface with solar panels of power conversion efficiency (PCE) of about 10%.[16,17] On the other hand, H<sub>2</sub>, a clean and energy efficient fuel, is mainly produced in the industry from fossil fuels such as by steam methane reforming[18] at high temperatures (up to 900 °C) and pressures (1.5–3 MPa). [19,20] Generation of H<sub>2</sub> from solar energy will promote a plethora of new possibilities in realizing a H<sub>2</sub> driven economy in the future.

## 1.4 Solar spectrum and solar energy conversion

The sun can be approximately modeled as a black body emitting at the temperature of 5800 K. The spectral irradiance of a black body is defined using Planck's radiation law[21], shown in eqn. 1.1

$$F(\lambda) = \frac{2\pi hc^2}{\lambda^5 (\exp\left(\frac{hc}{k\lambda T}\right) - 1)} \quad 1.1$$

Where,  $\lambda$  is the wavelength of light, T is the temperature of the blackbody in Kelvin (K), F is the spectral irradiance in  $\text{Wm}^{-2}\mu\text{m}^{-1}$ ; and h is the Planck constant, c is the speed of light in the vacuum and k is the Boltzmann constant.

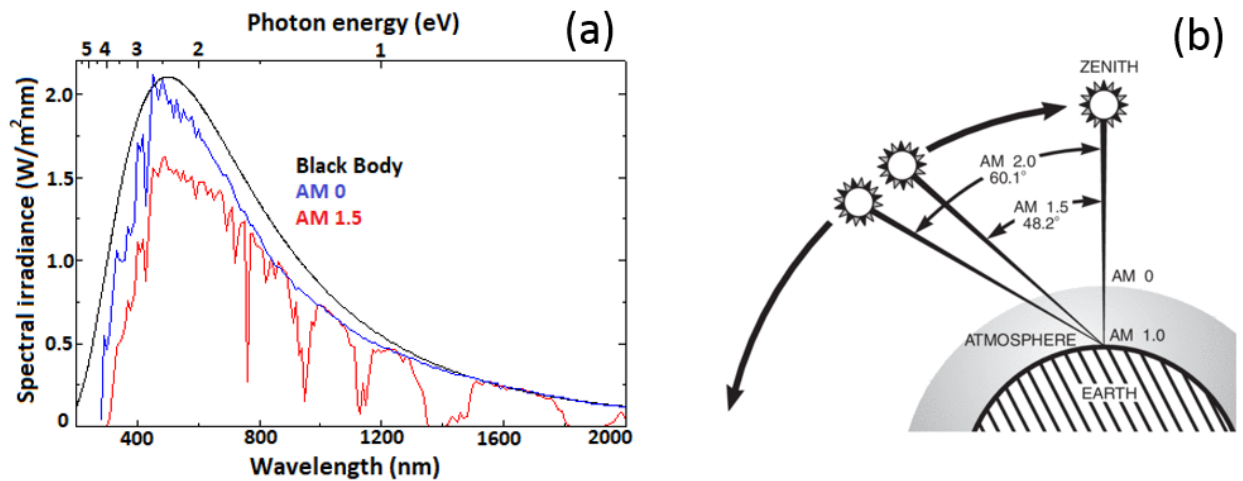


Figure 1.3 Comparison of spectral irradiance: black body radiation (black) at 5800 K, AM0 irradiation in space (blue), AM1.5 irradiation in central Europe and north American latitudes (red).[22] The path length in air mass unit as a function of the zenith angle.[23]

Solar radiation is attenuated more and more by scattering and absorption as it passes through the earth's atmosphere. The ozone layer is primarily responsible for the absorption of UV region, while water vapor and carbon dioxide are accountable for a portion of IR absorption. The solar spectrum outside the earth's atmosphere is referred to as AM 0.[24] The AM is defined as the path length which sunlight travels through the atmosphere normalized to the shortest path length, i.e.

when the sun is directly overhead. If  $L$  is the path length of light, and  $L_0$  is the thickness of the atmosphere layer, and through this layer,  $\theta$  is the zenith angle, then the AM coefficient (as shown in eqn. 1.2) is defined as:

$$AM = \frac{L}{L_0} \approx \frac{1}{\cos\theta} \quad 1.2$$

The standard reference spectrum used for characterizing solar cells and PEC cells for  $H_2$  generation is AM 1.5G, which corresponds to a solar irradiance at a zenith angle of  $48.2^\circ$  and represents the overall yearly average of solar irradiance for mid-latitudes.[22,25] Figure 1.3(a) depicts the comparison of the black body spectrum at 5800 K, AM 0 and AM 1.5G spectra. AM 1.5G spectra, which consists of both direct and diffused radiation of incident sunlight, and corresponds to an intensity of  $\sim 1000 \text{ W/m}^2$  or  $100 \text{ mW/cm}^2$  is utilized for PV measurements.[26,27] Some of the fundamental limitations that govern the performance of solar cells were studied by Shockley and Queisser in 1961.[28] Under an illumination of AM 1.5 solar spectrum, the Shockley-Queisser limit suggested that, for an optimum photo conversion,[29]  $\sim 33\%$  of the solar energy can be theoretically converted to electricity for a single junction solar cell with a band gap ( $E_g$ ) of 1.4 eV. The rest of the solar energy,  $\sim 47\%$  gets converted to heat, primarily phonons, 18% of the photons transmits through the solar cell unabsorbed, and around 2% of the energy is lost from recombination of newly generated electrons and holes.[28–32]

#### **1.4.1 Solar cell**

The phenomenon of conversion of light into electrical energy was first observed by the French scientist Alexandre Edmond Becquerel in 1839, when he observed that, upon exposure to light, a minute amount of electric current is generated between a silver chloride and platinum electrode in an electrolyte.[15] This was later coined the “Photovoltaic effect” or “Becquerel effect” after the

scientist himself. A few decades later, a photovoltaic effect was observed by William Adams, while illuminating a junction between selenium and platinum in 1877.[33] The first selenium solar cell was constructed by inventor Charles Fritts in 1883 using selenium on a thin layer of gold.[34] The solar cell had an efficiency of only 1 to 2%, but marked the beginning of the PV technology. The theory of “photovoltaic effect” was first explained by Albert Einstein in his 1905 by a simple description of light quanta later termed as photons.[35] which won him the Nobel Prize in physics in 1921. Following the patent by Russell Ohl 1946,[36] the first practically feasible solar cell was developed by Bell laboratories in 1954, implementing a silicon p-n junction, which reached an efficiency ~6%.[37]

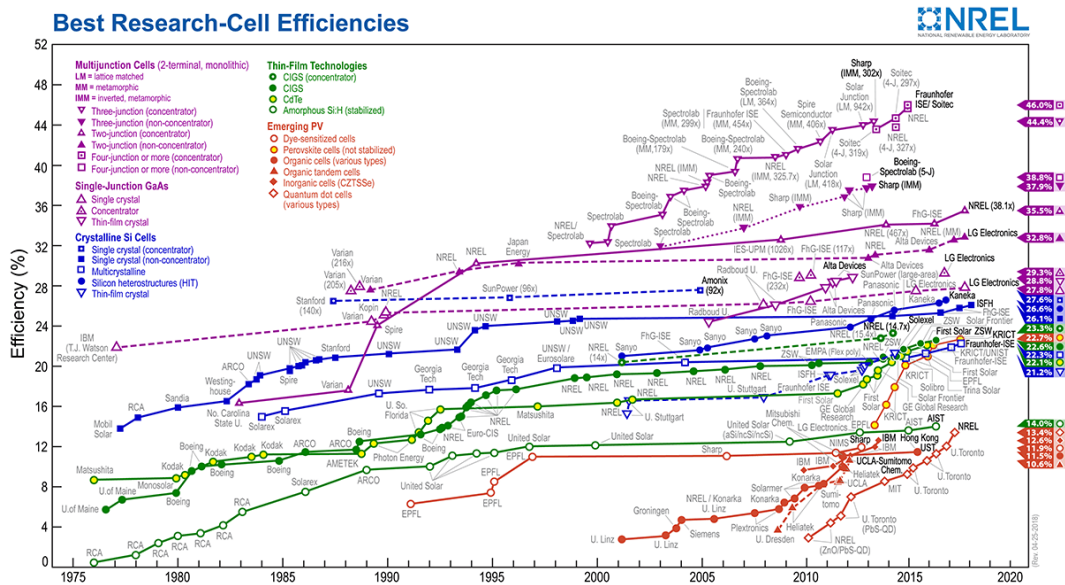


Figure 1.4: Evolution of power conversion efficiency records of solar cells over time since 1976.[38]

PV technology can be broadly categorized into three generations. The first generation photovoltaics primarily relies on crystalline silicon. Although silicon is abundantly found in nature, high energy is required for the purification and manufacturing of defect free silicon, thereby increasing the cost per generated power.[39] Although, this class of solar cells can achieve high efficiency, close to the Shockley-Queisser limit,[28] high production costs demands a new cost

effective technology. The second generation photovoltaics mainly constitutes of thin film technologies like CdTe, CIGS, and amorphous silicon[40] fabricated on cheaper glass and ceramic substrates, thereby significantly reducing the production cost, however PCE is relatively low.[39] To effectively combine the advantages of both the first and second generation photovoltaics, third generation technology was introduced.[41,42] The third generation photovoltaic technology involve emerging technologies like DSSCs and perovskite solar cells, which demonstrate remarkable efficiency,[43,44] where the photogenerated excitons and the charge transport are spatially separated, thereby requiring lower purity semiconductors, hence reducing the cost. The PCE records of different generations of PV technologies since 1976 are depicted in Figure 1.4.[45]

#### **1.4.1.1 Dye Sensitized Solar Cells**

The fundamental research that lead to the pioneering work of DSSC was carried out during the era of 1970-1990.[46–49] It was only in 1991 when Grätzel and O’Regan, in their revolutionary work, introduced a mesoporous semiconductor architecture with high surface to volume ratio, yielding a remarkable initial PCE of 7.9%.[50] The working mechanism of DSSCs are based on the principle of photosynthesis in plants.[16]



Figure 1.5: DSSC façade at the SwissTech convention center at École polytechnique fédérale de Lausanne.[51]

The mesoporous layer of a wide band gap semiconductor covered with a monolayer of molecular dye in a DSSC absorbs sunlight identical to the chlorophyll in green leaves.[7] DSSCs outperform traditional silicon solar cells in low indoor light or diffused outdoor sunlight (during cloudy days) conditions and is less dependent on light AOI compared to conventional solar cells,[52–54] which depends on solar tracking systems. DSSC panels are lightweight, which can be manufactured industrially by simple roll-to-roll technique[55] with the possibility to be fabricated on flexible substrates.[56,57] Figure 1.5 exhibits a DSSC façade at the Swiss Tech convention center at EPFL[58] which showcases the semi-transparency and the multi-color possibilities of DSSCs. This is an excellent example of building integrated photovoltaics, where the DSSC façade not only introduces an exceptional window tint with superb aesthetics, but also generates a 8,000 kWh of electricity every year.[51]

#### 1.4.1.1.1 Key components of a DSSC

The structure of a conventional DSSC is illustrated in Figure 1.6. A typical DSSC is mainly composed of five components;

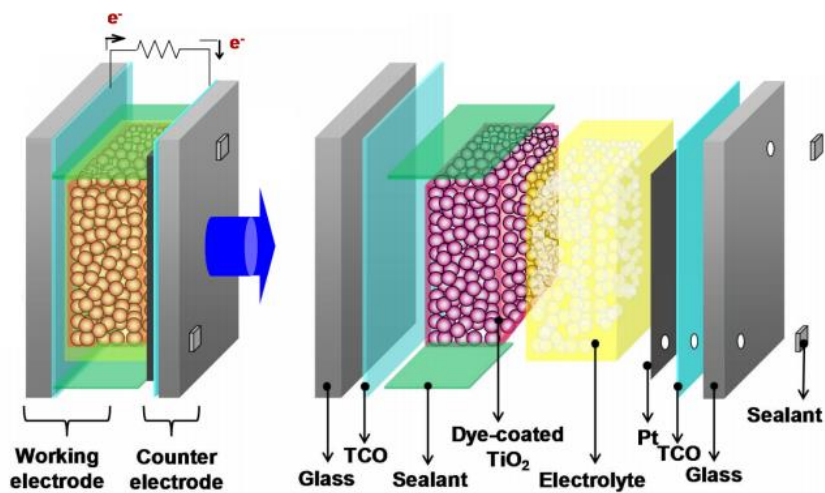


Figure 1.6: Schematic diagram [59] of a typical DSSC, individual components are shown in details on the right

A transparent conducting oxide substrate, a mesoporous wide-band gap semiconductor thin film (also known as the photoanode), a photosensitizer i.e. dye molecules adsorbed on the mesoporous photoanode, a redox-couple electrolyte, and finally a CE to complete the cell.

#### **1.4.1.1.1. Transparent conducting substrate**

To fabricate the TCO substrate, a thin layer of ~200 nm of TCO film is coated on glass substrates. Glass substrates offer good protection against penetration of water or oxygen.[60] The principal criteria for choosing a TCO layer is (i) it has to be optically transparent in a major portion of the AM 1.5G solar spectrum to be able to transmit the incident photons to the light absorber of DSSC, and (ii) it has to be electrically conductive (low sheet resistance) to be able to extract the electrons to the outer circuit. For DSSC applications, FTO or ITO based thin films fabricated with RF magnetron sputtering[61] are commonly used as the because of their low sheet resistance (5-15  $\Omega/\square$ ),[60] high optical transparency in the solar spectrum and relatively low cost.[59] Moreover, to get a higher conductive film i.e. with low sheet resistance, results in a film with lower transmittance, typically FTO has a sheet resistance of ~15  $\Omega/\square$  with a transmittance of ~85% in the visible region.[62] ITO is not preferred since the sheet resistance of an ITO coated film sharply increases with temperatures above 350 °C, [61] which is necessary for sintering of the photoanode of a typical DSSC.

#### **1.4.1.1.1.2. Nanocrystalline photoanode**

In the early literature, a monolayer of semiconductor material was used in PEC systems, which limited the amount of dye that could be adsorbed on the surface of the semiconductor material, thereby leading to a limited absorption of sunlight.[63] By introducing a mesoporous structure of nanoparticles the surface area can be enhanced 1000-fold compared to a thin film of similar thickness.[63] The efficiency of dye solar cells was limited to less than 1% until the major

breakthrough of Grätzel with the introduction of a mesoporous photoanode in 1991.[50] This is because, the nanocrystalline mesoporous network provided a high surface area for maximizing the absorption of the dye molecules.[64]

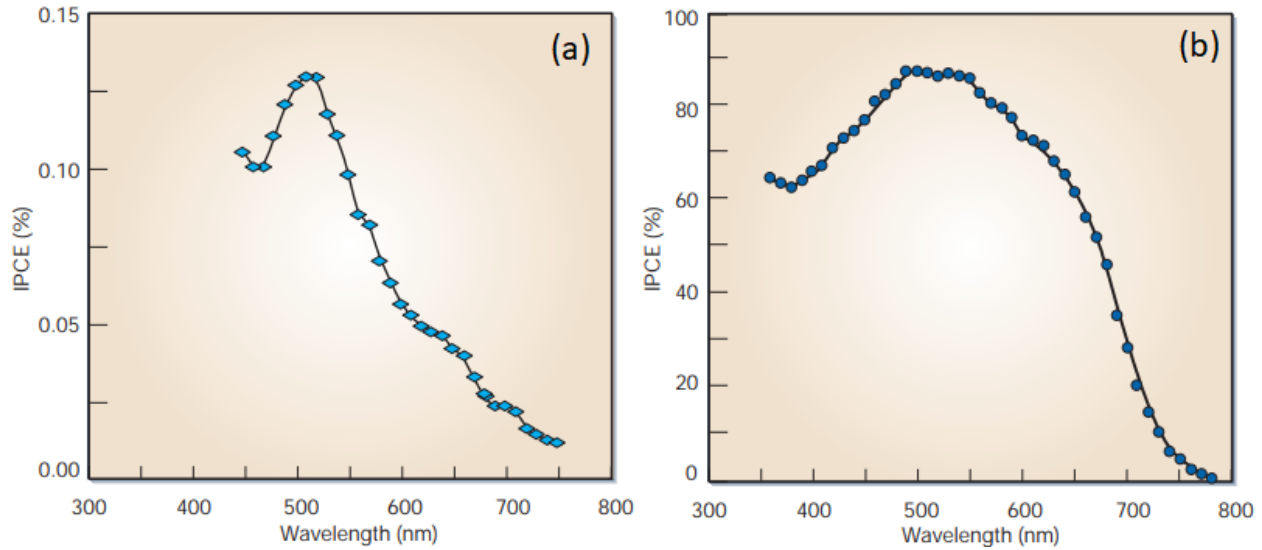


Figure 1.7: The effect of using a mesoporous photoanode in DSSCs: IPCE as a function of the excitation wavelength; (a) Single-crystal anatase TiO<sub>2</sub> cut along (101) plane, (b) Mesoporous anatase TiO<sub>2</sub> film. In both cases, TiO<sub>2</sub> photoanodes were sensitized by the same dye and same electrolyte was used.[16]

Commonly, wide band gap semiconducting materials are chosen as photoanode for a typical DSSC. The semiconductor materials, which possess an energy band gap of an excess of 3 eV are specified as wide bandgap semiconductors, since they cannot absorb visible light radiation. The incident light radiation (except UV radiation) passes through the wide band gap semiconductors, so that it can be efficiently absorbed by the adsorbed dye molecules on their surface. Wide bandgap semiconductors have proven to be potential electron acceptors in DSSCs.[60] To fabricate the photoanode of a DSSC, usually, the nanocrystalline wide band gap semiconducting metal oxide coating is applied on the top of the TCO substrate by the screen printing or doctor blading technique. In this thesis, we fabricate the mesoporous photoanode mainly by doctor blading a paste

of the nanocrystalline semiconducting metal oxide. The photoanode architecture of the DSSC is the focus of our research in this thesis, and will be explained in more detail. The advantage of using a mesoporous photoanode in DSSCs has been depicted in Figure 1.7, where IPCE is plotted as a function of wavelength, the values of IPCE are three orders of magnitude higher[16] for the mesoporous anatase TiO<sub>2</sub> film, in comparison to the single-crystal anatase TiO<sub>2</sub> cut along (101) plane.

#### 1.4.1.1.1.3. Dye sensitizer

The photosensitizer dye, acts as the primary absorber of incident solar radiation and is one of the major components of a DSSC. When a DSSC is illuminated, the dye molecules should absorb the incident photons, generate excitons i.e. electrons in the LUMO and holes in the HOMO, and the excited electrons should be injected efficiently in the CB of the photoanode.

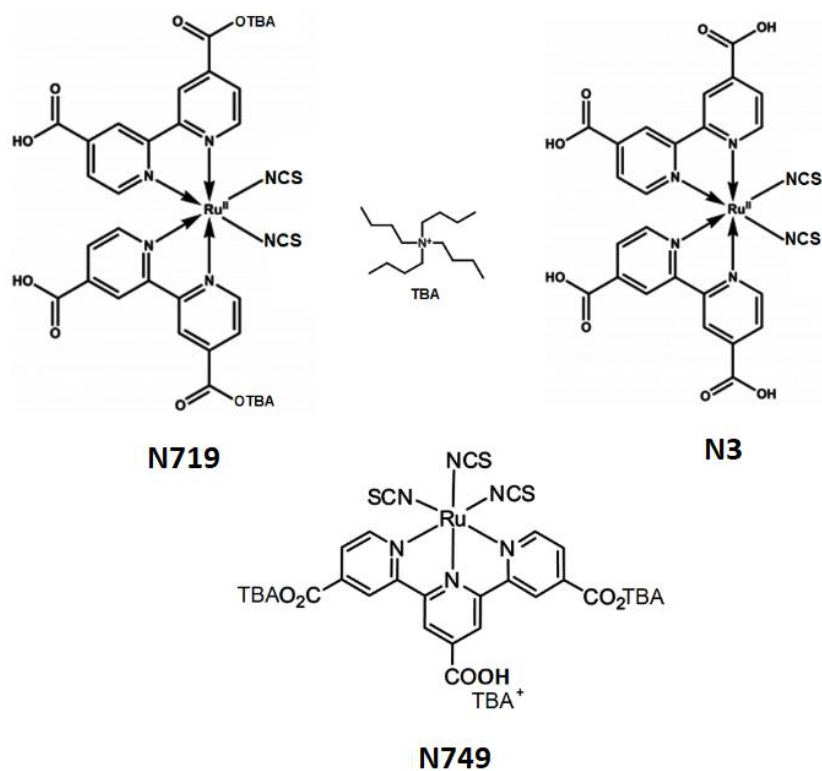


Figure 1.8: Examples of several Ruthenium polypyridyl dyes used in DSSCs.[65]

To be an efficient photosensitizer, the dye molecules should conform to the following essential requirements. (i) The dye molecules must strongly bind onto the surface of the photoanode nanoparticles with the help of an anchoring group for efficient electron injection and to prevent recombination with the electrolyte, rich in holes.[66] (ii) The LUMO or the excited state of the dye must be energetically at a slightly higher position than the CB of the photoanode material, for efficient electron injection and minimization of energetic potential losses[60] and (iii) the HOMO or the ground state of the dye must be energetically at a lower position compared to the redox potential level of the electrolyte for efficient regeneration[60,67] of the oxidized dye. (iv) The dye should absorb light, covering a broad span of wavelengths. (v) The electron injection from the dye to the photoanode should be faster than recombination of electrons from the excited state to the ground state of the dye.[66,68] Photosensitizers can be classified mainly into three categories, namely, metal complex sensitizers,[69] natural sensitizers,[70] and organic sensitizers.[71] Although, transition metals based photosensitizers are considered to be the most suitable option for DSSCs.[72] Figure 1.8 demonstrates[65] the three main Ruthenium polypyridyl dyes used in DSSCs, which yield PCE over 10 %.[73]

#### **1.4.1.1.1.4. Redox Electrolyte**

The redox shuttle electrolyte plays a key role in facilitating charge transfer in a typical DSSC. The electrolyte regenerates the oxidized dye and thereby completes the electron transportation between the photoanode and the counter-electrode, via the load. The essential requirements for an ideal electrolyte are: (i) The redox potential level must be energetically at a higher position than the HOMO of the dye molecules, to be able to regenerate the dye. (ii) On the other hand, the redox potential level should not be at a sufficiently higher position, or else it may reduce the open circuit voltage ( $V_{oc}$ ) of the DSSC.[74] (iii) The electrolyte should not have strong absorption in the visible

spectrum. (iv) Electron transfer rate should be very fast from the CE to the electrolyte. (v) The electrolyte should be chemically inert to other components of the DSSC.[59,75] (vi) The redox-couple must be completely soluble in the solvent, to guarantee high charge carrier concentration.[59] Typically, in DSSCs, Iodide/triiodide ( $I^-/I_3^-$ ) in acetonitrile is commonly used as an electrolyte because of the proven versatility of the redox couple and excellent long-term stability.[76]

#### **1.4.1.1.1.5. Counter electrode**

The role of a CE in a conventional DSSC is to transfer the electrons from the external circuit to replenish the redox electrolyte. Furthermore, it can act as a reflector for the light transmitted by the photoanode, thereby increasing the light absorption. The CE is a FTO glass coated with a thin layer of platinum (Pt). Pt shows high catalytic activity and stability towards the  $I^-/I_3^-$  iodide/triiodide redox electrolyte.[77–79] Pt is an expensive element, but only a thin layer, ~ few nanometers on the FTO substrate exhibits an excellent thermal and electrical conductivity[80] with high catalytic activity, but does not increase the overall cost of the cell to a great extent. However, extensive research effort has been conducted to look for alternative CE materials to replace Pt. Potential materials such as transition metal carbides/nitrides/oxides, carbon materials, conducting polymers has been investigated to fabricate a low cost Pt-free CE.[80,81]

#### **1.4.1.1.2. Working Mechanism of a DSSC**

The working mechanism of a typical DSSC is illustrated in Figure 1.9. A conventional DSSC is fabricated on a glass substrate coated with a transparent conducting layer such as FTO. In our experiments, we create a mesoporous photoanode of  $SnO_2$  by simple doctor blading technique and sensitize with dye molecules, which absorb sunlight. The DSSC is closed with a Pt counter

electrode and a redox couple electrolyte is injected inside the DSSC, which acts a hole transporting medium. The detailed working mechanism of a DSSC is explained below:

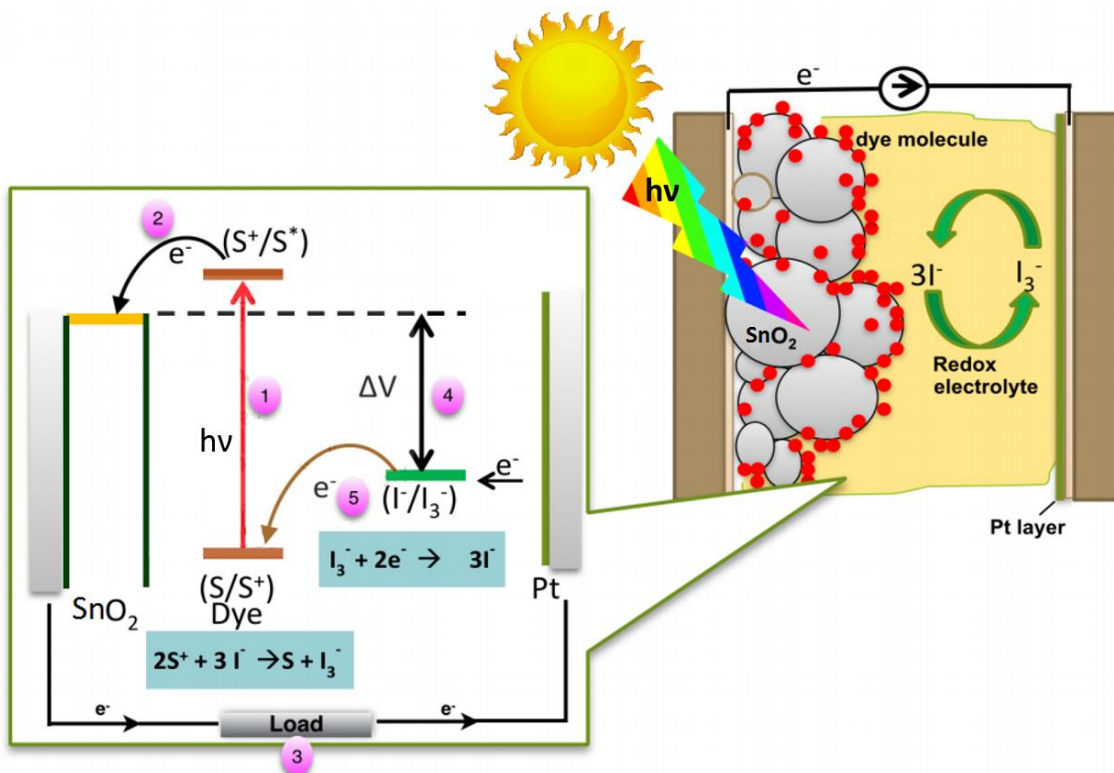


Figure 1.9: A schematic representation of a typical DSSC illustrating the different charge transfer mechanisms;[59] The structure of a classical DSSC is shown in the inset.

1. The dye molecules absorb photons upon light irradiation and promotes an electron from the ground state (HOMO) to the excited state of the dye (LUMO). The excited state of the photo sensitizing dye is denoted as  $S^*$ , as shown in eqn. 1.3:

**Light absorption by the photo sensitizing dye**



2. The electrons excited to the LUMO of the dye are injected to the CB of the semiconductor photoanode (PA) and the dye sensitizer is oxidized to  $S^+$ , as shown in eqn. 1.4:

### Electron injection



3. The electrons injected in the conduction band of the mesoporous PA traverse through the nanocrystalline architecture of the PA via diffusion mechanism and reach the CE through the FTO and outer circuit thereby performing electrical work, as shown in eqn. 1.5:

### Electron transportation



4. The electron from the redox couple electrolyte restores the original state (S) of the photo sensitizing dye and thereby itself gets reduced and shown in eqn. 1.6:

### Dye regeneration



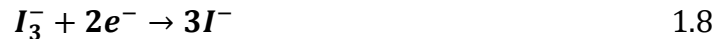
However, the electron in the PA can recombine with oxidized sensitizer, shown in eqn.1.7:

### Recombination



5. At the CE, the iodide is regenerated by reducing tri-iodide by receiving an electron from the outer circuit, shown in eqn. 1.8:

### Iodine regeneration



#### 1.4.1.1.3. Dynamic competition in a DSSC

The performance of a typical DSSC depends on the dynamic competition between the different charge transfer and charge transport processes and several recombination reactions, which hinder

the charge transport mechanism. Mainly, the beneficial processes for a DSSC are light absorption by the sensitizer, electron injection from the sensitizer to the photoanode, charge transport in the photoanode and the regeneration of the dye sensitizer.

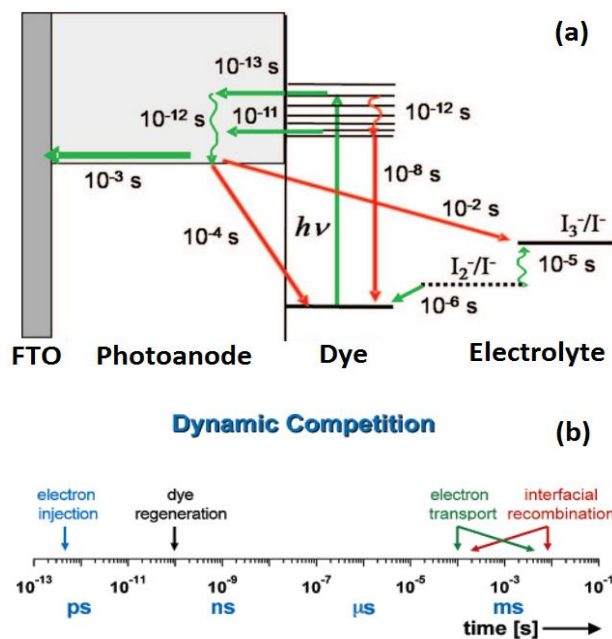


Figure 1.10: Different charge transport and recombination mechanisms in a typical DSSC.[82] Time scale of different processes in a DSSC.[83]

The main processes that hinder efficient charge transport are the relaxation of the excited electron in the sensitizer and the recombination of the injected electron in the photoanode to the oxidized dye and electrolyte. Usually, the injection of the photoexcited electron occurs in the time regime of fs to ps,[84] and the excited state lifetime of the dye in case of Ru- complexes are in the order of tens of ns,[85,86] thus in most cases electron injection is most likely than relaxation of electrons in the dye. For DSSCs to be practically implementable, the life cycle has to be over  $10^8$ ,[82] the regeneration of the dye should be in the range of  $\mu$ s which is found for best Ru-complex dyes.[87] The charge transport within a photoanode of a DSSC takes place by electron hopping[82] from

one nanocrystal to the next via diffusion mechanism, which is generally less than ms. This competes with the recombination of the injected electron to the holes in the electrolyte, which represents the electron lifetime and is generally in ms to seconds time scale.[83] The different charge transfer mechanisms and recombination and the time scales are demonstrated in Fig. 1.10.

#### 1.4.1.1.4. Role of the photoanode of a DSSC

The photoanode of the DSSC is the most crucial component, which determines the overall performance of the cell. Due to its importance, the photoanodes have fascinated researchers around the globe much more than any other component of the DSSC. Figure 1.11 demonstrates [67] the importance of photoanodes in DSSC in terms of publication interest.

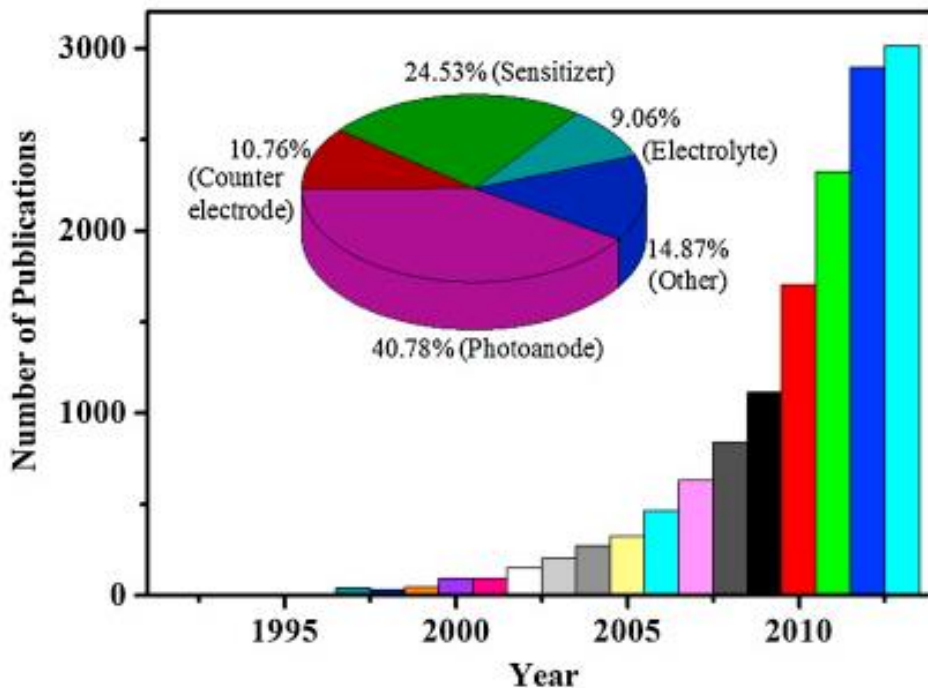


Figure 1.11: Evolution of the number of research publications in DSSC. Inset shows the distribution of publications for each DSSC component in 2012.[67]

The essential criteria for a photoanode of a DSSC are:

- **High surface area:** The photoanode must possess a high surface to volume ratio, to be able to anchor enough quantity of dye molecules. Large number of dye molecules will increase the photon absorption and thereby generate enough photoelectrons to contribute to the photocurrent density. Hence, increasing the overall PCE of the device.[50,64]
- **Suitable band alignment:** The CB of the photoanode should be in a favorable position energetically with the LUMO of the dye for efficient electron injection. The CB of the photoanode material must be energetically at a slightly lower position than the LUMO of the dye for minimization of energetic potential losses.[60]
- **High electron mobility:** The electron transport in a DSSC occurs by electron hopping from trap states present in the nanocrystalline photoanode which occurs in the ms time regime. For an electron to be collected by the outer circuit it has to partake in dynamic competition with the recombination processes, thus high electron mobility in the photoanode will ensure efficient electron transport.

#### 1.4.1.1.5. DSSC photoanode material

Essentially, a thin nanocrystalline layer of wide-band gap semiconductor with high surface roughness[50,64] is considered as a potential electron acceptor and utilized as a photoanode material in a DSSC. Among different wide-band gap oxide materials, such as TiO<sub>2</sub>,[88,89] SnO<sub>2</sub>,[90–92] ZnO,[93,94] Nb<sub>2</sub>O<sub>5</sub>,[95] WO<sub>3</sub>[96] and other ternary oxides like Zn<sub>2</sub>SnO<sub>4</sub>,[97] TiO<sub>2</sub> is the common preference for DSSCs because of its low-cost, availability, non-toxicity and good chemical stability.[85] Depending on the annealing temperature, TiO<sub>2</sub> can exist in three crystalline phases, namely anatase, rutile and brookite.[98–100] However, anatase TiO<sub>2</sub> is widely used as the

photoanode in DSSCs because of its wider band gap,  $E_g = 3.2$  eV for anatase in comparison to  $E_g = 3.0$  eV for rutile structure, which corresponds to an absorption edge of  $\lambda_g \sim 390$  nm for anatase  $\text{TiO}_2$  and  $\lambda_g \sim 410$  nm for rutile  $\text{TiO}_2$ . [101] Since the position of the valence bands are similar [102] for both the crystalline phases, the wider band of anatase  $\text{TiO}_2$  translates to a higher conduction band edge, which leads to higher Fermi level and open circuit voltage,  $V_{oc}$  in anatase  $\text{TiO}_2$  DSSCs. [72]

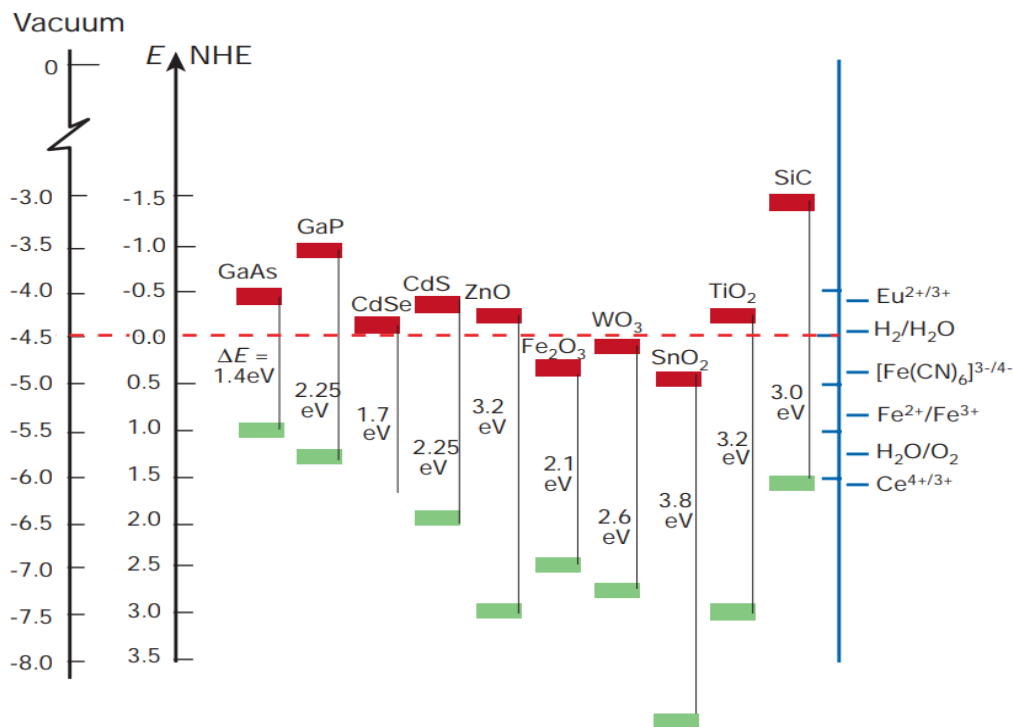


Figure 1.12: Energy band positions [16] of different semiconductors with reference to normal hydrogen electrode (NHE) or the vacuum level.

Usually, the ZnO photoanode based DSSC is considered to be an alternative where anatase  $\text{TiO}_2$  is not used. The valence and conduction band positions of ZnO is very similar to anatase  $\text{TiO}_2$ , which is demonstrated in Fig. 1.12. Thus, energetically, ZnO has the same advantages as anatase  $\text{TiO}_2$ . Additionally, ZnO has higher electron mobility than anatase  $\text{TiO}_2$ , which facilitates electron

transport within the photoanode. However, the poor stability of ZnO in both acidic and basic solutions limits its use. Carboxylic acid anchoring groups present in a typical DSSC dissolve ZnO resulting in  $Zn^{2+}$  ions.[63] These  $Zn^{2+}$  ions form insoluble complexes along with commonly used ruthenium dyes such as N3 and N719.[63] The insoluble complexes, then precipitate in the mesoporous photoanode structure[63] and hinder charge transfer processes.

#### 1.4.1.1.6. Various photoanode architectures in DSSCs

Typically nanoparticles of size  $\sim 18\text{-}20$  nm are utilized to fabricate the photoanode using different techniques such as doctor-blading,[50,64] screen printing,[103,104] etc., which can provide a large surface area for dye adsorption as well as a relatively high porosity[105] for efficient dye penetration. Although this photoanode consisting of small nanoparticles is effective for dye sensitization, there is no scattering for the incoming light since they are transparent to the visible spectrum, thereby hindering light harvestation.[106,107]

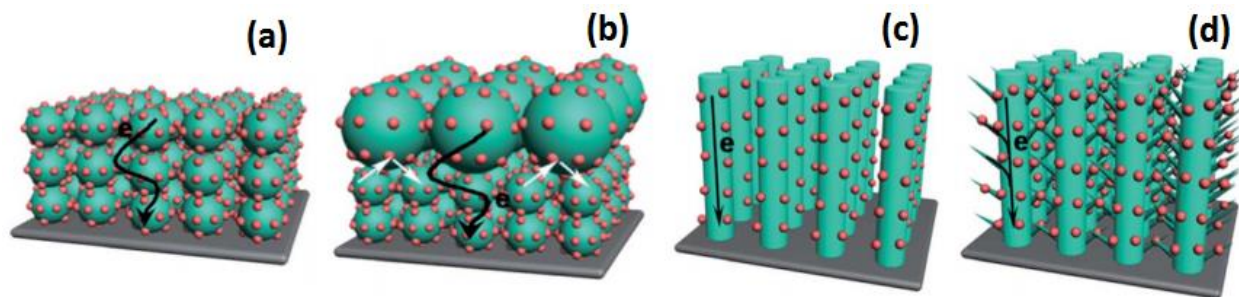


Figure 1.13: (a) Typical photoanode structure consisting of small nanoparticles presenting random electron transport pathways; (b) bi-layer photoanode structure where light is scattered by the top layer of bigger nanoparticles; (c) directional electron transport in 1D nanowires and (d) hierarchical 1D nanowire architectures.[105]

In order to scatter the incident light back to the photoanode, which would typically pass through un-absorbed in a traditional photoanode, a bi-layer structure was implemented. The second layer

of large nanoparticles, usually ~200-500 nm in size, are also doctor-bladed on top of the transparent film. These large nanoparticles trap the incoming light radiation within the photoanode, thereby increasing the light harvesting efficiency.[108–111]

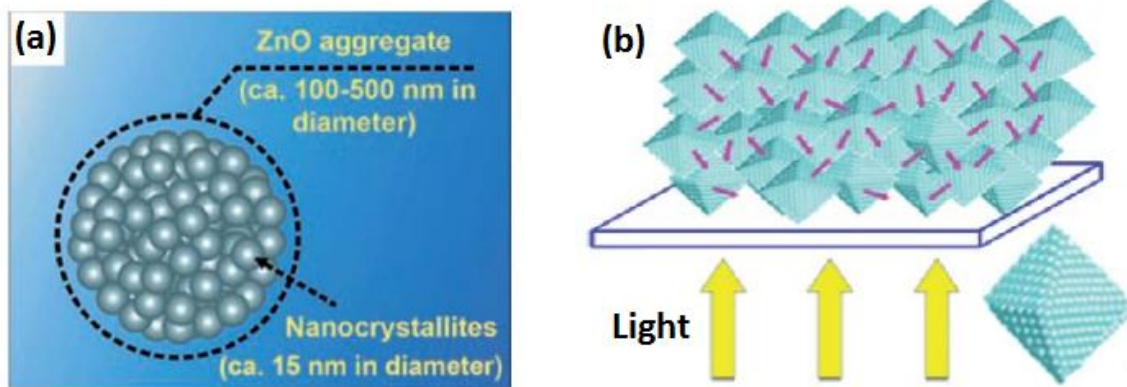


Figure 1.14: (a) Schematic representation of a hierarchical ZnO sphere consisting of densely packed ZnO nanoparticles;[112] (b) Enhanced light-scattering effect in a photoanode based on SnO<sub>2</sub> octahedra, the structure of a SnO<sub>2</sub> octahedra is shown on the bottom right.[113]

Furthermore, incorporation of one dimensional (1D) nanostructures in the photoanode, such as nanowires, nanorods has improved electron collection efficiency in DSSCs.[105] 1D nanostructure based photoanodes have generated considerable interest because of their high crystallinity, and low surface defects, which can promote electron transport and reduce interfacial recombination.[105,114–116] Moreover, the internal electric field present in 1D nanostructures drives the transport of photoinjected electrons,[105] and can extend the diffusion length to be as long as ~100  $\mu\text{m}$ .[117] Different photoanode structures including bi-layer and 1D nanostructures are depicted in Fig. 1.13. Bi-functional spherical ZnO nanoparticle assembly architectures were developed by Zhang et al.[112] have been demonstrated in Fig. 1.14 (a) The 100-500 nm sized hierarchical ZnO spheres constituted of densely packed small ZnO nanoparticles of 15 nm in diameter. The aim of the bi-functional structure was to provide a high surface area for dye loading

by small nanoparticles, and enhanced light scattering with the help of sub-micron sized hierarchical ZnO aggregates.[112,118,119]

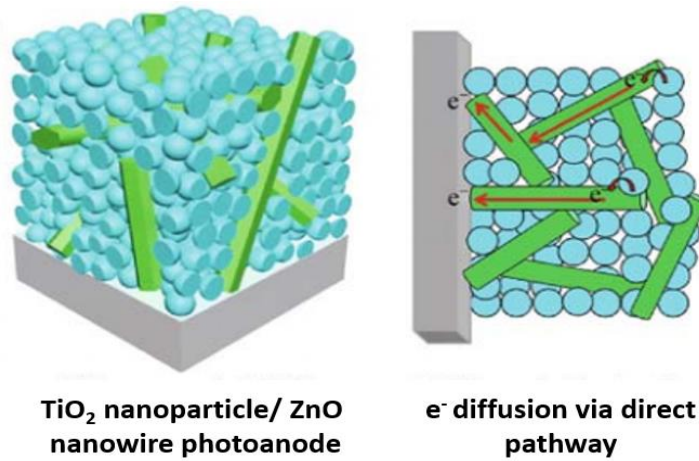


Figure 1.15: Schematic illustration of a TiO<sub>2</sub> nanoparticle/ZnO nanowire composite photoanode.[120]

Other hierarchical structures include SnO<sub>2</sub> octahedrons of ~1 μm in size that was constructed by small SnO<sub>2</sub> nanoparticles of ~30 nm in size, which is illustrated in Fig. 1.14 (b). In spite of the fact that the surface area to volume ratio of the SnO<sub>2</sub> octahedrons was decreased in comparison to the SnO<sub>2</sub> nanoparticles, the hierarchical structure showed enhanced photovoltaic performance, which was attributed to light scattering effect.[105,113]

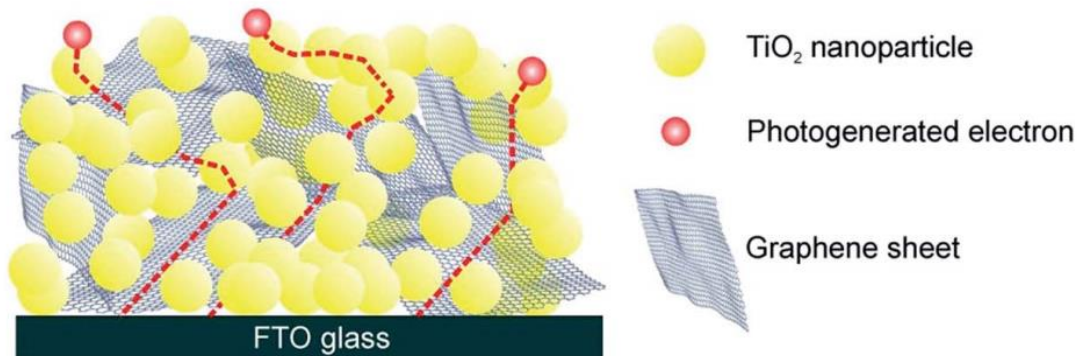


Figure 1.16: Schematic representation of improved charge collection mechanism in a photoanode based on a graphene network embedded in a TiO<sub>2</sub> nanoparticle network.[121]

Composite photoanode architectures using not only different structures but implementing different wide band gap semiconductors were reported by Bai et al. Small amounts of ZnO nanowires were used in a mesoporous network of TiO<sub>2</sub> nanoparticles. The ZnO nanowire network not only increase the light scattering within the photoanode but also promote electron transfer. The advantageous effect of incorporating ZnO nanowires[120] is illustrated in Fig. 1.15. Various carbon materials such as graphene, SWCNTs, MWCNTs, reduced graphene oxide, nitrogen doped graphene oxide were incorporated within the TiO<sub>2</sub> nanoparticle matrix to increase the electron mobility in the photoanode.[121–126] CNTs[123] and graphene microplatelets[121] possess high transparency and high electrical conductivity.[121] The absorbance of a monolayer of graphene sheet in the visible range is ~ 2.3%.[121] So, the addition of a small amount of graphene in the photoanode does not affect the transparency,[121] but creates an electron percolating network. Graphene microplatelets incorporated in a TiO<sub>2</sub> nanoparticle matrix (illustrated in the schematic in Fig. 1.16), not only offers fast electron transport within the photoanode, but also facilitates fast collection of electrons[121] in the FTO. The introduction of MWNTs in the photoanode also reduces electron recombination and enhances the roughness factor.[124,127] In chapter 4.2 of our thesis we have introduced graphene based photoanodes to boost the performance of our DSSCs.

#### **1.4.1.1.7. SnO<sub>2</sub> as a photoanode of DSSCs**

TiO<sub>2</sub> photoanode based DSSCs have reached the highest efficiencies to date, essentially due to low overpotential w.r.t commonly used dyes and high surface to volume ratio. Also, the superior dye loading of anatase TiO<sub>2</sub> and ZnO, which results from the high isoelectric point of TiO<sub>2</sub> (pH 6-7) and ZnO (pH ~9) in comparison to low isoelectric point of SnO<sub>2</sub> (pH 4-5), which facilitates higher photocurrent density in TiO<sub>2</sub> and ZnO.[128,129] However, SnO<sub>2</sub> has been utilized in dye sensitization since the beginning of 1980's.[130–132] Since, charge transport in DSSCs is

diffusion mediated, electron mobility is one of the key characteristics, which defines efficient electron percolation. One of the most attractive properties of SnO<sub>2</sub> is high electron mobility compared to other widely used semiconductors in DSSCs.

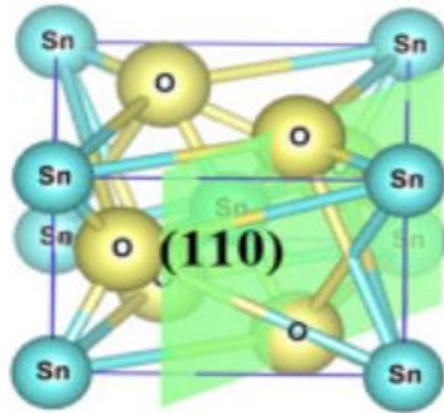


Figure 1.17: Schematic diagram of tetragonal rutile crystal structure of SnO<sub>2</sub>, [132] the (110) crystal plane shown in green.

The electron mobility ( $\mu_e$ ) of SnO<sub>2</sub> is  $\sim 250 \text{ cm}^2 \text{ V}^{-1} \text{ s}^{-1}$  for single crystals and  $\sim 150 \text{ cm}^2 \text{ V}^{-1} \text{ s}^{-1}$  in the case of nanostructures, which is orders of magnitude higher than that of its main competitor TiO<sub>2</sub> which has an electron mobility  $\mu_e \sim 1 \text{ cm}^2 \text{ V}^{-1} \text{ s}^{-1}$  in single crystals and  $\sim 10^{-5} \text{ cm}^2 \text{ V}^{-1} \text{ s}^{-1}$  in nanostructures. [132–136] Electron mobility can be estimated by  $\mu_e = e \frac{\tau_s}{m_e}$ , where  $e$  is the electronic charge,  $\tau_s$  is the collision frequency and  $m_e$  is the effective mass. [132] The high electron mobility of SnO<sub>2</sub> is achieved because of its low effective mass  $m_e \sim 0.17\text{--}0.30 m_o$  [137–139] whereas, the high effective mass  $m_e \sim 1\text{--}50 m_o$  [140–143] in case of TiO<sub>2</sub> limits its electron mobility. The schematic diagram of the tetragonal rutile crystal structure of SnO<sub>2</sub> is demonstrated in Fig. 1.17. In this SnO<sub>2</sub> crystalline structure, each Sn atom is placed at the center of an octahedron, which is surrounded by six oxygen atoms. [132,144] The lattice parameters of the rutile structure are  $a = b = 4.737 \text{ \AA}$ ,  $c = 3.18 \text{ \AA}$ . The (110) crystal plane with an interplanar spacing,  $d_{110} = 3.3470 \text{ \AA}$ , is

shown in the Fig. 1.17, which has the most prominent peak in tetragonal rutile SnO<sub>2</sub>. In our thesis, devices with SnO<sub>2</sub> rutile structure has been studied in depth.

#### **1.4.2 Hydrogen Production from solar energy**

Hydrogen is a non-carbon based energy resource,[145] which has the potential to replace fossil fuels since the by-product upon combustion is water. Moreover, molecular H<sub>2</sub>, which has the highest energy content per unit weight[146] drives the quest towards building a hydrogen driven economy. Although H<sub>2</sub> itself is a clean energy resource, the present industrial production of H<sub>2</sub> fuel mainly relies on the use of fossil fuels. Natural gas, oil, coal, and electrolysis are the main sources for producing hydrogen commercially.[147] In the industry, mass production of hydrogen is usually carried out via steam reforming of methane or natural gas, which is the most cost effective at present.[148] This process involves an endothermic reaction, reaching temperatures above 1000 °C in the presence of steam. This reaction splits the methane molecules and carbon monoxide (CO), H<sub>2</sub> are formed. The major drawback with the present industrial H<sub>2</sub> manufacturing is that, it is mainly dependent on fossil fuels, for example, steam methane reforming, which is one of the cleanest H<sub>2</sub> generation processes, produces ~10 kg CO<sub>2</sub> per kg of H<sub>2</sub>. [149]

The necessity for H<sub>2</sub> generation and the challenges with current methodologies to derive the same, motivates us to look for more possibilities. Although H<sub>2</sub> production by electrolysis is considered to be a solution, but the electricity required for electrolysis of water may be derived from fossil fuel-based resources. To rule out those possibilities, solar energy can be considered as a potential energy resource to split water into its constituents O<sub>2</sub> and H<sub>2</sub>. H<sub>2</sub> production from solar energy is considered to be the ultimate solution for sustainable energy[150] as it is green-house emission free and it utilizes the two most abundant and readily available resources sunlight and water.

Utilizing the thermal energy from the sun, water molecules can be directly split, with or without the assistance of some other additional intermediate chemicals.[151] Some examples of H<sub>2</sub> production from solar energy include thermolysis, thermal decomposition and thermochemical methods.[152] In principle, direct water decomposition starts at temperatures above 2000 °C, without the use of additional chemicals.[151] Although, presently, high temperatures up to 3500 °C can be attained by solar concentrating furnaces,[153,154] the temperature of direct thermolysis is very high for building the apparatus required and the selection of refractory materials.[152] Moreover, the product of thermolysis process is a mixture of hydrogen and oxygen gas, which pose a considerable threat for explosion[152] at such an elevated temperature. Thus, direct water thermolysis has to undergo radical development to become an industrial practice.

#### 1.4.2.1 Hydrogen generation using PEC cells

In 1972 scientists Fujishima and Honda constructed a photoelectrochemical cell,[155] which decomposed water into hydrogen and oxygen (illustrated in Fig. 1.18). TiO<sub>2</sub> was used as the photoanode, and platinum as the cathode immersed in water. In their pioneering work, they observed that when a TiO<sub>2</sub> photoanode was illuminated by UV light, oxygen evolution occurred at the TiO<sub>2</sub> photoanode and H<sub>2</sub> at the cathode.

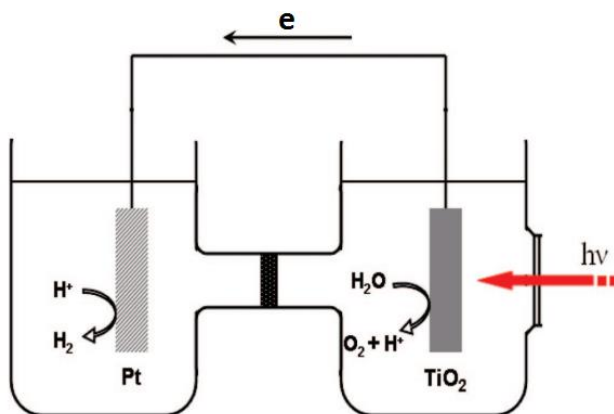


Figure 1.18: Schematic diagram of the PEC cell used by Fujishima and Honda.[155]

Upon excitation by a simulated sunlight source, the photocatalyst such as TiO<sub>2</sub> absorbs UV and/or visible irradiation, and the valence band electrons in the photocatalyst are promoted to the conduction band, leaving behind holes in the valence band. These are termed as excitons. After the photoexcitation, the excitons migrate to the photocatalyst surface. The water molecules are reduced by the electrons to form H<sub>2</sub> and are oxidized by the holes to form O<sub>2</sub> to complete the overall water splitting reaction. This phenomenon of exciton generation when the incident illumination energy is higher than the band gap of the photocatalyst, and the H<sub>2</sub> and O<sub>2</sub> evolution has been demonstrated in Fig. 1.19.

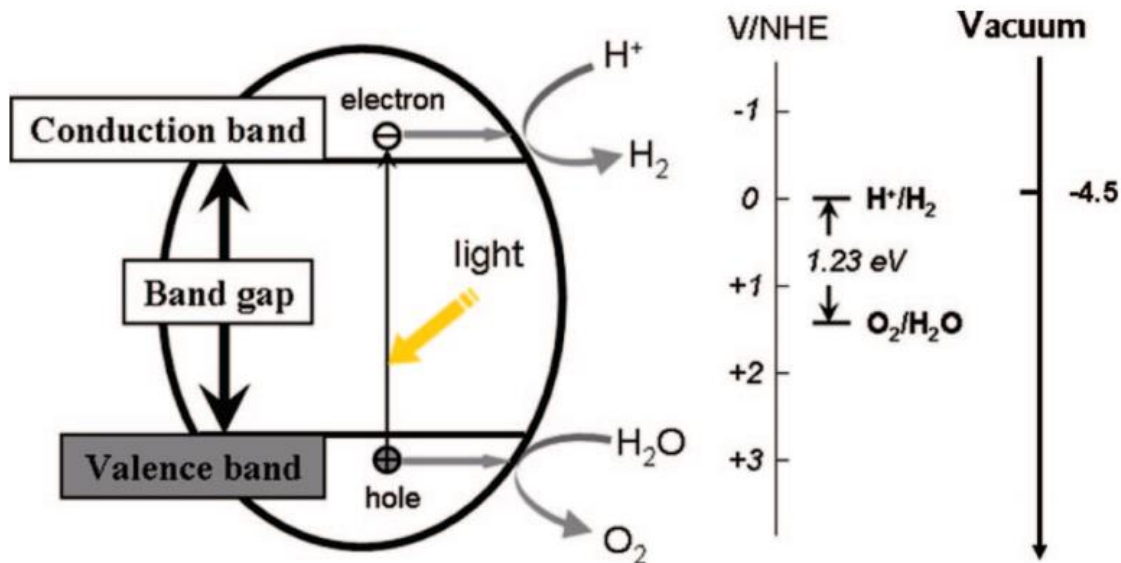
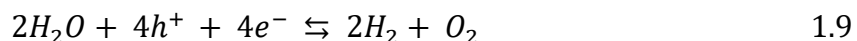


Figure 1.19: Fundamental mechanism of semiconductor-based photocatalytic water splitting for hydrogen generation.[156]

Under normal conditions, to achieve photoelectrochemical water splitting, an incident energy of  $\Delta G = 237.1$  kJ/mol is required which corresponds to a thermodynamic electrochemical potential of 1.23 V.[157] The overall water splitting reaction is shown in equation 1.9. The two reactions occurring, i.e. the OER is represented in equation 2.0 and the HER is shown in equation 2.1





For efficient PEC water splitting, the band gap energy ( $E_g$ ) of the photocatalyst must be  $>1.23$  eV. Additionally, The conduction band minima of the photocatalyst must be more negative than the reduction potential of  $H^+/H_2$  (0 V vs NHE), whereas the valence band maxima must be more positive than the oxidation potential of  $O_2/H_2O$  (1.23 V).[156]

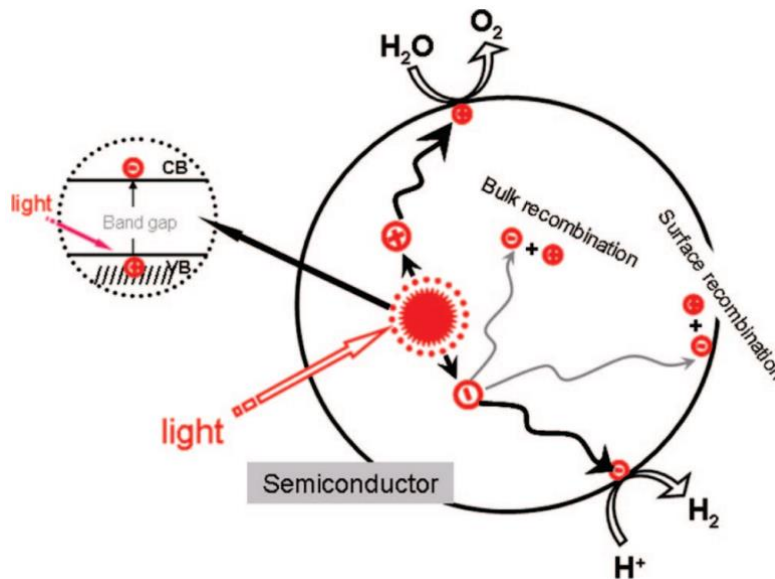


Figure 1.20: The main processes for charge transport and recombination in photocatalytic water splitting.[156]

The major processes in the photocatalytic hydrogen generation system are illustrated in Fig. 1.20. All the different processes such as light absorption by the semiconductor photocatalyst, generation and separation of excitons, migration of the electrons and holes to the surface of the photocatalyst, bulk and/or surface recombination of the electrons, as well as transfer of excited charges to water or other molecules affect the final generation[156] of hydrogen from the semiconductor

photocatalyst system. The amount of excited electrons in the water/ photocatalyst interface determines the total amount of hydrogen evolution.[156]

### 1.4.2.1.1 Semiconductor photoanodes for PEC cells

Since Honda-Fujishima's pioneering work on PEC water-splitting, there has been immense interest in the scientific community in developing semiconductor materials for efficient photoelectrodes.

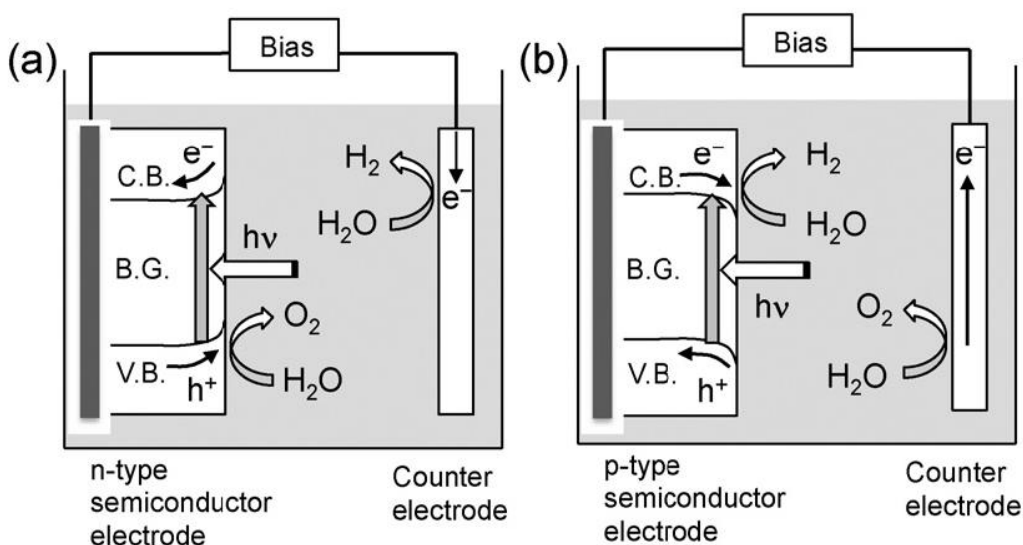


Figure 1.21: PEC based water splitting systems implementing (a) n-type semiconductor photoanode, and (b) p-type semiconductor photocathode.[158]

Fig. 1.21 illustrates the different PEC water splitting setups, Fig. 1.21 (a) shows a PEC setup based on n-type semiconductors and Fig. 1.21 (b) demonstrates a typical PEC setup based on p-type semiconductors. In the configuration shown in Fig. 1.21 (a), when an n-type semiconductor absorb photons with energies higher than its band gap, excitons are created. The excited electrons migrate to the CE through the external circuit and reduce water to generate  $H_2$ . The holes, on the other hand, reach the semiconductor surface to oxidize water into  $O_2$ . Whereas, in the configuration

shown in Fig. 1.21 (b), water gets reduced on the semiconductor surface to produce  $H_2$ , while  $O_2$  is generated at the CE by oxidizing water.[158] In chapter 4.3 of our thesis, we utilize a PEC setup using heterostructured photoanodes in the configuration shown in Fig. 1.21 (a). Traditionally, wide band gap semiconductor oxides, which exhibit excellent stability against photocorrosion are utilized as photoanodes.[158]

#### 1.4.2.1.1.1 Quantum Dot based PEC cells

Wide band gap semiconductors like  $TiO_2$  perform exceptionally in PEC systems because of their excellent stability against photocorrosion, but a major drawback in wide band gap semiconductors is that they can only absorb UV radiation. QDs which possess size tunable optical properties can extend the absorption of wide band gap semiconductors to the visible and near IR spectrum.

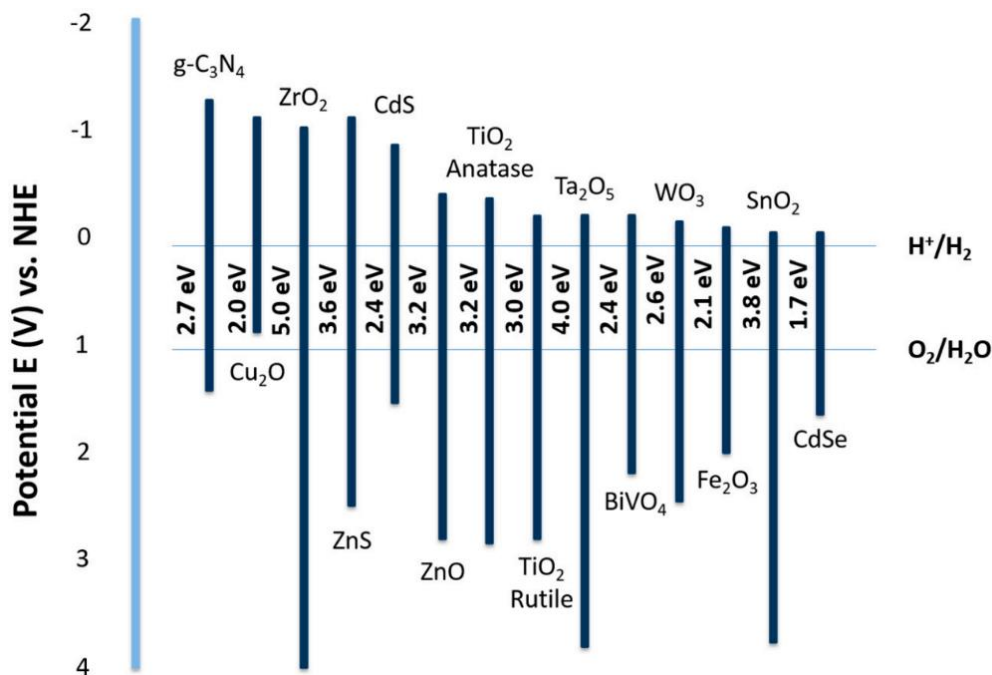


Figure 1.22: Band structure of different semiconductors with respect to the redox potentials of water splitting.[18]

The band edge positions of different semiconductors with respect to the redox potentials of water splitting are presented in Fig. 1.22. Since QD sensitized photoanodes can expand the absorption range of wide band gap semiconductors higher H<sub>2</sub> generation efficiencies can be achieved.[159,160] Although QD sensitized PEC cells have been extensively studied for their excellent efficiency in H<sub>2</sub> generation, stability is still a major setback, which drives the quest for a highly stable photoanode material for QD based PEC cells. The poor stability in the QD based PEC cells, mainly originates from the formation of UV induced deep traps[161] in metal oxides such as TiO<sub>2</sub>, which promotes the formation of excess holes in TiO<sub>2</sub>. These holes act as non-radiative recombination centres, which largely contribute to the photooxidation process of the QDs. In this thesis, we introduce novel SnO<sub>2</sub>-TiO<sub>2</sub>/ graphene photoanodes to alleviate this issue.

# Chapter 2

## 2.1 Research objectives

This thesis is divided into two parts with two corresponding objectives:

### 2.1.1. Part I: Fabrication and characterization of DSSCs with novel heterostructure photoanode

DSSCs have been emerging as an alternative to conventional silicon PV devices over the past two decades because of their low cost, abundant raw material and facile fabrication process. Compared to traditional semiconductors in p-n junction solar cells, the semiconductor material in a DSSC photoanode is allowed to have lower purities, hence reducing the overall production cost. One of the key roles in DSSCs is being played by its photoanode. TiO<sub>2</sub> nanoparticle mesoporous thin films have been widely used as a photoanode material in DSSCs owing to its very fast electron injection rates from the excited state of the dye into the TiO<sub>2</sub> nanoparticle conduction band. However, due to limited electron mobility in TiO<sub>2</sub>, the high electron recombination rates lead to degradation of PCE. While on the other hand, SnO<sub>2</sub> is a promising oxide material because of its higher electronic mobility and large band gap (3.8 eV). The mobility for both single crystal and nanostructured SnO<sub>2</sub> is orders of magnitude higher than in single crystal TiO<sub>2</sub>. However, due to faster electron recombination kinetics and lower trapping density in SnO<sub>2</sub>, resulting from a 300 mV positive shift of the conduction band relative to TiO<sub>2</sub>, it results in an increased dark current, limiting the device open circuit voltage.[162,163] Furthermore, SnO<sub>2</sub> has a lower IEP at pH 4-5 than anatase TiO<sub>2</sub> (IEP at pH 6-7),[129] which leads to lower dye adsorption with acidic carboxyl groups,[163] decreasing the optical density of the photoanode and its ability to absorb solar radiation.

In DSSCs, the FTO glass can directly come in contact with the liquid electrolyte, since the mesoporous photoanode cannot uniformly cover the entire FTO surface. At the interface of FTO

and liquid electrolyte, interface charge recombination limits electron collection and affects PCE.[164–168] Modification of FTO/electrolyte interface plays a key role in boosting the DSSC performance by suppressing the recombination of electrons from the FTO to the electrolytes. One approach of such interface modification is to add a compact metal oxide blocking layer on FTO that would inhibit back electron transport from FTO to the electrolyte.[169] Also,  $\text{TiO}_2$ - $\text{SnO}_2$  based heterojunctions can be considered to mitigate the problem of low electron mobility in case of  $\text{TiO}_2$  and fast electron recombination in case of  $\text{SnO}_2$ . In fact, the CB edge of  $\text{SnO}_2$  is at a lower position than  $\text{TiO}_2$ , so the electrons injected from the dye to  $\text{TiO}_2$  can be efficiently injected to  $\text{SnO}_2$ , which in turn also has a higher mobility. As a result, the overall electron conductivity of the system can be enhanced.[170] The  $\text{SnO}_2$ - $\text{TiO}_2$  heterojunctions create a cascading band structure when layered with the N719 dye.[171,172] Multistep electron transport down a cascading band structure increases carrier lifetime and reduces charge recombination.[173] In addition, a thin  $\text{TiO}_2$  passivating layer at the surface of  $\text{SnO}_2$  nanoparticles can reduce recombination of electrons from the  $\text{SnO}_2$  photoanode to the electrolyte, which is one of the driving factors for poor performance of  $\text{SnO}_2$  solar cells.

To address the above mentioned issues of recombination in a  $\text{SnO}_2$  mesoporous photoanode DSSC, and gain more understanding on DSSCs fabricated with  $\text{SnO}_2$  photoanode, we plan to implement a modified  $\text{SnO}_2$  photoanode, in which, the concept of efficient electron injection is pursued in a  $\text{SnO}_2$ - $\text{TiO}_2$  heterojunction, to form a cascading band structure by modifying the  $\text{SnO}_2$  photoanode with  $\text{TiCl}_4$  or  $\text{TiO}_x$  precursor solution, and treating the FTO substrates with the same precursor solutions to form a blocking layer. Furthermore, the photogenerated electrons in the photoanode of a DSSC have to travel through the network of semiconductor particles, and thereby encounter innumerable grain boundaries during the transit, making it prone to recombination with the holes

present in the electrolyte. So addition of a small amount of MWCNT and graphene to the anode can create a highly conducting 3D percolating network, by acting as charge directing pathways.[121,174]

1. Fabricating a blocking layer on FTO/glass substrates and a passivating layer on the SnO<sub>2</sub> mesoporous photoanode with TiO<sub>x</sub> and TiCl<sub>4</sub> precursor solution, to inhibit the electron hole recombination process, thus creating a SnO<sub>2</sub>-TiO<sub>2</sub> heterojunction.
2. Studying the role of TiCl<sub>4</sub> and TiO<sub>x</sub> precursor solution on the SnO<sub>2</sub> mesoporous structure of the photoanode, and understand the combined effect of the blocking layer and the passivation layer on photovoltaic performance of the devices.
3. Investigating the photovoltaic performance of SnO<sub>2</sub>-TiO<sub>2</sub> photoanode DSSCs with the introduction of graphene microplatelets and its role in improving the charge transfer properties in the photoanode.
4. Studying the effect of introduction of graphene microplatelets in the long term stability of the functional parameters of the DSSC.

### **2.1.2 Part II: Investigation of novel heterostructure photoanode for PEC based H<sub>2</sub> generation**

H<sub>2</sub>, which has the highest energy content per unit weight[146] in comparison to other known gaseous fuels. Although, H<sub>2</sub> is considered to be a clean fuel since it only results in water as a reaction product upon oxidation,[175] but presently, large scale production of H<sub>2</sub> mainly relies on extraction from hydrocarbons such as methane utilizing fossil fuels. Production of H<sub>2</sub> from water utilizing PEC cells using solar energy, is a very attractive approach. PEC cells, which generally use wide band gap semiconductors as photoanodes, can be further sensitized by QDs to extend their absorption spectrum, thereby improving their H<sub>2</sub> generation efficiency.[159,160] Although

QD sensitized PEC cells have been extensively studied for their considerable efficiency in H<sub>2</sub> production, stability still remains a major concern. Poor stability in colloidal QD based PEC cells drives us to explore a highly stable photoanode material. Owing to its fascinating photocatalytic properties, anatase TiO<sub>2</sub> is primarily exploited for fabrication of the photoanode in a PEC cell. However, the wider band gap (3.6 eV) of SnO<sub>2</sub> as compared to anatase TiO<sub>2</sub> (3.2 eV) creates fewer oxidative holes in the valence band under UV illumination,[176] This can play a crucial role in improving the long-term stability of PEC cells. Until now, SnO<sub>2</sub> has been investigated considerably less for PEC water splitting applications, primarily because its CB minimum is lower than the reduction potential of water,[177] and it suffers from a limited exciton separation rate.[178] On the other hand, TiO<sub>2</sub> has a favorable band alignment for water splitting, however, UV degradation is setback. To address these challenges, we designed a SnO<sub>2</sub>-TiO<sub>2</sub> heterojunction, to integrate the advantages of both SnO<sub>2</sub> and TiO<sub>2</sub> (i.e. the higher CB edge of TiO<sub>2</sub>, and the high stability and exceptional electronic mobility of SnO<sub>2</sub>). In addition, a type-II band alignment in case of the SnO<sub>2</sub>-TiO<sub>2</sub> heterojunction promotes charge transport and separation, which can boost the performance of PEC cells.[177,179]

Therefore, the objectives for Part II are:

1. Fabricating and implementing SnO<sub>2</sub>-TiO<sub>2</sub>/graphene photoanode in PEC cells for H<sub>2</sub> generation application.
2. Investigating the charge transfer kinetics in the photoanode with characterization techniques such as transient photoluminescence and ultrafast absorption spectroscopy.
3. Studying the performance and the stability of our heterostructured photoanode in PEC cells.

## **2.2 Thesis organization**

This thesis is divided into five chapters, which are organized as follows:

**Chapter 1:** Introduction: Fundamental concepts of the background are briefly introduced here.

**Chapter 2:** Research objectives: The motivation and main goals of this thesis are presented in this chapter.

**Chapter 3:** Experiments and characterization: The experimental details of fabrication process of heterostructured photoanodes for DSSCs and PEC cells for H<sub>2</sub> generation are described here. Essential characterization techniques are also discussed in this chapter.

**Chapter 4.1:** Surface modified SnO<sub>2</sub> photoanodes for DSSCs: the publication related to this chapter is: Enhanced photovoltaic properties in dye sensitized solar cells by surface treatment of SnO<sub>2</sub> photoanodes. Kaustubh Basu, Daniele Benetti, Haiguang Zhao, Lei Jin, Fiorenzo Vetrone, Alberto Vomiero, Federico Rosei. *Sci. Rep.* 6 (2016) 23312, 1-10.

**Chapter 4.2:** Graphene based SnO<sub>2</sub>-TiO<sub>2</sub> photoanodes for DSSCs: the publication related to this chapter is: Graphene modified SnO<sub>2</sub>-TiO<sub>2</sub> photoanodes for efficient and stable dye sensitized solar cell. Kaustubh Basu, Gurpreet Singh Selopal, Mahyar Mohammadnezad, Rusoma Akalimali, Zhiming M. Wang, Haiguang Zhao, Fiorenzo Vetrone, Federico Rosei. In preparation.

**Chapter 4.3:** SnO<sub>2</sub>-TiO<sub>2</sub> photoanodes for application in colloidal QD based PEC cells: the publication related to this chapter is Highly stable photoelectrochemical cells for hydrogen production using SnO<sub>2</sub>-TiO<sub>2</sub>/quantum dot heterostructured photoanode. Kaustubh Basu, Hui Zhang, Haiguang Zhao, Sayantan Bhattacharya, Prasanta Kumar Datta, Lei Jin, Shuhui Sun, Fiorenzo Vetrone, Federico Rosei. Published in *Nanoscale*.

**Chapter 5:** Conclusions: Concluding remarks are described in this chapter.

Most of work in this thesis was done by Kaustubh Basu, however, some parts were conducted through collaboration. All collaborators who participated in experiments have been duly

acknowledged by adding them as co-authors in the manuscripts. Following the main body of this thesis is an appendix containing a summary of this thesis in French according to INRS guidelines.

## Chapter 3: Materials and methods

In this chapter, the experimental details for the preparation of the SnO<sub>2</sub> paste, preparation of SnO<sub>2</sub>-TiO<sub>2</sub> photoanode, fabrication and characterization of the photoanode structure and the entire PEC cells, namely the DSSC, and PEC cell for H<sub>2</sub> generation are reported. The first section mainly introduces the preparation of SnO<sub>2</sub>-TiO<sub>2</sub> photoanode, and SnO<sub>2</sub>-TiO<sub>2</sub>/graphene photoanode and the fabrication and characterization of the entire DSSC structure. The second section focuses on the preparation of the SnO<sub>2</sub>-TiO<sub>2</sub> photoanode, SnO<sub>2</sub>-TiO<sub>2</sub>/graphene photoanode and the fabrication and characterization of the PEC cell for application in H<sub>2</sub> generation. The SnO<sub>2</sub> paste was deposited on fluorine doped tin oxide (FTO) coated glass substrates using a simple doctor blade technique followed by annealing in air ambience, SnO<sub>2</sub>-TiO<sub>2</sub> photoanode was fabricated by different precursor solution routes. Finally, to fabricate the SnO<sub>2</sub>-TiO<sub>2</sub>/graphene photoanode, different concentrations of graphene (dispersed in ethanol) were systematically introduced and the photoanodes were sensitized by dye via dip coating technique. To fabricate the photoanodes for PEC based H<sub>2</sub> generation, similar approach was undertaken, here the photoanodes were sensitized by colloidal core-shell quantum dots (QDs) using Electrophoretic deposition (EPD) technique.

### 3.1 Materials

FTO coated glass substrates were purchased from Pilkington glasses with a sheet resistance of 8 Ω/□. SnO<sub>2</sub> nanopowder (99.9% tin(IV) oxide), to fabricate the photoanode, was obtained from American Elements. Graphene microplatelets were purchased from Raymor Inc. The redox couple electrolyte, consisting of iodine and tri-iodide (I<sup>-</sup>/I<sub>3</sub><sup>-</sup>), ruthenium based N719 dye (Ruthenizer 535-bisTBA), and Meltonix thermoplastic spacers were bought from Solaronix. Titanium(IV) chloride (0.09 M in 20% HCl), titanium isopropoxide (99.999%), hydrochloric acid (37%), alpha-terpineol, ethyl cellulose, sulfur (100%), oleylamine (OLA) (technical grade, 70%), cadmium oxide (99%),

oleic acid (OA), Rhodamine 6G and octadecene (ODE), selenium pellet ( $\geq 99.999\%$ ), trioctyl phosphine oxide (TOPO), trioctyl phosphine (TOP) (97%), zinc acetate dihydrate ( $\geq 98\%$ ), sodium sulfide ( $\text{Na}_2\text{S}$ ), sodium hydroxide, sodium sulfite ( $\text{Na}_2\text{SO}_3$ ), hexane, toluene, methanol, acetone, ethanol and isopropanol (IPA) were obtained from Sigma-Aldrich Inc. All the starting chemicals used in this work, were used without further purification.

## **3.2 Methods**

### **3.2.1 Experimental details relevant to DSSC fabrication with $\text{SnO}_2$ photoanodes with different post treatment routes**

#### **3.2.1.1 Preparation of $\text{SnO}_2$ paste**

The  $\text{SnO}_2$  nanoparticles  $\sim 20$  nm (American Elements 99.9% tin(IV) oxide) of APS were used. To prepare the paste, 1 g of  $\text{SnO}_2$  powder was mixed with 5 ml of ethanol which acts as solvent, 1 ml of alpha-terpineol as dispersant, 0.5 g of ethyl cellulose as thickener and 1ml of water. All of these ingredients were mixed in a beaker under overnight magnetic stirring. By continuous magnetic stirring of the mixture while connecting it to a pump, the solvent was removed until the volume reduced to half of our starting volume.

#### **3.2.1.2 Pre- and post-treatment of the $\text{SnO}_2$ photoanode**

The pre-treatment of the  $\text{SnO}_2$  photoanode, i.e. deposition of the blocking layer of  $\text{TiO}_2$  was carried out by spin coating the precursor solution of  $\text{TiO}_x$  flat film at 2,000 r.p.m. for 60 s and followed by annealing at 500 °C for 30 min.[180] Alternatively, by soaking the FTO substrates in 50 mM  $\text{TiCl}_4$  aqueous solution and 90 mM  $\text{TiCl}_4$  aqueous solution, pre-treatment was also performed for 30 min at 70 °C. After that they were flushed with deionized water and sintered at 450 °C for 30

min.[181] For post treatment of the SnO<sub>2</sub> film, the same procedure as pre-treatment was followed with the TiO<sub>x</sub> and TiCl<sub>4</sub> precursor solutions.

### **3.2.1.3 DSSC fabrication**

Fluorine doped tin oxide (FTO) coated glass substrates were bought from Hartford Glass Co. Inc., USA with sheet resistance 15 Ω/□. For the removal of traces of glue from packaging, the FTO substrates were sonicated for 30 min with 2% Triton X-100 in deionized water, followed by 30 min sonication in isopropyl alcohol and then thoroughly rinsed with deionized water and finally dried in a filtered air stream. Subsequently using the techniques described above, a blocking layer of TiO<sub>2</sub> was deposited on the substrate. Then, using a simple doctor blade technique, a layer of the prepared SnO<sub>2</sub> paste was deposited and dried in air for 10 -15 min and then annealed using a hot plate at 150 °C for 6 min. After cooling down to ambient temperature, another layer was tape casted, followed by 500 °C for 30 min annealing and then again cooled back to room temperature. Then a passivating layer of TiO<sub>2</sub> along with the SnO<sub>2</sub> film was coated using the methods which are already described in the experimental methods section entitled “Pre- and Post-Treatment of the SnO<sub>2</sub> Photoanode”.

### **3.2.1.4 Dye sensitization and DSSC assembly**

To sensitize the treated anodes with dye, they were immersed in a 0.5 mM ethanolic solution of the commercial N719 dye (Ruthenizer 535-bisTBA from Solaronix) for 18 h and then washed away with ethanol to remove any unabsorbed excess dye molecules. To make the counter electrode a 10 nm layer of platinum was sputtered on FTO substrates. A thick spacer Meltonix 1170-25 of 25 μm was used to prevent the cell from short circuiting and a redox couple iodide/tri-iodide HI-30 was injected through the spacer.

## **3.2.2 Experimental details relevant to DSSC fabrication with SnO<sub>2</sub>-TiO<sub>2</sub> photoanodes with graphene**

### **3.2.2.1 Fabrication of the SnO<sub>2</sub>-TiO<sub>2</sub>/graphene photoanodes and DSSCs**

First, the FTO coated glass substrates were cleaned and consequently a blocking layer was prepared following methods described in section 3.2.1.2 and 3.2.1.3, respectively. Subsequently, graphene microplatelets of different weight concentrations ranging from 0% to 0.5% was mixed with SnO<sub>2</sub> paste (preparation method described in 3.2.1.1). Using simple tape casting technique, the prepared SnO<sub>2</sub> paste was applied on the blocking layer (BL) TiO<sub>2</sub> following previously reported procedure.[174] After that it was dried at room temperature for 15 min, followed by annealing on a hot plate at 150 °C for 6 min. After cooling the substrates to room temperature, using the similar drying procedure another layer of paste of the same recipe was tape casted and then annealed in ambience air in a furnace at 500 °C for 30 min and again cooled down to room temperature. To create a SnO<sub>2</sub>-TiO<sub>2</sub> heterostructure, the SnO<sub>2</sub> photoanodes were dip-coated in 50 mM TiCl<sub>4</sub> precursor solution for 30 min at 70 °C, then they were flushed with deionized water and subsequently annealed at 500 °C for 30 min. Finally, the photoanodes were sensitized in N719 dye and the DSSCs were assembled using the procedures explained in section 3.2.1.3.

## **3.2.3 Experimental details relevant to colloidal QD based PEC H<sub>2</sub> generation**

### **3.2.3.1 Synthesis of CdSe QDs**

Using the hot-injection approach, synthesis of CdSe QDs of diameter 1.65 nm were carried out.[160,182] Typically, at room temperature, TOPO (1 g) and Cd-oleate (0.38 mM, 1 mL) in 8 mL of ODE were purged by N<sub>2</sub> for 30 min. The reaction system was evacuated for 30 min at 100 °C, and then the temperature was raised to 300 °C. The mixture of 3mL of OLA, TOP-Se (4

mM, 4 mL) and 1 mL of ODE at room temperature was injected rapidly into the Cd-oleate suspension while stirring the mixture vigorously. After injection, the reaction cell was quenched with cold water. After that 20 mL of Ethanol was added and then the suspension was centrifuged. Finally the supernatant was removed and the QDs were dispersed in toluene.

### 3.2.3.2 Synthesis of CdSe/CdS “giant” QDs

According to the procedure described in Ghosh et al[160,183], the deposition of CdS layers on CdSe QDs was obtained by successive ionic layer adsorption and reaction (SILAR). The synthesis of the “Giant” CdSe/CdS QDs were obtained by growing CdS monolayers over the CdSe core. Typically, in a 100 mL round-bottom flask, 5 mL of ODE, 5 mL of OLA and CdSe QDs ( $\sim 2 \times 10^{-7}$  M in hexane) were degassed at 110 °C for 30 min. While re-storing the reaction flask in N<sub>2</sub>, the temperature was increased to 240 °C with stirring. Subsequently, the Cd(OA)<sub>2</sub> which was dispersed in ODE (0.25 mL, 0.2 M) was added drop by drop in the the mixture and was allowed to react for 2.5 h, followed by, 0.2 M sulfur in ODE was added dropwise with the same volume. All subsequent shells were annealed at 240 °C for ~10 min succeeding the injection of sulfur, and ~2.5 h following drop by drop addition of the Cd(OA)<sub>2</sub> in ODE. Sulfur/Cd(OA)<sub>2</sub> addition volumes for shell addition cycles 1-13 were as follows: 0.25, 0.36, 0.49, 0.63, 0.8, 0.98, 1.18, 1.41, 1.66, 1.92, 2.2, 2.51 and 2.8 mL, respectively.[160] Using cold water, the reaction was cooled down to room temperature. Ethanol was added to the mixture was which to get the suspension which was centrifuged and the supernatant was removed. The QDs were then dispersed in toluene for further characterization.

### **3.2.3.3 Sensitization of the SnO<sub>2</sub> film with CdSe/CdS “giant” QDs**

To sensitize the SnO<sub>2</sub> film with CdSe/CdS “giant” QDs, electrophoretic deposition (EPD) process was carried out. In this method, the SnO<sub>2</sub> composite films coated on FTO substrate were dipped in the QD solution vertically, so that the deposited films were facing each other. Maintaining a fixed distance of 1 cm, a direct current (DC) bias of 200 V was applied in the case of SnO<sub>2</sub>-TiO<sub>2</sub> photoanode for 20 min and TiO<sub>2</sub> photoanode for 2 h.[184] To remove the unbounded QDs on the anode surface, the photoanodes were rinsed several times with toluene and subsequently dried using N<sub>2</sub> at room temperature.

### **3.2.3.4 ZnS capping layer**

ZnS capping layer was fabricated using the SILAR process in which Zn<sup>2+</sup> ions were deposited from 0.1 M solution of Zn(CH<sub>3</sub>COO)<sub>2</sub> in ethanol. The sulfide source was prepared using 0.1 M solution of Na<sub>2</sub>S in water. In a single SILAR cycle, the SnO<sub>2</sub>-TiO<sub>2</sub> or the TiO<sub>2</sub> working electrode were dip-coated for 1 min into the metal precursors (Zn<sup>2+</sup>), followed by into the sulfide solutions. After each bath, by immersing the photoanode in the corresponding solvent (methanol or methanol and water, respectively), it was cleaned rigorously to remove the chemical residuals from the surface and then dried with a N<sub>2</sub> gun. To create the ZnS capping layer, two SILAR cycles were performed.

## **3.3 Characterization techniques**

### **3.3.1 SEM and TEM characterizations**

SEM is an important technique to study the surface morphology of different materials. HRTEM can be used to study the morphology and reveal the fine crystalline structure of samples. The morphological characterizations of the SnO<sub>2</sub>-TiO<sub>2</sub> heterostructure was studied using SEM and

TEM. SEM images were recorded using JEOL JSM840 at an accelerating voltage of 10 kV. Bright field TEM and high resolution HRTEM imaging at 200 kV and EDS were carried out using a JEOL JEM-2100F.

### **3.3.2 XRD characterizations**

XRD is a non-destructive analytical technique which is used to determine the atomic and molecular structure ranging from fluids to powder and crystals. In this process, monochromatic X-rays are used to diffract into many specific directions by the crystalline atoms thus to determine the inter planar spacing of the unknown material.[185] Incident X-rays are scattered by a crystalline sample according to Bragg's law:  $n\lambda = 2d \sin\theta$  [185] where  $\lambda$  is the wavelength of the X-ray beam,  $\theta$  is the incident angle, and  $d$  is the distance between crystal planes. The value for  $d$  is dependent on the Miller indices  $h$ ,  $k$  and  $l$ . In this thesis, the measurements of powdered samples were analyzed by XRD (Bruker D8 Advanced Diffractometer, Cu  $K\alpha$  radiation).

### **3.3.3 DRS measurements**

DRS is an exceptional tool for measuring diffused reflectance for powdered or crystalline materials. To characterize the sample DRS uses a focused spectrometer beam into the sample from where it is reflected, scattered and some part transmitted through the sample. Subsequently the back scattered and diffusely scattered light are collected and transferred to the detector to analyze.[186] Diffuse reflectance spectroscopy of SnO<sub>2</sub> photoanode, and SnO<sub>2</sub> photoanode treated with TiO<sub>x</sub> flat film precursor solution was carried out using UV-Visible-NIR spectrometer, Perkin Elmer, Lambda 750 in the wavelength range of 250-800 nm with resolution of 2 nm. K-M function, was calculated following literature procedure,[187] and was plotted as a function of photon energy. K-M function was used to determine the band gap of SnO<sub>2</sub> photoanode before and after post-treatment.

### 3.3.4 UPS measurements

UPS is a very useful technique used to determine the molecular orbital energies in the valence region by analyzing the kinetic energy spectra of photoelectrons emitted by molecules which have absorbed UV photons.[188] SnO<sub>2</sub> photoanode, and SnO<sub>2</sub> photoanode treated with TiO<sub>x</sub> precursor solution were studied with UPS collected using VG ESCALAB 3 Mark II high vacuum system. During the UPS measurement, illumination at 21.21 eV was provided by the He (I) emission line from a helium discharge lamp. Cutoff energies were determined from the intersection of a linear extrapolation of the cutoff region to a linear extrapolation of the baseline.

### 3.3.5 PL measurements

PL spectroscopy is a non-destructive versatile method to examine the electronic structure of materials. In this process, from a monochromatic source, light is directed onto a sample where it is absorbed and re-emitted very rapidly in the form of emission of light, or luminescence. As the luminescence is caused due to photo-excitation, hence it is called photoluminescence. The emitted light from the sample can be collected and analysed spectrally, spatially and temporally and depending upon the intensity and spectral content, various material properties can be identified from it.[189] The PL lifetime of the QDs in the photoanode films were measured using a TCSPC mode with a 408 nm and 444 nm laser. The fitting for the decay curves was carried out using a three-component exponential decay, which gave the best fitting results. The intensity-weighted average lifetime  $\langle \tau \rangle$  is evaluated by the following equation:

$$\langle \tau \rangle = \frac{a_1\tau_1^2 + a_2\tau_2^2 + a_3\tau_3^2}{a_1\tau_1 + a_2\tau_2 + a_3\tau_3} \quad 3.1$$

Where  $a_i$  ( $i=1, 2, 3$ ) are the coefficients of the fitting of PL decay and  $\tau_i$  ( $i = 1, 2, 3$ ) are the characteristic lifetimes, respectively. The electron transfer rate,  $K_{et}$  is calculated from the following

equation:[190] ZrO<sub>2</sub>-QDs system was used as a reference, since electron transfer is not favourable from the QDs to ZrO<sub>2</sub>.

$$K_{et} = \frac{1}{\langle \tau \rangle_{QDs/e\ scavenger}} - \frac{1}{\langle \tau \rangle_{QDs/ZrO_2}} \quad 3.2$$

Where  $\langle \tau \rangle_{QDs/e\ scavenger}$  and  $\langle \tau \rangle_{QDs/ZrO_2}$  are the average PL lifetimes of the QDs/TiO<sub>2</sub> and QDs/ZrO<sub>2</sub>, respectively.

### 3.3.6 Ultrafast TAS measurements

Transient spectroscopy utilizing a pump-probe technique is one of the most powerful methods which is used to investigate the short lived excited states of photochemically/photophysically relevant molecules.[191] For our experiment, TAS of the TiO<sub>2</sub> and ZrO<sub>2</sub> photoanodes sensitized by QDs were carried out with a commercially available transient absorption spectrometer from Newport. A Ti: sapphire (Coherent, Libra) regenerative amplifier laser system was used as laser source. The output of the regenerative amplifier was centered at 808 nm, at a repetition rate of 1 kHz with an average pulse energy of 3.5 mJ and pulse width of 50 fs. The beam was split into two parts by a 70/30 (R/T) beam splitter. A major portion of the beam was used to generate the pump beam from an optical parametric amplifier (TOPAS-Prime). A small portion of the fundamental beam was allowed to pass through a computer-controlled motorized delay stage (ILS-LM, Newport) and was used to generate a WLC with a spectral range of 350–850 nm by focusing it onto a 3-mm CaF<sub>2</sub> crystal. Pump and probe beams were focused on the photoanode with a spot size of 210 μm and 80 μm, respectively. The maximum time delay that could be achieved between pump and probe beams in our set-up is 3 ns. After passing through the photoanode WLC probe was collected by a fiber coupled spectrometer coupled to a Si photodiode array (MS-260i, Oriel Instrument). Both the TiO<sub>2</sub>-QD and ZrO<sub>2</sub>-QD photoanodes were pumped at 350, 400 and 450 nm, respectively, and differential absorbance spectra ( $\Delta A$ ) from a broadband probe were collected in

transmission geometry using a spectrometer. The electron transfer rate,  $K_{et}$  is calculated from the following equation:

$$K_{et} = \frac{1}{\tau_{S(TiO_2)}} + \frac{1}{\tau_{S(ZrO_2)}} \quad 3.3$$

### 3.3.7 PV measurements

One of the most essential measurement to determine the performance of a solar cell is the current-voltage (I-V) characteristics. By analyzing the I-V curve, information regarding solar cell parameters such as the  $I_{sc}$ , the  $V_{oc}$ , the  $I_{max}$  and the  $V_{max}$  at the  $P_{max}$ , the FF and the  $\eta$  can be determined.[63] To determine the performance of our prepared DSSCs, the photocurrent density-voltage (J-V) characteristics were measured under simulated sunlight (1 sun = AM 1.5G, 100 mW/cm<sup>2</sup>) using a Class AAA Solar Simulator from Photo Emission Tech (SS50AAA) with a Keithley 2400 sourcemeter. The simulator used has a class as per ASTM E927, AAA with non-uniformity of irradiance of 2% or lower over 2x2 inch area. The system for device characterization was calibrated with a Si reference diode. The sourcemeter was controlled by a computer using an application written under TESTPOINT software platform. The FF and the PCE were calculated from the following equations.[82]

$$FF = \frac{P_{max}}{J_{sc} \times V_{oc}} = \frac{J_{max} \times V_{max}}{J_{sc} \times V_{oc}} \quad 3.4$$

$$PCE(\%) = \frac{P_{max}}{P_{in}} \times 100\% = \frac{J_{sc} \times V_{oc} \times FF}{P_{in}} \times 100\% \quad 3.5$$

where  $P_{max}$  is the maximum power output,  $J_{sc}$  is the short-circuit current density,  $V_{oc}$  is the open-circuit voltage.  $J_{max}$ ,  $V_{max}$  are the current density and the voltage at maximum power output in the J-V curves respectively.  $P_{in}$  is the incident light power.

For the EQE or IPCE measurements of our devices, we used the Oriel IQE-200 certified system, which is calibrated using NREL certified Si and Ge detectors. The solar cells were connected using a probe station.

### **3.3.8 Electrochemical impedance spectroscopy measurements**

EIS is a powerful tool to characterize DSSCs to provide several information such as charge transport, transfer and accumulation processes in the cells.[192] For carrying out our experiments, EIS was studied under dark ambience using a SOLARTRON 1260A Impedance/Gain-Phase Analyzer. All spectra were collected by applying an external bias between 0 and 800 mV, on a 100 mHz-300 kHz frequency range. The measurements were carried out inside a Faraday cage for all the samples.

### **3.3.9 PEC performance analysis**

The PEC performance of the photoelectrodes were evaluated in a typical three-electrode configuration, consisting of a QD-sensitized SnO<sub>2</sub>-TiO<sub>2</sub> heterostructured photoanode as the working electrode, Pt as the counter electrode, and an Ag/AgCl (saturated KCl) as a reference electrode.[193] The sample's surface (except for the active area) was covered with insulating epoxy resin, to avoid any direct contact between the electrolyte and the conducting back-contact and/or the connecting wire. Subsequently, the sample was fully immersed in the electrolyte containing 0.25 M Na<sub>2</sub>S and 0.35 M Na<sub>2</sub>SO<sub>3</sub> (pH ~13) as the sacrificial hole scavenger. The electrolyte solution was purged by N<sub>2</sub> to remove any dissolved oxygen before PEC analysis. All potentials, measured with respect to the reference electrode of Ag/AgCl during the PEC measurements, were converted to the RHE scale according to the following equation  $V_{\text{RHE}} = V_{\text{Ag/AgCl}} + 0.197 + \text{pH} \times (0.059)$ . [193] The photoresponse was measured by using a Class AAA Solar Simulator (model SLB-300A by Sciencetech Inc.) equipped with a 300 W Xenon arc lamp

as a light source with an AM 1.5 G filter under 1 sun illumination. Prior to each measurement, the light intensity was monitored by a power meter and was adjusted to  $100 \text{ mW/cm}^2$ . All the current versus potential measurements were carried out at a  $20 \text{ mV/s}$  sweep rate.

## Chapter 4: Results

The results section is presented in three different parts, each of which represents different articles.

The Chapter 4.1, in full, is a reprint of the material as it appears in Scientific reports, vol.6, 2016.

Kaustubh Basu, Daniele Benetti, Haiguang Zhao, Lei Jin, Fiorenzo Vetrone, Alberto Vomiero, Federico Rosei. The dissertation author was the primary investigator of this paper.

### **4.1 Enhanced photovoltaic properties in dye sensitized solar cells by surface treatment of SnO<sub>2</sub> photoanodes**

Kaustubh Basu<sup>1</sup>, Daniele Benetti<sup>1</sup>, Haiguang Zhao<sup>1</sup>, Lei Jin<sup>1</sup>, Fiorenzo Vetrone<sup>1,4</sup>, Alberto Vomiero<sup>2,\*</sup>, Federico Rosei<sup>1,3,4,\*</sup>

<sup>1</sup> Institut National de la Recherche Scientifique - Énergie, Matériaux et Télécommunications, Université du Québec, Varennes, QC, Canada

<sup>2</sup> Department of Engineering Sciences and Mathematics, Luleå University of Technology, 971 98, Luleå, Sweden

<sup>3</sup> Institute for Fundamental and Frontier Science, University of Electronic Science and Technology of China, Chengdu 610054, PR China

<sup>4</sup> Centre for Self-Assembled Chemical Structures, McGill University, Montreal, QC, Canada

**\* Corresponding authors:**

**Alberto Vomiero: [alberto.vomiero@ltu.se](mailto:alberto.vomiero@ltu.se)**

**Federico Rosei: [rosei@emt.inrs.ca](mailto:rosei@emt.inrs.ca)**

## Abstract

We report the fabrication and testing of dye sensitized solar cells (DSSC) based on tin oxide ( $\text{SnO}_2$ ) particles of average size  $\sim 20$  nm. Fluorine-doped tin oxide (FTO) conducting glass substrates were treated with  $\text{TiO}_x$  or  $\text{TiCl}_4$  precursor solutions to create a blocking layer before tape casting the  $\text{SnO}_2$  mesoporous anode. In addition,  $\text{SnO}_2$  photoelectrodes were treated with the same precursor solutions to deposit a  $\text{TiO}_2$  passivating layer covering the  $\text{SnO}_2$  particles. We found that the modification enhances the short circuit current, open-circuit voltage and fill factor, leading to nearly 2-fold increase in power conversion efficiency, from 1.48% without any treatment, to 2.85% achieved with  $\text{TiCl}_4$  treatment. The superior photovoltaic performance of the DSSCs assembled with modified photoanode is attributed to enhanced electron lifetime and suppression of electron recombination to the electrolyte, as confirmed by electrochemical impedance spectroscopy (EIS) carried out under dark condition. These results indicate that modification of the FTO and  $\text{SnO}_2$  anode by titania can play a major role in maximizing the photo conversion efficiency.

## Introduction

Over the last two decades, dye sensitized solar cells (DSSCs) have been widely explored as potential alternatives to conventional silicon photovoltaic (PV) devices due to their low cost, abundance of raw material, facile fabrication process and overall good photovoltaic performance (record efficiency above 14%).<sup>1,2</sup> Compared to typical semiconductors used in p-n junction solar cells, the materials employed in a DSSC photoanode may have lower purities,<sup>3</sup> thereby leading to lower production costs.<sup>4,5</sup> However, to become a realistic candidate to replace traditional solar cells, several challenges have to be addressed to enhance device performance. The photoanode material plays a major role for such purposes: TiO<sub>2</sub> nanoparticle films have been widely used in DSSCs thanks to the very fast electron injection rates from the excited state of the dye into the TiO<sub>2</sub> nanoparticle conduction band, of the order of femtoseconds. On the other hand, due to limited electron mobility in TiO<sub>2</sub>, the high electron recombination rate leads to degradation of photo conversion efficiency (PCE).<sup>6</sup>

Other potentially suitable semiconducting metal oxides were recently considered, such as ZnO and SnO<sub>2</sub>.<sup>7-10</sup> These are appealing candidate materials, due to their higher electron mobility, as compared to TiO<sub>2</sub><sup>11,12</sup> and specific advantages, such as: (i) the ZnO band gap and band positioning is energetically similar to TiO<sub>2</sub>;<sup>1</sup> (ii) SnO<sub>2</sub> on the other hand is a promising oxide material because of its higher electronic mobility and large band gap (3.8 eV).<sup>13</sup> The mobilities reported in both single crystal SnO<sub>2</sub><sup>14</sup> as well as nanostructures<sup>15</sup> are orders of magnitude higher than in single crystal TiO<sub>2</sub>.<sup>6</sup> The high electron mobility in SnO<sub>2</sub> compared to its counterpart TiO<sub>2</sub>, leads to faster diffusion-mediated transport of photoinjected electrons. The wider bandgap of SnO<sub>2</sub>, compared to anatase TiO<sub>2</sub> (3.2 eV) creates fewer oxidative holes in the valence band under UV illumination, so as to minimize dye degradation rate and long term stability of DSSCs.<sup>16,17</sup>

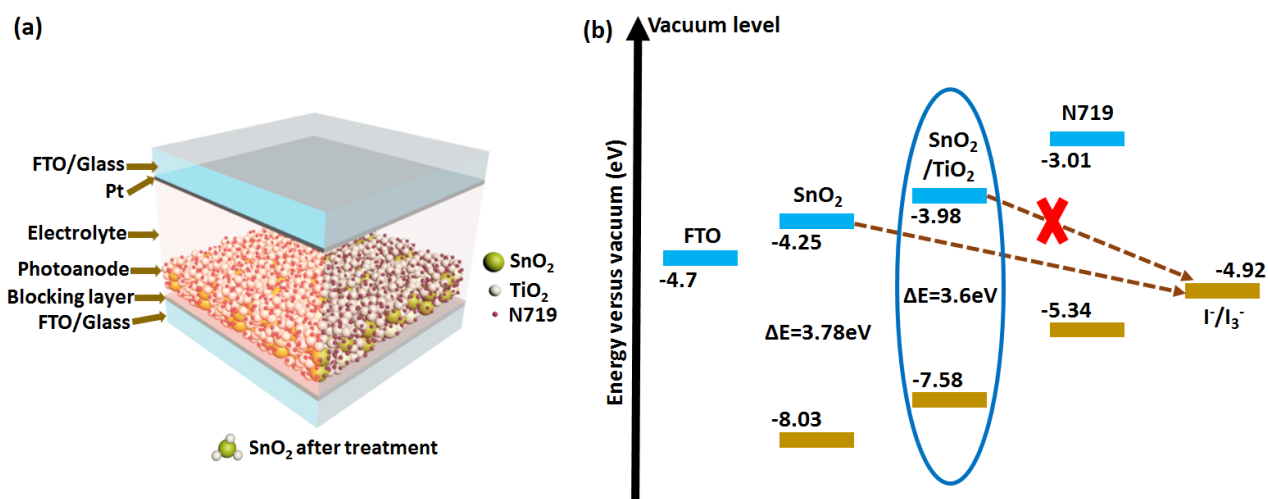


Figure 1. (a) Proposed schematic representation of DSSC. (b) Electronic band diagram showing the beneficial effect of the present methodology to modify SnO<sub>2</sub> anode by TiO<sub>2</sub> (encircled) in alleviating charge recombination from anode to electrolyte as opposed to only using SnO<sub>2</sub> anode. The conduction band, valence band positions and band gap values of present SnO<sub>2</sub> anode and SnO<sub>2</sub> anode modified by TiO<sub>2</sub> are calculated from data acquired from the combination of UPS and diffuse reflectance spectroscopy. All other values are from reported literature.<sup>61-63</sup>

Because of these appealing properties, SnO<sub>2</sub> has been recently utilized in other advanced applications,<sup>18-20</sup> including Hydrogen gas sensing.<sup>21,22</sup> Various synthesis techniques of SnO<sub>2</sub> nanocomposites have also been reported in recent literature.<sup>23,24</sup> In the specific field of DSSCs, a drawback of SnO<sub>2</sub> is its faster electron recombination kinetics and lower trapping density compared to TiO<sub>2</sub>, resulting from a 300 mV positive shift of conduction band relative to TiO<sub>2</sub>, which results in an increased dark current, thereby limiting the open circuit voltage.<sup>25,26</sup> In addition, SnO<sub>2</sub> has a lower isoelectric point (IEP, at pH 4-5) than anatase TiO<sub>2</sub> (IEP at pH 6-7),<sup>27</sup> which leads to lower dye adsorption with acidic carboxyl groups,<sup>26</sup> decreasing the optical density of the photoanode and its ability to absorb solar radiation. In DSSCs, the FTO glass can directly come in contact with the electrolyte, since the mesoporous photoanode cannot uniformly cover the entire FTO surface. At the FTO-electrolyte interface, charge recombination limits electron collection and

affects PCE.<sup>28-32</sup> Modification of the FTO/electrolyte interface plays a key role in boosting DSSC performance by suppressing the recombination of electrons from the FTO to the electrolytes. A promising approach for such interface modification is to add a compact metal oxide blocking layer on FTO that would inhibit back electron transport from FTO to the electrolyte.<sup>33</sup> Also, TiO<sub>2</sub>-SnO<sub>2</sub> based heterojunctions can be potentially considered to mitigate the problem of low electron mobility in TiO<sub>2</sub> and fast electron recombination in SnO<sub>2</sub>. In fact, the conduction band edge of SnO<sub>2</sub> is at a lower position than that of TiO<sub>2</sub>, so the electrons injected from the dye to TiO<sub>2</sub> can be efficiently injected into SnO<sub>2</sub>, which in turn also has a higher mobility, so that the overall electron conductivity of the system can be enhanced.<sup>13</sup> The TiO<sub>2</sub>-SnO<sub>2</sub> heterojunction creates a cascading band structure when layered with the N719 dye.<sup>34,35</sup> Recently, a new record conversion efficiency around 7.4% has been set with SnO<sub>2</sub> multiporous nanofibers DSSC with TiCl<sub>4</sub> treatment by Qamar Wali and co-workers.<sup>19</sup> Multistep electron transport down a cascading band structure increases carrier lifetime and reduces charge recombination.<sup>36</sup> Also, a thin TiO<sub>2</sub> passivating layer at the surface of SnO<sub>2</sub> nanoparticles can reduce recombination of electrons from the SnO<sub>2</sub> photoanode to the electrolyte, which is one of the main contributors that cause poor performance of SnO<sub>2</sub> solar cells.

In this manuscript, we implement a modified SnO<sub>2</sub> photoanode, in which the concept of efficient electron injection is pursued in a SnO<sub>2</sub>-TiO<sub>2</sub> heterojunction (Figure 1), to form a cascading band structure<sup>34,35</sup> by modifying the SnO<sub>2</sub> photoanode with TiCl<sub>4</sub> or TiO<sub>x</sub> precursor solution, and treating the FTO substrates with the same precursor solutions to form a blocking layer. The morphological characterization of the photoanode indicates an interconnected structure of SnO<sub>2</sub> and TiO<sub>2</sub> nanoparticles, where small TiO<sub>2</sub> nanoparticles grow on top of each other forming wire-like structures connecting the mesoporous SnO<sub>2</sub> photoanode. The functional characterization of

the entire solar cell (which demonstrate a marked improvement of photovoltaic parameters) indicated an overall increase of ~90% in the PCE from 1.48% without any treatment, to 2.85% achieved with  $\text{TiCl}_4$  treatment.

## Results and Discussion

Size tuning of nanoparticles is very important in determining the performance of DSSCs. The optimum size is around 20 nm, because for larger nanoparticles, less surface per unit volume is available for dye adsorption. On the other hand, in the case of smaller sized nanoparticles, a larger number of grain boundaries can be found, which increases the probability of electron trapping,<sup>37-40</sup> and smaller pore size, which can inhibit dye penetration during the sensitization process.<sup>41</sup> We chose  $\text{SnO}_2$  nanoparticles ~20 nm in diameter for photoanode preparation. The surface morphology of different photoanodes, with/without treatment is illustrated in Figure 2(a-d). The typical mesoporous structure is visible after sintering. The  $\text{TiCl}_4$  treatment (Figure 2b and Figure 2c) induces the formation of small nanoparticles of about 5 nanometers (nm), which are confirmed to be composed of titanium oxide by energy dispersive X-ray spectroscopy (EDX) selectively performed on a single nanoparticle, as shown in Figure 3. The  $\text{TiO}_2$  nanoparticles preferentially form short interconnected nanowires (Figure 2b and Figure 2c). The higher the  $\text{TiCl}_4$  molar concentration, the more connected is the wire-like structure (see comparison of Figure 2b and c and Figure 2f and g). The  $\text{TiO}_x$  treatment induces the formation of completely different structures compared to  $\text{TiCl}_4$ : the  $\text{TiO}_2$  structures seem to cover the larger  $\text{SnO}_2$  particles. If we compare the scanning electron microscope (SEM) and transmission electron microscope (TEM) images from Figure 2, we can more clearly observe the influence of the different precursors on bare  $\text{SnO}_2$  nanoparticles. Inspection of TEM images reveals that the pure  $\text{SnO}_2$  sample consists of spherical nanoparticles whose average size is about 20 nm (Figure 2e). However, TEM images Figure 2f

through Figure 2h indicate that spherical nanoparticles of size around 20 nm are decorated with smaller size nanoparticles, which sometimes grow on top of one another to form nanowire like structures (SEM images 2b and 2c) and sometimes cover the SnO<sub>2</sub> nanoparticles (Figure 2d).

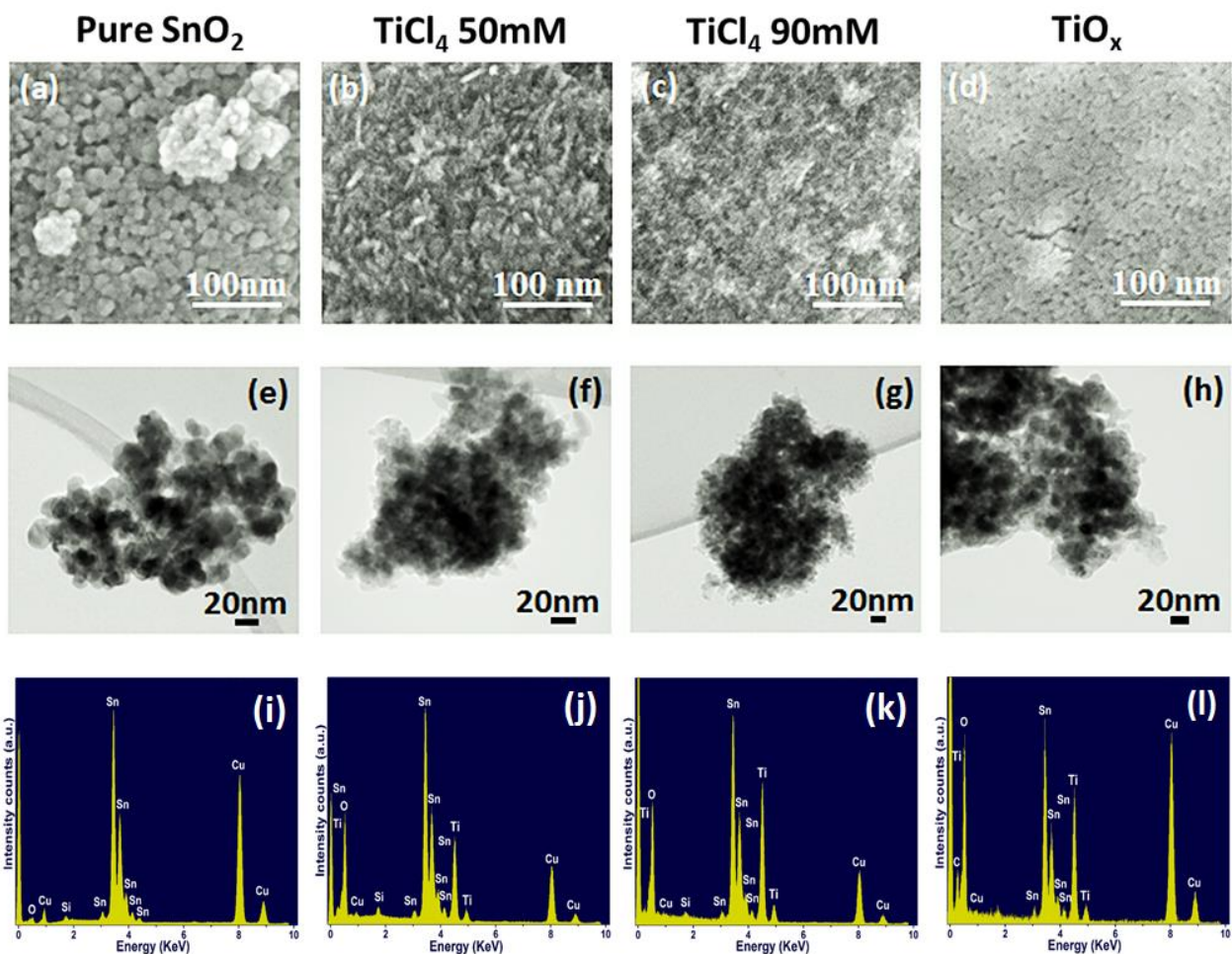


Figure 2. SEM images (a-d), TEM images (e-h), and EDX spectra on different SnO<sub>2</sub> photoanodes, confirming the presence of the constituent elements, (a, e, i) before treatment; (b, f, j) treated with 50 mM TiCl<sub>4</sub>; (c, g, k) treated with 90 mM TiCl<sub>4</sub>; (d, h, l) treated with TiO<sub>x</sub>.

EDX mapping analysis is reported in Figure 2. The elemental characterization of the SnO<sub>2</sub> photoanode is shown in Figure 2i. EDX carried out on SnO<sub>2</sub> mesoporous photoanode treated with 50 mM TiCl<sub>4</sub>, 90 mM TiCl<sub>4</sub> and TiO<sub>x</sub> are shown in Figure 2j, k and l, respectively and confirm the

presence of the constituent elements of SnO<sub>2</sub> and TiO<sub>2</sub>. High Resolution Transmission Electron Microscopy (HRTEM) was carried out on treated samples to examine their fine structure. The results are reported in Figure 3, which shows the crystalline structure of the SnO<sub>2</sub> and the TiO<sub>2</sub> nanoparticles. Distinct lattice fringes in the HRTEM images highlight the presence of crystalline phases for both SnO<sub>2</sub> (green coloured text) and TiO<sub>2</sub> (red coloured text). HRTEM indicates that the crystalline phase of both SnO<sub>2</sub> and TiO<sub>2</sub> can be indexed to a rutile structure, (JCPDS No. 00-041-1445 and JCPDS No. 01-088-1175, respectively). This finding is consistent for both TiCl<sub>4</sub> and TiO<sub>x</sub> treatments. X-ray diffraction (XRD) analysis was performed to further confirm the crystalline structure of our anodes and is reported in Figure S2. In all the cases the diffraction pattern matches with rutile SnO<sub>2</sub> (JCPDS No. 00-041-1445). XRD reveals that the crystal structure of SnO<sub>2</sub> nanoparticles did not change after TiO<sub>x</sub> treatment or after the photoanalysis process. TiO<sub>2</sub> peaks could not be found for the treated samples since the quantity is most likely below the detection limit.

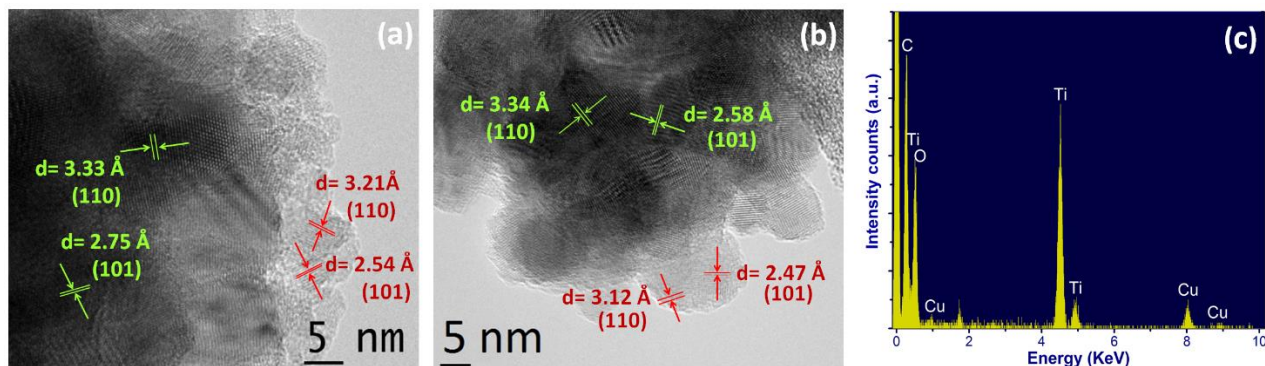


Figure 3. HRTEM images of (a) TiCl<sub>4</sub> treated and (b) TiO<sub>x</sub> treated SnO<sub>2</sub> nanoparticles. (c) EDX spectra confirming the presence of constituent elements of TiO<sub>2</sub> when selectively done on the TiO<sub>2</sub> nanoparticles covering the SnO<sub>2</sub> nanoparticles, the presence of Cu and C is due to the grid used as sample holder.

To determine the band gap of SnO<sub>2</sub> photoanode before and after post-treatment, diffuse reflectance spectroscopy measurement were carried out. Kubelka Munk function was used to

calculate the band gap of SnO<sub>2</sub> photoanode before and after TiO<sub>x</sub> post-treatment (Figure 4). The band gap of SnO<sub>2</sub> photoanode was found to be 3.78eV, which is consistent with literature<sup>37</sup> and the band gap of SnO<sub>2</sub> photoanode after TiO<sub>x</sub> post-treatment was found to be 3.6eV.

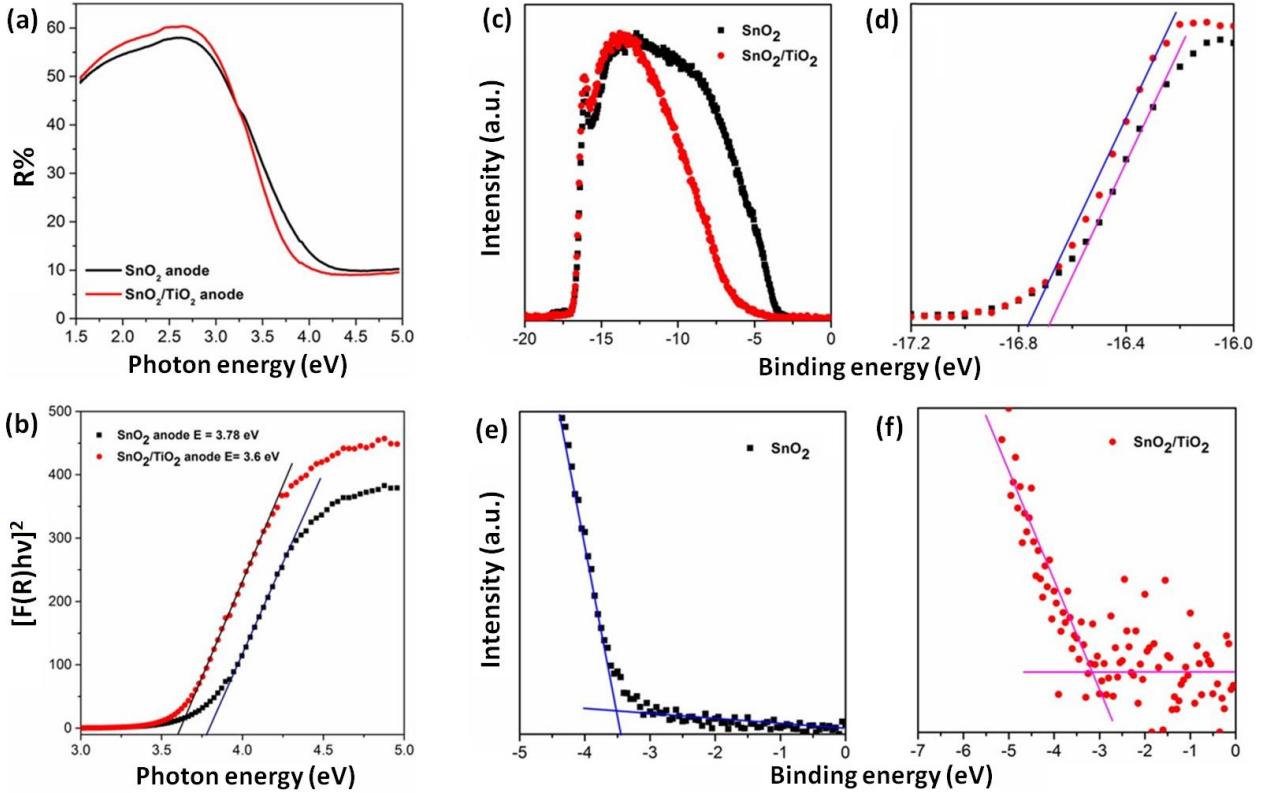


Figure 4 (a) Diffuse Reflectance spectra plotted with respect to photon energy for SnO<sub>2</sub> anode and SnO<sub>2</sub> anode after TiO<sub>x</sub> post-treatment; (b) Kubelka-Munk transformed spectra for SnO<sub>2</sub> anode and SnO<sub>2</sub> anode after treatment;(c) Complete UPS of SnO<sub>2</sub> and treated SnO<sub>2</sub> anodes; (d) magnified view of high binding energy cut-off (Fermi level) and (e, f) low binding energy cut-off (VB edge) of SnO<sub>2</sub> anodes.

Ultraviolet Photoelectron spectroscopy (UPS) analysis (Figure 4c-4e), was performed to identify the band positions of the various photoanodes. The valence band (VB) edge for SnO<sub>2</sub> anode is -8.03 eV, which shifts to a higher value of -7.58 eV after TiO<sub>x</sub> post-treatment. The energy band gap values from Kubelka-Munk transformed diffuse reflectance spectra for SnO<sub>2</sub> anode and SnO<sub>2</sub> anode after TiO<sub>x</sub> post-treatment along with values of valence band edge from UPS measurement

reveals the lowest position of the conduction band (CB) for both the samples. The values of CB minima, VB maxima, and the band gap for SnO<sub>2</sub> anode and SnO<sub>2</sub> anode after TiO<sub>x</sub> post-treatment are reported in Figure 1b. X-ray photoelectron spectroscopy analysis (XPS), was performed to detect any possible shift in the binding energy for the Ti 2p and Sn 3d peaks. The high resolution XPS of Ti 2p of the treated anode and the treated anode after photoanalysis process (Figure S2) shows that there is no significant change for Ti 2p peaks after the cell operation, which means that the chemical state of Ti<sup>4+</sup> does not change during the photoanalysis process. Similar inference can be also drawn in the case of Sn 3d peaks, which are reported in Figure S3, confirming that the chemical state of Sn<sup>4+</sup> does not change.

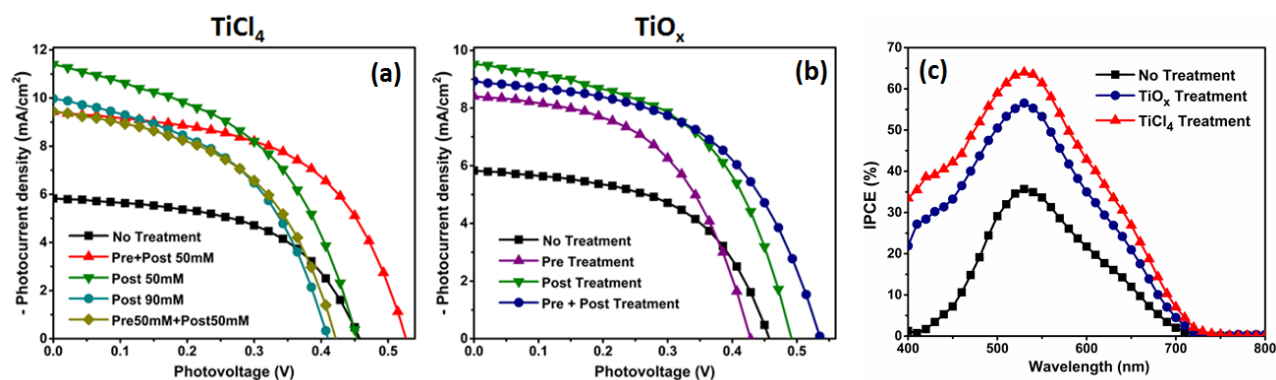


Figure 5. (a) Photocurrent density–photovoltage (J-V) characteristics of SnO<sub>2</sub> nanoparticle based DSSCs, under 1 Sun illumination, obtained from pre- and post-treatment of different concentration of TiCl<sub>4</sub> precursor; (b) J-V characteristics obtained from pre- and post-treatment of TiO<sub>x</sub> precursor; (c) Dependence of absolute IPCE of the solar cells with dye-sensitized nanocrystalline SnO<sub>2</sub> electrodes modified with TiO<sub>x</sub> and TiCl<sub>4</sub> treatment.

To understand the influence of the different treatments on the cell performance, the functional properties of the solar cells were investigated under standard AM1.5G simulated sun irradiation. The results are presented in Figure 5, and the PV parameters (open circuit voltage ( $V_{oc}$ ), short circuit photocurrent density ( $J_{sc}$ ), fill factor (FF), and PCE) are shown in Table 1. A maximum PCE

of 2.85% is achieved in the TiCl<sub>4</sub>-treated cell (with pre- and post-treatment) and 2.66% for TiO<sub>x</sub> pre- and post-treatment, compared to 1.48% for the pristine SnO<sub>2</sub> photoanode.

<b>DSSC</b>	<b>Treatment type</b>	<b>V<sub>oc</sub> (V)</b>	<b>J<sub>sc</sub> (mA/cm<sup>2</sup>)</b>	<b>Fill Factor (FF)</b>	<b>Efficiency (%)</b>
<b>SnO<sub>2</sub>_1</b>	No Treatment	0.45	5.83	0.56	1.48
<b>TiCl<sub>4</sub>_1</b>	TiCl <sub>4</sub> Pre 50 mM + Post 50 mM	0.53	9.43	0.57	2.85
<b>TiCl<sub>4</sub>_2</b>	TiCl <sub>4</sub> Pre 50 mM + Post 90 mM	0.43	9.44	0.53	2.15
<b>TiCl<sub>4</sub>_3</b>	TiCl <sub>4</sub> Post 50 mM	0.45	11.4	0.51	2.64
<b>TiCl<sub>4</sub>_4</b>	TiCl <sub>4</sub> Post 90 mM	0.41	9.98	0.52	2.13
<b>TiO<sub>x</sub>_1</b>	TiO <sub>x</sub> Pre Treatment	0.43	8.41	0.54	1.96
<b>TiO<sub>x</sub>_2</b>	TiO <sub>x</sub> Pre + Post Treatment	0.53	8.94	0.56	2.66
<b>TiO<sub>x</sub>_3</b>	TiO <sub>x</sub> Post Treatment	0.49	9.52	0.55	2.59

Table 1. Photovoltaic properties of DSSC with different configurations of TiO<sub>x</sub> and TiCl<sub>4</sub> treatment

This marked improvement in the PCE originates from the higher  $V_{oc}$  and  $J_{sc}$  of the cells, which in turn are induced by the treatments. A possible explanation in the increase of  $V_{oc}$  can be due to an increase of electron density in SnO<sub>2</sub> as a consequence of effectively suppressed recombination, the Fermi level shifts to a more negative value<sup>42</sup> and since  $V_{oc}$  is the difference between the Fermi level in the semiconductor and the redox potential of I<sup>-</sup>/I<sup>3-</sup> of the electrolyte, a higher value of open circuit voltage is recorded for all treated anodes. A high  $V_{oc}$  of 0.53 V can be observed for the best TiCl<sub>4</sub> and TiO<sub>x</sub> treated cells. Also due to the treatment, the electronic contact between the nanoparticles is improved because of broadened contact interface and the increased contact point which make the electrons traverse the film more easily,<sup>43</sup> which further confirms the reduction of recombination. In addition, interconnection between the nanoparticles facilitate the percolation of electrons from one nanoparticle to other and lead to a global increase of current.<sup>43</sup> However, when we introduce additional TiO<sub>2</sub> by treating our anodes with higher molar concentration of TiCl<sub>4</sub>, due

to the increase in nucleation and growth of nanoparticles, which leads to higher concentration and density of the nanoparticles, there is a reduction of film porosity, which may lead to a decrease of dye adsorption, thus deteriorating the PV properties.<sup>44,45</sup> For  $\text{TiCl}_4$  modification, the  $J_{sc}$  increases by ~60% from the untreated cell and for  $\text{TiO}_x$  modification, an increase of 53% is observed. The family of IPCE curves in Figure 5 are constructed with the IPCE spectra of a normal  $\text{SnO}_2$  photoanode cell and the best cells with both  $\text{TiO}_x$  and  $\text{TiCl}_4$  treatment. The curves are in accordance with the current density versus voltage curves where we observe a marked improvement as a result of treatment. As already established from SEM images, in case of  $\text{TiCl}_4$  treatment, the small titania nanoparticles connect with each other, forming nanowire like structures. On the other hand, in the case of  $\text{TiO}_x$  treatment,  $\text{TiO}_2$  particles cover the  $\text{SnO}_2$ , effectively reducing direct contact of  $\text{SnO}_2$  with the electrolyte, possibly decreasing recombination, thereby leading to an enhancement of IPCE.

We performed electrochemical impedance spectroscopy (EIS) analysis to understand the physical-chemical processes which regulate charge dynamics in our cells. Figure 6 displays the EIS spectra under dark condition of our pristine  $\text{SnO}_2$  cell and the two best cells after  $\text{TiCl}_4$  and  $\text{TiO}_x$  treatments. The treated cells were subjected to a pre-treatment that forms a blocking layer (BL) and a post-treatment that influenced film morphology and PV performances.<sup>3,46,47</sup> The role of the BL in DSSCs is still under debate; different hypotheses have been formulated. Cameron and Peter, and more recently Park and co-workers demonstrated the ability of the BL to prevent back reaction (i.e. electron recombination from FTO to electrolyte) of electrons and attributed the improved performance to the charge transfer resistance at the BL/electrolyte interface. Hence, BL was effective in reducing charge losses at the FTO/anode interface.<sup>48,49</sup> On the other hand, Fabregat and co-workers indirectly deduced that the main factor leading to the enhancement in PCE was

the improved physical contact between the coated FTO and the  $\text{TiO}_2$  film.<sup>50</sup> Figure 6a compares the Nyquist plots of three different cells (bare  $\text{SnO}_2$ ,  $\text{TiCl}_4$  and  $\text{TiO}_x$  treatment) under dark condition and at bias voltage equals to  $V_{oc}$ . Three semicircles are clearly visible: the high frequency arc is attributed to the redox reaction at the platinum counter electrode, the medium arc takes in account the oxide/electrolyte interface and the low frequency arc is related to the Nerst diffusion in the electrolyte.<sup>51,52</sup>

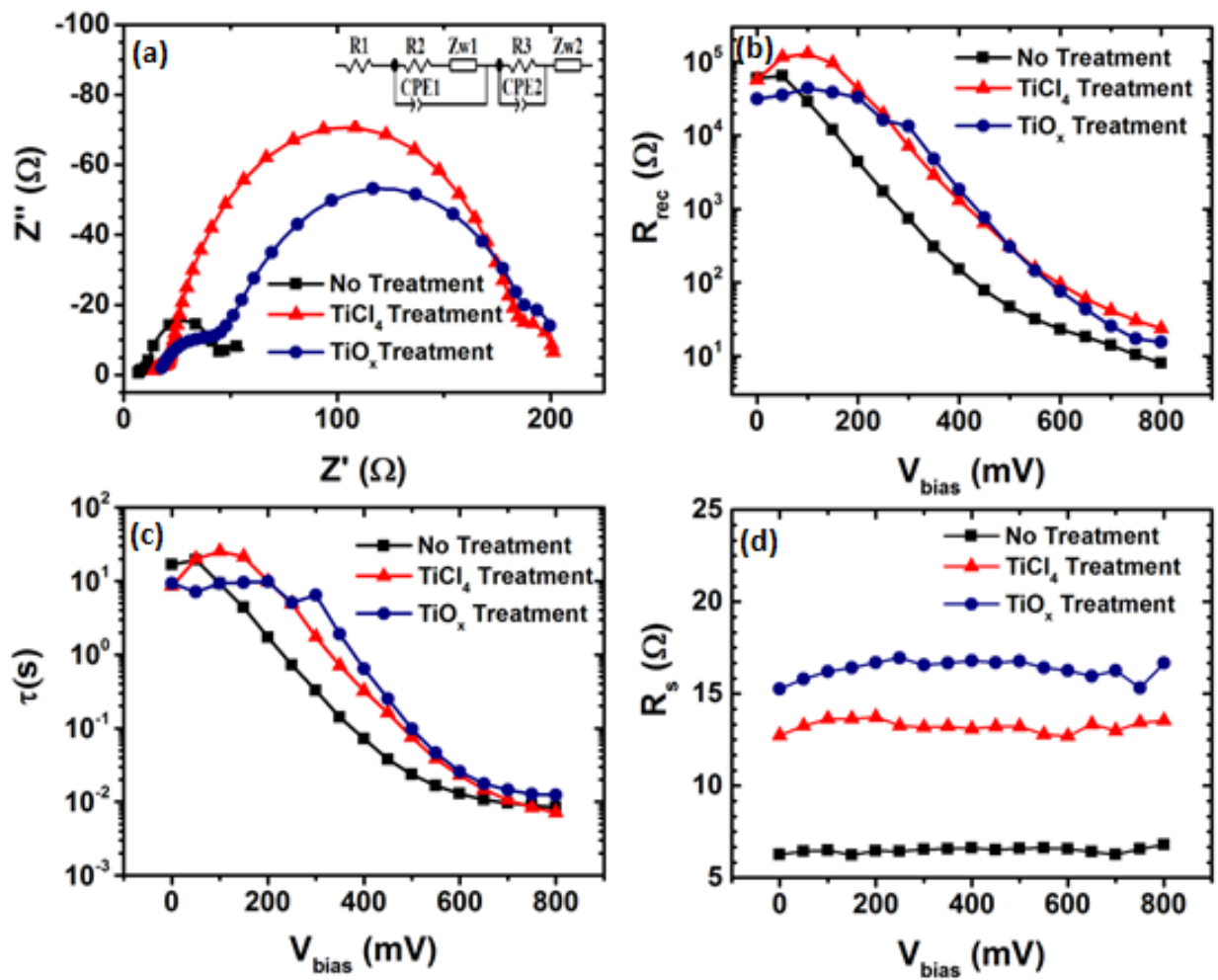


Figure 6. Nyquist plots of devices with and without treatment, under dark condition and around  $V_{oc}$ . The inset shows the model used for fitting the data. From left to right: series resistance ( $R_1$ ), electron transport and back reaction at the  $\text{TiO}_2$ /electrolyte interface, charge transfer at electrolyte/Pt-FTO interface and diffusion of ions in the electrolyte.

- (b) Recombination resistance as calculated from EIS analysis. (c) Electron lifetime obtained from the product  $R_{\text{rec}} * C_{\mu}$ .  
(d) Series resistance calculated from EIS analysis.

The medium arc is evidently larger for the treated cells, indicating that the methods used increase the resistance, thus lowering the recombination processes, at the oxide/electrolyte interface. Figure 6b shows the trend of the recombination resistance ( $R_{\text{rec}}$ ) as a function of applied bias. For both treatments the values of  $R_{\text{rec}}$  are increased compared to the pristine cell, thus indicating reduced recombination after treatment. The overall trend of  $R_{\text{rec}}$  clearly shows that after the treatment the recombination resistance is increased across the whole bias range, confirming a decrease in recombination phenomena. The region at low bias (below  $\sim 250$  mV) is dominated by the charge recombination and capacitance of the back layer.<sup>53,54</sup> In this region it is thus possible to observe the different contributions to the recombination resistance due to the different back layer (in fact, without and with the blocking layers the response of the system will be different: without BL, increased FTO/electrolyte back reaction occurs).<sup>48,55</sup> In our case, we can observe that  $R_{\text{rec}}$  increases, in particular for the  $\text{TiCl}_4$  treatment, indicating the effectiveness of the BL to reduce charge recombination at this interface. The increase in  $R_{\text{rec}}$  for  $\text{TiO}_x$  treatment is lower compared to the  $\text{TiCl}_4$ , probably due to presence of more voids in the blocking layer, which allow the electrolyte to come in contact with the FTO.<sup>56</sup>

In general, the combined effect of the pre- and post-treatment on the cells is an increase of the electrons lifetime, as shown in Figure 6c: the lifetime is systematically higher for the treated cells. Similar results can be found in the literature where the presence of the BL suppresses the charge recombination at the FTO/electrolyte interface.<sup>49,57,58</sup> The main contribution of the post treatment is more difficult to observe in the EIS spectra, because this kind of treatment usually affects the morphology of the sample, modifying, for example, the total surface area. This in turn favors a

higher dye loading and greater light harvesting,<sup>46</sup> yet has less influence on the electronic processes related to charge transport and recombination. As already found by Fabregat and co-workers, the treated cells present a higher value of the series resistance ( $R_s$ ) Figure 6d, which is detrimental for the overall PCE of the cell.<sup>50</sup> However, this effect is largely compensated by a much higher reduction of the charge recombination at the FTO/electrolyte interface, so that the net result is the enhancement of the PCE.

### **Conclusions and perspectives**

In summary, we demonstrated the synthesis of SnO<sub>2</sub> photoelectrodes prepared with SnO<sub>2</sub> nanoparticles of average size 20 nm, treated with TiCl<sub>4</sub> precursor solution and TiO<sub>x</sub> flat film precursor solution. The modified photoanodes exhibit a significant relative increase in power conversion efficiency of the solar cell, which is attributed to the enhancement of functional properties of the DSSC. The blocking layer inhibits the transport of electrons back to the electrolytes, which are collected by the FTO, while passivation of the SnO<sub>2</sub> mesoporous layer blocks the back-reaction pathway of photoinjected electrons from semiconductor anode to electrolyte. The enhancement of open circuit voltage was made possible due to the modification of the electronic band alignment because of the reduced charge recombination. The effect of interconnection of the electrode nanoparticles provides a better path for electron flow and plays a major role in enhancing the short circuit current of the device. The increase of  $R_{rec}$ , and higher lifetime for solar cells with treated anodes further confirms reduced recombination and greater diffusion length of an electron before recombination, thus enhancing the functional properties of the DSSC, which led to nearly a 2-fold improvement in overall PCE.

We obtained experimental evidence (through UPS and diffuse reflectance) of the possibility to modify the electronic band structure in SnO<sub>2</sub> photoanodes, which facilitates efficient electron

transport in treated photoanodes, by suppressing charge recombination and thus improving the functional properties of the DSSC.

## **Experimental Methods**

**Preparation of SnO<sub>2</sub> paste.** The SnO<sub>2</sub> powder used consists of nanoparticles of average particle size ~20 nm (American Elements 99.9% tin(IV) oxide). 1g SnO<sub>2</sub> powder was mixed with 5ml ethanol as a solvent, 1ml alpha-terpineol as dispersant, 0.5g ethyl cellulose which acts as a thickener and 1ml of water. The mixing of these ingredients were carried out in a beaker under overnight magnetic stirring. The solvent was removed by continuous magnetic stirring while connecting it to a pump until the volume of the mixture reduced to half of our starting volume.

**Pre- and post-treatment of the SnO<sub>2</sub> photoanode.** The pre-treatment of the SnO<sub>2</sub> photoanode, i.e. a blocking layer with TiO<sub>2</sub> was deposited by spin coating the TiO<sub>x</sub> flat film precursor solution at 2,000 r.p.m. for 60 s and subsequently heating at 500° C for 30 min.<sup>59</sup> Alternatively, pre-treatment was also carried out by soaking the FTO substrates in 50 mM TiCl<sub>4</sub> aqueous solution and 90 mM TiCl<sub>4</sub> aqueous solution for 30 min at 70 °C, then they were flushed with deionized water and sintered at 450 °C for 30 min<sup>3</sup>. For post treatment of the SnO<sub>2</sub> film, the same procedure as pretreatment was followed with the TiO<sub>x</sub> and TiCl<sub>4</sub> precursor solutions.

**Diffuse reflectance spectroscopy.** Diffuse reflectance spectroscopy of SnO<sub>2</sub> photoanode, and SnO<sub>2</sub> photoanode treated with TiO<sub>x</sub> flat film precursor solution was carried out using UV-Visible-NIR spectrometer, Perkin Elmer, Lambda 750 in the wavelength range of 250-800nm with resolution of 2nm. Kubelka Munk (K-M) function, was calculated following literature procedure,<sup>60</sup> and was plotted as a function of photon energy. K-M function was used to determine the band gap of SnO<sub>2</sub> photoanode before and after post-treatment.

**Ultraviolet Photoelectron Spectroscopy.** SnO<sub>2</sub> photoanode, and SnO<sub>2</sub> photoanode treated with TiO<sub>x</sub> precursor solution were studied with Ultraviolet Photoelectron Spectroscopy (UPS) collected using VG ESCALAB 3 Mark II high vacuum system. During the UPS measurement, illumination at 21.21 eV was provided by the He (I) emission line from a helium discharge lamp. Cutoff energies were determined from the intersection of a linear extrapolation of the cutoff region to a linear extrapolation of the baseline.

**DSSC assembly.** Fluorine doped tin oxide (FTO) coated glass substrates (Pilkington, bought from Hartford Glass Co. Inc., USA) with sheet resistance 15 Ω/□ were sonicated for 30 min with 2% Triton X-100 in deionized water to remove traces of glue from packaging, then they were cleaned by 30 min sonication in isopropyl alcohol and then thoroughly rinsed with deionized water and dried in a filtered air stream. Subsequently a blocking layer with TiO<sub>2</sub> was deposited using the techniques described above. Then, a layer of the prepared SnO<sub>2</sub> paste was deposited using a simple doctor blade technique and dried in air for 10 -15 min and then fired on a hot plate at 150 °C for 6 min. When the substrates cooled down, another layer was doctor bladed, followed by annealing at 500 °C for 30 min in air and then cooled back to room temperature. Then the SnO<sub>2</sub> film was coated with a passivating layer of TiO<sub>2</sub> by methods described already in the experimental methods section of Pre- and Post-Treatment of the SnO<sub>2</sub> Photoanode. The treated anodes were then sensitized by dye, upon immersion in a 0.5 mM ethanolic solution of the commercial N719 dye (Ruthenizer 535-bisTBA from Solaronix) for 18 h and then washed with ethanol to remove any excess of unabsorbed dye molecules. Solar cells were assembled using a sputtered 10 nm thick platinumized counter electrode on FTO glass substrate, 25 μm thick spacer Meltonix 1170-25 (to prevent the cell from short circuiting when the working and counter electrodes are clamped together), and iodide/tri-iodide redox couple HI-30 as the electrolyte.

**PV measurements.** Photocurrent density-voltage (J-V) characteristics were measured under simulated sunlight (1 sun = AM 1.5G, 100 mW/cm<sup>2</sup>) using a Class AAA Solar Simulator from Photo Emission Tech (SS50AAA) with a Keithley 2400 sourcemeter. The simulator used has a class as per ASTM E927, AAA with non-uniformity of Irradiance of 2% or lower over 2x2 inch area. The system for device characterization was calibrated with a Si reference diode. The sourcemeter was controlled by a computer using an application written under TESTPOINT software platform. The fill factor (FF) and the power conversion efficiency (PCE) were calculated from the following equations<sup>2</sup>.

$$FF = \frac{P_{\max}}{J_{sc} \times V_{oc}} = \frac{J_{\max} \times V_{\max}}{J_{sc} \times V_{oc}} \quad (1)$$

$$PCE(\%) = \frac{P_{\max}}{P_{in}} \times 100\% = \frac{J_{sc} \times V_{oc} \times FF}{P_{in}} \times 100\% \quad (2)$$

Where,  $P_{\max}$  is the maximum power output,  $J_{sc}$  is the short-circuit current density,  $V_{oc}$  is the open-circuit voltage,  $J_{\max}$  is the current density and  $V_{\max}$  is the voltage at maximum power output in the J-V curves, and  $P_{in}$  is the incident light power.

For the external quantum efficiency (EQE) or incident photon to current efficiency (IPCE) measurements of our devices, we used the Oriel IQE-200 certified system, which is calibrated using NREL certified Si and Ge detectors. The solar cells were connected using a probe station.

**EIS measurements.** Electrochemical impedance spectroscopy (EIS) was studied under dark ambience using a SOLARTRON 1260A Impedance/Gain-Phase Analyzer. All spectra were collected by applying an external bias between 0 and 800 mV, on a 100 mHz-300 kHz frequency range. The measurements were carried out inside a Faraday cage for all the samples.

**Materials characterization.** The morphology of the samples was studied using Scanning Electron Microscopy (SEM) and Transmission Electron Microscopy (TEM). SEM images were recorded using JEOL JSM840 at an accelerating voltage of 10kV. Bright field TEM and high resolution HR-TEM imaging at 200 kV and energy dispersive X-ray spectroscopy (EDS) were carried out using a JEOL JEM-2100F.

### **Acknowledgements**

We acknowledge funding from NSERC in the form of Discovery Grants and a Strategic Project Grant in partnership with Canadian Solar. This work was partially funded by MDEIE through the international project WIROX. H.Z. is grateful to NSERC for a personal post-doctoral fellowship. A.V. thanks partial support under EC contract WIROX no. 295216 and F-Light no.299490, and acknowledges Kempestiftelserna and Luleå University of Technology Labfonden program for financial support for equipment. F.R. acknowledges NSERC for funding and partial salary support from an E.W.R. Steacie Memorial Fellowship.

### **Author Contributions**

K.B. designed the device optimization strategy, fabricated and characterized the devices. K.B and H.Z. analyzed the results. D.B. carried out EIS experiments, analyzed the results and provided their interpretation. L.J. carried out XPS experiments. H.Z., A.V., F.V. and F.R. supervised the experiments. A.V. and F.R. designed the project. K.B. wrote the manuscript. H.Z., A.V., F.V. and F.R. reviewed and corrected the manuscript. All the authors participated in the discussion and commented on the paper.

## Additional information

Supplementary information accompanies this paper at <http://www.nature.com/scientificreports>.

**Competing financial interests:** The authors declare no competing financial interests.

## References

- 1 Gratzel, M. Photoelectrochemical cells. *Nature* **414** (2001) 338-344.
- 2 Hagfeldt, A., Boschloo, G., Sun, L., Kloo, L. & Pettersson, H. Dye-Sensitized Solar Cells. *Chem. Rev.* **110** (2010) 6595-6663.
- 3 Sommeling, P. M. *et al.* Influence of a TiCl<sub>4</sub> Post-Treatment on Nanocrystalline TiO<sub>2</sub> Films in Dye-Sensitized Solar Cells. *J. Phys. Chem. B* **110** (2006) 19191-19197.
- 4 Späth, M. *et al.* Reproducible manufacturing of dye-sensitized solar cells on a semi-automated baseline. *Progress in Photovoltaics: Research and Applications* **11** (2003) 207-220.
- 5 Kroon, J. M., O'Regan, B. C., van Roosmalen, J. A. M., Sinke, W. C. *Handbook of Photochemistry and Photobiology*. Vol. Dye-sensitized solar cells. Inorganic photochemistry 1–47 (American Scientific, 2003).
- 6 Hendry, E., Koeberg, M., O'Regan, B. & Bonn, M. Local field effects on electron transport in nanostructured TiO<sub>2</sub> revealed by terahertz spectroscopy. *Nano Lett.* **6** (2006) 755-759.
- 7 Concina, I. & Vomiero, A. Metal Oxide Semiconductors for Dye- and Quantum-Dot-Sensitized Solar Cells. *Small* **11** (2015) 1744-1774.
- 8 Memarian, N. *et al.* Hierarchically Assembled ZnO Nanocrystallites for High-Efficiency Dye-Sensitized Solar Cells. *Angew. Chem. Int. Ed.* **50** (2011) 12321-12325.

- 9 Fukai, Y., Kondo, Y., Mori, S. & Suzuki, E. Highly efficient dye-sensitized SnO<sub>2</sub> solar cells having sufficient electron diffusion length. *Electrochem. Comm.* **9** (2007) 1439-1443.
- 10 Katoh, R. *et al.* Efficiencies of Electron Injection from Excited N3 Dye into Nanocrystalline Semiconductor (ZrO<sub>2</sub>, TiO<sub>2</sub>, ZnO, Nb<sub>2</sub>O<sub>5</sub>, SnO<sub>2</sub>, In<sub>2</sub>O<sub>3</sub>) Films. *J. Phys. Chem. B* **108** (2004) 4818-4822.
- 11 Look, D. C. *et al.* Electrical properties of bulk ZnO. *Solid State Comm.* **105** (1998) 399-401.
- 12 Seager, C. H. & Myers, S. M. Quantitative comparisons of dissolved hydrogen density and the electrical and optical properties of ZnO. *J. Appl. Phys.* **94** (2003) 2888-2894.
- 13 Gubbala, S., Chakrapani, V., Kumar, V. & Sunkara, M. K. Band-edge engineered hybrid structures for dye-sensitized solar cells based on SnO<sub>2</sub> nanowires. *Adv. Func. Mater.* **18** (2008) 2411-2418.
- 14 Jarzebski, Z. M. & Marton, J. P. Physical Properties of SnO<sub>2</sub> Materials: II . Electrical Properties. *J. Electrochem. Soc.* **123** (1976) 299C-310C.
- 15 Arnold, M. S., Avouris, P., Pan, Z. W. & Wang, Z. L. Field-Effect Transistors Based on Single Semiconducting Oxide Nanobelts. *J. Phys. Chem. B* **107** (2002) 659-663.
- 16 Shang, G. *et al.* Preparation of hierarchical tin oxide microspheres and their application in dye-sensitized solar cells. *J. Mater. Chem.* **22** (2012) 25335-25339.
- 17 Fonstad, C. G. & Rediker, R. H. Electrical Properties of High-Quality Stannic Oxide Crystals. *J. Appl. Phys.* **42** (1971) 2911-2918.

- 18 Duan, Y. *et al.* Enhancing the performance of dye-sensitized solar cells: doping SnO<sub>2</sub> photoanodes with Al to simultaneously improve conduction band and electron lifetime. *J. Mater. Chem. A* **3** (2015) 3066-3073.
- 19 Wali, Q. *et al.* Multiporous nanofibers of SnO<sub>2</sub> by electrospinning for high efficiency dye-sensitized solar cells. *J. Mater. Chem. A* **2** (2014) 17427-17434.
- 20 Dong, Z. *et al.* Quintuple-Shelled SnO<sub>2</sub> Hollow Microspheres with Superior Light Scattering for High-Performance Dye-Sensitized Solar Cells. *Adv. Mater.* **26** (2014) 905-909.
- 21 ANSARI, S. G., GOSAVI, S. W., GANGAL, S. A., KAREKAR, R. N. & AIYER, R. C. Characterization of SnO<sub>2</sub>-based H<sub>2</sub> gas sensors fabricated by different deposition techniques. *J. Mater. Sci.: Mater. El.* **8** (1997) 23-27.
- 22 Ansari, S. G. *et al.* Effect of thickness on H<sub>2</sub> gas sensitivity of SnO<sub>2</sub> nanoparticle-based thick film resistors. *J. Mater. Sci.: Mater. El.* **7** (1996) 267-270.
- 23 Ansari, S. A., Khan, M. M., Ansari, M. O., Lee, J. & Cho, M. H. Visible light-driven photocatalytic and photoelectrochemical studies of Ag-SnO<sub>2</sub> nanocomposites synthesized using an electrochemically active biofilm. *RSC Adv.* **4** (2014) 26013-26021.
- 24 Ansari, S. A., Khan, M. M., Omaish Ansari, M., Lee, J. & Cho, M. H. Highly photoactive SnO<sub>2</sub> nanostructures engineered by electrochemically active biofilm. *New J. Chem.* **38** (2014) 2462-2469.
- 25 Green, A. N. M., Palomares, E., Haque, S. A., Kroon, J. M. & Durrant, J. R. Charge Transport versus Recombination in Dye-Sensitized Solar Cells Employing Nanocrystalline TiO<sub>2</sub> and SnO<sub>2</sub> Films. *J. Phys. Chem. B* **109** (2005) 12525-12533.

- 26 Qian, J. *et al.* TiO<sub>2</sub>-Coated Multilayered SnO<sub>2</sub> Hollow Microspheres for Dye-Sensitized Solar Cells. *Adv. Mater.* **21** (2009) 3663-3667.
- 27 Kay, A. & Grätzel, M. Dye-Sensitized Core–Shell Nanocrystals: Improved Efficiency of Mesoporous Tin Oxide Electrodes Coated with a Thin Layer of an Insulating Oxide. *Chem. Mater.* **14** (2002) 2930-2935.
- 28 Zhu, K., Schiff, E. A., Park, N.-G., van de Lagemaat, J. & Frank, A. J. Determining the locus for photocarrier recombination in dye-sensitized solar cells. *Appl. Phys. Lett.* **80** (2002) 685-687.
- 29 Fabregat-Santiago, F., Bisquert, J., Garcia-Belmonte, G., Boschloo, G. & Hagfeldt, A. Influence of electrolyte in transport and recombination in dye-sensitized solar cells studied by impedance spectroscopy. *Sol. Ener. Mater. Sol. Cells* **87** (2005) 117-131.
- 30 Kim, Y. J. *et al.* Effect of Layer-by-Layer Assembled SnO<sub>2</sub> Interfacial Layers in Photovoltaic Properties of Dye-Sensitized Solar Cells. *Langmuir* **28** (2012) 10620-10626.
- 31 Wang, Q. *et al.* Characteristics of High Efficiency Dye-Sensitized Solar Cells. *J. Phys. Chem. B* **110** (2006) 25210-25221.
- 32 Fabregat-Santiago, F., Garcia-Belmonte, G., Mora-Sero, I. & Bisquert, J. Characterization of nanostructured hybrid and organic solar cells by impedance spectroscopy. *Phys. Chem. Chem. Phys.* **13** (2011) 9083-9118.
- 33 Ito, S. *et al.* Control of dark current in photoelectrochemical (TiO<sub>2</sub>/I<sup>-</sup>-I<sup>3-</sup>) and dye-sensitized solar cells. *Chem. Comm.* **34** (2005) 4351-4353.
- 34 Snaith, H. J. & Ducati, C. SnO<sub>2</sub>-Based Dye-Sensitized Hybrid Solar Cells Exhibiting Near Unity Absorbed Photon-to-Electron Conversion Efficiency. *Nano Lett.* **10** (2010) 1259-1265.

- 35 Liu, Z. *et al.* The performances of the mercurochrome-sensitized composite semiconductor photoelectrochemical cells based on TiO<sub>2</sub>/SnO<sub>2</sub> and ZnO/SnO<sub>2</sub> composites. *Thin Solid Films* **468** (2004) 291-297.
- 36 Gust, D., Moore, T. A. & Moore, A. L. Mimicking Photosynthetic Solar Energy Transduction. *Acc. Chem. Res.* **34** (2000) 40-48.
- 37 Gracia, F., Holgado, J. P. & González-Elipe, A. R. Photoefficiency and Optical, Microstructural, and Structural Properties of TiO<sub>2</sub> Thin Films Used as Photoanodes. *Langmuir* **20** (2004) 1688-1697.
- 38 Hagfeldt, A. *et al.* A system approach to molecular solar cells. *Coord. Chem. Rev.* **248** (2004) 1501-1509.
- 39 Gregg, B. A. Interfacial processes in the dye-sensitized solar cell. *Coord. Chem. Rev.* **248** (2004) 1215-1224.
- 40 Gregg, B. A. Excitonic Solar Cells. *J. Phys. Chem. B* **107** (2003) 4688-4698.
- 41 Grant, C. D. *et al.* Characterization of nanocrystalline and thin film TiO<sub>2</sub> solar cells with poly(3-undecyl-2,2'-bithiophene) as a sensitizer and hole conductor. *J. Electroanal. Chem.* **522** (2002) 40-48.
- 42 Gu, F. *et al.* Improved photoelectric conversion efficiency from titanium oxide-coupled tin oxide nanoparticles formed in flame. *J. Power Sources* **268** (2014) 922-927.
- 43 Barbé, C. J. *et al.* Nanocrystalline Titanium Oxide Electrodes for Photovoltaic Applications. *J. Amer. Cer. Soc.* **80** (1997) 3157-3171.
- 44 Zhong, M., Shi, J., Zhang, W., Han, H. & Li, C. Charge recombination reduction in dye-sensitized solar cells by depositing ultrapure TiO<sub>2</sub> nanoparticles on “inert” BaTiO<sub>3</sub> films. *Mater. Sci. Eng.: B* **176** (2011) 1115-1122.

- 45 Weiwei, X. *et al.* Influence of Different Surface Modifications on the Photovoltaic Performance and Dark Current of Dye-Sensitized Solar Cells. *Plasma Science and Tech.* **9** (2007) 556-559.
- 46 Lee, S.-W., Ahn, K.-S., Zhu, K., Neale, N. R. & Frank, A. J. Effects of TiCl<sub>4</sub> Treatment of Nanoporous TiO<sub>2</sub> Films on Morphology, Light Harvesting, and Charge-Carrier Dynamics in Dye-Sensitized Solar Cells. *J. Phys. Chem. C* **116** (2012) 21285-21290.
- 47 O'Regan, B. C., Durrant, J. R., Sommeling, P. M. & Bakker, N. J. Influence of the TiCl<sub>4</sub> Treatment on Nanocrystalline TiO<sub>2</sub> Films in Dye-Sensitized Solar Cells. 2. Charge Density, Band Edge Shifts, and Quantification of Recombination Losses at Short Circuit. *J. Phys. Chem. C* **111** (2007) 14001-14010.
- 48 Cameron, P. J., Peter, L. M., & Hore, S. . How important is the back reaction of electrons via the substrate in dye-sensitized nanocrystalline solar cells? *J. Phys. Chem. B* **109** (2005) 930-9366.
- 49 Yoo, B. *et al.* Chemically deposited blocking layers on FTO substrates: Effect of precursor concentration on photovoltaic performance of dye-sensitized solar cells. *J. Electroanal. Chem.* **638** (2010) 161-166.
- 50 Goes, M. S. *et al.* Impedance Spectroscopy Analysis of the Effect of TiO<sub>2</sub> Blocking Layers on the Efficiency of Dye Sensitized Solar Cells. *J. Phys. Chem. C* **116** (2012) 12415-12421.
- 51 Fabregat-Santiago, F. *et al.* Correlation between photovoltaic performance and impedance spectroscopy of dye-sensitized solar cells based on ionic liquids. *J. Phys. Chem. C* **2** (2007) 6550-6560.

- 52 Wang, Q., Moser, J.-E. & Grätzel, M. Electrochemical impedance spectroscopic analysis of dye-sensitized solar cells. *J. Phys. Chem. B* **109** (2005) 14945-14953.
- 53 Bisquert, J. Theory of the Impedance of Electron Diffusion and Recombination in a Thin Layer. *J. Phys. Chem. B* **106** (2002) 325-333.
- 54 Bisquert, J., Mora-Sero, I. & Fabregat-Santiago, F. Diffusion-Recombination Impedance Model for Solar Cells with Disorder and Nonlinear Recombination. *ChemElectroChem* **1** (2014) 289-296.
- 55 Gregg, B. A., Pichot, F., Ferrere, S. & Fields, C. L. Interfacial Recombination Processes in Dye-Sensitized Solar Cells and Methods To Passivate the Interfaces. *J. Phys. Chem. B* **105** (2001) 1422-1429.
- 56 Kavan, L., Tétreault, N., Moehl, T. & Grätzel, M. Electrochemical Characterization of TiO<sub>2</sub> Blocking Layers for Dye-Sensitized Solar Cells. *J. Phys. Chem. C* **118** (2014) 16408-16418.
- 57 Selopal, G. S. *et al.* Effect of Blocking Layer to Boost Photoconversion Efficiency in ZnO Dye-Sensitized Solar Cells. *ACS Appl. Mater. & Interf.* **6** (2014) 11236–11244.
- 58 Choi, H. *et al.* The effect of TiCl<sub>4</sub>-treated TiO<sub>2</sub> compact layer on the performance of dye-sensitized solar cell. *Curr. Appl. Phys.* **12** (2012) 737-741.
- 59 Docampo, P., Ball, J. M., Darwich, M., Eperon, G. E. & Snaith, H. J. Efficient organometal trihalide perovskite planar-heterojunction solar cells on flexible polymer substrates. *Nat. Comm.* **4** (2013) 1-6.
- 60 Morales, A. E., Mora, E.S., & Pal, U. Use of diffuse reflectance spectroscopy for optical characterization of un-supported nanostructures. *Revista Mexicana de Fisica S* **53** (2007) 18-22.

- 61 Chen, W. *et al.* Hybrid interfacial layer leads to solid performance improvement of inverted perovskite solar cells. *En. & Env. Sci.* **8** (2015) 629-640.
- 62 Cariello, M. *et al.* An investigation of the role increasing [small pi]-conjugation has on the efficiency of dye-sensitized solar cells fabricated from ferrocene-based dyes. *RSC Adv.* **6** (2016) 9132-9138.
- 63 Zhang, J. *et al.* Energy barrier at the N719-dye/CsSnI<sub>3</sub> interface for photogenerated holes in dye-sensitized solar cells. *Sci. Rep.* **4** (2014) 6954.

## Supplementary Information

### Enhanced photovoltaic properties in dye sensitized solar cells by surface treatment of SnO<sub>2</sub> photoanodes

Kaustubh Basu<sup>1</sup>, Daniele Benetti<sup>1</sup>, Haiguang Zhao<sup>1</sup>, Lei Jin<sup>1</sup>, Fiorenzo Vetrone<sup>1,4</sup>, Alberto Vomiero<sup>2\*</sup>, Federico Rosei<sup>1,3,4\*</sup>

<sup>1</sup> Institut National de la Recherche Scientifique - Énergie, Matériaux et Télécommunications, Université du Québec, Varennes, QC, Canada

<sup>2</sup> Department of Engineering Sciences and Mathematics, Luleå University of Technology, 971 98, Luleå, Sweden

<sup>3</sup> Institute for Fundamental and Frontier Science, University of Electronic Science and Technology of China, Chengdu 610054, PR China

<sup>4</sup> Centre for Self-Assembled Chemical Structures, McGill University, Montreal, QC, Canada

#### 1. X-ray diffraction Analysis (XRD)

XRD analysis has been performed using Bruker D8 Advance X-ray diffractometer for the SnO<sub>2</sub> nanoparticle powder sample, SnO<sub>2</sub> photoanode, SnO<sub>2</sub> photoanode after TiO<sub>x</sub> post-treatment, SnO<sub>2</sub> photoanode after photoanalysis process, and SnO<sub>2</sub> photoanode with TiO<sub>x</sub> post-treatment after photoanalysis process reported in Figure S1. In all cases the diffraction pattern matches with rutile SnO<sub>2</sub> (JCPDS No. 00-041-1445). XRD reveals that the crystal structure of SnO<sub>2</sub> nanoparticles did not change after the treatment or the photoanalysis process. TiO<sub>2</sub> peaks could not be found for the

treated samples since the quantity is possibly below XRD detection limit. However  $\text{TiO}_2$  rutile structure corresponding to JCPDS card no. 01-088-1175 was confirmed from HRTEM images shown in Figure 3 in our manuscript.

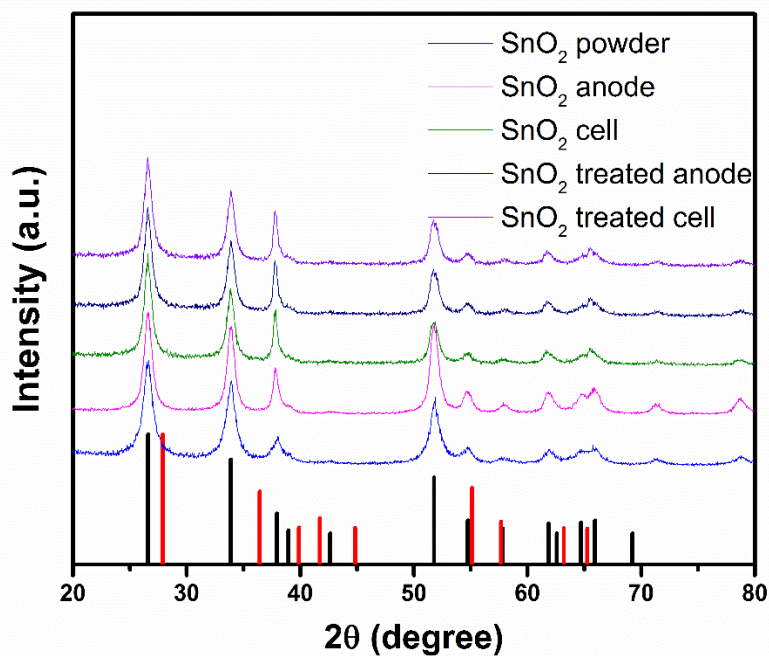


Figure S1: X-ray diffraction patterns of  $\text{SnO}_2$  nanoparticle powder sample,  $\text{SnO}_2$  photoanode,  $\text{SnO}_2$  photoanode after  $\text{TiO}_x$  post-treatment,  $\text{SnO}_2$  photoanode after photoanalysis process, and  $\text{SnO}_2$  photoanode with  $\text{TiO}_x$  post-treatment after photoanalysis process. Black bars show peak positions of rutile  $\text{SnO}_2$  structure of JCPDS card No. 00-041-1445 and red bars shows peak positions of  $\text{TiO}_2$  rutile structure of JCPDS card no. 01-088-1175

## 2. X-ray photoelectron spectroscopy analysis (XPS)

XPS Analysis was performed using a VG Escalab 220i-XL equipped with an Al source. The XPS data were analyzed by using CasaXPS software. Shirley subtraction is used for background correction<sup>1</sup> and then the shape of the peaks used for the deconvolution is Gaussian-Lorentzian shape. Figure S2 shows the high resolution XPS of Ti 2p of the  $\text{SnO}_2$  photoanode after  $\text{TiO}_x$  post-

treatment and the SnO<sub>2</sub> photoanode after TiO<sub>x</sub> post-treatment after photoanalysis process. There is no significant change for Ti<sup>4+</sup> after the cell operation.

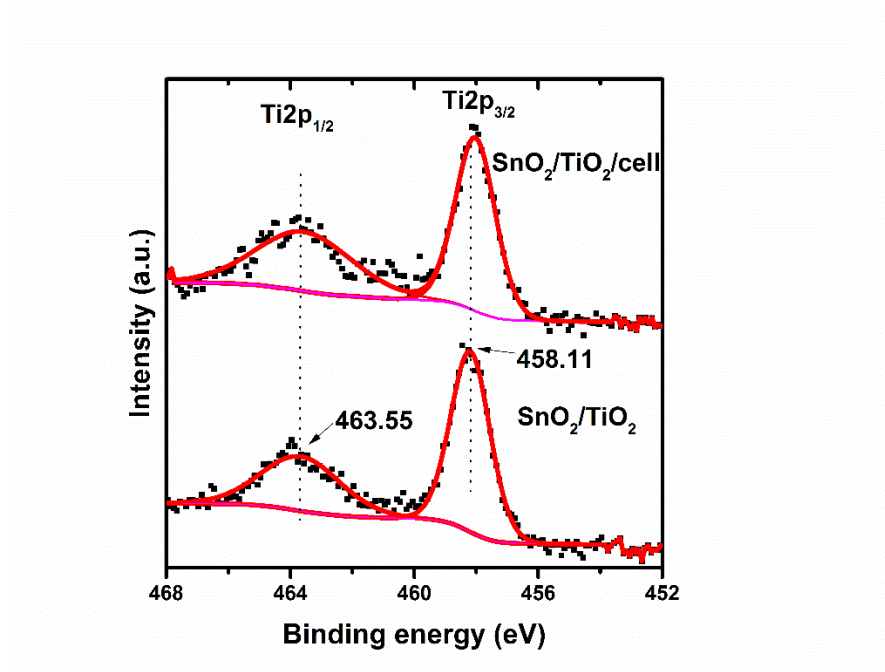


Figure S2: High-resolution X-ray Photoelectron peak spectra and curve fit of Ti 2p for SnO<sub>2</sub> photoanode after treatment, SnO<sub>2</sub> photoanode after photoanalysis process, and SnO<sub>2</sub> photoanode with treatment after photoanalysis process.

In Figure S3, we report the Sn 3d peaks for SnO<sub>2</sub> photoanode, SnO<sub>2</sub> photoanode after treatment, SnO<sub>2</sub> photoanode after photoanalysis process, and the treated anode after photoanalysis process. The XPS clearly reveals that there is no significant change in the Sn<sup>4+</sup> state after the post treatment and also after cell fabrication and photoanalysis process. Since there is no significant shift in the Sn 3d peak position, so, from our XPS results we confirm that there is no oxidation/reduction of SnO<sub>2</sub>.

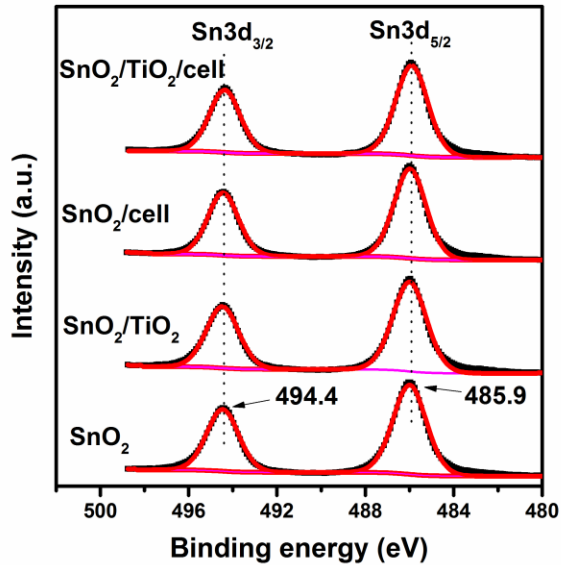


Figure S3: High-resolution X-ray Photoelectron peak spectra and curve fit of Sn 3d for SnO<sub>2</sub> photoanode, SnO<sub>2</sub> photoanode after treatment, SnO<sub>2</sub> photoanode after photoanalysis process, and the treated anode after photoanalysis process

## Reference

1. Akhavan, O. Lasting antibacterial activities of Ag–TiO<sub>2</sub>/Ag/a-TiO<sub>2</sub> nanocomposite thin film photocatalysts under solar light irradiation. *Journal of Colloid and Interface Science* **336**, 117-124, doi:<http://dx.doi.org/10.1016/j.jcis.2009.03.018> (2009).

The Chapter 4.2, in full, is a reprint of the material as it appears in *Nanoscale*, 2018. Kaustubh Basu, Gurpreet Singh Selopal, Mahyar Mohammadnezhad, Rusoma Akalimali, Zhiming M. Wang, Haiguang Zhao, Fiorenzo Vetrone, Federico Rosei. The dissertation author was the primary investigator of this paper.

## **4.2 Hybrid graphene/metal oxide photoanodes for efficient and stable dye sensitized solar cell**

Kaustubh Basu<sup>1</sup>, Gurpreet Singh Selopal<sup>1,2\*</sup>, Mahyar Mohammadnezhad<sup>1</sup>, Rusoma Akalimali<sup>1</sup>  
Zhiming M. Wang<sup>2</sup>, Haiguang Zhao<sup>3\*</sup>, Fiorenzo Vetrone<sup>1,2</sup>, Federico Rosei<sup>1,2\*</sup>

<sup>1</sup>Institut National de la Recherche Scientifique, Centre Énergie, Matériaux et Télécommunications,  
1650 Boulevard Lionel-Boulet, Varennes, Québec J3X 1S2, Canada

<sup>2</sup>Institute for Fundamental and Frontier Science, University of Electronic Science and Technology  
of China, Chengdu 610054, PR China

<sup>3</sup> College of Physics &The State Key Laboratory, Qingdao University, No. 308 Ningxia Road,  
Qingdao 266071, PR China

**\* Corresponding authors:**

**Gurpreet Singh Selopal:** gurpreet.selopal@emt.inrs.ca

**Haiguang Zhao:** hgzhao@qdu.edu.cn

**Federico Rosei:** rosei@emt.inrs.ca

## **Abstract**

We report the effect of incorporating graphene microplatelets into a SnO<sub>2</sub>-TiO<sub>2</sub> mesoporous heterostructure photoanode, to enhance the efficiency and long-term stability of dye sensitized solar cells (DSSCs). DSSCs were fabricated by introducing different concentrations of graphene microplatelets (up to 0.50 wt.%) into the SnO<sub>2</sub>-TiO<sub>2</sub> mesoporous network, realizing a fast and large area-scalable approach. At an optimized concentration of 0.03 wt.% of graphene microplatelets, the highest photoconversion efficiency (PCE) of 3.37% was achieved. This PCE is ~16% higher than the one measured for DSSCs based on standard SnO<sub>2</sub>-TiO<sub>2</sub> photoanodes. This improvement of PCE can be attributed to enhanced electron lifetime and reduced charge recombination in the hybrid SnO<sub>2</sub>-TiO<sub>2</sub>/graphene heterostructure photoanodes, confirmed by transient photovoltage decay and impedance spectroscopy. In addition, we recorded long-term stability of the DSSCs during 200 hours of continuous illumination under one sun simulated sunlight (AM 1.5G). Our investigation demonstrated that the addition of graphene microplatelets (0.03 wt.%) in the DSSCs made with the hybrid photoanode shows superior long-term stability than the control device. The PCE drop in the SnO<sub>2</sub>-TiO<sub>2</sub>/graphene hybrid photoanode cells was a mere 8%, while a sharp plummet of ~30% in PCE was observed in control devices. These findings demonstrate the SnO<sub>2</sub>-TiO<sub>2</sub>/graphene heterostructure architecture as a promising photoanode towards efficient and stable DSSCs.

**Key words:** Graphene microplatelets, SnO<sub>2</sub>-TiO<sub>2</sub>, electron transport, charge recombination.

## Introduction

The direct conversion of solar energy into electricity presents a promising opportunity to reduce the dependence from non-renewable energy sources such as fossil fuels, also reducing the related carbon footprint which is the root cause of climate change.[1] Dye sensitized solar cells (DSSCs) are viewed as potential alternatives to first and second generation solar cells due to their promising attributes such as being environmentally benign, low cost and large area scalability.[2] The highest photoconversion efficiency (PCE) reported for DSSCs reaches 14.3%,[3] still lower than typical commercial values of single-crystal silicon solar cells (PCE of 20%) [4,5]. Such low values are primarily due to recombination events during charge transport and the limited absorption spectrum of dyes.[6] Typically, a DSSC consists of a mesoporous wide-band-gap semiconductor oxide film with high specific surface area deposited on a fluorine doped tin oxide (FTO) transparent conductive glass as an electron transporter, dye molecules as a light harvester, anchored to the mesoporous film, a redox couple electrolyte as a hole transport medium and platinum (Pt) coated FTO as a counter electrode.[6]

The semiconducting oxide film plays a crucial role in the electron transport kinetics of a DSSC and offers a scaffold to anchor the dye molecules. [6] The photo-injected electrons have to traverse a significant path encountering grain boundaries,[7] which act as charge traps or recombination centers. Until now, various strategies have been realized to alleviate this problem, by the application of one dimensional (1-D) oxide nanostructures such as nanotubes,[8,9] nanowires,[10,11] nanorods,[12,13] composite systems,[14,15] or hierarchically assembled photoanodes of separate wide band gap semiconductors.[16,17] In addition, carbonaceous materials, such as carbon nanotubes (CNTs) or graphene, and their composites, have attracted great attention, due to their unique structural and optoelectronic properties and low cost,[18–22] which

can play a significant role to enhance the charge collection and transport. Our previous studies demonstrated that the incorporation of carbonaceous materials like CNTs, graphene and graphene nanoribbons in TiO<sub>2</sub>, assists in enhancing the electron transport by directing the electron flow towards the FTO conducting electrode.[23–25] The high specific area of carbon allotropes also improves dye loading resulting in an enhancement of overall photovoltaic performance through increased short circuit photocurrent density ( $J_{sc}$ ) and PCE.[18,24,26] Until now, carbonaceous materials have been mostly incorporated in TiO<sub>2</sub> based photoanodes for DSSCs. TiO<sub>2</sub> is widely preferred as the photoanode material for DSSCs, mainly because of its favorable band alignment with extensively used dyes (N719, black dye, etc.), which facilitates fast electron injection from the lowest unoccupied molecular orbital (LUMO) of excited dye molecules to the conduction band of TiO<sub>2</sub>. On the other hand, SnO<sub>2</sub> is a promising alternative photoanode material due to its large band gap (3.8 eV),[11] and higher electronic mobility of  $\sim 125 \text{ cm}^2/\text{V.s}$  [27,28] than its counterpart TiO<sub>2</sub> (mobility of  $\sim 1 \text{ cm}^2/\text{V.s}$  for rutile crystalline structure).[29] In addition, SnO<sub>2</sub> (3.8 eV) creates fewer oxidative holes in the valence band under UV illumination as compared to TiO<sub>2</sub> (3.2 eV). This is a major concern in DSSCs based on TiO<sub>2</sub> photoanodes, since the oxidative holes in the valence band promotes dye degradation rate and hinders long-term stability of DSSCs, which are detrimental for DSSC technology.[30] Moreover, higher electron mobility in SnO<sub>2</sub>, leads to fast transport of photo-injected electrons within the nanoparticle network. Therefore, an effective approach for producing an efficient and stable DSSC, is to combine the advantages of both SnO<sub>2</sub> and TiO<sub>2</sub> materials by fabricating a SnO<sub>2</sub>-TiO<sub>2</sub> heterostructure photoanode. Although DSSCs hold significant promise in terms of PCE,[3] long duration stability still remains a key challenge. Several mechanisms such as thermal and mechanical stress are responsible for the deterioration of the performance of DSSCs in the long

run.[31] Therefore, degradation mechanisms on the performance of DSSCs under long-term operation needs to be thoroughly investigated. However, carbon allotropes were proven to alleviate the thermal stability degradation mechanism in DSSCs.[32]

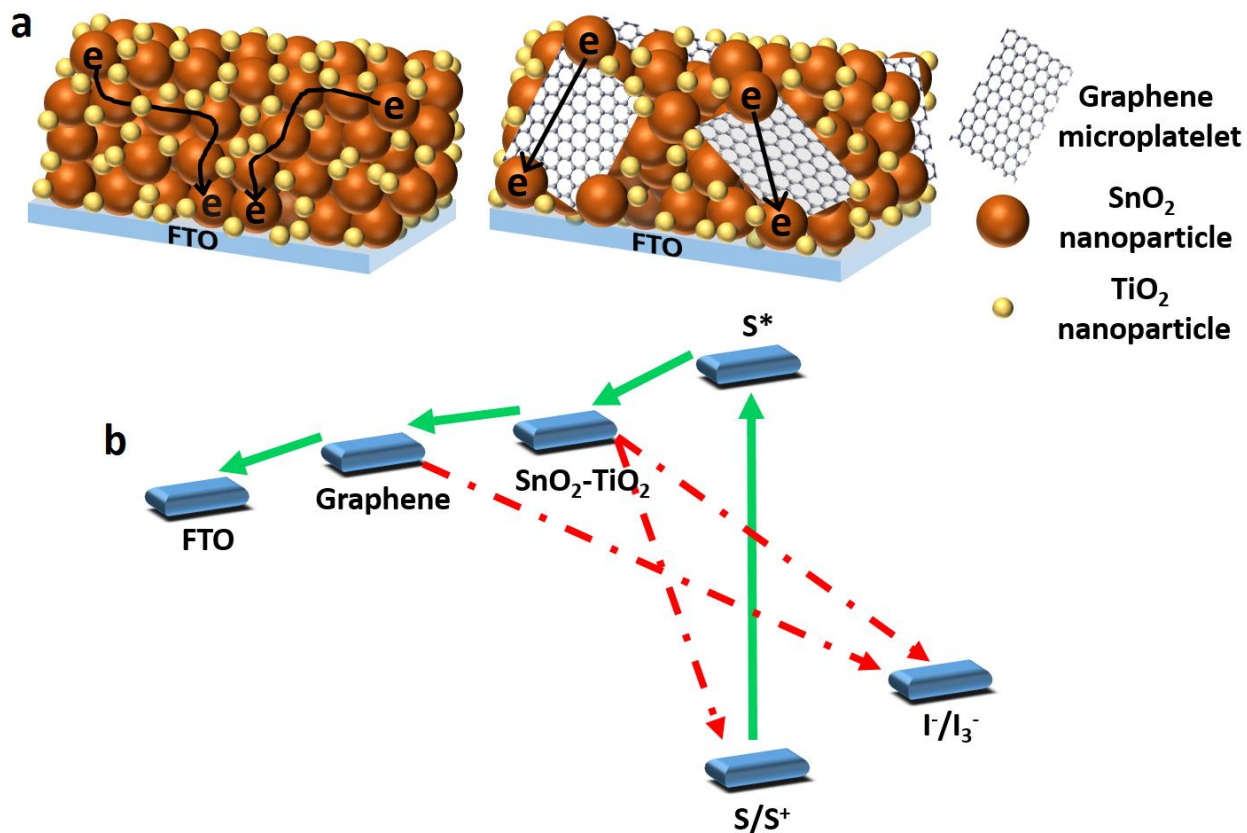


**Figure 1.** (a) Schematic illustration of improved charge transport in the anode, charge collection in the FTO with the introduction of graphene microplatelets. (b) Electronic band diagram of the DSSC incorporated with graphene microplatelets.

Herein, we fabricated a SnO<sub>2</sub>-TiO<sub>2</sub>/graphene hybrid heterostructure photoanode, by introducing different concentrations (up to 0.50 wt.%) of graphene microplatelets. The schematic in Fig. 1(a) shows the advantage of introducing graphene microplatelets in the photoanode to directing the carrier path toward FTO. At an optimum concentration of 0.03 wt.% of graphene microplatelets, a PCE of 3.37% was achieved as opposed to 2.91% for the control device. The enhancement of PCE can be attributed to higher electron lifetime and reduced charge recombination in graphene-

based hybrid photoanodes as confirmed by transient photovoltage decay and impedance spectroscopy measurements. Furthermore, the performance of the solar cells was studied for 200 hours of continuous illumination under simulated sunlight (AM 1.5G). Introduction of graphene microplatelets results in superior stability of the DSSCs, which establish our novel SnO<sub>2</sub>-TiO<sub>2</sub>/graphene heterostructure photoanode, as an efficient and stable photoanode architecture for DSSCs. Besides, to the best of our knowledge, stable and efficient DSSCs with graphene microplatelets in a SnO<sub>2</sub>-TiO<sub>2</sub> scaffold has been implemented for the first time.

### **Experimental procedure**

**Materials:** FTO coated glass substrates were purchased from Pilkington glasses with a sheet resistance of 8 Ω/□. SnO<sub>2</sub> nanopowder (99.9% tin (IV) oxide), to fabricate the photoanode, was obtained from American Elements. Graphene microplatelets were purchased from Raymor Inc. The redox couple electrolyte, consisting of iodine and tri-iodide (I<sup>-</sup>/I<sub>3</sub><sup>-</sup>), ruthenium based N719 dye (Ruthenizer 535-bisTBA), and Meltonix thermoplastic spacers were bought from Solaronix. Titanium (IV) chloride (0.09 M in 20% HCl), alpha-terpineol, ethyl cellulose, ethanol and isopropanol (IPA) were obtained from Sigma-Aldrich Inc.

**Preparation of SnO<sub>2</sub> paste:** The SnO<sub>2</sub> nanopowder utilized to prepare the paste consisted of 20 nm (average particle size) nanoparticles. 1g of SnO<sub>2</sub> nanopowder was mixed with 0.5 g of ethyl cellulose, 1 mL of alpha-terpineol, 1 mL of water and 5 mL of ethanol [33] in a beaker under 12 hours of magnetic stirring. The solvent was evaporated by connecting the beaker to a rotary pump, while under continuous magnetic stirring, until the volume of the mixture reduced to half of the initial volume.[33]

**Fabrication of DSSCs:** First, the FTO coated glass substrates were sonicated with 2% Triton X-100 in deionized water for 30 min to remove the adhesive from the packaging, then the FTO was

cleaned in IPA by sonication for 30 min and subsequently flushed with deionized water and dried using compressed air. FTO substrates were soaked in 50 mM  $\text{TiCl}_4$  solution for 20 min at 70 °C and subsequently rinsed with deionized water and annealed at 500 °C for 30 min to deposit a thin and compact  $\text{TiO}_2$  blocking layer (BL) on the FTO substrates.[33,34] Next, an ethanolic solution of graphene microplatelets were prepared with a concentration of 0.13 mg/ml. A calibration curve, shown in Fig. S1 for the graphene microplatelet concentration was constructed utilizing UV/Vis/near-infrared (NIR) spectrophotometry to ensure reproducibility. Subsequently,  $\text{SnO}_2$  paste (preparation methodology described earlier) was mixed with different weight concentrations of graphene microplatelets with respect to the  $\text{SnO}_2$  nanopowder weight (from 0 wt.% to 0.50 wt.%) and applied on the BL by the doctor blading technique following previously reported procedure.[24] The substrates were dried at room temperature for 15 min, followed by heating at 150 °C for 6 min on a hot plate to create the first layer. After the substrates were cooled down to room temperature, another layer of paste of the same recipe was tape casted using the similar drying procedure and annealed in a furnace at 500 °C for 30 min in air and cooled down to room temperature. The annealed  $\text{SnO}_2$  photoanodes were dip-coated in 50 mM  $\text{TiCl}_4$  precursor solution following a procedure described in the literature,[34] thereby creating a  $\text{SnO}_2$ - $\text{TiO}_2$  heterostructure. The photoanodes were then immersed in a 0.5 mM ethanolic solution of the commercial N719 dye for 18 hours, and subsequently rinsed with ethanol to remove the unabsorbed dye molecules.[33] A 10 nm thick Pt deposited on FTO glass substrate was used as a counter electrode. To prevent the DSSCs from short circuiting when the photoanode and counter electrode are clamped together, a 60  $\mu\text{m}$  thick thermoplastic spacer was used. An iodide/tri-iodide redox couple electrolyte was injected through the spacers, which act as the hole transporting medium.

**PV measurements:** A Class AAA Solar Simulator from Photo Emission Tech (SS50AAA) coupled with a Keithley 2400 sourcemeter was used to measure the current density vs voltage (J-V) under simulated sunlight of 1 sun AM 1.5G irradiation (100 mW/cm<sup>2</sup>). The power intensity of the simulated sunlight was calibrated with a Si reference diode. The Keithley 2400 sourcemeter was controlled with a computer software written using the TESTPOINT platform. The fill factor (FF) and the PCE were calculated using the following equations.[6]

$$FF = \frac{P_{\max}}{J_{sc} \times V_{oc}} = \frac{J_{\max} \times V_{\max}}{J_{sc} \times V_{oc}}$$

$$PCE(\%) = \frac{P_{\max}}{P_{in}} \times 100\% = \frac{J_{sc} \times V_{oc} \times FF}{P_{in}} \times 100\%$$

Where,  $P_{\max}$  is the maximum power output,  $J_{sc}$  is the short-circuit current density,  $V_{oc}$  is the open-circuit voltage.  $J_{\max}$  and  $V_{\max}$  are the current density and the voltage at maximum power output in the J-V curves respectively.  $P_{in}$  is the incident light power.

**Electrochemical impedance spectroscopy (EIS) measurements:** EIS was studied in the dark using a SOLARTRON 1260A impedance/gain-phase analyzer. The measurements for all the samples were carried out inside a Faraday cage in the 100 mHz-300 kHz frequency range, by applying an external bias between 200 and 600 mV. All impedance measurements were analyzed using their relevant equivalent circuit model with Z-View software (v3.5, Scribner Associate, Inc.).

**Dye loading measurements:** Dye loading measurements of SnO<sub>2</sub>-TiO<sub>2</sub> photoanodes with different concentrations of graphene microplatelets, were performed by UV-Vis-NIR spectrophotometry. Dye molecules were removed from the photoanodes by washing the anodes with 0.1 M NaOH aqueous solution. Optical absorption spectra were collected of the removed dye molecules solutions by using a Cary 5000 UV-Vis-NIR spectrophotometer (Varian) with a scan speed of 600 nm/min. One cubic centimeter quartz cuvettes were used for liquid samples.

**Materials characterization:** The morphology of the samples was studied using scanning electron microscopy (SEM) and Raman analysis. SEM images were recorded using a focused ion beam (FIB) integrated with a SEM Tescan LYRA 3XMH at an accelerating voltage of 20 kV. Raman analysis of the samples were carried out employing a WITec alpha 300 micro Raman, which uses a 532 nm fiber coupled laser for excitation.

## Results and Discussion

SnO<sub>2</sub> nanoparticles of 20 nm size were used to fabricate the photoanode of the DSSCs, which offer adequate surface area for dye adsorption, and relatively less number of grain boundaries, in comparison with smaller sized nanoparticles, that increase the electron trapping probability.[35–39] To create the SnO<sub>2</sub>-TiO<sub>2</sub> heterostructured photoanode, we fabricated a SnO<sub>2</sub> photoanode by the doctor blade technique, and consequent hydrothermal treatment of the anodes with an aqueous TiCl<sub>4</sub> solution. Different approaches to create this heterostructured photoanode have been studied extensively in our previous work,[33] and an aqueous TiCl<sub>4</sub> hydrothermal treatment was proven to be favorable for fabricating high efficiency DSSCs.[33] To enhance the electron transport within the photoanode, we introduced graphene microplatelets in the SnO<sub>2</sub>-TiO<sub>2</sub> nanoparticle framework. The morphologies of the samples, with or without graphene microplatelets were investigated using SEM. Fig 2(a)-(b) displays the SEM of the bare photoanode and the photoanode with optimum loading of graphene (0.03 wt.%), which shows similar morphology in both cases, confirming that the minute addition of graphene microplatelets does not alter the morphology of the mesoporous film. When we further introduced more graphene, i.e. at 0.50 wt.% by weight in SnO<sub>2</sub>, SEM images shown in Fig. 2(c) reveal the formation of micro-cracks within the mesoporous framework. Previous literature reports [18,19,40] have demonstrated that the presence of carbonaceous materials inside the photoanode induces cracks or leads to an increase in the porosity of the

photoanode, which is detrimental for the performance of DSSCs. Graphene microplatelets may be directly observed by techniques like SEM, only at very high concentrations.[18,19] The SnO<sub>2</sub>-TiO<sub>2</sub>/graphene composite photoanodes with different graphene contents were investigated using Raman spectroscopy. The Raman spectra for the three different contents of graphene, namely, 0, 0.03 and 0.50 wt.% in the SnO<sub>2</sub>-TiO<sub>2</sub> photoanodes are presented in Fig. 2 (d). In the high concentration graphene sample (0.50 wt.%), three prominent features are observed, the G peak ~ 1580 cm<sup>-1</sup>, D peak ~ 1350 cm<sup>-1</sup> and a 2D peak ~ 2700 cm<sup>-1</sup> (Fig. 2 (d) inset). The G peak arises from the doubly degenerate phonon mode (E<sub>2g</sub> symmetry),[41] which confirms the existence of the sp<sup>2</sup> carbon networks present in graphene.[42] We can see the presence of the G peak in both the photoanode with 0.50 wt.% graphene and the photoanode with a very minute quantity of graphene (0.03 wt.%). On the other hand, the D peak, which is attributed to the disorder induced mode primarily present in graphene with defects,[42] does not appear in the 0.03 wt.% photoanode. Usually, the intensity of the G peak (I<sub>G</sub>) is higher than that of the D peak (I<sub>D</sub>) for low defect or defect free graphene and the relative intensity ratio (I<sub>D</sub>/I<sub>G</sub>) determines the quantity of defects present in the graphene.[43] At very low concentration (0.03 wt.%) of graphene in our sample, we are unable to detect the presence of the D peak, since the intensity of the G peak is already very low. However, the 2D peak at ~2700 cm<sup>-1</sup>, which is considered a second order overtone of the D peak (not related to defects) [42] is detected in our sample with 0.03 wt.% graphene, which clearly demonstrates that the graphene preserves its original structure at low concentrations, even after sintering at high temperature (500 °C) for device fabrication.

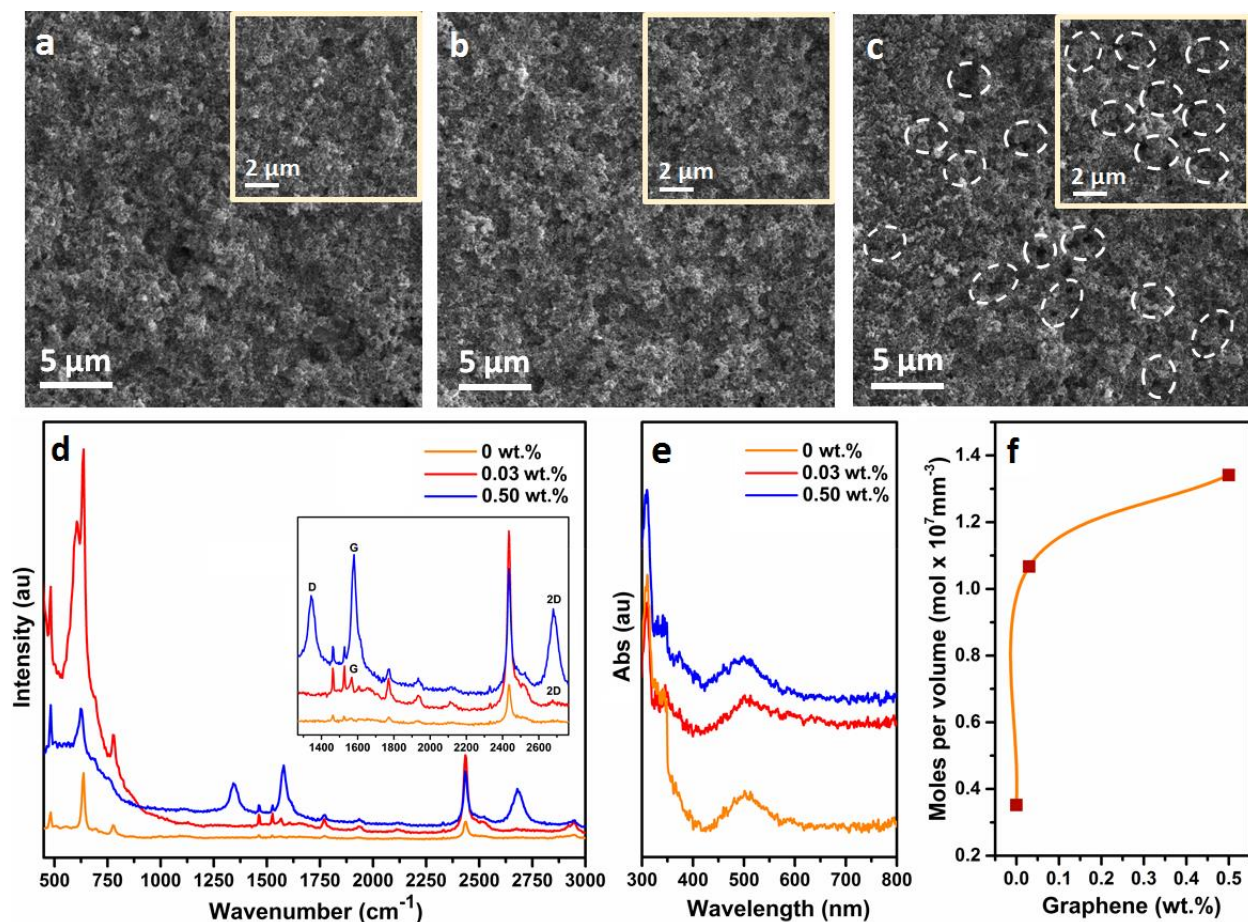


**Figure 2:** SEM images of the SnO<sub>2</sub>-TiO<sub>2</sub> film with different concentrations (wt.%) of graphene microplatelets deposited on FTO substrate: (a) bare SnO<sub>2</sub>-TiO<sub>2</sub>; (b) 0.03 wt.% of graphene microplatelets in SnO<sub>2</sub>-TiO<sub>2</sub>; (c) 0.50 wt.% of graphene microplatelets in SnO<sub>2</sub>-TiO<sub>2</sub>. The dashed ovals in the inset highlight the presence of cracks. (d) Raman spectra for the bare photoanode, and with 0.03 and 0.50 wt.% of graphene microplatelets; (e, f) Dye loading measurement for the bare photoanode, and with 0.03 and 0.50 wt.% of graphene microplatelets.

Fig. 2 (e) shows the comparison of the absorption spectra of the N719 dye molecule solution extracted from the SnO<sub>2</sub>-TiO<sub>2</sub>/graphene composite photoanodes with different concentrations of graphene microplatelets. The absorption increases with increased concentration of graphene microplatelets. Based on the absorption spectra, the calculated average amount of dye molecules

mole per unit volume is shown in Fig. 2(f). The results demonstrated that with the increase in graphene content, the dye loading amount increases. Higher dye loading with increased concentration of graphene (0.50 wt.%), is mainly attributed to adsorption of multilayered dye molecules. These multilayered dye molecules can not participate in electron injection into the photoanode and hence reduce the overall device performance. These findings are consistent with our previous studies on the negative effect of higher loading of carbonaceous materials in carbonaceous-TiO<sub>2</sub> hybrid photoanodes based solar cells.[18,24]

To understand the role of the graphene microplatelets on the photovoltaic performance of the devices, we studied the J-V characteristics under simulated sunlight of one sun (AM 1.5G, 100 mW/cm<sup>2</sup>), which is displayed in Fig. 3(a). The functional parameters, which include the open circuit photovoltage ( $V_{oc}$ ),  $J_{sc}$ , the fill factor (FF) and the PCE are reported in Table 1. From Fig. 3(a) we observed that, with the increase of graphene microplatelets concentration, from 0 to 0.03 wt%, there is a steady increment of  $J_{sc}$ , which reflects on the overall PCE of the device.

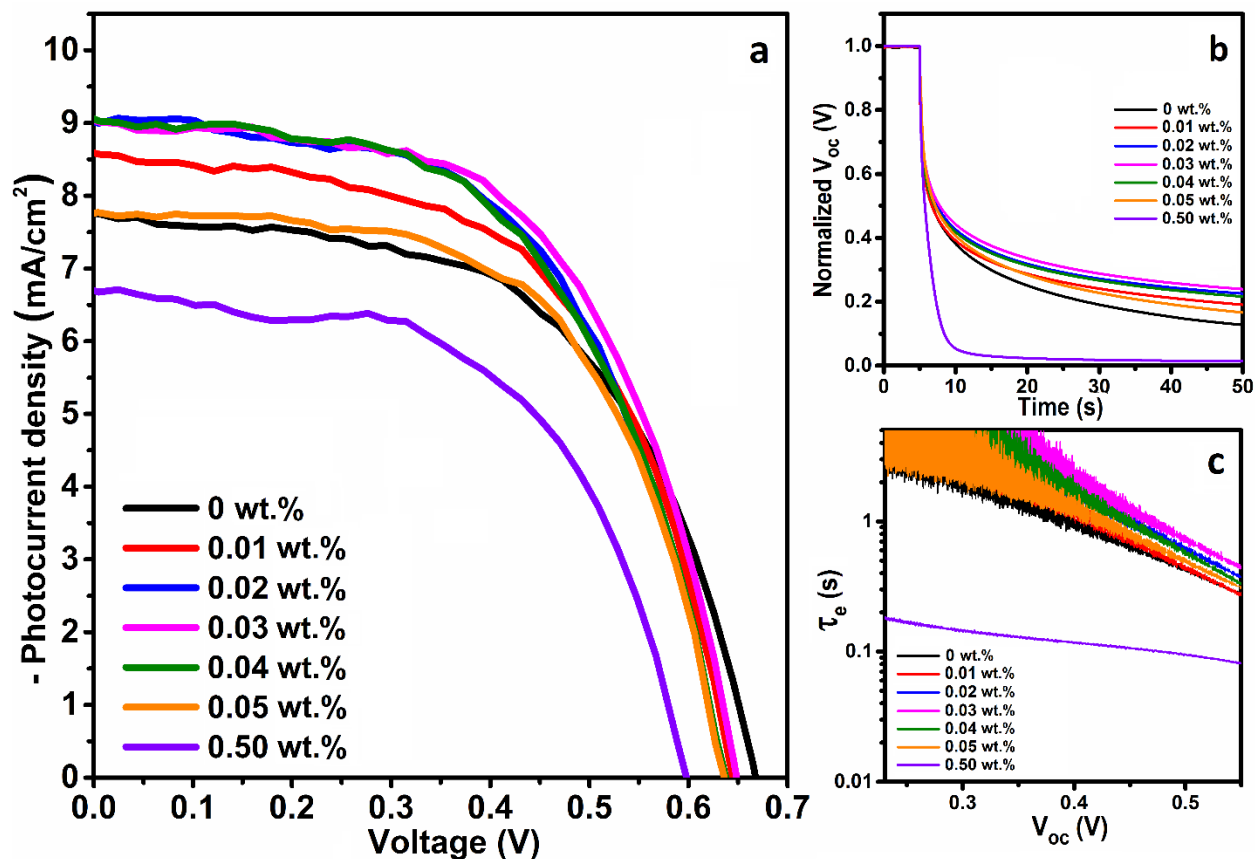


**Figure 3:** (a) J-V curves of devices with different concentrations (by wt.%) of graphene microplatelets in the SnO<sub>2</sub>-TiO<sub>2</sub> photoanode under one sun illumination (AM1.5G, 100 mW/cm<sup>2</sup>); (b) Normalized transient open circuit photovoltage ( $V_{oc}$ ) decay curves of the corresponding devices; (c) Computed electron lifetime values from  $V_{oc}$  decay dynamics.

Table 1: Functional parameters of DSSCs with different concentrations of graphene microplatelets.

Graphene Wt. %	$V_{oc}$ (V)	$J_{sc}$ (mA/cm <sup>2</sup> )	FF	PCE (%)
0	0.67	7.76	0.56	2.91
0.01	0.65	8.59	0.57	3.14
0.02	0.64	9.01	0.57	3.27
0.03	0.65	9.03	0.58	3.37
0.04	0.64	9.06	0.56	3.22
0.05	0.63	7.77	0.60	2.96
0.50	0.60	6.69	0.56	2.24

The introduction of a controlled amount of graphene microplatelets can create three-dimensional (3D) percolating networks within the photoanode, [18] which facilitate charge transport and hence significantly boost  $J_{sc}$  of the device. Moreover, addition of MWCNTs and graphene improves the effective surface area for efficient dye adsorption,[44–46] hence we confirmed a better dye loading with the introduction of graphene microplatelets, which is presented in Fig. 2(e), (f). However, with further increase of graphene concentration, the  $J_{sc}$  of the DSSCs deteriorate, which is primarily because at higher loading of graphene microplatelets, they tend to agglomerate. This enables direct contact between the graphene microplatelets and the electrolyte, adding a new recombination pathway.[23] In addition, higher concentration of graphene provokes a light-harvesting competition between the graphene microplatelets and the dye,[47] and since the photons absorbed by the graphene microplatelets do not contribute to photocurrent generation,[23] the DSSC performance deteriorates. Besides, an excess of graphene microplatelets may form large pores at the micron scale [40] resulting in a less compact photoanode layer, which is detrimental for electron transport. This behavior of  $J_{sc}$  as a function of the graphene concentration is reported in Fig. S2 (c). The addition of graphene microplatelets, however, reduces the  $V_{oc}$  of the devices, although the effect is overcompensated by a systematic increase of the  $J_{sc}$  and the FF. This behavior can be explained from the band alignment illustrated in Figure 1b. With an increase in graphene concentration, the conduction band edge [18] of the  $\text{SnO}_2\text{-TiO}_2/\text{graphene}$  hybrid heterostructure system downshifts with respect to  $\text{SnO}_2\text{-TiO}_2$ , resulting in a systematic decrease of the  $V_{oc}$  of the final device from 670 mV in  $\text{SnO}_2\text{-TiO}_2$  photoanode to 600 mV in 0.50 wt.%  $\text{SnO}_2\text{-TiO}_2/\text{graphene}$  hybrid photoanode as presented in Fig. S2 (a). The trend for PCE as a function of graphene loading, has been displayed in Fig. S2 (d), which demonstrates similar behavior like  $J_{sc}$ . The PCE increases from ~ 2.9 % to ~ 3.4% until the optimum concentration of 0.03 wt.% is reached, but with further

increase in graphene microplatelets loading, the magnitude of PCE deteriorates, the primary driving factor being the reduction in  $J_{sc}$ .

To better understand the effect of different concentrations of graphene microplatelets on the carrier dynamics of the DSSCs, we performed the transient photovoltage decay measurement, which provides an insight of photogenerated carrier recombination at the  $\text{SnO}_2\text{-TiO}_2/\text{dye}/\text{electrolyte}$  interface. DSSCs were irradiated with one sun simulated sunlight (AM 1.5G,  $100 \text{ mW}/\text{cm}^2$ ) until  $V_{oc}$  was attained. Few seconds after the  $V_{oc}$  was stable, the shutter of the sun simulator was closed and the transient voltage decay was recorded under dark conditions. Fig. 3(b) displays the transient  $V_{oc}$  decay curves for DSSCs based on  $\text{SnO}_2\text{-TiO}_2/\text{graphene}$  photoanodes of different concentrations (by wt.%) of graphene. We observe, that the  $V_{oc}$  decay is fastest for the DSSC with graphene of 0.50 wt.% and slowest in the case of the optimal concentration of 0.03 wt.%, which is consistent with the “J-V” characteristics.

The electron lifetime ( $\tau_e$ ) was determined from the  $V_{oc}$  decay measurements by using the following equation [48,49]

$$\tau_e = \left( \frac{k_B T}{e} \right) / \left( \frac{dV_{oc}}{dt} \right)$$

Where,  $k_B$  is the Boltzmann constant,  $T$  is the absolute temperature, and  $e$  is the elementary charge. From Fig. 3 (c), we notice that the magnitude of  $\tau_e$  systematically increases as further graphene microplatelets were incorporated until the optimum concentration of 0.03 wt.% is reached, where the magnitude of  $\tau_e$  is the highest. Higher value of  $\tau_e$  suggests longer diffusion length,[6] which confirms reduced carrier recombination. Thus, controlled quantity of graphene microplatelets can boost the electron transport in the photoanode. On the other hand, for further increase the graphene

loading we observed that the magnitude of  $\tau_e$  decreases sharply and reaches the lowest value at the maximum concentration (0.50 wt.%) of graphene microplatelets. This is due to the formation of micro-cracks at high loading of graphene microplatelets confirmed by SEM image presented in Fig. 2(c). The presence of micro-cracks inhibits a continuous pathway of transport for the photo-generated electron. Furthermore, the abundance of interpenetrating electrolyte in these cracks act as electron trapping centers, which hinder efficient electron percolation, thereby limiting the electron lifetime of the devices.

EIS spectra were measured under dark conditions by applying an external potential from 200 mV to 600 mV in the frequency range of 100 mHz-300 kHz. The Nyquist plots of EIS for DSSCs based on bare SnO<sub>2</sub>-TiO<sub>2</sub> and the optimized SnO<sub>2</sub>-TiO<sub>2</sub>/graphene hybrid photoanodes is shown in Fig. 4(a). By fitting the EIS data with suitable equivalent circuit, charge transfer resistance ( $R_{ct}$ ) at different value of applied was calculated for DSSCs based on SnO<sub>2</sub>-TiO<sub>2</sub> photoanode with and without graphene. The systematic comparison of  $R_{ct}$  of both DSSCs (with and without graphene) is shown in Fig. 4(d). The results demonstrated that the  $R_{ct}$  is lower for DSSC with SnO<sub>2</sub>-TiO<sub>2</sub>/graphene hybrid photoanodes than the DSSC with SnO<sub>2</sub>-TiO<sub>2</sub> photoanodes. This is mainly attributed to the efficient path offered to the electrons by graphene microplatelets within the SnO<sub>2</sub>-TiO<sub>2</sub>/graphene hybrid photoanode.

The electron lifetime was calculated from the Bode phase plot of cells by using the equation:  $\tau_e = 1/(2\pi f_{max})$ , where  $f_{max}$  is the peak frequency in the bode plot. The shift in the  $f_{max}$  is directly related to the electron lifetime value. The comparison of the calculated electron lifetime values of DSSCs with bare SnO<sub>2</sub>-TiO<sub>2</sub> and SnO<sub>2</sub>-TiO<sub>2</sub>/graphene hybrid photoanodes is shown in Fig. 4(c). The electron lifetime of the DSSC based on SnO<sub>2</sub>-TiO<sub>2</sub>/graphene hybrid photoanodes is higher than the DSSC based on the graphene-SnO<sub>2</sub>-TiO<sub>2</sub> photoanode. On the basis of the EIS results, we can

demonstrate that this improvement in PCE of DSSCs with the addition of an optimized amount of graphene microplatelets in SnO<sub>2</sub>-TiO<sub>2</sub> heterostructured photoanodes is due to reduced R<sub>ct</sub> and improved electron lifetime values as compared to the bare SnO<sub>2</sub>-TiO<sub>2</sub> heterostructured photoanodes.

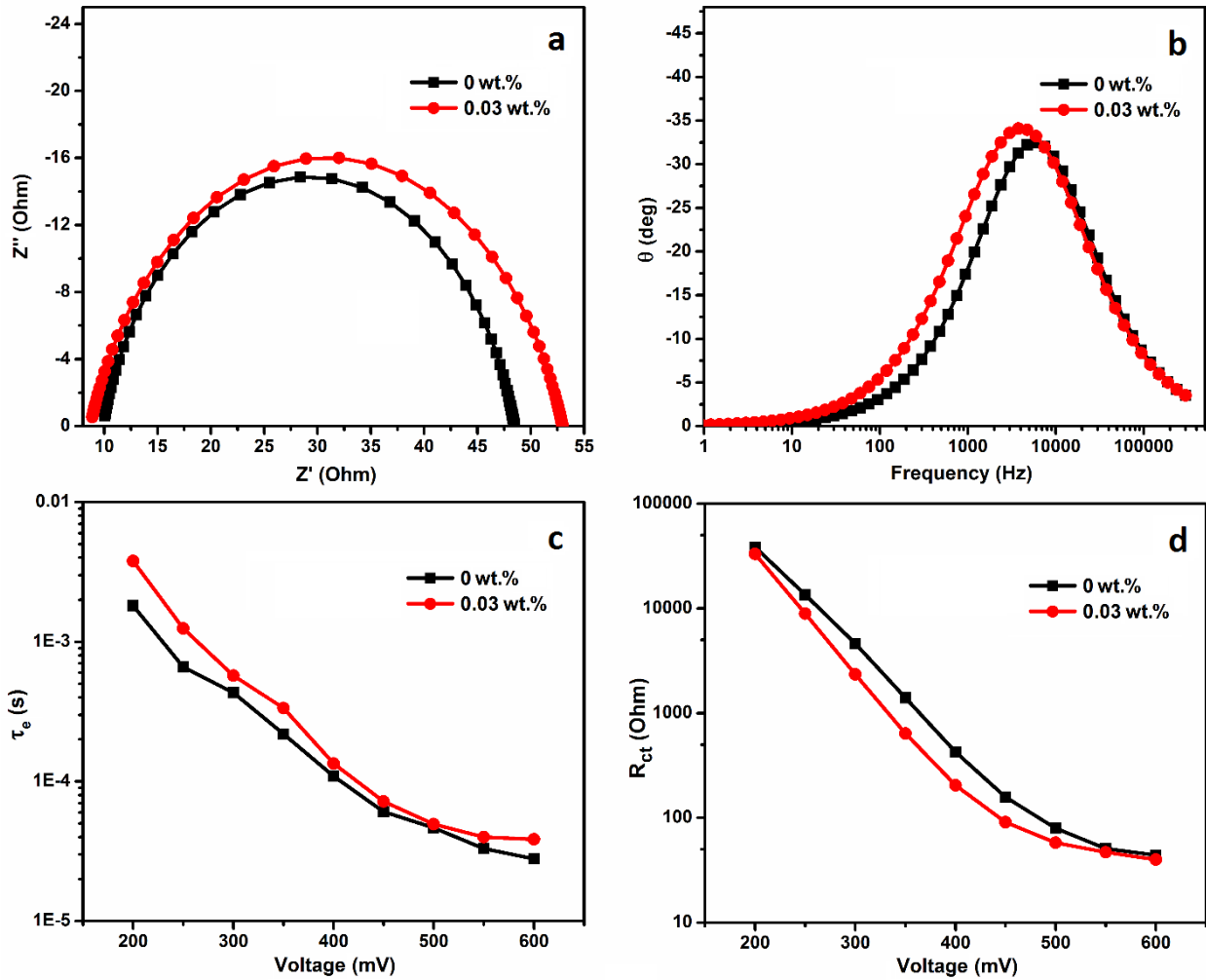


**Figure 4.** EIS analysis of DSSCs with different graphene microplatelet concentrations under dark condition and around V<sub>oc</sub>: (a) Nyquist plots recombination resistance; (b) Phase Bode plots. (c) Electron lifetime of devices. (d) Charge transfer resistances.

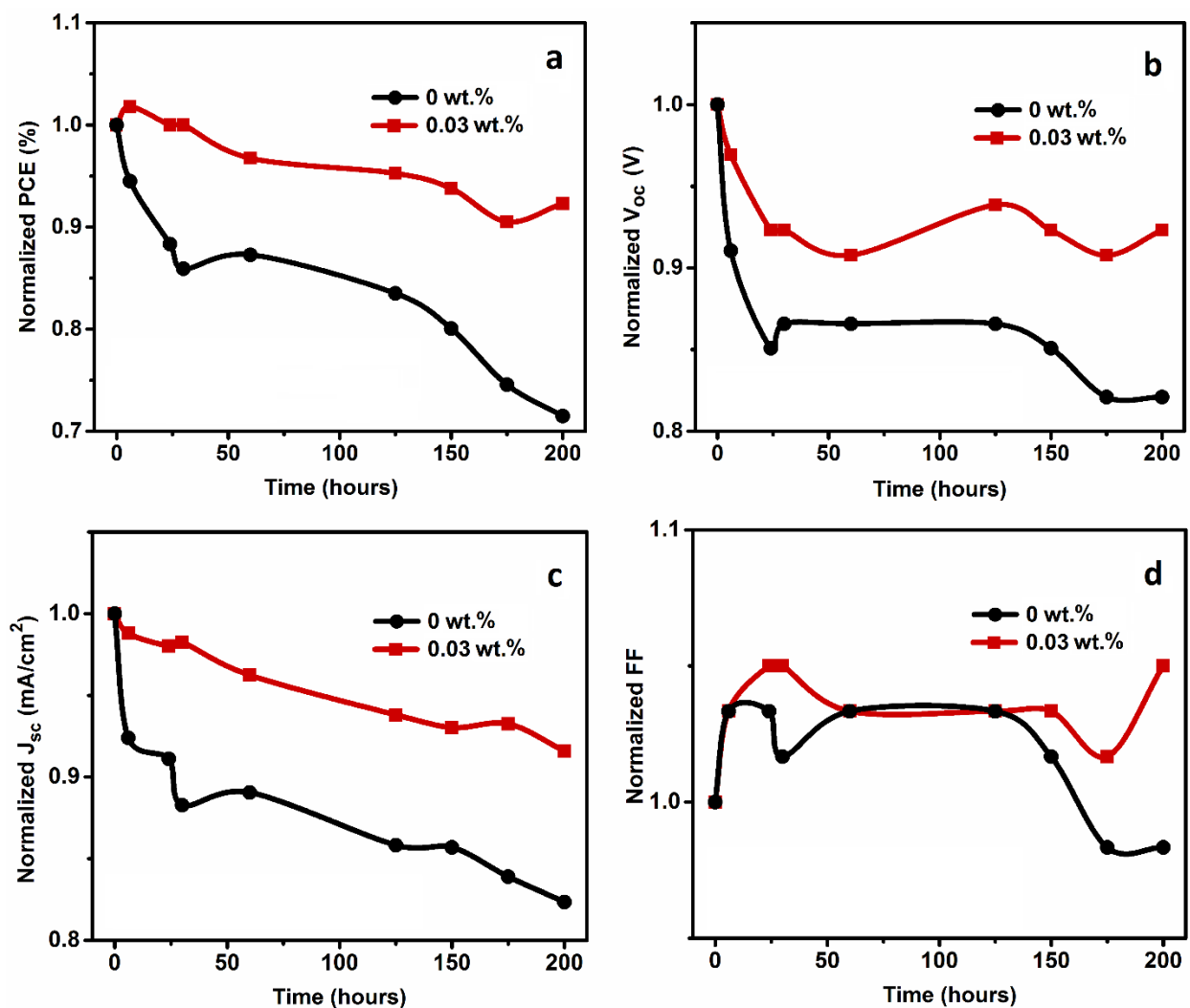


**Figure 5:** Functional parameters of the DSSCs with or without graphene microplatelets under continuous irradiation of 1 Sun (AM 1.5G, 100 mW/cm<sup>2</sup>) for 200 hours: (a) normalized PCE (%); (b) normalized  $V_{oc}$  (V); (c) normalized  $J_{sc}$  (mA/cm<sup>2</sup>) and (d) normalized FF.

In addition to the excellent PCE in DSSCs, long-term stability is also a critical issue to commercialize this technology. Hence, we furthermore, carried out long-term stability tests for both the DSSCs with the SnO<sub>2</sub>-TiO<sub>2</sub>/graphene photoanode with the optimum concentration of graphene microplatelets and bare SnO<sub>2</sub>-TiO<sub>2</sub> photoanode. The DSSCs fabricated with these photoanodes were irradiated under 1 sun simulated sunlight (AM 1.5G, 100mW/cm<sup>2</sup>) for a period of 200 hours and their performance was measured at regular time intervals. The stability tests

displayed in Fig. 5 shows that the DSSC with graphene exhibits significantly better stability in comparison to the bare one. The PCE of the graphene incorporated DSSC retains ~92% of its initial value after 200 hours, whereas the bare sample retains only 71% of its initial value. This impressive performance of graphene incorporated DSSCs was only possible due to the exceptional stability of the photocurrent density, shown in Fig. 5(c), which drops only ~ 8% after 200 hours of continuous illumination. It has been reported that carbon microstructures like graphene/MWCNTs improve particle bonding, [44,50] which improves the stability of the solar cells. Besides, the optimized graphene photoanode is ~10% more stable for  $V_{oc}$  and ~7% more stable for FF over the bare photoanode after 200 hours of continuous illumination, which further contributes to better performance of the  $\text{SnO}_2\text{-TiO}_2/\text{graphene}$  based DSSCs. Moreover, continuous illumination can induce thermal stress, but the addition of CNTs/graphene can improve the stability because they have excellent thermal conductivity. [51–53]. Thus, DSSCs fabricated with  $\text{SnO}_2\text{-TiO}_2/\text{graphene}$  photoanode offer a realistic approach towards implementing an efficient and stable DSSC.

## **Conclusions**

In summary, we successfully demonstrate DSSCs with novel  $\text{SnO}_2\text{-TiO}_2/\text{graphene}$  mesoporous photoanode architecture. A systematic investigation was carried out on the functional parameters and long-term stability of the DSSCs by incorporating different concentrations of graphene microplatelets into the  $\text{SnO}_2\text{-TiO}_2$  mesoporous framework. A PCE of 3.37% was achieved under 1 sun simulated irradiation, AM 1.5G, for  $\text{SnO}_2\text{-TiO}_2/\text{graphene}$  DSSC by optimization of graphene concentration, which is ~16% higher than the  $\text{SnO}_2\text{-TiO}_2$  DSSCs. This enhancement of PCE can be accredited to higher electron lifetime and reduced charge recombination in  $\text{SnO}_2\text{-TiO}_2/\text{graphene}$  hybrid photoanodes as confirmed by EIS and consistent with our findings from  $V_{oc}$  decay experiments. In addition, the performance of the solar cells was recorded for 200 hours of

continuous illumination under simulated sunlight (AM 1.5G). Results demonstrated that the incorporation of graphene microplatelets in SnO<sub>2</sub>-TiO<sub>2</sub> significantly improve the long-term stability with respect to bare SnO<sub>2</sub>-TiO<sub>2</sub> DSSCs. These results establish SnO<sub>2</sub>-TiO<sub>2</sub>/graphene architecture as a promising photoanode towards highly efficient and stable DSSCs.

### **Acknowledgements**

We acknowledge funding from the Natural Sciences and Engineering Research Council (NSERC) of Canada in the form of Discovery Grants and a Strategic Project Grant in partnership with Canadian Solar, the Canada Foundation for Innovation for infrastructure and its operation. We also acknowledge the Fonds de Recherche du Québec-Nature et technologies (FRQNT) for Équipe (team) grants. This work was partially funded by the Ministère du Développement économique de l'Innovation et de l'Exportation (MDEIE) of Québec through the international project WIROX. F.R. acknowledges NSERC for funding and partial salary support from an E.W.R. Steacie Memorial Fellowship. G. S. Selopal acknowledges the UNESCO Chair in MATECSS for a Post-Doctoral Fellowship Excellence Scholarship and funding from the University of Electronic Science and Technology of China. H.G. Zhao acknowledges the start fund from Qingdao University and the funding from the Natural Science Foundation of Shandong Province (ZR2018MB001).

### **References**

- [1] L. Suganthi, A.A. Samuel, Energy models for demand forecasting—A review, *Renew. Sustain. Energy Rev.* 16 (2012) 1223–1240.
- [2] B. O'Regan, M. Grätzel, A low-cost, high-efficiency solar cell based on dye-sensitized colloidal TiO<sub>2</sub> films, *Nature*. 353 (1991) 737-740.

- [3] K. Kakiage, Y. Aoyama, T. Yano, K. Oya, J. Fujisawa, M. Hanaya, Highly-efficient dye-sensitized solar cells with collaborative sensitization by silyl-anchor and carboxy-anchor dyes, *Chem. Commun.* 51 (2015) 15894–15897.
- [4] K. Yoshikawa, H. Kawasaki, W. Yoshida, T. Irie, K. Konishi, K. Nakano, T. Uto, D. Adachi, M. Kanematsu, H. Uzu, K. Yamamoto, Silicon heterojunction solar cell with interdigitated back contacts for a photoconversion efficiency over 26%, *Nat. Energy*. 2 (2017) 1-8.
- [5] J. Benick, A. Richter, R. Müller, H. Hauser, F. Feldmann, P. Krenckel, S. Riepe, F. Schindler, M.C. Schubert, M. Hermle, A.W. Bett, S.W. Glunz, High-Efficiency n-Type HP mc Silicon Solar Cells, *IEEE J. Photovolt.* 7 (2017) 1171–1175.
- [6] A. Hagfeldt, G. Boschloo, L. Sun, L. Kloo, H. Pettersson, Dye-Sensitized Solar Cells, *Chem. Rev.* 110 (2010) 6595–6663.
- [7] M. Grätzel, Photoelectrochemical cells, *Nature*. 414 (2001) 338-344.
- [8] A. Vomiero, V. Galstyan, A. Braga, I. Concina, M. Brisotto, E. Bontempi, G. Sberveglieri, Flexible dye sensitized solar cells using TiO<sub>2</sub> nanotubes, *Energy Environ. Sci.* 4 (2011) 3408–3413.
- [9] O.K. Varghese, M. Paulose, C.A. Grimes, Long vertically aligned titania nanotubes on transparent conducting oxide for highly efficient solar cells, *Nat. Nanotechnol.* 4 (2009) 592–597.
- [10] J.B. Baxter, E.S. Aydil, Nanowire-based dye-sensitized solar cells, *Appl. Phys. Lett.* 86 (2005) 0531141-05311413.

- [11] S. Gubbala, V. Chakrapani, V. Kumar, M.K. Sunkara, Band-Edge Engineered Hybrid Structures for Dye-Sensitized Solar Cells Based on SnO<sub>2</sub> Nanowires, *Adv. Funct. Mater.* 18 (2008) 2411–2418.
- [12] B. Liu, E.S. Aydil, Growth of Oriented Single-Crystalline Rutile TiO<sub>2</sub> Nanorods on Transparent Conducting Substrates for Dye-Sensitized Solar Cells, *J. Am. Chem. Soc.* 131 (2009) 3985–3990.
- [13] S.H. Kang, S.-H. Choi, M.-S. Kang, J.-Y. Kim, H.-S. Kim, T. Hyeon, Y.-E. Sung, Nanorod-Based Dye-Sensitized Solar Cells with Improved Charge Collection Efficiency, *Adv. Mater.* 20 (2008) 54–58.
- [14] B. Tan, Y. Wu, Dye-Sensitized Solar Cells Based on Anatase TiO<sub>2</sub> Nanoparticle/Nanowire Composites, *J. Phys. Chem. B.* 110 (2006) 15932–15938.
- [15] A. Vomiero, I. Concina, M.M. Natile, E. Comini, G. Faglia, M. Ferroni, I. Kholmanov, G. Sberveglieri, ZnO/TiO<sub>2</sub> nanonetwork as efficient photoanode in excitonic solar cells, *Appl. Phys. Lett.* 95 (2009) 1931041-1931043.
- [16] Q. Zhang, T.P. Chou, B. Russo, S.A. Jenekhe, G. Cao, Aggregation of ZnO nanocrystallites for high conversion efficiency in dye-sensitized solar cells, *Angew. Chem. Int. Ed Engl.* 47 (2008) 2402–2406.
- [17] N. Memarian, I. Concina, A. Braga, S.M. Rozati, A. Vomiero, G. Sberveglieri, Hierarchically assembled ZnO nanocrystallites for high-efficiency dye-sensitized solar cells, *Angew. Chem. Int. Ed Engl.* 50 (2011) 12321–12325.
- [18] K.T. Dembele, G.S. Selopal, R. Milan, C. Trudeau, D. Benetti, A. Soudi, M.M. Natile, G. Sberveglieri, S. Cloutier, I. Concina, F. Rosei, A. Vomiero, Graphene below the percolation threshold in TiO<sub>2</sub> for dye-sensitized solar cells, *J. Mater. Chem. A.* 3 (2015) 2580–2588.

- [19] N. Yang, J. Zhai, D. Wang, Y. Chen, L. Jiang, Two-Dimensional Graphene Bridges Enhanced Photoinduced Charge Transport in Dye-Sensitized Solar Cells, *ACS Nano*. 4 (2010) 887–894.
- [20] J. Durantini, P.P. Boix, M. Gervaldo, G.M. Morales, L. Otero, J. Bisquert, E.M. Barea, Photocurrent enhancement in dye-sensitized photovoltaic devices with titania–graphene composite electrodes, *J. Electroanal. Chem.* 683 (2012) 43–46.
- [21] D.W. Zhang, X.D. Li, H.B. Li, S. Chen, Z. Sun, X.J. Yin, S.M. Huang, Graphene-based counter electrode for dye-sensitized solar cells, *Carbon*. 49 (2011) 5382–5388.
- [22] T. Hasobe, S. Fukuzumi, P.V. Kamat, Organized Assemblies of Single Wall Carbon Nanotubes and Porphyrin for Photochemical Solar Cells: Charge Injection from Excited Porphyrin into Single-Walled Carbon Nanotubes, *J. Phys. Chem. B*. 110 (2006) 25477–25484.
- [23] D. Benetti, K. Therese Dembele, J. Benavides, H. Zhao, S. Cloutier, I. Concina, A. Vomiero, F. Rosei, Functionalized multi-wall carbon nanotubes/TiO<sub>2</sub> composites as efficient photoanodes for dye sensitized solar cells, *J. Mater. Chem. C*. 4 (2016) 3555–3562.
- [24] K.T. Dembele, G.S. Selopal, C. Soldano, R. Nechache, J.C. Rimada, I. Concina, G. Sberveglieri, F. Rosei, A. Vomiero, Hybrid Carbon Nanotubes–TiO<sub>2</sub> Photoanodes for High Efficiency Dye-Sensitized Solar Cells, *J. Phys. Chem. C*. 117 (2013) 14510–14517.
- [25] R. Akilimali, G.S. Selopal, D. Benetti, I. Serrano-Esparza, P.A. Algarabel, J.M. De Teresa, Z.M. Wang, B. Stansfield, H. Zhao, F. Rosei, Hybrid TiO<sub>2</sub>-Graphene nanoribbon photoanodes to improve the photoconversion efficiency of dye sensitized solar cells, *J. Power Sources*. 396 (2018) 566–573.

- [26] J. Fan, S. Liu, J. Yu, Enhanced photovoltaic performance of dye-sensitized solar cells based on TiO<sub>2</sub> nanosheets/graphene composite films, *J. Mater. Chem.* 22 (2012) 17027–17036.
- [27] M.S. Arnold, P. Avouris, Z.W. Pan, Z.L. Wang, Field-Effect Transistors Based on Single Semiconducting Oxide Nanobelts, *J. Phys. Chem. B.* 107 (2003) 659–663.
- [28] Z.M. Jarzebski, J.P. Marton, Physical Properties of SnO<sub>2</sub> Materials II . Electrical Properties, *J. Electrochem. Soc.* 123 (1976) 299-310.
- [29] E. Hendry, M. Koeberg, B. O'Regan, and M. Bonn, Local Field Effects on Electron Transport in Nanostructured TiO<sub>2</sub> Revealed by Terahertz Spectroscopy, *Nano Lett.* 6 (2006) 755–759.
- [30] S.K. Pathak, A. Abate, P. Ruckdeschel, B. Roose, K.C. Gödel, Y. Vaynzof, A. Santhala, S.-I. Watanabe, D.J. Hollman, N. Noel, A. Sepe, U. Wiesner, R. Friend, H.J. Snaith, U. Steiner, Performance and Stability Enhancement of Dye-Sensitized and Perovskite Solar Cells by Al Doping of TiO<sub>2</sub>, *Adv. Funct. Mater.* 24 (2014) 6046–6055.
- [31] M. Imran Asghar, K. Miettunen, J. Halme, P. Vahermaa, M. Toivola, K. Aitola, P. Lund, Review of stability for advanced dye solar cells, *Energy Environ. Sci.* 3 (2010) 418–426.
- [32] M. Mohammadnezhad, G.S. Selopal, Z.M. Wang, B. Stansfield, H. Zhao, F. Rosei, Towards Long-Term Thermal Stability of Dye-Sensitized Solar Cells Using Multiwalled Carbon Nanotubes, *ChemPlusChem.* 83 (2018) 682–690.
- [33] K. Basu, D. Benetti, H. Zhao, L. Jin, F. Vetrone, A. Vomiero, F. Rosei, Enhanced photovoltaic properties in dye sensitized solar cells by surface treatment of SnO<sub>2</sub> photoanodes, *Sci. Rep.* 6 (2016) 1-10.

- [34] P.M. Sommeling, B.C. O'Regan, R.R. Haswell, H.J.P. Smit, N.J. Bakker, J.J.T. Smits, J.M. Kroon, J.A.M. van Roosmalen, Influence of a  $\text{TiCl}_4$  Post-Treatment on Nanocrystalline  $\text{TiO}_2$  Films in Dye-Sensitized Solar Cells, *J. Phys. Chem. B.* 110 (2006) 19191–19197.
- [35] F. Gracia, J.P. Holgado, A.R. González-Elipe, Photoefficiency and Optical, Microstructural, and Structural Properties of  $\text{TiO}_2$  Thin Films Used as Photoanodes, *Langmuir.* 20 (2004) 1688–1697.
- [36] A. Hagfeldt, G. Boschloo, H. Lindström, E. Figgemeier, A. Holmberg, V. Aranyos, E. Magnusson, L. Malmqvist, A system approach to molecular solar cells, *Coord. Chem. Rev.* 248 (2004) 1501–1509.
- [37] B.A. Gregg, Interfacial processes in the dye-sensitized solar cell, *Coord. Chem. Rev.* 248 (2004) 1215–1224.
- [38] B.A. Gregg, Excitonic Solar Cells, *J. Phys. Chem. B.* 107 (2003) 4688–4698.
- [39] C.D. Grant, A.M. Schwartzberg, G.P. Smestad, J. Kowalik, L.M. Tolbert, J.Z. Zhang, Characterization of nanocrystalline and thin film  $\text{TiO}_2$  solar cells with poly(3-undecyl-2,2'-bithiophene) as a sensitizer and hole conductor, *J. Electroanal. Chem.* 522 (2002) 40–48.
- [40] C.-Y. Yen, Y.-F. Lin, S.-H. Liao, C.-C. Weng, C.-C. Huang, Y.-H. Hsiao, C.-C.M. Ma, M.-C. Chang, H. Shao, M.-C. Tsai, C.-K. Hsieh, C.-H. Tsai, F.-B. Weng, Preparation and properties of a carbon nanotube-based nanocomposite photoanode for dye-sensitized solar cells, *Nanotechnology.* 19 (2008) 3753051-3753059.
- [41] A.C. Ferrari, J.C. Meyer, V. Scardaci, C. Casiraghi, M. Lazzeri, F. Mauri, S. Piscanec, D. Jiang, K.S. Novoselov, S. Roth, A.K. Geim, Raman spectrum of graphene and graphene layers, *Phys. Rev. Lett.* 97 (2006) 1874011-1874014.

- [42] M.A. Pimenta, G. Dresselhaus, M.S. Dresselhaus, L.G. Cançado, A. Jorio, R. Saito, Studying disorder in graphite-based systems by Raman spectroscopy, *Phys. Chem. Chem. Phys.* 9 (2007) 1276–1291.
- [43] A. Gupta, G. Chen, P. Joshi, S. Tadigadapa, P.C. Eklund, Raman scattering from high-frequency phonons in supported n-graphene layer films, *Nano Lett.* 6 (2006) 2667–2673.
- [44] A. Jitianu, T. Cacciaguerra, R. Benoit, S. Delpeux, F. Béguin, S. Bonnamy, Synthesis and characterization of carbon nanotubes–TiO<sub>2</sub> nanocomposites, *Carbon.* 42 (2004) 1147–1151.
- [45] X. Li, J. Niu, J. Zhang, H. Li, Z. Liu, Labeling the Defects of Single-Walled Carbon Nanotubes Using Titanium Dioxide Nanoparticles, *J. Phys. Chem. B.* 107 (2003) 2453–2458.
- [46] E. Bekyarova, E.T. Thostenson, A. Yu, H. Kim, J. Gao, J. Tang, H.T. Hahn, T.-W. Chou, M.E. Itkis, R.C. Haddon, Multiscale Carbon Nanotube–Carbon Fiber Reinforcement for Advanced Epoxy Composites, *Langmuir.* 23 (2007) 3970–3974.
- [47] K.T. Dembele, R. Nechache, L. Nikolova, A. Vomiero, C. Santato, S. Licoccia, F. Rosei, Effect of multi-walled carbon nanotubes on the stability of dye sensitized solar cells, *J. Power Sources.* 233 (2013) 93–97.
- [48] J. Bisquert, F. Fabregat-Santiago, I. Mora-Seró, G. Garcia-Belmonte, S. Giménez, Electron Lifetime in Dye-Sensitized Solar Cells: Theory and Interpretation of Measurements, *J. Phys. Chem. C.* 113 (2009) 17278–17290.
- [49] A. Zaban, M. Greenshtein, J. Bisquert, Determination of the Electron Lifetime in Nanocrystalline Dye Solar Cells by Open-Circuit Voltage Decay Measurements, *ChemPhysChem.* 4 (2003) 859–864.

- [50] J. Bisquert, A. Zaban, M. Greenshtein, I. Mora-Seró, Determination of Rate Constants for Charge Transfer and the Distribution of Semiconductor and Electrolyte Electronic Energy Levels in Dye-Sensitized Solar Cells by Open-Circuit Photovoltage Decay Method, *J. Am. Chem. Soc.* 126 (2004) 13550–13559.
- [51] X. Dang, H. Yi, M.-H. Ham, J. Qi, D.S. Yun, R. Ladewski, M.S. Strano, P.T. Hammond, A.M. Belcher, Virus-templated self-assembled single-walled carbon nanotubes for highly efficient electron collection in photovoltaic devices, *Nat. Nanotechnol.* 6 (2011) 377–384.
- [52] R.S. Ruoff, D.C. Lorents, Mechanical and thermal properties of carbon nanotubes, *Carbon.* 33 (1995) 925–930.
- [53] A. Moisala, Q. Li, I.A. Kinloch, A.H. Windle, Thermal and electrical conductivity of single- and multi-walled carbon nanotube-epoxy composites, *Compos. Sci. Technol.* 66 (2006) 1285–1288.

# Supplementary information

## Hybrid Graphene/metal oxide Photoanodes for Efficient and Stable Dye Sensitized Solar Cell

Kaustubh Basu<sup>1</sup>, Gurpreet Singh Selopal<sup>1,2\*</sup>, Mahyar Mohammadnezhad<sup>1</sup>, Rusoma Akalimali<sup>1</sup>  
Zhiming M. Wang<sup>2</sup>, Haiguang Zhao<sup>3\*</sup>, Fiorenzo Vetrone<sup>1,2</sup>, Federico Rosei<sup>1,2\*</sup>

<sup>1</sup>Institut National de la Recherche Scientifique, Centre Énergie, Matériaux et Télécommunications,  
1650 Boulevard Lionel-Boulet, Varennes, Québec J3X 1S2, Canada

<sup>2</sup>Institute for Fundamental and Frontier Science, University of Electronic Science and Technology  
of China, Chengdu 610054, PR China

<sup>3</sup> College of Physics &The State Key Laboratory, Qingdao University, No. 308 Ningxia Road,  
Qingdao 266071, PR China

**\* Corresponding authors:**

**Gurpreet Singh Selopal:** gurpreet.selopal@emt.inrs.ca

**Haiguang Zhao:** hgzhao@qdu.edu.cn

**Federico Rosei:** rosei@emt.inrs.ca

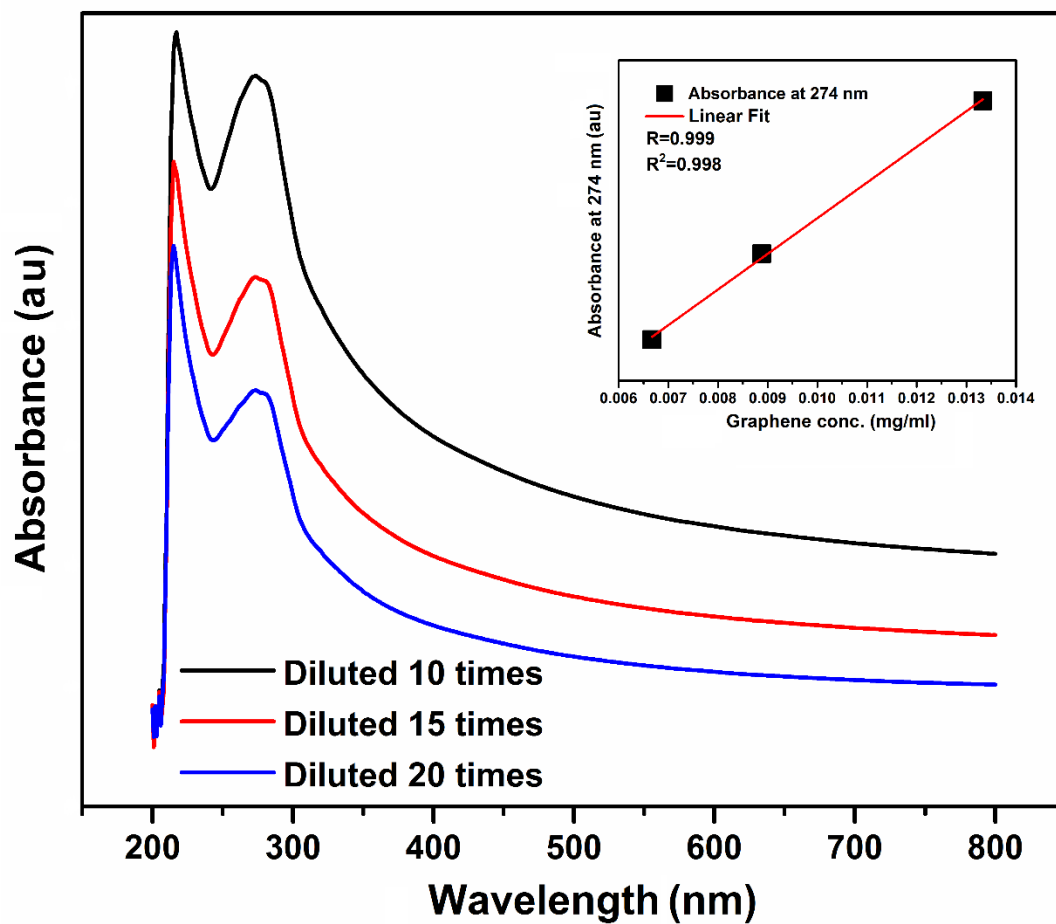


Figure S1: UV-Vis-near-infrared spectrophotometry of diluted ethanolic solutions of graphene microplatelets; The inset shows a linear fit of the graphene absorption peak ~274 nm.

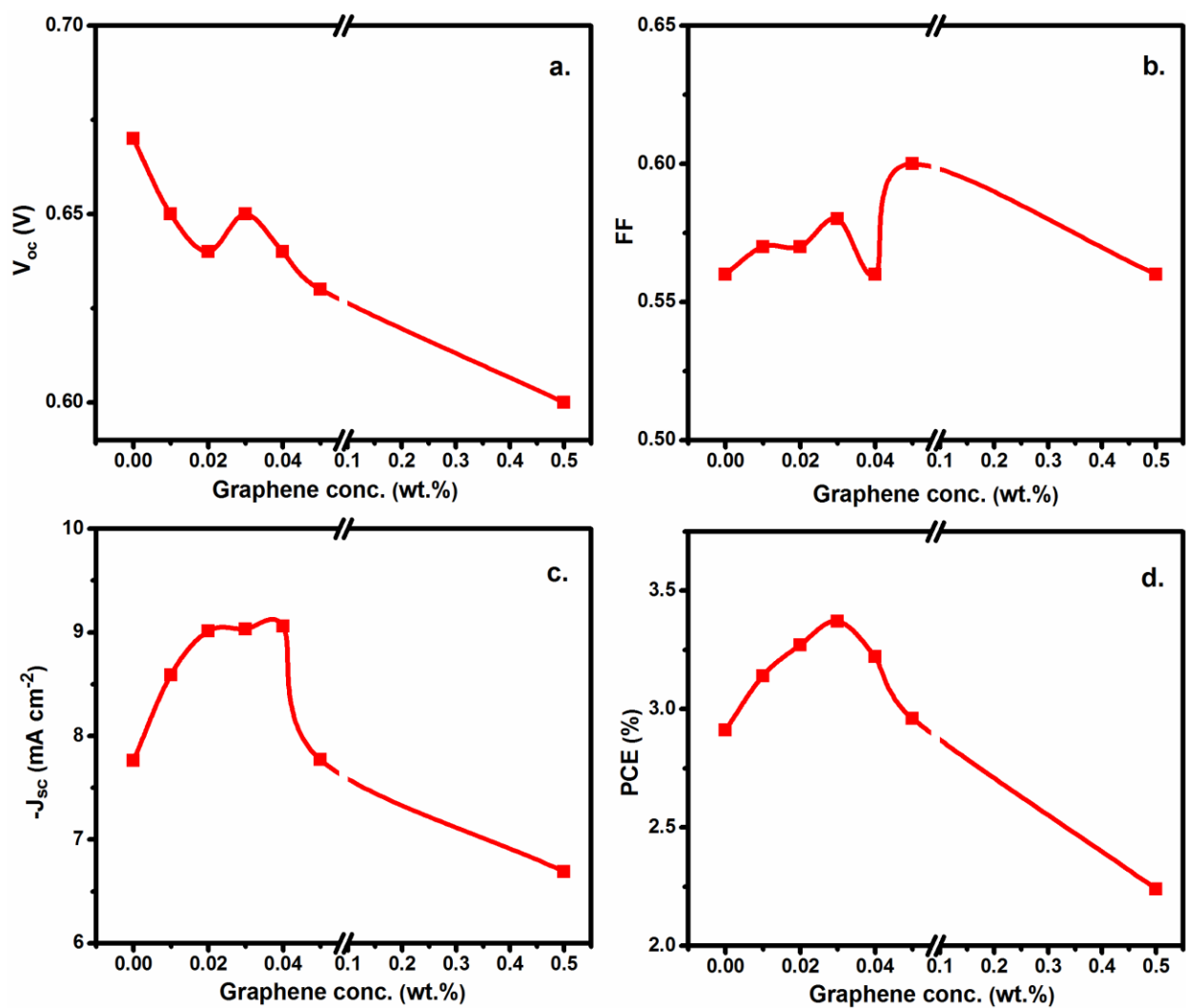


Figure S2: Dependence of the functional parameters of the DSSCs with different graphene microplatelet concentration (by wt.%) in the SnO<sub>2</sub>-TiO<sub>2</sub> heterostructure under one sun illumination (AM1.5G, 100 mW cm<sup>-2</sup>) with graphene concentration: (a)  $V_{oc}$  (V); (b) FF; (c)  $J_{sc}$  (mA.cm<sup>-2</sup>); (d) PCE (%).

### **4.3 Highly stable photoelectrochemical cells for hydrogen production using**

#### **SnO<sub>2</sub>-TiO<sub>2</sub>/quantum dot heterostructured photoanode**

Kaustubh Basu<sup>1</sup>, Hui Zhang<sup>1</sup>, Haiguang Zhao<sup>2\*</sup>, Sayantan Bhattacharya<sup>3</sup>, Fabiola Navarro-Pardo<sup>1,4</sup>, Prasanta Kumar Datta<sup>3</sup>, Lei Jin<sup>1</sup>, Shuhui Sun<sup>1</sup>, Fiorenzo Vetrone<sup>1,4</sup>, Federico Rosei<sup>1,4\*</sup>

<sup>1</sup>Institut National de la Recherche Scientifique, Centre Énergie, Matériaux et Télécommunications, Université du Québec, 1650 Boulevard Lionel-Boulet, Varennes, Québec J3X 1S2, Canada

<sup>2</sup>The Cultivation Base for State Key Laboratory, Qingdao University, No. 308 Ningxia Road, Qingdao 266071, PR China

<sup>3</sup>Department of Physics, Indian Institute of Technology Kharagpur, Kharagpur 721302, India

<sup>4</sup>Institute of Fundamental and Frontier Sciences, University of Electronic Science and Technology of China, Chengdu 610054, PR China

**\* Corresponding authors:**

**Haiguang Zhao: hgzhao@qdu.edu.cn**

**Federico Rosei: rosei@emt.inrs.ca**

## Abstract

Photoelectrochemical (PEC) water splitting implementing colloidal quantum dots (QDs) as sensitizers is a promising approach for hydrogen ( $H_2$ ) generation, due to the QD's size-tunable optical properties. However, the challenge of long term stability of the QDs is still unresolved. Here, we introduce a highly stable QD-based PEC device for  $H_2$  generation using a photoanode based on a  $SnO_2$ - $TiO_2$  heterostructure, sensitized by CdSe/CdS core/thick-shell "giant" QDs. This hybrid photoanode architecture leads to an appreciable saturated photocurrent density of  $\sim 4.7$   $mA/cm^2$ , retaining an unprecedented  $\sim 96\%$  of its initial current density after two hours, and sustaining  $\sim 93\%$  after five hours of continuous irradiation under AM 1.5G ( $100$   $mW/cm^2$ ) simulated solar spectrum. Transient photoluminescence (PL) measurements demonstrate that the heterostructured  $SnO_2$ - $TiO_2$  photoanode exhibits faster electron transfer compared with the bare  $TiO_2$  photoanode. The lower electron transfer rate in the  $TiO_2$  photoanode can be attributed to slow electron kinetics in the ultraviolet regime, revealed by ultrafast transient absorption spectroscopy. Graphene microplatelets were further introduced into the heterostructured photoanode, which boosted the photocurrent density to  $\sim 5.6$   $mA/cm^2$ . Our results demonstrate that  $SnO_2$ - $TiO_2$  heterostructured photoanode holds significant potential for developing highly stable PEC cells.

## Introduction

The demand for clean and renewable energy is ever growing, due to the limited availability of fossil fuels and the increasing concern of climate change caused by carbon emissions. Molecular hydrogen ( $H_2$ ), which has the highest energy content per unit weight<sup>1</sup> amongst the known gaseous fuels, is a clean fuel as the only reaction byproduct upon oxidation is water.<sup>2</sup> Although  $H_2$  is not present in nature by itself, it is the main constituent element of water, which is plentiful on the earth's surface. Currently, however,  $H_2$  is extracted from methane ( $CH_4$ ), as the rupture of a water molecule is an exothermic reaction. As such, it must be aided by the use of an external source of “freely” available energy.

Photoelectrochemical (PEC)  $H_2$  generation is a promising approach to produce  $H_2$  from water using solar energy, which is the cleanest and the most abundant form of renewable energy available on our planet. Due to the relative ease of  $H_2$  storage, as opposed to other forms, such as heat and electricity,<sup>3</sup> PEC  $H_2$  generation holds significant promise for solar energy conversion. PEC cells use wide band gap semiconductors as photoanodes, which are further sensitized using quantum dots (QDs) to extend their absorption in the visible or near-infrared (NIR) region, thereby improving their  $H_2$  generation efficiency.<sup>4,5</sup> Although QD sensitized PEC cells have been widely studied for their appreciable efficiency in  $H_2$  production, stability is still a major concern, which drives the quest for a highly stable photoanode<sup>6,7</sup> material for QD based PEC cells. To the best of our knowledge, the highest stability ever recorded, recently reported for a QD-based PEC cell, is ~94.9% of the initial current density value after two hours under one sun illumination for “giant” core/alloyed-shell  $CdSe/Pb_xCd_{1-x}S/CdS$  QDs.<sup>8</sup>

Recently, a myriad of photocatalyst materials such as  $\alpha-Fe_2O_3$ ,<sup>9-11</sup>  $TiO_2$ ,<sup>12-16</sup>  $ZnO$ ,<sup>17,18</sup> and  $WO_3$ <sup>19,20</sup> have been extensively studied for PEC  $H_2$  production. Graphitic carbon nitride<sup>21</sup> and

other novel materials,<sup>22–25</sup> have also generated immense interest in H<sub>2</sub> and oxygen evolution reactions in recent years.<sup>26–30</sup> Compared with other photocatalysts, SnO<sub>2</sub> is a promising semiconducting oxide, because of its high electron mobility ( $\sim 100\text{--}200\text{ cm}^2\text{V}^{-1}\text{s}^{-1}$ ),<sup>31,32</sup> as well as its good activity and stability during irradiation, both in acidic and basic media.<sup>33,34</sup> In addition, SnO<sub>2</sub> has a wider band gap (3.6 eV), compared to the widely used anatase TiO<sub>2</sub> (3.2 eV). This creates fewer oxidative holes in the valence band under ultraviolet (UV) illumination,<sup>35</sup> which can play a pivotal role in improving the long-term stability of PEC devices. So far, for PEC water splitting applications, SnO<sub>2</sub> has been investigated considerably less because its conduction band minimum is lower than the reduction potential of water,<sup>36</sup> it suffers from low light absorption efficiency and a limited exciton separation rate.<sup>37</sup> On the other hand, TiO<sub>2</sub> has a favorable band alignment for water splitting, however UV degradation is a major drawback. To address these challenges, we designed a SnO<sub>2</sub>-TiO<sub>2</sub> heterojunction, to combine the advantages of the higher conduction band edge of TiO<sub>2</sub>, and the high stability and exceptional electronic mobility of SnO<sub>2</sub>. Moreover, the SnO<sub>2</sub>-TiO<sub>2</sub> heterojunction has a type-II band alignment, which facilitates charge separation and transport, and has been reported<sup>36,38</sup> to boost the performance of PEC cells. Herein, we introduced a novel multi-heterojunction SnO<sub>2</sub>-TiO<sub>2</sub>/QD photoanode for highly stable PEC H<sub>2</sub> generation. SnO<sub>2</sub> mesoporous thin films were treated with the TiCl<sub>4</sub> precursor to form TiO<sub>2</sub> nanoparticles connecting the SnO<sub>2</sub> nanoparticle mesoporous framework<sup>39</sup>, thereby creating a SnO<sub>2</sub>-TiO<sub>2</sub> heterojunction for efficient electron percolation within the anode. The metal oxide composite anode was sensitized by core/thick-shell “giant” CdSe/CdS QDs. We obtained a saturated photocurrent density of  $\sim 4.7\text{ mA/cm}^2$  in a PEC cell under one sun illumination (AM 1.5G, 100 mW/cm<sup>2</sup>). The composite photoanode exhibited exceptional stability, sustaining  $\sim 93\%$  of its initial current density after 5 hours of continuous irradiation. Furthermore, the incorporation

of 0.1 wt.% of graphene in the photoanode increases the photocurrent density up to 5.6 mA/cm<sup>2</sup>. To the best of our knowledge, this device architecture has never before been investigated for PEC H<sub>2</sub> production, and we report the highest ever stability in a QD-based PEC device for efficient H<sub>2</sub> production.

### **Experimental procedure**

**Materials:** Fluorine-doped tin oxide (FTO) coated glass substrates of dimensions 2 cm × 1.5 cm with a sheet resistance of 10 Ω/□ were purchased from Pilkington glasses. Ti-Nanoxide BL/SC was purchased from Solaronix and SnO<sub>2</sub> nanopowder (99.9% tin(IV) oxide) from American Elements. Graphene microplatelets (D type) were supplied by Nanoxplore Inc., titanium(IV) chloride (0.09 M in 20% HCl), titanium isopropoxide (99.999%), hydrochloric acid (37%), alpha-terpineol, ethyl cellulose, sulfur (100%), oleylamine (OLA) (technical grade, 70%), cadmium oxide (99%), oleic acid (OA), octadecene (ODE), selenium pellet (≥99.999%), trioctyl phosphine oxide (TOPO), trioctyl phosphine (TOP) (97%), zinc acetate dihydrate (≥98%), sodium sulfide (Na<sub>2</sub>S), sodium hydroxide, sodium sulfite (Na<sub>2</sub>SO<sub>3</sub>), hexane, toluene, methanol, acetone, ethanol and isopropanol (IPA) were obtained from Sigma-Aldrich Inc.

**Preparation of SnO<sub>2</sub>, TiO<sub>2</sub> and ZrO<sub>2</sub> paste:** The SnO<sub>2</sub> nanopowder utilized, consisted of nanoparticles with average particle size of ~20 nm. To prepare the SnO<sub>2</sub> paste, 1 g of SnO<sub>2</sub> nanopowder was mixed with 1 mL of water, 1 mL alpha-terpineol, 5 mL of ethanol and 0.5 g ethyl cellulose.<sup>39</sup> These ingredients were mixed in a beaker under 12 h magnetic stirring. The solvent was removed by connecting it to a rotary pump, while under continuous magnetic stirring, until the volume of the mixture reduced to half of our starting volume. ZrO<sub>2</sub> was utilized as a control photoanode, to determine charge transfer dynamics in TiO<sub>2</sub> and SnO<sub>2</sub>-TiO<sub>2</sub> heterojunction

photoanodes, because charge transfer from QDs to  $ZrO_2$  is unfavourable. To make  $TiO_2$  and  $ZrO_2$  pastes, an identical recipe to that of  $SnO_2$  paste was followed to achieve similar film thickness.

**Photoanode preparation:** FTO coated glass substrates were cleaned by 30 min sonication in IPA and then thoroughly rinsed with deionized water and subsequently dried under a filtered air stream.<sup>39</sup> A thin and compact blocking layer (BL) of  $TiO_2$  was deposited on the FTO substrate by soaking the FTO substrates in 50 mM  $TiCl_4$  solution for 20 min at 70 °C, then they were flushed with deionized water and consequently annealed at 500 °C for 30 min. As a control experiment, to compare the performance of  $TiO_2$  BL fabricated with  $TiCl_4$  precursor, commercial  $TiO_2$  BL was spin coated on FTO glass substrates at 5000 rpm for 30 s by using the solution Ti-Nanoxide BL/SC (Solaronix), followed by annealing in air at 500 °C for 30 min, and cooled down to room temperature. Subsequently,  $SnO_2$  paste (preparation method described earlier) was mixed with different weight concentrations of graphene and applied on the BL by the tape casting technique and dried at room temperature for 15 min to fabricate the first layer, followed by heating on a hot plate at 150 °C for 6 min. After drying, another layer of paste of the same recipe was tape casted using the similar drying procedure and annealed in an air ambience in a furnace at 500 °C for 30 min and cooled down to room temperature. The sintered  $SnO_2$  photoanodes were dip-coated in 50 mM  $TiCl_4$  precursor solution for 30 min at 70 °C, then they were flushed with deionized water and subsequently annealed at 500 °C for 30 min. Separately,  $TiO_x$  post-treatment was carried out by spin-coating a  $TiO_x$  flat film precursor solution at 2000 rpm for 60 s followed by heating at 500 °C for 30 min.<sup>40</sup>

**CdSe QDs synthesis:** The synthesis of CdSe QDs of diameter 1.65 nm was carried out using the hot-injection approach.<sup>5,41</sup> TOPO (1 g) and Cd-oleate (0.38 mmol, 1 mL) in 8 mL of ODE were purged at room temperature by  $N_2$  for 30 min. The reaction system was evacuated at 100 °C for

30 min, and subsequently the temperature was increased to 300 °C. The mixture of 3 mL of OLA, TOP-Se (4 mmol, 4 mL) and 1 mL of ODE at room temperature was injected rapidly into the Cd-oleate suspension while stirring the mixture vigorously. After injection, the reaction cell was quenched with cold water. Subsequently, 20 mL of ethanol was added and then the suspension was centrifuged. Finally the supernatant was removed and the QDs were dispersed in toluene.

**Synthesis of CdSe/CdS “giant” QDs:** According to the procedure mentioned in Ghosh et al.<sup>5,42</sup>, the deposition of CdS layers on CdSe QDs were achieved by successive ionic layer adsorption and reaction (SILAR). “Giant” CdSe/CdS QDs were prepared by subsequently growing CdS monolayers over the CdSe core. Typically, in a round-bottom flask of 100 mL, ODE (5 mL), OLA (5 mL), and CdSe QDs ( $\sim 2 \times 10^{-7}$  mol in hexane) were degassed for 30 min at 110 °C. While restoring the reaction flask in N<sub>2</sub>, the temperature was increased to 240 °C under magnetic stirring. Subsequently, the Cd(OA)<sub>2</sub> which was dispersed in ODE (0.25 mL, 0.2 M) was added drop by drop in the mixture, and was allowed to react for 2.5 h, followed by addition of 0.2 M sulfur in ODE, dropwise, with the same volume. Subsequently, the shell was annealed further for 10 min. All further shells were annealed at 240 °C for ~10 min succeeding the injection of sulfur, and ~2.5 h following the addition of the Cd(OA)<sub>2</sub> in ODE. The addition volumes of sulfur/Cd(OA)<sub>2</sub> for shell addition cycles 1-13 were as follows: 0.25, 0.36, 0.49, 0.63, 0.8, 0.98, 1.18, 1.41, 1.66, 1.92, 2.2, 2.51 and 2.8 mL, respectively.<sup>5</sup> Using cold water, the reaction was cooled down to room temperature. Adding ethanol, centrifugation of the suspension was carried out to separate the supernatant. The supernatant was collected and finally the QDs were dispersed in toluene.

**Sensitization of the SnO<sub>2</sub> film with CdSe/CdS “giant” QDs:** Electrophoretic deposition (EPD) process was carried out to sensitize the SnO<sub>2</sub>-TiO<sub>2</sub> photoanode with CdSe/CdS “giant” QDs. The SnO<sub>2</sub>-TiO<sub>2</sub> composite photoanodes on FTO substrate were vertically immersed in the QD solution,

in such a manner, that the deposited films faced each other with a distance of 1 cm between them. A direct current (DC) bias of 200 V was applied for 20 min in case of SnO<sub>2</sub>-TiO<sub>2</sub> photoanode and 2 h for TiO<sub>2</sub> photoanode.<sup>43</sup> The photoanodes were cleaned several times with toluene to wash off the unbounded QDs on the photoanode surface, and subsequently dried with N<sub>2</sub> at room temperature.

**ZnS capping layer:** The ZnS capping layer was fabricated using the SILAR process. In the usual SILAR deposition cycle, Zn<sup>2+</sup> ions were deposited from 0.1 M solution of Zn(CH<sub>3</sub>COO)<sub>2</sub> in ethanol. The sulfide source was prepared using 0.1 M solution of Na<sub>2</sub>S in deionized water. Each SILAR cycle consisted of 1 min of dip-coating the SnO<sub>2</sub>-TiO<sub>2</sub> or the TiO<sub>2</sub> photoanode into the Zn<sup>2+</sup> precursors, followed by the sulfide solutions. To remove the chemical residue from the surface, the photoanode was thoroughly rinsed by dipping it into the corresponding solvent (methanol or methanol and water) after each bath, and subsequently dried with a N<sub>2</sub> gun. Two SILAR cycles were employed to form the ZnS capping layer.

**Structural Characterizations of the photoanode:** The morphology of the photoanode was characterized using a JSM-7401F scanning electron microscope and the chemical composition was characterized by energy-dispersive X-ray spectroscopy (EDS) analysis. XRD analysis was carried out using Panalytical X-Pert PRO MRD system in a Bragg-Brentano geometry and Xpert Highscore was used to analyse the data. X-ray Photoelectron spectra of SnO<sub>2</sub>-TiO<sub>2</sub>/QD photoanode were collected using a VG Scientific Escalab 220i-XL equipped with an aluminium monochromatic source of 1486.6 eV energy, and CasaXPS software was used for data analysis.

**Photoluminescence (PL) Measurements:** The PL lifetime of the QDs in the photoanode films were measured using a time-correlated single-photon counting (TCSPC) mode with a 408 nm and 444 nm laser. The fitting for the decay curves was carried out using a three-component exponential

decay, which gave the best fitting results. The intensity-weighted average lifetime  $\langle \tau \rangle$  for the PL decay was evaluated by the following equation:<sup>5</sup>

$$\langle \tau \rangle = \frac{a_1\tau_1^2 + a_2\tau_2^2 + a_3\tau_3^2}{a_1\tau_1 + a_2\tau_2 + a_3\tau_3} \quad (1)$$

Where  $a_i$  ( $i=1, 2, 3$ ) are the fitting coefficients of the PL decay and  $\tau_i$  ( $i = 1, 2, 3$ ) are the characteristic lifetimes. The electron transfer rate,  $K_{et}$  is calculated from the following equation:<sup>44</sup> ZrO<sub>2</sub>-QDs system was used as a reference, since electron transfer is not favorable from the QDs to ZrO<sub>2</sub>.

$$K_{et} = \frac{1}{\langle \tau \rangle_{QDs/e\ scavenger}} - \frac{1}{\langle \tau \rangle_{QDs/ZrO_2}} \quad (2)$$

Where  $\langle \tau \rangle_{QDs/e\ scavenger}$  and  $\langle \tau \rangle_{QDs/ZrO_2}$  are the average PL lifetimes of the QDs/TiO<sub>2</sub> and QDs/ZrO<sub>2</sub>, respectively.

**Ultrafast transient absorption measurement:** Transient absorption spectroscopy (TAS) of the TiO<sub>2</sub> and ZrO<sub>2</sub> photoanodes sensitized by QDs were carried out with a commercially available transient absorption spectrometer from Newport. A Ti:Sapphire (Coherent, Libra) regenerative amplifier laser system was used as the laser source. The output of the regenerative amplifier was centered at 808 nm, at a repetition rate of 1 kHz with an average pulse energy of 3.5 mJ and pulse width of 50 fs. The beam was split into two parts by a 70/30 Reflection/Transmission (R/T) ratio beam-splitter. A major portion of the beam was used to generate the pump beam from an optical parametric amplifier (TOPAS-PRIME). A small portion of the fundamental beam was allowed to pass through a computer-controlled motorized delay stage (ILS-LM, Newport) and was used to generate a white-light continuum (WLC) with a spectral range of 350–850 nm by focusing it onto a 3 mm CaF<sub>2</sub> crystal. Pump and probe beams were focused on the photoanode with a spot size of 210  $\mu\text{m}$  and 80  $\mu\text{m}$ , respectively. The maximum time delay that could be achieved between pump and probe beams in our set-up is 3 ns. After passing through the photoanode WLC probe was

collected by a fiber coupled spectrometer coupled to a Si photodiode array (MS-260i, Oriol Instrument). Both the TiO<sub>2</sub>-QD and ZrO<sub>2</sub>-QD photoanodes were pumped at 350, 400 and 450 nm, respectively, and differential absorbance spectra ( $\Delta A$ ) from a broadband probe were collected in transmission geometry using a spectrometer. The electron transfer rate,  $K_{et}$  is calculated from the following equation:

$$K_{et} = \frac{1}{\tau_{S(TiO_2)}} - \frac{1}{\tau_{S(ZrO_2)}} \quad (3)$$

**PEC performance analysis:** The PEC performance of the photoanodes were evaluated in a typical three-electrode arrangement, consisting of a QD-sensitized SnO<sub>2</sub>-TiO<sub>2</sub> heterostructured photoanode as the working electrode, Pt as the counter electrode, and an Ag/AgCl (saturated KCl) as a reference electrode.<sup>4</sup> The sample's surface (except for the active area) was covered with insulating epoxy resin, to inhibit exposure of the conducting back-contact with the electrolyte. The prepared samples were immersed in the electrolyte comprising of 0.25 M Na<sub>2</sub>S and 0.35 M Na<sub>2</sub>SO<sub>3</sub> (pH ~13), which acts as the sacrificial hole scavenger. The electrolyte solution was continuously purged by N<sub>2</sub> to remove any dissolved oxygen before PEC analysis. During PEC measurements, the potentials measured with respect to the reference Ag/AgCl electrode were converted to the reversible hydrogen electrode (RHE) scale following the equation  $V_{RHE} = V_{Ag/AgCl} + 0.197 + pH \times (0.059)$ .<sup>45</sup> The photoresponse was measured by using a Class AAA Solar Simulator (model SLB-300A by Sciencetech Inc.) equipped with a 300 W Xenon arc lamp as a light source with an AM 1.5 G filter under 1 sun illumination. Before every measurement, the light intensity was calibrated using a power meter and was adjusted back to 100 mW/cm<sup>2</sup>. The sweep rate for every “current versus potential” measurement was fixed at 20 mV/s.

## Results and discussion

**Structure of the photoanode.** SnO<sub>2</sub> nanoparticles ~20 nm in diameter were used for photoanode preparation. Systematic investigation of the effect of TiO<sub>x</sub> and TiCl<sub>4</sub> treatment on the morphology and the performance in photovoltaic devices has been carried out in previous work,<sup>39</sup> where we found from the morphological characterizations that small TiO<sub>2</sub> nanoparticles of about 5 nm preferentially form short interconnected nanostructures in the case of TiCl<sub>4</sub> treatment. Whereas in the case of TiO<sub>x</sub> treatment, the TiO<sub>2</sub> nanoparticles seem to cover the SnO<sub>2</sub> nanoparticles. This kind of surface treatment plays an important role in modifying the band alignment for efficient charge separation and electron transport<sup>39</sup> in the photoanode, as shown in detail in Fig. S1 of the supplementary information, where the band diagram has been constructed by combining data from ultraviolet photoelectron spectroscopy (UPS) and diffuse reflectance spectroscopy (DRS). The advantage of using the SnO<sub>2</sub>-TiO<sub>2</sub> heterostructure is apparent in Fig. S2, which shows that the conduction band (CB) minima for the heterostructured photoanode has moved upwards, which eliminates the problem for lower CB edge position in the case of pure SnO<sub>2</sub>.

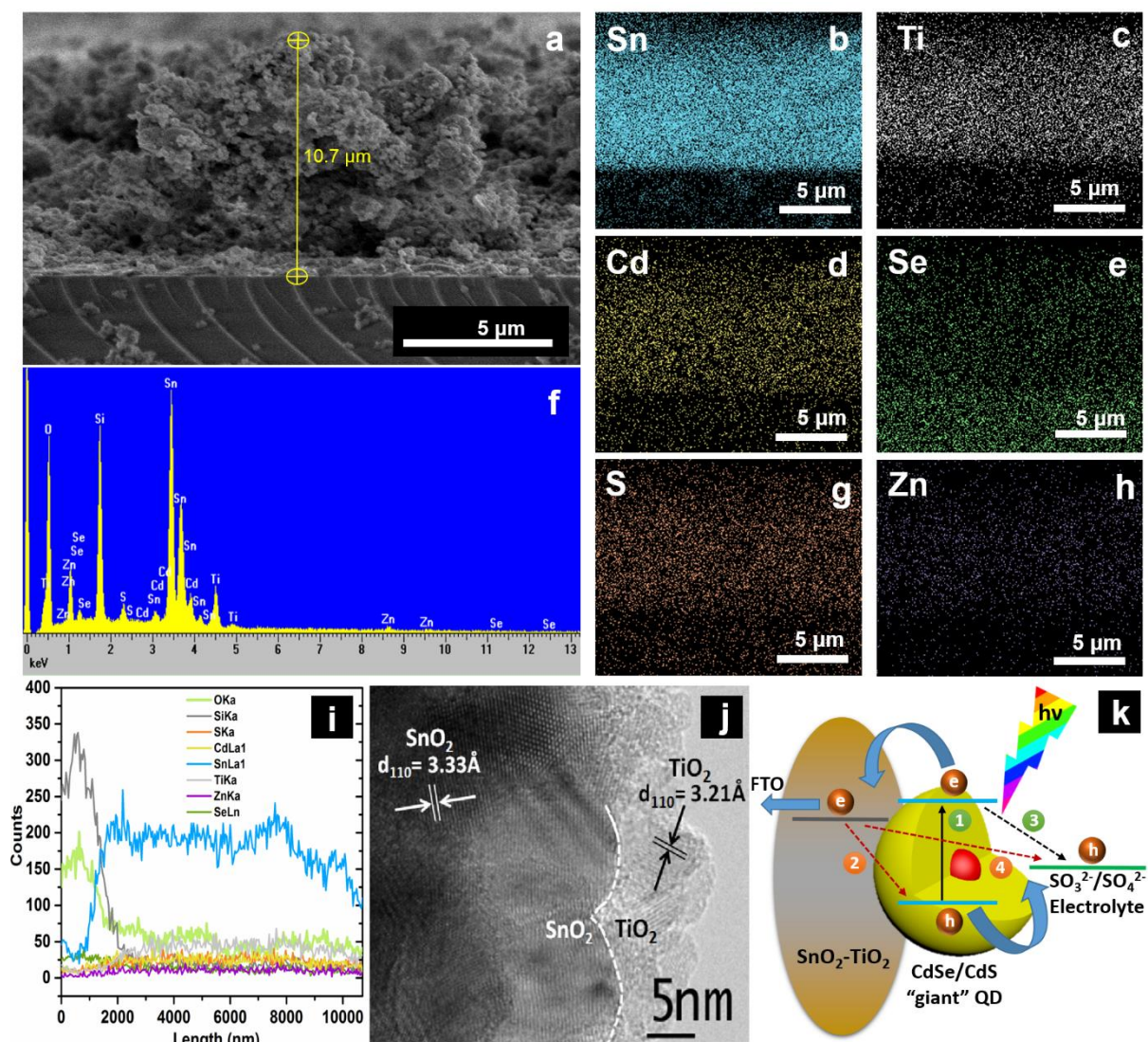


**Figure 1:**(a) Cross-sectional SEM image of our composite photoanode after CdSe/CdS core/shell “giant” QD sensitization. (b) EDS maps of all the elements including (b) Sn, (c) Ti, (d) Cd, (e) Se, (g) S and (h) Zn (f) EDS spectrum of the SnO<sub>2</sub>-TiO<sub>2</sub> composite confirming the presence of its constituent elements and (i) EDS line mapping (j) HRTEM image of the SnO<sub>2</sub>-TiO<sub>2</sub> composite structure. (k) Charge transfer in our PEC cell consisting of SnO<sub>2</sub>-TiO<sub>2</sub><sup>39</sup> heterostructured photoanode sensitized by CdSe/CdS QD, in our electrolyte. (1) Excitation of electron from VB to CB of SnO<sub>2</sub>-TiO<sub>2</sub>, (2), (4) Recombination of injected electron in the photoanode to VB of QD and

redox potential of electrolyte, (3) Regeneration of electron from the electrolyte. The arrows denote the electron and hole transfer processes.

In the case of TiO<sub>2</sub>, which is the commonly preferred photoanode for PEC applications, UV radiation produces excess holes, which has been attenuated by our SnO<sub>2</sub>-TiO<sub>2</sub> heterostructured photoanode. We sensitized our composite photoanode with “giant” CdSe/CdS core/shell QDs consisting of a CdSe core of size 1.65 nm with a CdS shell of 4.3 nm thickness and a subsequent ZnS capping layer. “Giant” core/shell QD,<sup>46</sup> a very attractive kind of core/shell QD architecture, in which a very thick shell (from several up to 10 nm) is over-coated around the core, has gained considerable attention for their superior chemical and photo-stability over both traditional core QDs and thin-shell QDs.<sup>47,48</sup> By tailoring the shell thickness, these “giant” core/shell QD can be designed to form a quasi-type II band alignment such as in CdSe/CdS “giant” core/shell QD, where the electron and hole wave functions are spatially separated, which reduces the recombination probability, resulting in a prolonged lifetime.<sup>49</sup> These “giant” QDs were successfully realized very recently by Adhikari *et al.*<sup>5</sup> for sensitization of TiO<sub>2</sub> nanoparticles. We investigated the typical photoanode structure with SEM cross-sectional imaging, as reported in Fig. 1(a). The SEM analysis demonstrates the mesoporous structure of our photoanode and the thickness of our sensitized photoanode is estimated to be ~10.7 μm. Furthermore, the chemical composition of our photoanode, presented in Fig. 1(b-h), was investigated with EDS analysis. Two-dimensional (2D) mapping of the photoanode shows the presence of the constituent elements and confirms that the CdSe/CdS core/shell “giant” QDs penetrated through the mesoporous structure and are evenly distributed throughout the photoanode. Successful penetration of the QDs in the photoanode matrix suggests efficient sensitization of the overall mesoporous structure of the composite photoanode. Furthermore, EDS line-analysis pointed out that TiO<sub>2</sub> was homogeneously distributed within the

entire volume of the SnO<sub>2</sub>-TiO<sub>2</sub> photoanode, as displayed in Fig. 1(f). Additionally, semi-quantitative analyses of several regions indicated that the Sn:Ti elemental ratio is 11:1. The crystalline phases, for both SnO<sub>2</sub> and TiO<sub>2</sub> in the SnO<sub>2</sub>-TiO<sub>2</sub> heterostructured photoanode, can be ascribed to the rutile structure (JCPDS No. 00-041-1445 and JCPDS No. 01-088-1175 for SnO<sub>2</sub> and TiO<sub>2</sub>, respectively). This is confirmed by the high resolution transmission electron microscopy (HRTEM) image displayed in Fig. 1(j). The XRD peak pattern of the SnO<sub>2</sub>-TiO<sub>2</sub>/QD heterostructure sample is presented in Fig. S3(a). The peaks are consistent with rutile SnO<sub>2</sub> corresponding to JCPDS card no. 00-041-1445. Since the quantity of TiO<sub>2</sub> and the CdSe/CdS core/shell “giant” QDs are very low in comparison to SnO<sub>2</sub>, the effect was possibly below the detection limit of XRD. In addition, to determine the crystalline phase of the CdSe/CdS core/shell “giant” QDs, the same QD solution, which was introduced inside the photoanode to perform photoelectrochemical (PEC) tests, was drop-casted on a silicon (Si) substrate. XRD analysis was carried out using grazing angle incidence of 0.5 ° to nullify the peaks from the Si substrate. The XRD pattern for CdSe/CdS core/shell “giant” QDs is presented in Fig. S3(b) and matches perfectly with that of wurtzite CdS (JCPDS card no. 01-077-2306). Our data is consistent with previous studies, where the CdSe/CdS core/shell structure was used.<sup>50,51</sup> In Fig. S4, we report high resolution X-ray Photoelectron spectra (XPS) data for Sn 3d, Ti 2p, Cd 3d and S 2p peaks for the SnO<sub>2</sub>-TiO<sub>2</sub>/QD heterostructured photoanode. The peak positions of Sn 3d<sub>5/2</sub>, Sn 3d<sub>3/2</sub> and the difference in binding energy between the two peaks are shown in Fig. S4(a), and are consistent with the literature for the Sn<sup>4+</sup> state in the case of SnO<sub>2</sub>.<sup>52</sup> Also, as presented in Fig. S4(b), the peak position of Ti 2p<sub>3/2</sub> and Ti 2p<sub>1/2</sub> and the relative intensity ratio of these two peaks match perfectly with reports on Ti<sup>4+</sup> for TiO<sub>2</sub>.<sup>53,54</sup> The Cd 3d peak, which splits into Cd 3d<sub>5/2</sub> and Cd 3d<sub>3/2</sub> due to spin-orbit splitting, also agrees with the reported peak positions for Cd<sup>2+</sup>.<sup>55</sup> The S 2p core level

was deconvoluted into S 2p<sub>3/2</sub> and S 2p<sub>1/2</sub> and matches with S 2p<sub>3/2</sub> and S 2p<sub>1/2</sub> peak positions attributed to S<sup>2-</sup> state for CdS.<sup>56</sup> In this work, we introduce a “giant” QD with CdSe core and a thick CdS shell. Consequently, the amount of Se was very low, quantified from EDS analysis to be ~0.05 wt%, and therefore the signal from Se was not detected by XPS.

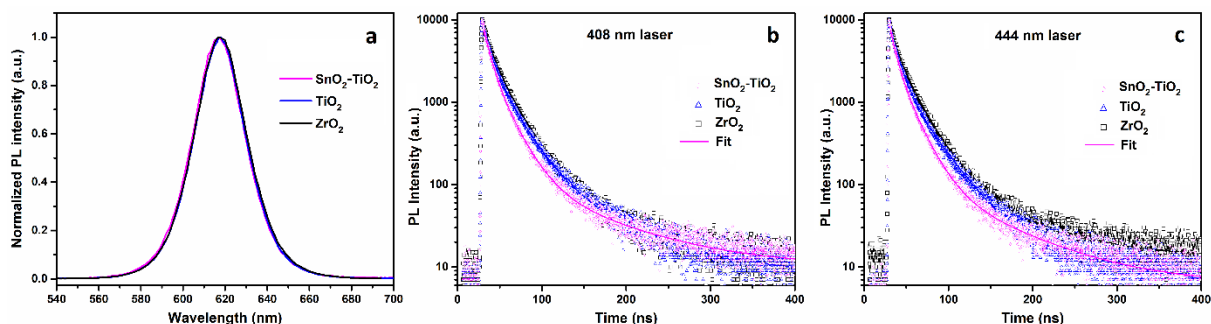


**Figure 2:** (a) PL spectra of CdSe/CdS “giant” QDs in different photoanodes. (b) PL decay dynamics for different anodes sensitized with CdSe/CdS “giant” QDs under 408 nm laser excitation. (c) PL decays for different anodes sensitized with CdSe/CdS “giant” QDs under excitation wavelength,  $\lambda = 444$  nm.

**Electron dynamics.** The scheme for the integrated PEC cell, illustrating different exciton generation, transport and recombination processes during the PEC test is displayed in Fig. 1(k). The modification of the SnO<sub>2</sub> photoanode, forming a SnO<sub>2</sub>-TiO<sub>2</sub> heterostructure, offers favorable band alignment for efficient electron injection into the photoanode. As shown in Fig. 1(k), the photogenerated exciton dissociation takes place at the QD, subsequently, the photogenerated electrons are injected into the heterostructured SnO<sub>2</sub>-TiO<sub>2</sub> mesoporous anode where the electron is transported via a diffusion mechanism and collected at the front electrode. The holes subsequently oxidize the hole scavengers at the photoanode and the electrons migrate to the Pt counter electrode to produce H<sub>2</sub>. PL spectra of CdSe/CdS “giant” QD-sensitized samples have been normalized and presented in Fig. 2(a). The PL denotes no significant change in the peak

positions for different samples, indicating good optical stability of the photoanode. The lifetime for the SnO<sub>2</sub>-TiO<sub>2</sub> and the TiO<sub>2</sub> samples in CdSe/CdS were estimated from PL decay curves shown in Fig. 2(b), and Fig. 2(c), which were carried out under laser excitations of 408 nm and 444 nm, respectively. The PL lifetime decay curves reveal that the SnO<sub>2</sub>-TiO<sub>2</sub> sample has a shorter lifetime (data presented in Table 1) of 24.19 ns, 22.02 ns compared to 27.45 ns, 24.44 ns in the case of the bare TiO<sub>2</sub> photoanode for 408 nm and 444 nm laser excitations, respectively. The ZrO<sub>2</sub> photoanode showed a lifetime of 29.17 ns and 29.01 ns at 408 nm and 444 nm, respectively. Based on these data, we further calculate the electron transfer rate ( $K_{et}$ ). As shown in Table 1, the  $K_{et}$  of the photoanode based on heterostructured SnO<sub>2</sub>-TiO<sub>2</sub> is faster than that of photoanode based on bare TiO<sub>2</sub>. The faster electron transfer rate indicates less probability of exciton recombination for the generated electrons and holes, thus a better stability of the photocurrent density is expected for the heterostructured SnO<sub>2</sub>-TiO<sub>2</sub> photoanode with respect to the bare TiO<sub>2</sub> anode. Moreover, we found that, at the shorter excitation wavelength, i.e. 408 nm, which is closer to UV illumination, the electron transfer rate is drastically faster (~3.5 fold) in the SnO<sub>2</sub>-TiO<sub>2</sub> photoanode ( $7.1 \times 10^6/s$ ) compared with that of the TiO<sub>2</sub> photoanode ( $2.2 \times 10^6/s$ ). The slower electron transfer rate of the TiO<sub>2</sub> photoanode compared to that of the SnO<sub>2</sub>-TiO<sub>2</sub> photoanode can be attributed to UV induced excess hole formation in the TiO<sub>2</sub> photoanode, which increases the probability for electron-hole recombination, other than electron transfer from QDs to oxide. When moving further away from UV excitation wavelengths, i.e. at longer wavelength (444 nm), this effect is less pronounced, where the electron transfer rate in the SnO<sub>2</sub>-TiO<sub>2</sub> photoanode is only ~1.5 higher than that of the bare TiO<sub>2</sub> photoanode. We also measured and calculated the hole transfer rate using Na<sub>2</sub>S and Na<sub>2</sub>SO<sub>3</sub> as hole scavengers using ZrO<sub>2</sub> as a scaffold. The hole transfer rate is  $\sim 9.5 \times 10^6/s$ , indicating the strong base solution (Na<sub>2</sub>S and Na<sub>2</sub>SO<sub>3</sub> in water) can serve as a very strong hole scavenger.

Photoanode	408 nm excitation		444 nm excitation	
	$\tau$ (ns)	$K_{et}$ ( $10^6/s$ )	$\tau$ (ns)	$K_{et}$ ( $10^6/s$ )
SnO <sub>2</sub> -TiO <sub>2</sub> with QDs	24.19	$7.1 \pm 0.5$	22.02	$10.9 \pm 0.5$
TiO <sub>2</sub> with QDs	27.45	$2.2 \pm 0.3$	24.44	$7.7 \pm 1.2$
ZrO <sub>2</sub> with QDs	29.17	----	29.01	----

**Table 1:** Lifetime and electron transfer rate constants from photoluminescence decay dynamics.

The measured error for the lifetime is around 0.1 ns.

**PEC performance.** The PEC performance of the SnO<sub>2</sub> photoanodes sensitized with “giant” QDs was studied using a three-electrode electrochemical cell configuration with Pt as the counter electrode, and a saturated Ag/AgCl as a reference electrode.<sup>38</sup> The voltage was linearly swept and converted to RHE, prior to plotting it against the photocurrent density generated under 1 sun illumination (AM 1.5G, 100 mW/cm<sup>2</sup>) and dark conditions.

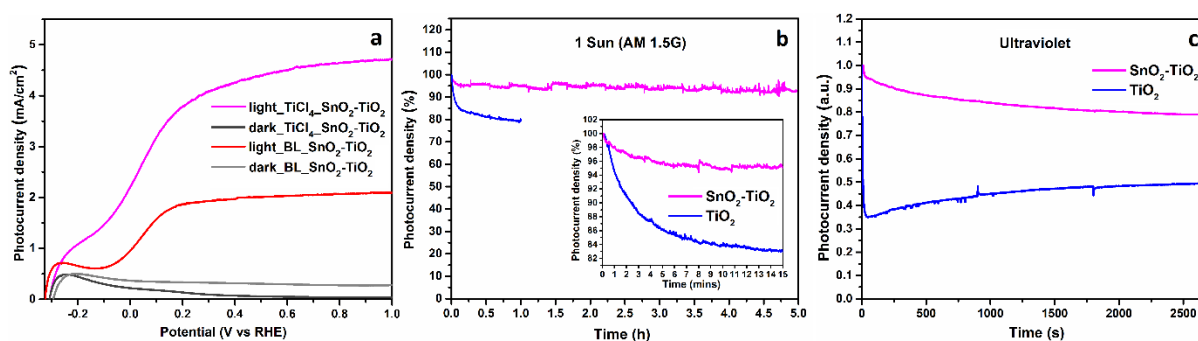


**Figure 3:** (a) Photocurrent density versus the applied voltage (vs RHE) for different configurations of SnO<sub>2</sub>- TiO<sub>2</sub> and core/shell QD in the dark and under 1 sun AM 1.5G illumination (100 mW/cm<sup>2</sup>) with commercial TiO<sub>2</sub> (BL) and TiCl<sub>4</sub> blocking layer. (b) Long duration stability test of 5 h for at 0.6 V (vs RHE) for SnO<sub>2</sub>-TiO<sub>2</sub> and 1 h for TiO<sub>2</sub> photoanode under 1 sun illumination using AM

1.5G filter. First 15 min of the long duration stability shown in the inset. (c) Stability of SnO<sub>2</sub>-TiO<sub>2</sub> and TiO<sub>2</sub> photoanode under UV illumination.

With the increase in voltage, the photocurrent density gradually increases under illumination, until a saturated current density is obtained (Fig. 3a). The effect of different BL samples such as the TiO<sub>2</sub> commercial BL and TiCl<sub>4</sub> BL, which were prepared with TiO<sub>x</sub> post treatment and TiCl<sub>4</sub> post-treatment, are shown in Fig. S5 and Fig. 3a, respectively. The TiCl<sub>4</sub> BL was fabricated following protocols described in the literature<sup>57</sup> where at the optimal thickness of the compact layer, the charge transfer resistance at the FTO interface is the lowest,<sup>5,46,49</sup> improving the charge collection and hence, the overall photocurrent density of the device. With the introduction of the TiCl<sub>4</sub> BL, the photocurrent density was improved by 50% from 1 mA/cm<sup>2</sup> to 1.5 mA/cm<sup>2</sup> for TiO<sub>x</sub> post treated devices, which is shown in Fig. S5 and nearly a 2.5-fold increment from 2 mA/cm<sup>2</sup> to 4.7 mA/cm<sup>2</sup> was achieved for the TiCl<sub>4</sub> post treated cell, which is presented in Fig. 3a. The photocurrent density was ~10 mA/cm<sup>2</sup> for the PEC cell based on the TiO<sub>2</sub>/QDs anode, which is two-fold higher than that of PEC cells based on SnO<sub>2</sub>-TiO<sub>2</sub>/QDs. Our typical three electrode PEC experimental arrangement is demonstrated in Fig. S6 (a) and evolution of H<sub>2</sub> bubbles on the surface of the Pt CE can be seen in Fig. S6 (b). In this work, the structure of the PEC cells are identical except for the type of metal oxide (TiO<sub>2</sub> or SnO<sub>2</sub> or SnO<sub>2</sub>-TiO<sub>2</sub>). As the band energy level of SnO<sub>2</sub> does not favor the efficient electron transfer from the QDs to SnO<sub>2</sub>, there is no photoresponse. As shown in Fig. 1k, the photogenerated electrons may recombine with the holes of QDs, or after transferring to TiO<sub>2</sub> (or SnO<sub>2</sub>-TiO<sub>2</sub>), the electrons may recombine with the holes in the QDs (2) or electrolyte (4) during the electron transfer process. In addition, the photogenerated electrons can directly react with the electrolyte (3). In our PEC set-up, the QDs, electrolyte, counter electrode (Pt), and reference electrode are the same, so the different photocurrent density is mainly due to

the electron transfer rate from the QDs to the metal oxide and the possible charge recombination between the photogenerated electrons and the electrolyte. In the TiO<sub>2</sub> photoanode, the charge transfer rate is much faster and the photoanode is very compact to facilitate the electron collection at the surface of the FTO glass before they react with the electrolyte. While in the SnO<sub>2</sub>-TiO<sub>2</sub> anode, as shown in Fig. 1a, the SnO<sub>2</sub> nanoparticles do not connect to each other very well even after the post-treatment of TiO<sub>2</sub>. This structure will lead to a great portion of the electrons reacting with the electrolyte before they reach the FTO glass substrate, which explains the lower current density compared to the PEC cell based on only on the TiO<sub>2</sub>/QDs anode. The better performance for TiCl<sub>4</sub> post treated samples in comparison with the TiO<sub>x</sub> post treated samples, is due to the morphological advantage of TiCl<sub>4</sub> treated samples, which exhibit enhanced interconnection between the nanoparticles, as compared to the TiO<sub>x</sub> post treated samples, which facilitate the percolation of electrons between the nanoparticles and lead to a global increase of current.<sup>58</sup>

The stability of the photoanodes was investigated under 1 sun (100 mW/cm<sup>2</sup>) AM 1.5G illumination in 0.25 M Na<sub>2</sub>S and 0.35 M Na<sub>2</sub>SO<sub>3</sub> (pH ~ 13) aqueous solution and the results are reported in Fig. 3(b). Three batches of PEC samples were measured with the same PEC set-up at identical temperatures (25 °C). The representative photoanodes based on heterostructured SnO<sub>2</sub>-TiO<sub>2</sub> exhibit remarkable stability. The photocurrent density of the PEC devices based on SnO<sub>2</sub>-TiO<sub>2</sub> retains ~93 ± 3% of its initial value after 5 h (100 mW/cm<sup>2</sup>). To the best of our knowledge, such remarkable stability has never been reported in the literature. The TiO<sub>2</sub> sample shows a rapid decay until it maintains only ~79% of its initial photocurrent density as compared to ~96% for the PEC cell based on SnO<sub>2</sub>-TiO<sub>2</sub>/QDs after 1 h of simulated solar illumination.

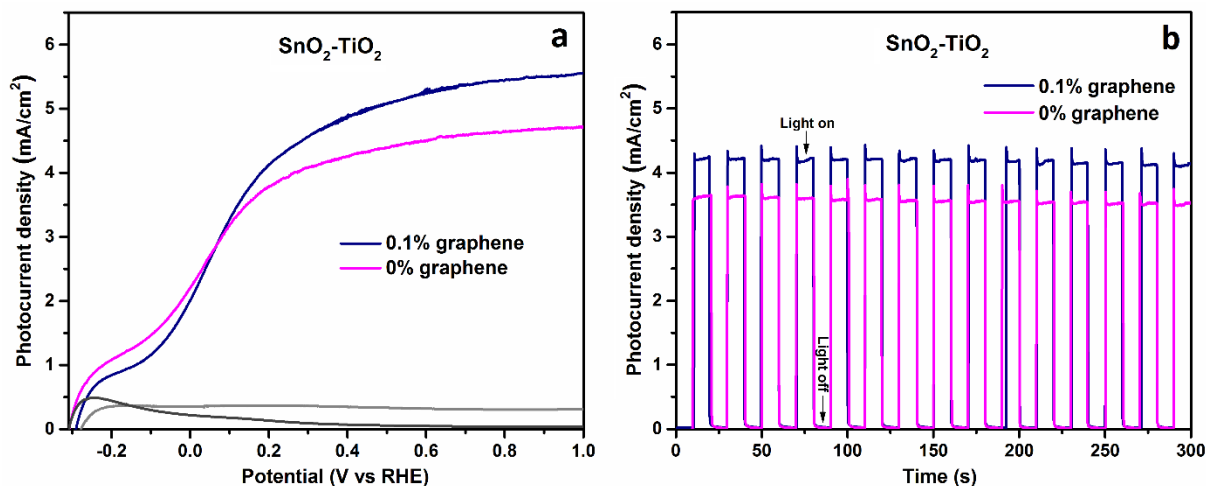


**Figure 4:**(a) Photocurrent density versus the applied voltage (vs RHE) for different graphene concentrations in the SnO<sub>2</sub>-TiO<sub>2</sub> photoanode PEC cells (b) 300 s chopped transient response of photocurrent density at 0.6 V (vs RHE) for the sample without any graphene and with 0.1% graphene.

Although the surface treatment enhances charge transport by implementing a SnO<sub>2</sub>-TiO<sub>2</sub> heterojunction, electrons in nanoparticle networks encounter a sufficiently large number of grain boundaries, which hinder efficient electron percolation. Recently, Dembele and co-workers demonstrated a simple and fast method to incorporate small quantities of graphene microplatelets into the TiO<sub>2</sub> photoanode of a DSSC.<sup>59</sup> Their investigation indicated that a small quantity of graphene does not bring a considerable reduction in the transparency of the photoanode, which is detrimental to solar cell performance, instead, small quantities of graphene increase the photocurrent density improving the overall efficiency of the photovoltaic device.<sup>59</sup> A similar technique, for the introduction of a small amount of graphene, has been implemented in our SnO<sub>2</sub>-TiO<sub>2</sub> photoanode architecture, where the mechanism of efficient fast electron transport through conducting graphene microplatelets has been illustrated in the proposed schematic in the Fig. S7. Compared to the SnO<sub>2</sub>-TiO<sub>2</sub> photoanode without any graphene, the photocurrent density in the

photoanode with 0.1% graphene loading is enhanced by ~20% from 4.7 mA/cm<sup>2</sup> to a value of ~5.6 mA/cm<sup>2</sup>, as seen in Fig. 4 (a). This remarkable enhancement of photocurrent density might be attributed to the exceptional charge directing properties of conducting graphene pathways,<sup>59</sup> which reduces the probability of carrier recombination, thus promoting better electron transport and collection. This value of photocurrent density corresponds to a faradaic efficiency (FE) of ~80% and a maximum applied bias photon-to-current conversion efficiency (ABPE) of 2.89%, see details in Note 1 of the supporting information. The chopped transient response of photocurrent density for the SnO<sub>2</sub>-TiO<sub>2</sub> photoanodes with and without graphene were studied for a time period of 300 s and is displayed in Fig. 3(b). The immediate transition of the photocurrent from the saturated current value to the zero value and vice versa when the shutter for the lamp source switched between on and off positions indicates efficient charge separation in our device. Further improvement of both the efficiency and stability of the PEC cells based on SnO<sub>2</sub>-TiO<sub>2</sub> anode, may focus on investigating the size effect of the SnO<sub>2</sub> nanoparticle, the thickness and crystalline structure of post-treated TiO<sub>2</sub> layer, and the size/shape/thickness of graphene microplatelets, etc.

**Mechanism of fast photocurrent decay in TiO<sub>2</sub>/QDs based photoanode.** Usually, several factors may affect the photostability of PEC cells, including, i) the formation of UV induced excess holes of metal oxides (such as TiO<sub>2</sub>), which induces the formation of non-radiative recombination centres, contributing to the photooxidation process of the QDs, ii) UV induced degradation of QDs, iii) the corrosion of QDs due to the strong base (electrolyte, pH of 13) and iv) slow hole transfer rate of QDs to electrolyte, which induces hole accumulation further leading to self-oxidation of the QDs. In our case, as the only difference between the PECs, is the metal oxides, the dominant factor for the substantial difference in the stability of PECs could be the UV induced reaction between the QDs and photoinduced holes in the metal oxide. In general, the weight concentration

of TiO<sub>2</sub> in the SnO<sub>2</sub>-TiO<sub>2</sub> photoanode is much lower compared to that of SnO<sub>2</sub> and of course, SnO<sub>2</sub> only absorbs UV light in the 300-330 nm range nm of the solar spectrum due to its large bandgap ( $E_g = 3.78$  eV). In the case of the TiO<sub>2</sub> anode, the excess holes under UV illumination will interact with the QDs. To confirm our hypothesis, we further carried out stability tests under UV illumination [bandpass filter (350 nm) on one sun illumination], which is reported in Fig. 3(c). In the case of the TiO<sub>2</sub> sample, ~49% of its initial photocurrent density is maintained after illumination under UV light for 45 min, which can be attributed to hole induced self-oxidative decomposition.<sup>60</sup> On the other hand, in the case of the PEC cell based on SnO<sub>2</sub>-TiO<sub>2</sub>, it retained 80% of its initial current density retained where decrease of 20% after 45 mins is mainly due to the UV-induced degradation of the QDs.

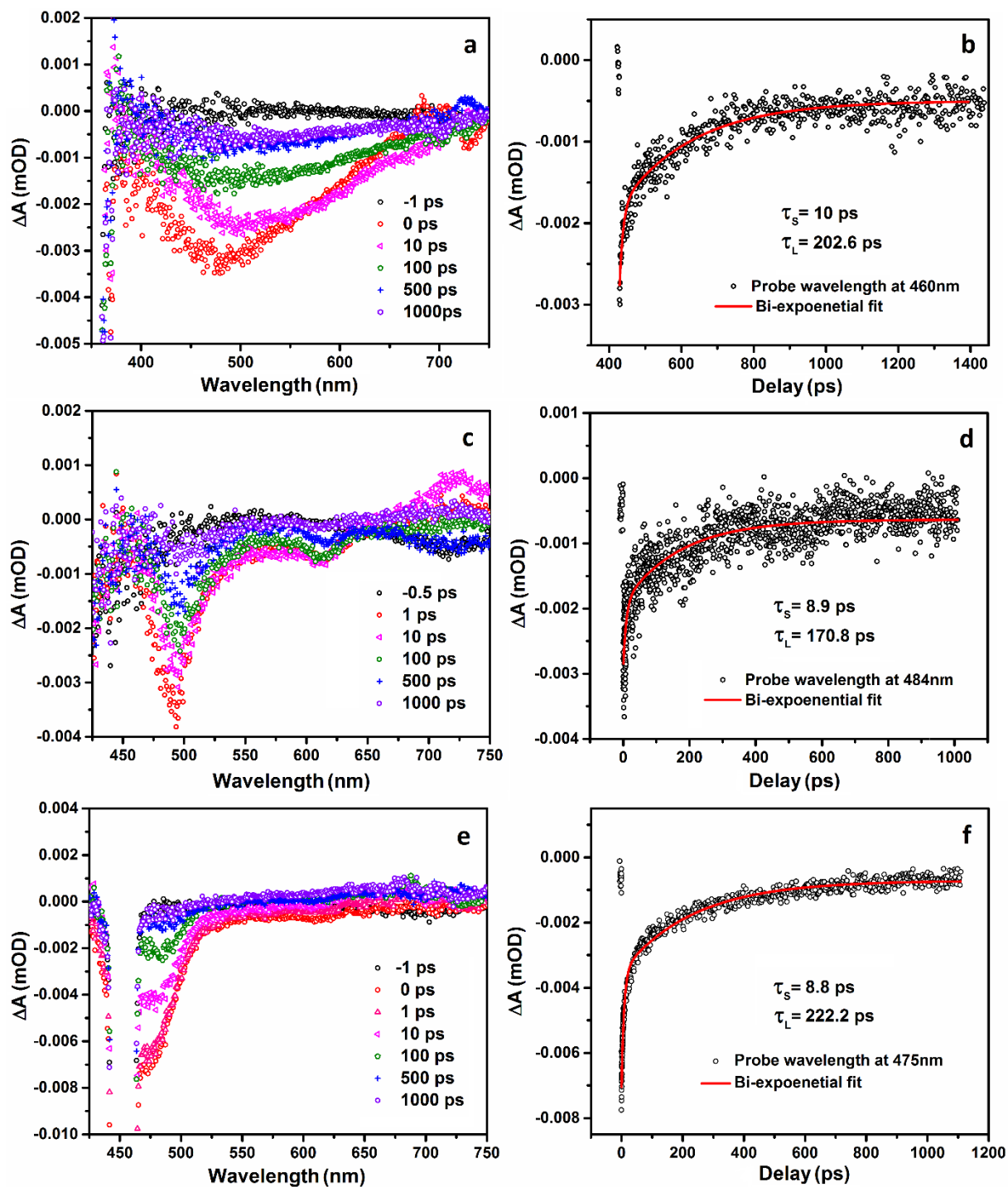


**Figure 5:** Transient absorption spectra of the TiO<sub>2</sub>-QD sample pumped at (a) 350 nm, (c) 400 nm, (e) 450 nm with 0.5  $\mu$ J pulse energy; Decay dynamics of the TiO<sub>2</sub>-QD sample pumped at (b) 350 nm, (d) 400 nm, and (f) 450 nm.

Pump Wavelength (at 0.5 $\mu$ J pulse energy)	Probe wavelength	Decay time ( $\tau$ ) in ps TiO <sub>2</sub> Sample		Decay time ( $\tau$ ) in ps ZrO <sub>2</sub> sample		K <sub>et</sub> (s <sup>-1</sup> ) [1/ $\tau_s$ (TiO <sub>2</sub> )- 1/ $\tau_s$ (ZrO <sub>2</sub> )]
		$\tau_s$	$\tau_L$	$\tau_s$	$\tau_L$	
350 nm (3.54 eV)	460 nm	10 $\pm$ 1.6	202.6 $\pm$ 7.6	15.8 $\pm$ 1	259.7 $\pm$ 17.8	3.67 $\times$ 10 <sup>10</sup>
400 nm (3.10 eV)	484 nm	8.9 $\pm$ 1.6	170.8 $\pm$ 9.2	14.9 $\pm$ 3.2	331.8 $\pm$ 11.3	4.52 $\times$ 10 <sup>10</sup>
450 nm (2.75 eV)	475 nm	8.8 $\pm$ 0.3	222.1 $\pm$ 4.5	17.4 $\pm$ 0.9	275.5 $\pm$ 5.2	5.61 $\times$ 10 <sup>10</sup>

**Table 2:** Decay times ( $\tau$ ) for TiO<sub>2</sub> and ZrO<sub>2</sub> sample and electron transfer rate (K<sub>et</sub>) in case of TiO<sub>2</sub> sample for pump wavelengths of 350 nm, 400 nm, and 450 nm.

To better understand the degradation of the photocurrent density for the TiO<sub>2</sub> photoanode, a detailed investigation of the electron kinetics in TiO<sub>2</sub>-QDs was carried out with ultrafast TAS. The photoanode was excited with different photon energies, 3.54 eV (350 nm), 3.1 eV (400 nm), and 2.75 eV (450 nm) and probed with wavelengths of 460 nm, 484 nm and 475 nm, respectively, at various pump–probe delays. The pulse energy of the pump beam was fixed at 0.5  $\mu$ J. The differential absorbance spectra ( $\Delta A$ ) from the broadband probe were collected in transmission geometry using a spectrometer, and the results are demonstrated in Fig. 5 (a,c,e) for the TiO<sub>2</sub>-QD sample. The fluence of the pump beams were chosen in such a manner that the Auger recombination of the charge carriers can be avoided. A negative magnitude in the differential absorbance spectra ( $\Delta A$ ) corresponds to photobleaching (PB), and ideally, the PB maximum coincides with the first exciton transition observed in their absorption spectrum.<sup>61</sup> When we introduce a pump beam of 3.54 eV energy (i.e. at 350 nm) to the TiO<sub>2</sub>-QD sample, we detect a broad response, which is possibly from the excited carriers of anatase TiO<sub>2</sub> (3.2 eV), CdS shell (2.5 eV) and the CdSe core (2.1 eV), and is depicted in Fig. 5(a). The prominent feature appearing

in all ( $\Delta A$ ) spectra is a PB signal at  $\sim 490$  nm, indicates the presence of excited carriers in the CdS shell, and has an absorption onset at  $\sim 490$  nm owing to its bandgap of 2.5 eV. In Fig. 5(c), we also notice the PB peak around 600 nm from CdSe, which has an absorption onset at  $\sim 590$  nm. A large PB is observed at  $\sim 450$  nm in Fig. 5(e) as a result of scattering of the pump signal of the same wavelength. The data for the decay dynamics of the TiO<sub>2</sub>-QD and ZrO<sub>2</sub>-QD samples, along with the electron injection rates in the TiO<sub>2</sub>-QD sample are presented in Table 2. Corresponding decay kinetics are fitted with a bi-exponential decay function, which resulted in a short ( $\tau_S$ ) and long ( $\tau_L$ ) lifetime. The long lifetime ( $\tau_L$ ) can be attributed to a combination of electron-hole radiative recombination and back electron transfer from the metal oxide to the QD, whereas the short lifetimes ( $\tau_S$ ) may be ascribed to either trapping or a convolution of trapping and electron transfer.<sup>62</sup> The ZrO<sub>2</sub>-QD sample (data presented in Fig. S8) is used as a benchmark to calculate the electron injection rates for the TiO<sub>2</sub>-QD sample, since electron transfer from QDs to ZrO<sub>2</sub> is not likely due to the fact that the CB minima of ZrO<sub>2</sub> is at a higher position than the CB minima of both CdSe and CdS QDs. The electron transfer rate of the TiO<sub>2</sub>-QD sample pumped in the UV regime (at 350 nm) is determined to be  $3.67 \times 10^{10}/s$ , which is lower than the electron transfer rate obtained from 400 and 450 nm pump wavelengths (i.e.  $4.52 \times 10^{10}/s$  and  $5.61 \times 10^{10}/s$ , respectively). This slow electron transfer rate with the 350 nm is primarily due to the electron recombining with the excess holes present in the TiO<sub>2</sub> nanoparticles. These excess holes originate from the formation of energetically deep traps in TiO<sub>2</sub>, which are induced by the UV illumination.<sup>63</sup> The electrons cannot escape the deep traps, so they recombine with the holes, thereby diminishing the electron transfer rate in the UV excitation. When the TiO<sub>2</sub>-QD sample was pumped at a wavelength of 450 nm, the highest electron transfer rate of  $5.61 \times 10^{10}/s$  is recorded. This result is expected, because amongst the utilized pump wavelengths, 450 nm is closest to the CdS absorption onset at  $\sim 490$  nm, thus

high electron transfer from the QDs is likely. The results from TAS measurements are in good agreement with data obtained from the PL analyses and provides insights into the low charge transfer phenomenon of TiO<sub>2</sub> photoanodes under UV pump excitation, thereby explaining the superior performance of our SnO<sub>2</sub>-TiO<sub>2</sub> heterostructured photoanode over traditional TiO<sub>2</sub> photoanodes.

### **Conclusions and perspectives**

In conclusion, we demonstrated a novel photoanode architecture based on heterostructured SnO<sub>2</sub>-TiO<sub>2</sub> mesoporous films, sensitized by “giant” CdSe/CdS core/shell QDs for PEC H<sub>2</sub> generation. We achieved a saturated photocurrent density of ~ 4.7 mA/cm<sup>2</sup> with unprecedented stability, retaining 93% of initial photocurrent density after 5 h of irradiation (100 mW/cm<sup>2</sup>). Detailed analysis with transient photoluminescence (PL) measurements demonstrates that the heterostructured SnO<sub>2</sub>-TiO<sub>2</sub> photoanode exhibits a faster electron transfer compared to a traditional TiO<sub>2</sub> photoanode. Lower electron transfer rates in the TiO<sub>2</sub> photoanode can be largely attributed to slow electron kinetics in the UV regime, as revealed by ultrafast transient absorption spectroscopy. In addition, 0.1% by weight of graphene microplatelets in the heterostructured photoanode improves the photocurrent density to ~ 5.6 mA/cm<sup>2</sup>. These results indicate that heterostructured SnO<sub>2</sub>-TiO<sub>2</sub> can serve as stable and efficient photoanode after sensitization by “giant” QDs, signifying this is a very promising photoanode architecture for PEC hydrogen generation.

### **Acknowledgements**

We thank Rajesh Adhikari for training in the photoanode preparation. We acknowledge funding from the Natural Sciences and Engineering Research Council (NSERC) of Canada in the form of individual Discovery Grants (F.V. and F.R.) and a Strategic Project Grant in partnership with

Canadian Solar, the Canada Foundation for Innovation for infrastructure and its operation. We also acknowledge the Fonds de Recherche du Québec-Nature et technologies (FRQNT) for Équipe (team) grants. H.Z. acknowledges his Ph.D. excellence scholarships from the UNESCO chair and FRQNT. L.J. acknowledges FRQNT for a Merit Scholarship Program. H.G Zhao acknowledges Shangdong Provincial National Science Foundation. This work was partially funded by the Ministère du Développement économique de l'Innovation et de l'Exportation (MDEIE) of Québec through the international project WIROX. F.R. acknowledges the Canada Research Chairs program for funding and partial salary support. F.R. is also grateful to the government of China for a Chang Jiang scholar short term award and to Sichuan Province for a 1000 talent short term award.

## References

- 1 D. T. Boyles, *Bio-energy: technology, thermodynamics, and costs* /, E. Horwood ; Chichester, West Sussex : 1984.
- 2 R. van de Krol, Y. Liang and J. Schoonman, *J. Mater. Chem.*, 2008, **18**, 2311–2320.
- 3 A. J. Nozik and R. Memming, *J. Phys. Chem.*, 1996, **100**, 13061–13078.
- 4 L. Jin, B. AlOtaibi, D. Benetti, S. Li, H. Zhao, Z. Mi, A. Vomiero and F. Rosei, *Adv. Sci.*, 2016, **3**, 1500345.
- 5 R. Adhikari, L. Jin, F. Navarro-Pardo, D. Benetti, B. AlOtaibi, S. Vanka, H. Zhao, Z. Mi, A. Vomiero and F. Rosei, *Nano Energy*, 2016, **27**, 265–274.
- 6 X. Tong, Y. Zhou, L. Jin, K. Basu, R. Adhikari, G. S. Selopal, X. Tong, H. Zhao, S. Sun, A. Vomiero, Z. M. Wang and F. Rosei, *Nano Energy*, 2017, **31**, 441–449.

- 7 L. Jin, G. Sirigu, X. Tong, A. Camellini, A. Parisini, G. Nicotra, C. Spinella, H. Zhao, S. Sun, V. Morandi, M. Zavelani-Rossi, F. Rosei and A. Vomiero, *Nano Energy*, 2016, **30**, 531–541.
- 8 R. Adhikari, K. Basu, Y. Zhou, F. Vetrone, D. Ma, S. Sun, F. Vidal, H. Zhao and F. Rosei, *J. Mater. Chem. A*, 2018, **6**, 6822–6829.
- 9 H. Dotan, K. Sivula, M. Grätzel, A. Rothschild and S. C. Warren, *Energy Environ. Sci.*, 2011, **4**, 958–964.
- 10 P. Zhang, A. Kleiman-Shwarscstein, Y.-S. Hu, J. Lefton, S. Sharma, A. J. Forman and E. McFarland, *Energy Environ. Sci.*, 2011, **4**, 1020–1028.
- 11 Y. Lin, S. Zhou, S. W. Sheehan and D. Wang, *J. Am. Chem. Soc.*, 2011, **133**, 2398–2401.
- 12 X. Chen, L. Liu, P. Y. Yu and S. S. Mao, *Science*, 2011, **331**, 746–750.
- 13 G. Wang, H. Wang, Y. Ling, Y. Tang, X. Yang, R. C. Fitzmorris, C. Wang, J. Z. Zhang and Y. Li, *Nano Lett.*, 2011, **11**, 3026–3033.
- 14 I. S. Cho, Z. Chen, A. J. Forman, D. R. Kim, P. M. Rao, T. F. Jaramillo and X. Zheng, *Nano Lett.*, 2011, **11**, 4978–4984.
- 15 J. H. Park, S. Kim and A. J. Bard, *Nano Lett.*, 2006, **6**, 24–28.
- 16 S. U. M. Khan, M. Al-Shahry and W. B. Ingler, *Science*, 2002, **297**, 2243–2245.
- 17 X. Yang, A. Wolcott, G. Wang, A. Sobo, R. C. Fitzmorris, F. Qian, J. Z. Zhang and Y. Li, *Nano Lett.*, 2009, **9**, 2331–2336.
- 18 Y. Qiu, K. Yan, H. Deng and S. Yang, *Nano Lett.*, 2012, **12**, 407–413.
- 19 W. Li, P. Da, Y. Zhang, Y. Wang, X. Lin, X. Gong and G. Zheng, *ACS Nano*, 2014, **8**, 11770–11777.

- 20 R. Liu, Y. Lin, L.-Y. Chou, S. W. Sheehan, W. He, F. Zhang, H. J. M. Hou and D. Wang, *Angew. Chem. Int. Ed.*, 2011, **50**, 499–502.
- 21 X. Fang, J. Song, T. Pu, C. Wang, C. Yin, J. Wang, S. Kang, H. Shi, Y. Zuo, Y. Wang and L. Cui, *Int. J. Hydrog. Energy*, 2017, **42**, 28183–28192.
- 22 J. Chakrabartty, D. Barba, L. Jin, D. Benetti, F. Rosei and R. Nechache, *J. Power Sources*, 2017, **365**, 162–168.
- 23 S. Li, J. Zhang, B.-P. Zhang, W. Huang, C. Harnagea, R. Nechache, L. Zhu, S. Zhang, Y.-H. Lin, L. Ni, Y.-H. Sang, H. Liu and F. Rosei, *Nano Energy*, 2017, **35**, 92–100.
- 24 S. Li, B. AlOtaibi, W. Huang, Z. Mi, N. Serpone, R. Nechache and F. Rosei, *Small*, 2015, **11**, 4018–4026.
- 25 H. Sameie, A. A. S. Alvani, N. Naseri, F. Rosei, G. Mul and B. T. Mei, *J. Electrochem. Soc.*, 2018, **165**, H353–H359.
- 26 D. Wu, Y. Wei, X. Ren, X. Ji, Y. Liu, X. Guo, Z. Liu, A. M. Asiri, Q. Wei and X. Sun, *Adv. Mater.*, 2018, **30**, 1705366, 1-7.
- 27 X. Ren, R. Ge, Y. Zhang, D. Liu, D. Wu, X. Sun, B. Du and Q. Wei, *J. Mater. Chem. A*, 2017, **5**, 7291–7294.
- 28 X. Ren, W. Wang, R. Ge, S. Hao, F. Qu, G. Du, A. M. Asiri, Q. Wei, L. Chen and X. Sun, *Chem. Commun.*, 2017, **53**, 9000–9003.
- 29 X. Ren, X. Ji, Y. Wei, D. Wu, Y. Zhang, M. Ma, Z. Liu, A. M. Asiri, Q. Wei and X. Sun, *Chem. Commun.*, 2018, **54**, 1425–1428.
- 30 X. Ren, D. Wu, R. Ge, X. Sun, H. Ma, T. Yan, Y. Zhang, B. Du, Q. Wei and L. Chen, *Nano Res.*, 2018, **11**, 2024–2033.
- 31 Z. M. Jarzebski and J. P. Marton, *J. Electrochem. Soc.*, 1976, **123**, 299C-310C.

- 32 M. S. Arnold, P. Avouris, Z. W. Pan and Z. L. Wang, *J. Phys. Chem. B*, 2003, **107**, 659–663.
- 33 D. E. Scaife, *Sol. Energy*, 1980, **25**, 41–54.
- 34 K. Gurunathan, P. Maruthamuthu and M. V. C. Sastri, *Int. J. Hydrog. Energy*, 1997, **22**, 57–62.
- 35 G. Shang, J. Wu, S. Tang, M. Huang, Z. Lan, Y. Li, J. Zhao and X. Zhang, *J. Mater. Chem.*, 2012, **22**, 25335–25339.
- 36 X.D. Li , Z.M. Zhang, L.L. Chen, Z.P. Liu, J.L. Cheng, W. Ni, E.Q. Xie and B. Wang, *J. Power Sources*, 2014, **269**, 866–872.
- 37 Z. Zhang, C. Gao, Z. Wu, W. Han, Y. Wang, W. Fu, X. Li and E. Xie, *Nano Energy*, 2016, **19**, 318–327.
- 38 J. Yu, Y. Wang and W. Xiao, *J. Mater. Chem. A*, 2013, **1**, 10727–10735.
- 39 K. Basu, D. Benetti, H. Zhao, L. Jin, F. Vetrone, A. Vomiero and F. Rosei, *Sci. Rep.*, 2016, **6**, 23312, 1-10.
- 40 P. Docampo, J. M. Ball, M. Darwich, G. E. Eperon and H. J. Snaith, *Nat. Commun.*, 2013, **4**, 2761.
- 41 B. O. Dabbousi, J. Rodriguez-Viejo, F. V. Mikulec, J. R. Heine, H. Mattoussi, R. Ober, K. F. Jensen and M. G. Bawendi, *J. Phys. Chem. B*, 1997, **101**, 9463–9475.
- 42 Y. Ghosh, B. D. Mangum, J. L. Casson, D. J. Williams, H. Htoon and J. A. Hollingsworth, *J. Am. Chem. Soc.*, 2012, **134**, 9634–9643.
- 43 L. Jin, H. Zhao, D. Ma, A. Vomiero and F. Rosei, *J. Mater. Chem. A*, 2015, **3**, 847–856.
- 44 H. McDaniel, N. Fuke, N. S. Makarov, J. M. Pietryga and V. I. Klimov, *Nat. Commun.*, 2013, **4**, 2887.

- 45 R. Trevisan, P. Rodenas, V. Gonzalez-Pedro, C. Sima, R. S. Sanchez, E. M. Barea, I. Mora-Sero, F. Fabregat-Santiago and S. Gimenez, *J. Phys. Chem. Lett.*, 2013, **4**, 141–146.
- 46 Y. Chen, J. Vela, H. Htoon, J. L. Casson, D. J. Werder, D. A. Bussian, V. I. Klimov and J. A. Hollingsworth, *J. Am. Chem. Soc.*, 2008, **130**, 5026–5027.
- 47 P. Reiss, M. Protière, L. Li, *Small*, 2009, **5**, 154-168.
- 48 H. Zhao, A. Vomiero and F. Rosei, *Small*, 2015, **11**, 5741–5746.
- 49 H. Zhu, N. Song, H. Lv, C. L. Hill and T. Lian, *J. Am. Chem. Soc.*, 2012, **134**, 11701–11708.
- 50 H. Chauhan, Y. Kumar and S. Deka, *Nanoscale*, 2014, **6**, 10347–10354.
- 51 L. Lu, X.-L. Xu, W.-T. Liang and H.-F. Lu, *J. Phys. Condens. Matter*, 2007, **19**, 406221, 1-10.
- 52 L. Liu, M. An, P. Yang and J. Zhang, *Sci. Rep.*, 2015, **5**, 9055, 1-10.
- 53 M. C. Biesinger, B. P. Payne, B. R. Hart, A. P. Grosvenor, N. S. McIntyre, L. W. Lau and R. S. Smart, *J. Phys. Conf. Ser.*, 2008, **100**, 012025, 1-4.
- 54 M. C. Biesinger, L. W. M. Lau, A. R. Gerson and R. S. C. Smart, *Appl. Surf. Sci.*, 2010, **257**, 887–898.
- 55 F. Xu, Y. Yuan, H. Han, D. Wu, Z. Gao and K. Jiang, *CrystEngComm*, 2012, **14**, 3615–3622.
- 56 E. Hernández-Rodríguez, M. Loeza-Poot, I. Riech, V. Rejón and J. L. Peña, *J. Phys. Appl. Phys.*, 2015, **48**, 255102, 1-6.
- 57 H. Choi, C. Nahm, J. Kim, J. Moon, S. Nam, D.-R. Jung and B. Park, *Curr. Appl. Phys.*, 2012, **12**, 737–741.
- 58 C. J. Barbé, F. Arendse, P. Comte, M. Jirousek, F. Lenzmann, V. Shklover and M. Grätzel, *J. Am. Ceram. Soc.*, 1997, **80**, 3157–3171.

- 59 K. T. Dembele, G. S. Selopal, R. Milan, C. Trudeau, D. Benetti, A. Souidi, M. M. Natile, G. Sberveglieri, S. Cloutier, I. Concina, F. Rosei and A. Vomiero, *J. Mater. Chem. A*, 2015, **3**, 2580–2588.
- 60 X. Chen, S. Shen, L. Guo and S. S. Mao, *Chem. Rev.*, 2010, **110**, 6503–6570.
- 61 I. Robel, M. Kuno and P. V. Kamat, *J. Am. Chem. Soc.*, 2007, **129**, 4136–4137.
- 62 K. Tvrdy, P. A. Frantsuzov and P. V. Kamat, *Proc. Natl. Acad. Sci*, 2011, **108**, 29–34.
- 63 S. K. Pathak, A. Abate, P. Ruckdeschel, B. Roose, K. C. Gödel, Y. Vaynzof, A. Santhala, S.-I. Watanabe, D. J. Hollman, N. Noel, A. Sepe, U. Wiesner, R. Friend, H. J. Snaith and U. Steiner, *Adv. Funct. Mater.*, 2014, **24**, 6046–6055.

# Supporting Information

## Highly stable Photoelectrochemical Cells for Hydrogen Production using SnO<sub>2</sub>-TiO<sub>2</sub>/Quantum Dots Heterostructured Photoanode

Kaustubh Basu<sup>1</sup>, Hui Zhang<sup>1</sup>, Haiguang Zhao<sup>2\*</sup>, Sayantan Bhattacharya<sup>3</sup>, Fabiola Navarro Pardo<sup>1,4</sup>, Prasanta Kumar Datta<sup>3</sup>, Lei Jin<sup>1</sup>, Shuhui Sun<sup>1</sup>, Fiorenzo Vetrone<sup>1,4</sup>, Federico Rosei<sup>1,4\*</sup>

<sup>1</sup>Institut National de la Recherche Scientifique, Centre Énergie, Matériaux et Télécommunications, 1650 Boulevard Lionel-Boulet, Varennes, Québec J3X 1S2, Canada

<sup>2</sup>The Cultivation Base for State Key Laboratory, Qingdao University, No. 308 Ningxia Road, Qingdao 266071, PR China

<sup>3</sup>Department of Physics, Indian Institute of Technology Kharagpur, Kharagpur 721302, India

<sup>4</sup>Institute for Fundamental and Frontier Science, University of Electronic Science and Technology of China, Chengdu 610054, PR China

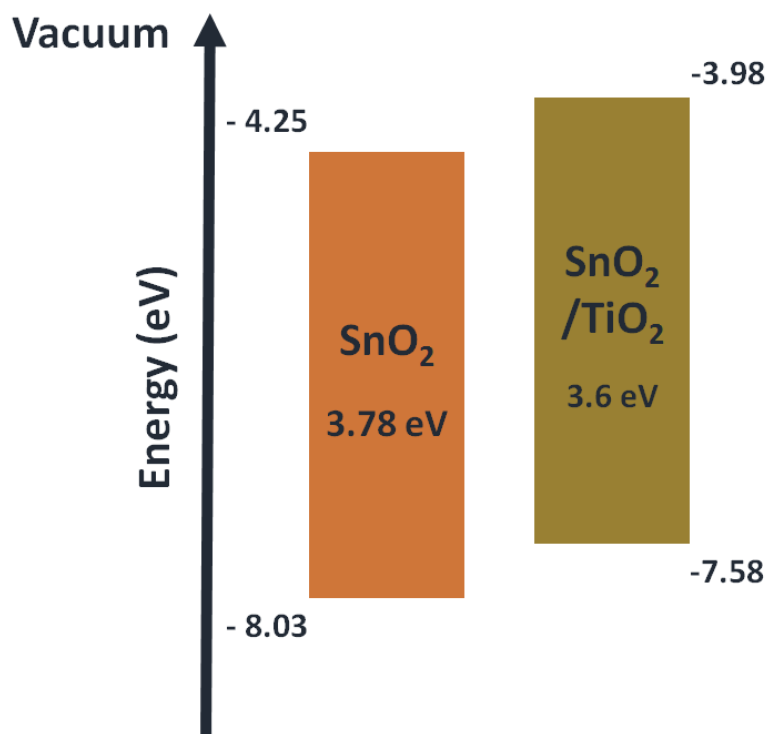


**Figure S1** Band diagram constructed by combining the data from UV photoelectron spectroscopy (UPS) and diffuse reflectance spectroscopy (DRS) of the SnO<sub>2</sub> and SnO<sub>2</sub>/TiO<sub>2</sub> photoanode.<sup>1</sup>

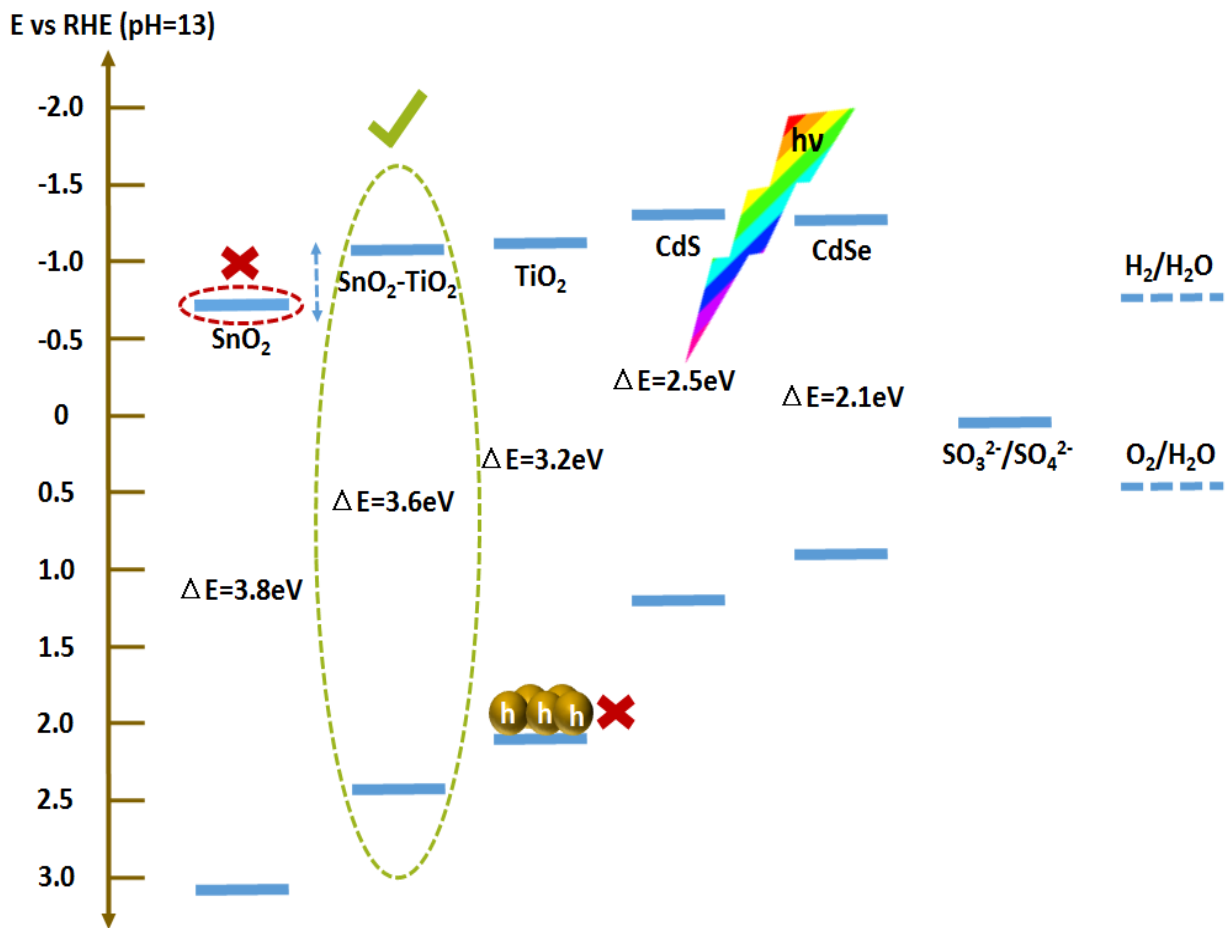


**Figure S2** Band diagram depicting the beneficial effect of using SnO<sub>2</sub>-TiO<sub>2</sub> over traditional TiO<sub>2</sub> photoanode. Approximate energy levels (corresponding to pH=13) of SnO<sub>2</sub>-TiO<sub>2</sub><sup>1</sup>, CdSe, CdS, along with related characteristic redox potentials. The band gap value of CdSe and CdS correspond to QD and bulk semiconductors, respectively. The arrows denote the electron and hole transfer mechanisms.

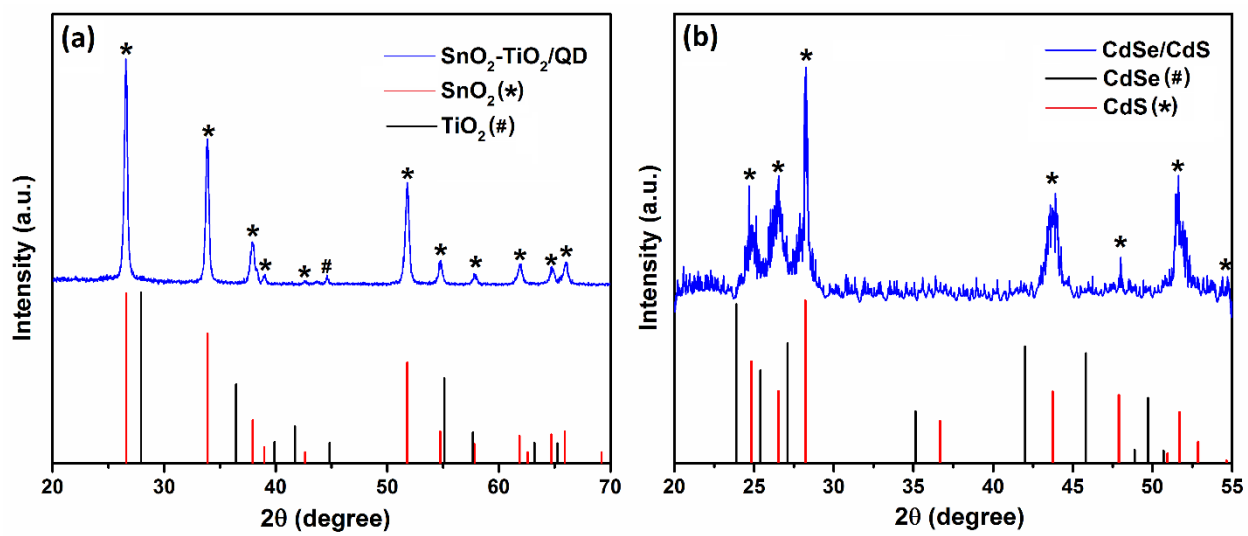


**Figure S3:** (a) X-ray diffraction patterns of the SnO<sub>2</sub>-TiO<sub>2</sub>/QD photoanode; (b) Grazing angle X-ray diffraction patterns of the CdSe/CdS core/shell QDs on Si substrate.

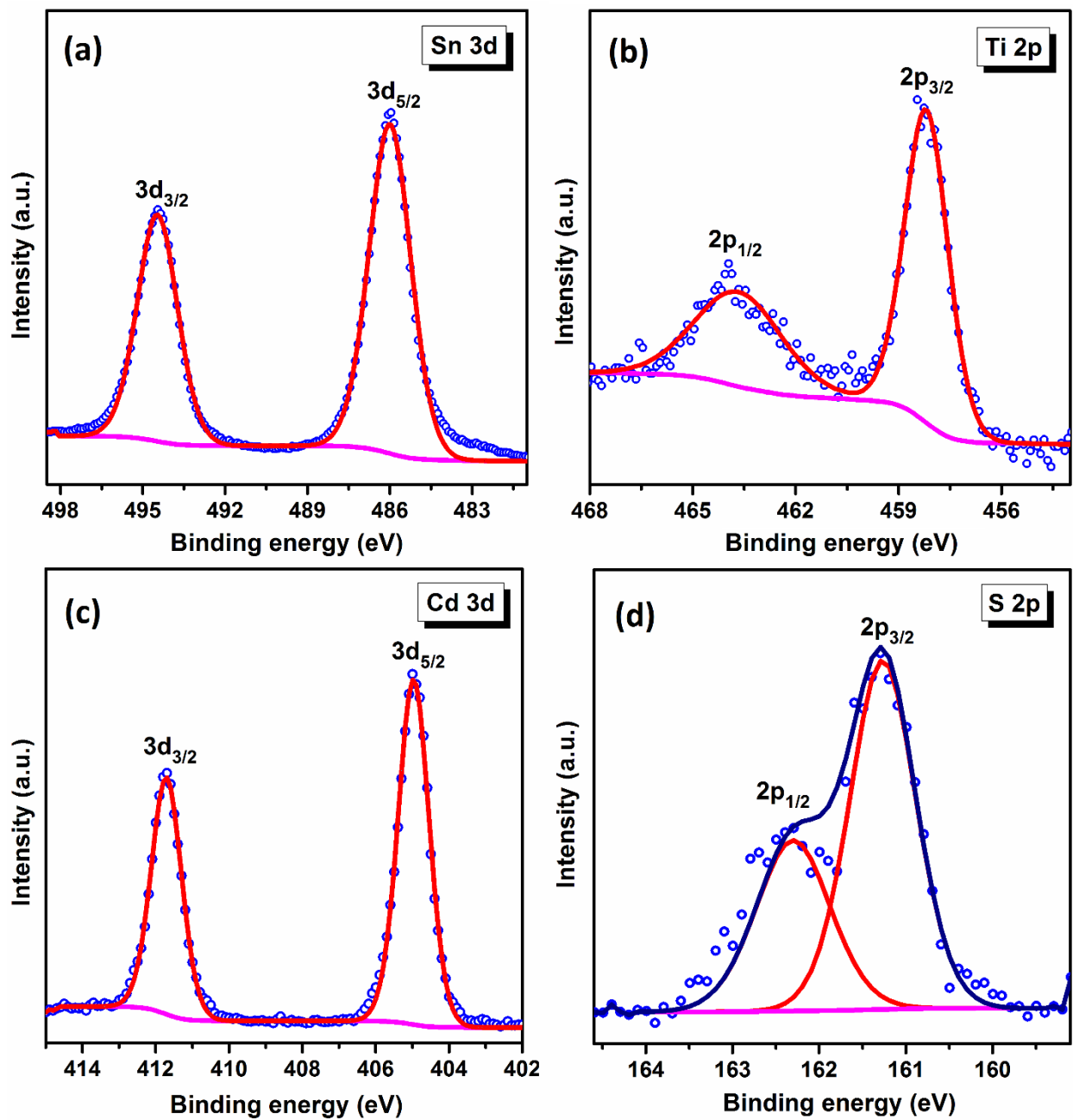


**Figure S4:** X-ray Photoelectron spectra and curve fit of; (a) Sn 3d peak , (b) Ti 2p peak (c) Cd 3d peak, and (d) S 2p peak for the SnO<sub>2</sub>-TiO<sub>2</sub>/QD photoanode.

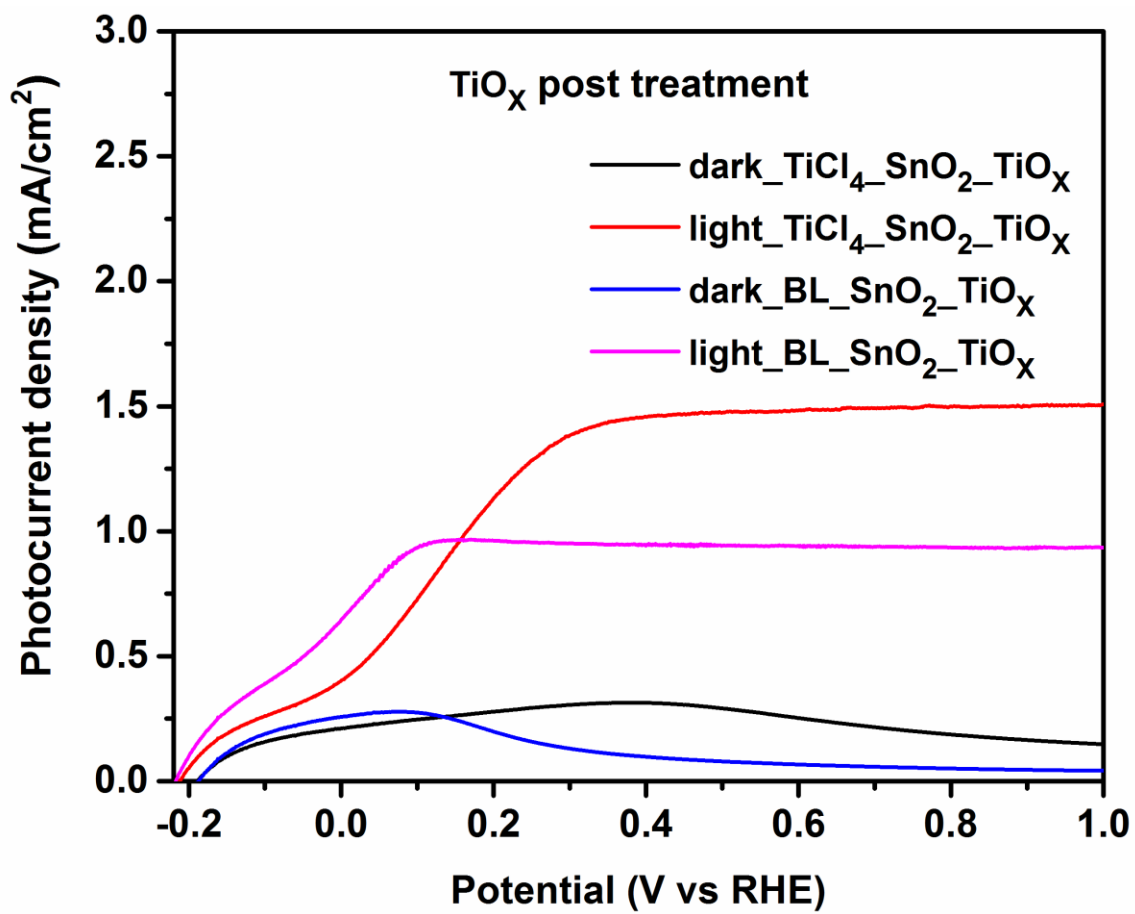


**Figure S5:** Photocurrent density versus the applied voltage (vs RHE) for SnO<sub>2</sub>-TiO<sub>2</sub> photoanode PEC cells with different blocking layers.

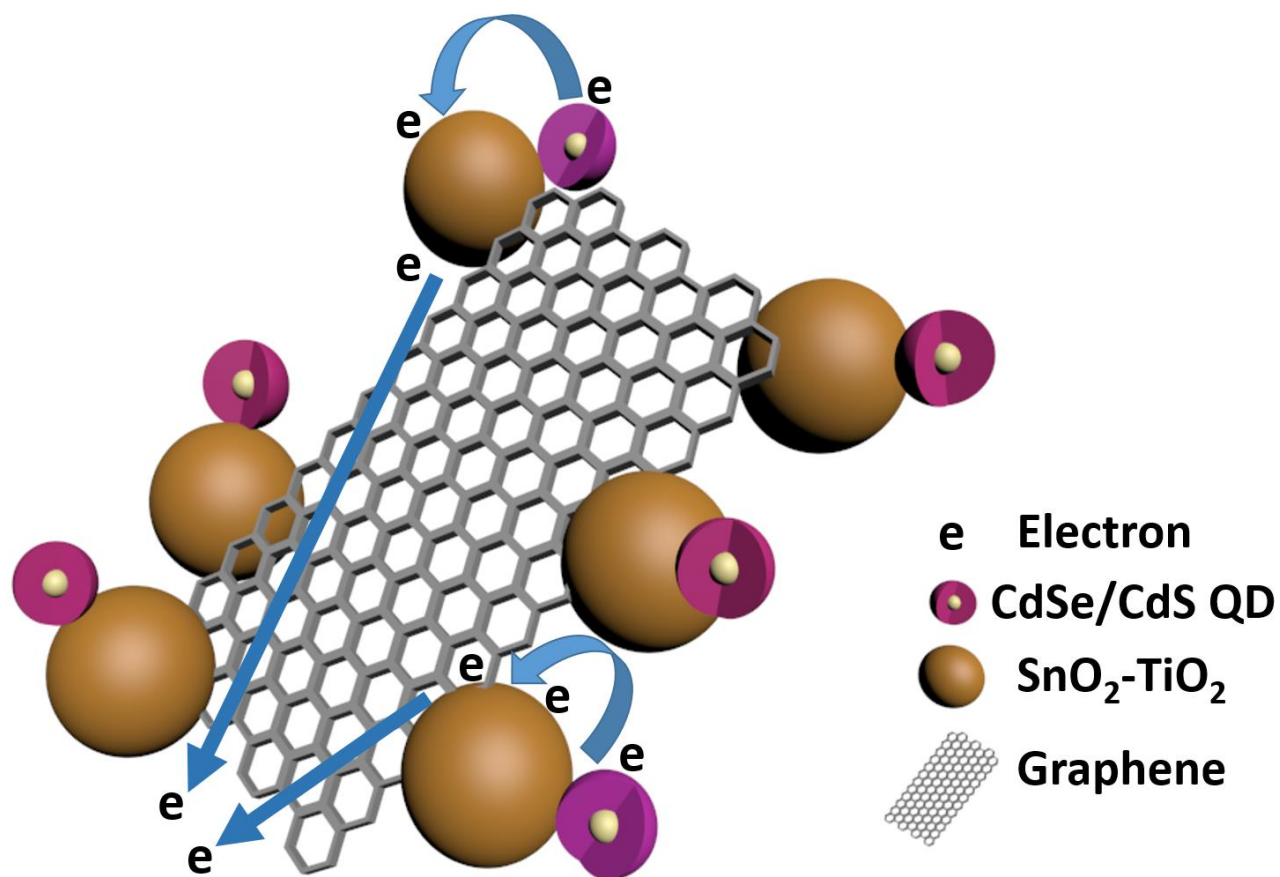


**Figure S6:** General schematic for efficient photoelectron transfer via graphene conducting pathways in the composite photoanode sensitized with giant QDs, arrows indicate the electron transfer processes.

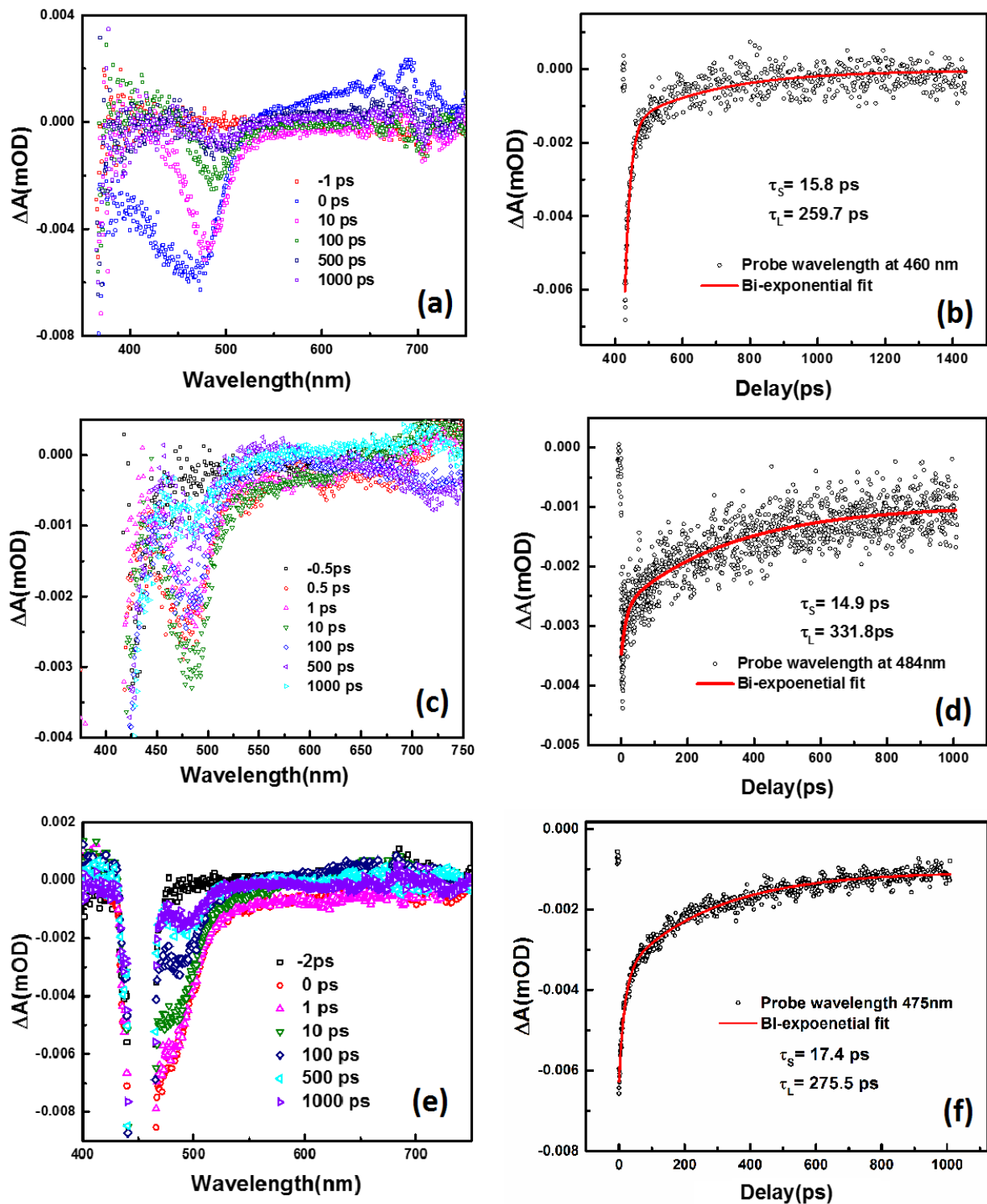


**Figure S7:** Transient absorption spectra of ZrO<sub>2</sub>-QD sample pumped at (a) 350 nm, (c) 400 nm, (e) 450 nm with 0.5  $\mu$ J pulse energy ; Decay dynamics of ZrO<sub>2</sub>-QD sample pumped at (b) 350 nm, (d) 400 nm, and (f) 450 nm.

### Note 1

We have estimated the H<sub>2</sub> gas evolution within our CdSe/CdS g-QD/SnO<sub>2</sub>-TiO<sub>2</sub> photoanode by using the H<sub>2</sub> evolution measurements conducted in a similar system composed of CdSe/CdS “giant”-QD /TiO<sub>2</sub> photoanode,<sup>2</sup> Pt as the counter-electrode and a Ag/AgCl saturated reference electrode. The produced H<sub>2</sub> gas in this benchmark system was detected using a ShimadzuGC-8A gas chromatography (GC) device equipped with a thermal conductivity detector. Argon was used as the carrier gas for GC analysis. An air-tight syringe was used for sampling from the vacuum sealed chamber. After 5610, 6280 and 7172 s, the H<sub>2</sub> gas measured was 23.55, 24.65 and 25.61 μmol, respectively. This approach is quite reliable because after 1.5 h, the evolution of the H<sub>2</sub> gas within our benchmark PEC system<sup>2</sup> stabilizes and the photocurrent density is similar to the one produced in this work with the incorporation of 0.1 wt% graphene microplatelets, (~5.6 mA/cm<sup>2</sup>).

The Faradaic Efficiency (FE) was calculated using the formula:<sup>3</sup>

$$FE(\%) = \frac{H_2 \text{ evolved (mol)} \times 2 \times F(\text{Cmol}^{-1})}{\text{Charge passed through WE (C)}} \times 100\%$$
$$= 81.27\%$$

Where, Faraday constant (F) = 96484.34 C/mol

The solar to hydrogen (STH) conversion efficiency was calculated using the formula:<sup>4</sup>

$$STH = \left[ \frac{\left| J_{sc} \left( \frac{\text{mA}}{\text{cm}^2} \right) \right| \times 1.23 \text{ (V)} \times FE}{P \left( \frac{\text{mW}}{\text{cm}^2} \right)} \right]_{AM\ 1.5G}$$
$$= 5.51 \%$$

Where  $J_{sc}$  is the photocurrent density,  $P$  is the input power provided by solar simulator.

When a photoanode for PEC based H<sub>2</sub> generation is used unassisted i.e. without a tandem cell, STH efficiency becomes irrelevant.<sup>4</sup> In such cases, applied bias photon-to-current conversion efficiency (ABPE) may be used to overcome this drawback.<sup>4</sup>

ABPE is defined as:<sup>4</sup>

$$ABPE = \left[ \frac{|J_{photo}| \times (1.23 - V)}{P} \right]_{AM\ 1.5G}$$

=2.89%

Where, V is the voltage that is applied to the cell from an external power source

J<sub>photo</sub> is the photocurrent measured at this voltage.

## References

- 1 K. Basu, D. Benetti, H. Zhao, L. Jin, F. Vetrone, A. Vomiero and F. Rosei, *Sci. Rep.*, 2016, **6**, 1-10.
- 2 R. Adhikari, L. Jin, F. Navarro-Pardo, D. Benetti, B. AlOtaibi, S. Vanka, H. Zhao, Z. Mi, A. Vomiero and F. Rosei, *Nano Energy*, 2016, **27**, 265–274.
- 3 D. W. Wakerley and E. Reisner, *Phys. Chem. Chem. Phys.*, 2014, **16**, 5739–5746.
- 4 H. Dotan, N. Mathews, T. Hisatomi, M. Grätzel and A. Rothschild, *J. Phys. Chem. Lett.*, 2014, **5**, 3330–3334.

## Chapter 5: Conclusion

Solar energy conversion implementing PEC cells is a promising technology towards building a clean carbon emission free future. Primarily, two types of PEC cells were introduced in this thesis, firstly DSSCs, that converts sunlight into electric power. Secondly, a PEC cell where solar energy can be converted into hydrogen which holds immense potential in future energy applications.

The photoanode of PEC cell plays a pivotal role in the charge dynamics of the overall device. Mesoporous nanoparticle based photoanodes, has garnered significant interest due to high surface area and facile fabrication techniques. Owing to ultrafast electron injection rates from the excited dye into TiO<sub>2</sub> nanoparticles, TiO<sub>2</sub> has been widely used as a photoanode in PEC cells. Although high electron recombination in TiO<sub>2</sub> due to poor electron mobility, limits its use. On the other hand, SnO<sub>2</sub> is a promising photoanode, which has electronic mobility that is orders of magnitude higher than TiO<sub>2</sub>. Furthermore, SnO<sub>2</sub> has a low sensitivity to UV degradation due to its larger band gap, and hence more stable. To address all the issues, in this thesis, we fabricated SnO<sub>2</sub>-TiO<sub>2</sub> heterostructure photoanodes by a straight forward chemical post treatment approach, to integrate the advantages of higher conduction band edge of TiO<sub>2</sub>, and the high stability and exceptional electronic mobility of SnO<sub>2</sub>. In addition, the type-II band alignment of SnO<sub>2</sub>-TiO<sub>2</sub> heterostructure facilitates charge separation and transport. The conclusion for the results in our thesis are divided into two parts, in the first part we implement SnO<sub>2</sub>-TiO<sub>2</sub> heterostructure in DSSCs, and in the second part, we study the performance of SnO<sub>2</sub>-TiO<sub>2</sub> heterostructure photoanodes in PEC cells for H<sub>2</sub> generation.

In part I of our thesis, we have demonstrated the synthesis of the SnO<sub>2</sub>-TiO<sub>2</sub> photoanode achieved following different precursor treatment routes such as TiO<sub>x</sub> and TiCl<sub>4</sub>. The blocking layer of TiO<sub>2</sub>

fabricated on FTO, inhibits the transport of photoinjected electrons back to the electrolytes, which were collected by FTO. In addition, the passivation of the SnO<sub>2</sub> with TiO<sub>2</sub> layer blocks the back-reaction pathway of photoinjected electrons from the heterostructure photoanode to the electrolyte. The enhancement of open circuit voltage was achieved due to the reduced charge recombination from modification of the electronic band alignment confirmed with UPS and diffuse reflectance. The effect of interconnection of the photoanode nanoparticles provides a better path for electron flow and plays a major role in enhancing the short circuit current of the device. Impedance spectroscopy analysis confirms the increase of R<sub>rec</sub>, and higher lifetime for solar cells with TiO<sub>2</sub> post treatment. This further confirms reduced recombination and greater diffusion length of an electron prior to recombination, thereby enhancing the functional properties of the DSSC, which led to nearly a 2-fold improvement in overall PCE. Therefore, SnO<sub>2</sub>-TiO<sub>2</sub> photoanode fabricated via different precursor treatment routes of TiO<sub>x</sub> and TiCl<sub>4</sub> demonstrated a marked improvement over conventional SnO<sub>2</sub> photoanode, and could be considered as a promising approach towards making high performance DSSCs.

Although, SnO<sub>2</sub>-TiO<sub>2</sub> based photoanode achieved a considerable improvement in comparison to traditional SnO<sub>2</sub> photoanode, we furthermore investigated and successfully demonstrated DSSCs with novel SnO<sub>2</sub>-TiO<sub>2</sub>/graphene mesoporous photoanode architecture. A systematic study was carried out on the photovoltaic performance and stability of DSSCs by incorporating different concentrations of graphene microplatelets inside the SnO<sub>2</sub>-TiO<sub>2</sub> network implementing a fast and large area-scalable methodology. A PCE of ~3.4 % was achieved under 1 sun simulated irradiation, AM 1.5G for SnO<sub>2</sub>-TiO<sub>2</sub>/graphene DSSC by optimization of the graphene concentration. This enhancement of PCE could be attributed to higher electron lifetime and reduced charge recombination in graphene based photoanodes which was confirmed by EIS. The reduced charge

recombination subsequently boosted  $J_{sc}$  from 7.76 mA/cm<sup>2</sup> to 9.03 mA/cm<sup>2</sup>. We also confirmed higher electron lifetime in SnO<sub>2</sub>-TiO<sub>2</sub>/graphene photoanode DSSCs in comparison to SnO<sub>2</sub>-TiO<sub>2</sub> photoanode DSSCs with the help of open circuit voltage decay experiments. To study the long duration stability of the DSSCs, we investigated the performance of the cells for 200 hours of continuous illumination under AM 1.5G simulated sunlight. We found that, introduction of optimized quantity of graphene microplatelets results in superior stability of all the functional parameters of our solar cells. These results establish SnO<sub>2</sub>-TiO<sub>2</sub>/graphene photoanode architecture as a promising photoanode towards efficient and stable DSSC.

In part II of the thesis, we have demonstrated the implementation of a novel photoanode architecture based on heterostructured SnO<sub>2</sub>-TiO<sub>2</sub> mesoporous films, sensitized by “giant” CdSe/CdS core/shell QDs for PEC H<sub>2</sub> generation. The “giant” CdSe/CdS core/shell QDs incorporated in the mesoporous photoanode structure by EPD technique, further extended the absorption of the photoanode to the visible spectrum. We achieved a saturated photocurrent density of ~ 4.7 mA/cm<sup>2</sup> under 1 sun simulated AM 1.5G irradiation, with an unprecedented stability of 93% of initial photocurrent density after 5 h of irradiation which is the highest value for QDs based PEC cells. Detailed investigation with transient PL measurements demonstrate that the heterostructured SnO<sub>2</sub>-TiO<sub>2</sub> photoanode architecture exhibits faster electron transfer compared to a traditional TiO<sub>2</sub> photoanode. Ultrafast transient absorption spectroscopy revealed lower electron transfer rates in the TiO<sub>2</sub> photoanode which can be largely attributed to slow electron kinetics of TiO<sub>2</sub> in the UV regime. Moreover, 0.1% by weight of graphene microplatelets in the heterostructured photoanode further enhances the photocurrent density to ~ 5.6 mA/cm<sup>2</sup>. These results show that heterostructured SnO<sub>2</sub>-TiO<sub>2</sub> photoanodes can serve as stable and efficient photoanodes after

sensitization by “giant” QDs, signifying this is a very promising photoanode architecture for PEC hydrogen generation.

## References

- [1] Key world energy statistics, Available at: [http://www.iea.org/publications/free\\_publications/publication/key-world-energy-statistics.html](http://www.iea.org/publications/free_publications/publication/key-world-energy-statistics.html).
- [2] Renewable energy, nuclear power and Galileo - climate science, awareness and solutions, Available at: <http://csas.ei.columbia.edu/2014/02/21/renewable-energy-nuclear-power-and-galileo>.
- [3] M. Dutta, L. Thirugnanam, N. Fukata, Si nanowire solar cells: Principles, device types, future aspects, and challenges, *Adv. Silicon Sol. Cells*, Springer, Cham, 2018: pp. 299–329.
- [4] The hidden costs of fossil fuels, Available at: <https://www.ucsusa.org/clean-energy/coal-and-other-fossil-fuels/hidden-cost-of-fossils>.
- [5] Trends in atmospheric carbon dioxide, Available at: <https://www.esrl.noaa.gov/gmd/ccgg/trends/global.html>.
- [6] Kyoto Protocol Introduction, UNFCCC, Available at: <https://unfccc.int/process/the-kyoto-protocol>.
- [7] S.A. Agarkar, Dye sensitized solar cell: Optimizing materials, methods and optoelectronic effects, phd, AcSIR, 2014, Available at: <http://ncl.csircentral.net/1770/>.
- [8] O. Ellabban, H. Abu-Rub, F. Blaabjerg, Renewable energy resources: Current status, future prospects and their enabling technology, *Renew. Sustain. Energy Rev.* 39 (2014) 748–764.
- [9] N. Armaroli, V. Balzani, Towards an electricity-powered world, *Energy Environ. Sci.* 4 (2011) 3193–3222.
- [10] Statistical review of world energy, energy economics, Available at: <https://www.bp.com/en/global/corporate/energy-economics/statistical-review-of-world-energy.html>.

- [11] Special report on renewable energy sources and climate change mitigation, Available at: <http://www.ipcc.ch/report/srren/>.
- [12] Benefits of Renewable Energy Use, Union Concerned Sci. Available at: <https://www.ucsusa.org/clean-energy/renewable-energy/public-benefits-of-renewable-power>.
- [13] M. Thirugnanasambandam, S. Iniyar, R. Goic, A review of solar thermal technologies, *Renew. Sustain. Energy Rev.* 14 (2010) 312–322.
- [14] M. S. Dresselhaus, I. L. Thomas, Alternative energy technologies, *Nature*. 414 (2001) 332–337.
- [15] Becquerel, Recherches sur les effets de la radiation chimique de la lumiere solaire au moyen des courants electriques, *Comptes Rendus L'Academie Sci.* 9 (1839) 145–149.
- [16] M. Grätzel, Photoelectrochemical cells, *Nature*. 414 (2001) 338–344.
- [17] B.A. Gonfa, Fabrication and investigation of heterojunction solar cells based on near infrared quantum dots and one dimensional nanostructures, phd, Université du Québec, Institut national de la recherche scientifique, 2015, Available at: <http://espace.inrs.ca/2797/>.
- [18] T. Jafari, E. Moharreri, A.S. Amin, R. Miao, W. Song, S.L. Suib, Photocatalytic water splitting-The untamed dream: A review of recent advances, *Mol. Basel Switz.* 21 (2016) 900.
- [19] G. L. Chiarello , M. H. Aguirre, E. Selli, Hydrogen production by photocatalytic steam reforming of methanol on noble metal-modified TiO<sub>2</sub> ,*Journal of Catalysis* 273 (2010) 182–190.
- [20] K. Hou, R. Hughes, The kinetics of methane steam reforming over a Ni/ $\alpha$ -Al<sub>2</sub>O catalyst, *Chem. Eng. J.* 82 (2001) 311–328.

- [21] Planck, Distribution of energy in the spectrum, *Ann. Phys.* 4 (1901) 553–563.
- [22] Irradiation spectrum, Available at: <http://www.superstrate.net/pv/illumination/spectrum.html>.
- [23] Introduction to Solar Radiation, Available at: <https://www.newport.com/t/introduction-to-solar-radiation>.
- [24] F. Kasten, A.T. Young, Revised optical air mass tables and approximation formula, *Appl. Opt.* 28 (1989) 4735–4738.
- [25] P. Würfel. *The physics of solar cells*. 2005.  
Available at: <http://www.worldscientific.com/worldscibooks/10.1142/p276>.
- [26] A. B. Meinel and Meinel, M. P., *Applied solar energy*. Addison Wesley Publishing Co., 1976. Available at: <http://adsabs.harvard.edu/abs/1977STIA...7733445M>
- [27] E.G. Laue, The measurement of solar spectral irradiance at different terrestrial elevations, *Sol. Energy.* 13 (1970) 43–57.
- [28] W. Shockley, H.J. Queisser, Detailed balance limit of efficiency of p-n junction solar cells, *J. Appl. Phys.* 32 (1961) 510–519.
- [29] S. Hilliard, Photocatalyse de décomposition de l'eau : conception et construction d'une cellule photoelectrocatalytique pour la photodissociation de l'eau, Paris 6, 2016, Available at: <http://www.theses.fr/2016PA066034>
- [30] A.J. Nozik, R. Memming, Physical chemistry of semiconductor–liquid interfaces, *J. Phys. Chem.* 100 (1996) 13061–13078.
- [31] Photons in, electrons out: basic principles of PV, published by imperial college press and distributed by world scientific publishing co., (2003) 17–39.
- [32] A. J. Bard, M. A. Fox, Artificial photosynthesis: solar splitting of water to hydrogen and oxygen, *Acc. Chem. Res.* 28 (1995) 141–145.

- [33] W.G. Adams, R.E. Day, V. The action of light on selenium, *Proc. R. Soc. Lond.* **25** (1877) 113–117.
- [34] C.E. Fritts, On a new form of selenium cell, and some electrical discoveries made by its use, *Am. J. Sci. Series 3 Vol. 26* (1883) 465–472.
- [35] A Einstein, Über einen die Erzeugung und Verwandlung des Lichtes betreffenden heuristischen Gesichtspunkt, *Annalen der Physik.* **17** (1905) 132–148.
- [36] R.S. Ohl, Light-sensitive electric device including silicon, US2443542A, 1948. Available at: <https://patents.google.com/patent/US2443542/en>.
- [37] D.M. Chapin, C.S. Fuller, G.L. Pearson, A new silicon p-n junction photocell for converting solar radiation into electrical power, *J. Appl. Phys.* **25** (1954) 676–677.
- [38] Photovoltaic Research | NREL, Available at: <https://www.nrel.gov/pv/>.
- [39] P.V. Kamat, Meeting the clean energy demand: Nanostructure architectures for solar energy conversion, *J. Phys. Chem. C.* **111** (2007) 2834–2860.
- [40] Solar Cells - The Three Generations, Available at: <http://www.top-alternative-energy-sources.com/solar-cells.html>.
- [41] Third generation photovoltaics: ultra-high conversion efficiency at low cost - green - 2001 - progress in photovoltaics: research and applications - Wiley online library, Available at: <https://onlinelibrary.wiley.com/doi/abs/10.1002/pip.360>.
- [42] G.F. Brown, J. Wu, Third generation photovoltaics, *Laser Photonics Rev.* **3** (2009) 394–405.
- [43] K. Kakiage, Y. Aoyama, T. Yano, K. Oya, J. Fujisawa, M. Hanaya, Highly-efficient dye-sensitized solar cells with collaborative sensitization by silyl-anchor and carboxy-anchor dyes, *Chem. Commun.* **51** (2015) 15894–15897.

- [44] W.S. Yang, B.-W. Park, E.H. Jung, N.J. Jeon, Y.C. Kim, D.U. Lee, S.S. Shin, J. Seo, E.K. Kim, J.H. Noh, S.I. Seok, Iodide management in formamidinium-lead-halide-based perovskite layers for efficient solar cells, *Science*. 356 (2017) 1376–1379.
- [45] NREL. Research Cell Efficiency Records. 2018; Available at: <https://www.nrel.gov/pv/assets/images/efficiency-chart.png>.
- [46] H. Tsubomura, M. Matsumura, Y. Nomura, T. Amamiya, Dye sensitised zinc oxide: aqueous electrolyte: platinum photocell, *Nature*. 261 (1976) 402–403.
- [47] R. Memming, Electron transfer processes with excited molecules at semiconductor electrodes, *Prog. Surf. Sci.* 17 (1984) 7–73.
- [48] J. Desilvestro, M. Graetzel, L. Kavan, J. Moser, J. Augustynski, Highly efficient sensitization of titanium dioxide, *J. Am. Chem. Soc.* 107 (1985) 2988–2990.
- [49] F. Willig, R. Eichberger, N.S. Sundaresan, B.A. Parkinson, Experimental time scale of Gerischer's distribution curves for electron-transfer reactions at semiconductor electrodes, *J. Am. Chem. Soc.* 112 (1990) 2702–2707.
- [50] B. O'Regan, M. Grätzel, A low-cost, high-efficiency solar cell based on dye-sensitized colloidal TiO<sub>2</sub> films, *Nature*. 353 (1991) 737-740.
- [51] E. Barraud, Stained glass solar windows for the swiss tech convention center, (2012). Available at: <https://actu.epfl.ch/news/stained-glass-solar-windows-for-the-swiss-tech-con/>.
- [52] C.-P. Lee, C.-A. Lin, T.-C. Wei, M.-L. Tsai, Y. Meng, C.-T. Li, K.-C. Ho, C.-I. Wu, S.-P. Lau, J.-H. He, Economical low-light photovoltaics by using the Pt-free dye-sensitized solar cell with graphene dot/PEDOT:PSS counter electrodes, *Nano Energy*. 18 (2015) 109–117.

- [53] Q. Tang, J. Wang, B. He, P. Yang, Can dye-sensitized solar cells generate electricity in the dark?, *Nano Energy*. 33 (2017) 266–271.
- [54] D. Freeman, N. Sridhar, A study of dye sensitized solar cells under indoor and low level outdoor lighting: comparison to organic and inorganic thin film solar cells and methods to address maximum power point tracking, 26th Eur. Photovolt. Sol. Energy Conf. Exhib. (2011) 232–236.
- [55] DSSC Manufacturing, G24 Power, GCell, G24. Available at: <http://gcell.com/about-g24-power/manufacturing-process>.
- [56] K. Yoo, J.-Y. Kim, J.A. Lee, J.S. Kim, D.-K. Lee, K. Kim, J.Y. Kim, B. Kim, H. Kim, W.M. Kim, J.H. Kim, M.J. Ko, Completely transparent conducting oxide-free and flexible dye-sensitized solar cells fabricated on plastic substrates, *ACS Nano*. 9 (2015) 3760–3771.
- [57] M.J. Yun, S.I. Cha, S.H. Seo, D.Y. Lee, Highly flexible dye-sensitized solar cells produced by sewing textile electrodes on cloth, *Sci. Rep.* 4 (2014) 1-6.
- [58] The beauty of dye-sensitized solar cells, Joshua Gallaway – Electrochemist, Available at: <http://www.joshuagallaway.com/?p=479>.
- [59] J. Khamwannah, Design and fabrication of efficient electrodes for dye sensitized solar cells, UC San Diego, 2015. Available at: <https://escholarship.org/uc/item/5sp6156d>.
- [60] K. Kalyanasundaram, *Dye-sensitized solar cells*, EPFL Press, 2010.
- [61] D.-J. Kwak, B.-H. Moon, D.-K. Lee, C.-S. Park, Y.-M. Sung, Comparison of transparent conductive indium tin oxide, titanium-doped indium oxide, and fluorine-doped tin oxide films for dye-sensitized solar cell application, *J. Electr. Eng. Technol.* 6 (2011) 684–687.
- [62] J.D. Roy-Mayhew, I.A. Aksay, Graphene materials and their use in dye-sensitized solar cells, *Chem. Rev.* 114 (2014) 6323–6348.

- [63] H. Ellis, Characterization of dye-sensitized solar cells : Components for environmentally friendly photovoltaics, Thesis, Uppsala University (2014). Available at: <http://urn.kb.se/resolve?urn=urn:nbn:se:uu:diva-229939>.
- [64] M.K. Nazeeruddin, A. Kay, I. Rodicio, R. Humphry-Baker, E. Mueller, P. Liska, N. Vlachopoulos, M. Graetzel, Conversion of light to electricity by cis-X<sub>2</sub>bis(2,2'-bipyridyl-4,4'-dicarboxylate)ruthenium(II) charge-transfer sensitizers (X = Cl-, Br-, I-, CN-, and SCN-) on nanocrystalline titanium dioxide electrodes, *J. Am. Chem. Soc.* 115 (1993) 6382–6390.
- [65] Dye-sensitised solar cells materials (DSSCs), Ossila. Available at: <https://www.ossila.com/pages/dye-sensitised-solar-cells-dsscs>.
- [66] N. Robertson, Optimizing dyes for dye-sensitized solar cells, *Angew. Chem. Int. Ed Engl.* 45 (2006) 2338–2345.
- [67] M. Ye, X. Wen, M. Wang, J. Iocozzia, N. Zhang, C. Lin, Z. Lin, Recent advances in dye-sensitized solar cells: from photoanodes, sensitizers and electrolytes to counter electrodes, *Mater. Today.* 18 (2015) 155–162.
- [68] S.A. Haque, E. Palomares, B.M. Cho, A.N.M. Green, N. Hirata, D.R. Klug, J.R. Durrant, Charge separation versus recombination in dye-sensitized nanocrystalline solar cells: the minimization of kinetic redundancy, *J. Am. Chem. Soc.* 127 (2005) 3456–3462.
- [69] A.S. Polo, M.K. Itokazu, N.Y. Murakami Iha, Metal complex sensitizers in dye-sensitized solar cells, *Coord. Chem. Rev.* 248 (2004) 1343–1361.
- [70] M.R. Narayan, Review: Dye sensitized solar cells based on natural photosensitizers, *Renew. Sustain. Energy Rev.* 16 (2012) 208–215.

- [71] A Mishra, Markus K. R. Fischer, P Bauerle, Metal-free organic dyes for dye-sensitized solar cells: From structure: Property relationships to design rules, *Angew. Chem. Int . Ed.* 48 (2009) 2474 – 2499.
- [72] T.G. Ulusoy, Development of photoanodes for performance enhanced dye sensitized solar cells, Thesis, Bilkent University, 2015 Available at: <http://repository.bilkent.edu.tr/handle/11693/29005>.
- [73] R. Buscaino, C. Baiocchi, C. Barolo, C. Medana, M. Gratzel, M.K. Nazeeruddin, G. Viscardi, A mass spectrometric analysis of sensitizer solution used for dye-sensitized solar cell, *Inorganica Chim. Acta.* 361 (2008) 798–805.
- [74] I. M. Radwan, Dye Sensitized Solar Cells Based on Natural Dyes Extracted from Plant Roots, Thesis, Islamic University of Gaza, Available at: <http://library.iugaza.edu.ps/thesis/115517.pdf>
- [75] Hauch, A., Characterization of the electrolyte-solid interfaces of dye-sensitized solar cells by means of impedance spectroscopy, in: 2nd World Conf. Photovolt. Sol. Energy Convers. 1998 Proc. Int. Conf. Vol1, 1998: pp. 260–263.
- [76] D. Shi, N. Pootrakulchote, R. Li, J. Guo, Y. Wang, S.M. Zakeeruddin, M. Gratzel, P. Wang, New efficiency records for stable dye-sensitized solar cells with low-volatility and ionic liquid electrolytes, *J. Phys. Chem. C.* 112 (2008) 17046–17050.
- [77] N. Papageorgiou, W.F. Maier, M. Gratzel, An Iodine/Triiodide reduction electrocatalyst for aqueous and organic media, *J. Electrochem. Soc.* 144 (1997) 876–884.
- [78] X. Fang, T. Ma, G. Guan, M. Akiyama, T. Kida, E. Abe, Effect of the thickness of the Pt film coated on a counter electrode on the performance of a dye-sensitized solar cell, *J. Electroanal. Chem.* 570 (2004) 257–263.

- [79] S.-S. Kim, Y.-C. Nah, Y.-Y. Noh, J. Jo, D.-Y. Kim, Electrodeposited Pt for cost-efficient and flexible dye-sensitized solar cells, *Electrochimica Acta*. 51 (2006) 3814–3819.
- [80] S. Thomas, T.G. Deepak, G.S. Anjusree, T.A. Arun, S.V. Nair, A.S. Nair, A review on counter electrode materials in dye-sensitized solar cells, *J. Mater. Chem. A*. 2 (2014) 4474–4490.
- [81] A. Kay, M. Grätzel, Low cost photovoltaic modules based on dye sensitized nanocrystalline titanium dioxide and carbon powder, *Sol. Energy Mater. Sol. Cells*. 44 (1996) 99–117.
- [82] A. Hagfeldt, G. Boschloo, L. Sun, L. Kloo, H. Pettersson, Dye-sensitized solar cells, *Chem. Rev.* 110 (2010) 6595–6663.
- [83] M. Grätzel, Solar energy conversion by dye-sensitized photovoltaic cells, *Inorg. Chem.* 44 (2005) 6841–6851.
- [84] T.G. Deepak, G.S. Anjusree, S. Thomas, T.A. Arun, S.V. Nair, A.S. Nair, A review on materials for light scattering in dye-sensitized solar cells, *RSC Adv.* 4 (2014) 17615–17638.
- [85] A. Hagfeldt, M. Grätzel, Molecular photovoltaics, *Acc. Chem. Res.* 33 (2000) 269–277.
- [86] S.E. Koops, B.C. O'Regan, P.R.F. Barnes, J.R. Durrant, Parameters influencing the efficiency of electron injection in dye-sensitized solar cells, *J. Am. Chem. Soc.* 131 (2009) 4808–4818.
- [87] P. Wang, B. Wenger, R. Humphry-Baker, J.-E. Moser, J. Teuscher, W. Kantelehner, J. Mezger, E.V. Stoyanov, S.M. Zakeeruddin, M. Grätzel, Charge separation and efficient light energy conversion in sensitized mesoscopic solar cells based on binary ionic liquids, *J. Am. Chem. Soc.* 127 (2005) 6850–6856.

- [88] D. Susanti, M. Nafi, H. Purwaningsih, R. Fajarin, G.E. Kusuma, The preparation of dye sensitized solar cell (DSSC) from TiO<sub>2</sub> and tamarillo extract, *Procedia Chem.* 9 (2014) 3–10.
- [89] H.-H. Wang, C. Su, H.-S. Chen, Y.-C. Liu, Y.-W. Hsu, N.-M. Hsu, W.-R. Li, Preparation of nanoporous TiO<sub>2</sub> electrodes for dye-sensitized solar cells, *J. Nanomater.* (2011) 1-7.
- [90] E. Ramasamy, J. Lee, Ordered mesoporous SnO<sub>2</sub>-based photoanodes for high-performance dye-sensitized solar cells, *J. Phys. Chem. C.* 114 (2010) 22032–22037.
- [91] K. Basu, D. Benetti, H. Zhao, L. Jin, F. Vetrone, A. Vomiero, F. Rosei, Enhanced photovoltaic properties in dye sensitized solar cells by surface treatment of SnO<sub>2</sub> photoanodes, *Sci. Rep.* 6 (2016) 1-10.
- [92] A. Birkel, Y.-G. Lee, D. Koll, X.V. Meerbeek, S. Frank, M.J. Choi, Y.S. Kang, K. Char, W. Tremel, Highly efficient and stable dye-sensitized solar cells based on SnO<sub>2</sub> nanocrystals prepared by microwave-assisted synthesis, *Energy Environ. Sci.* 5 (2012) 5392–5400.
- [93] C.Y. Jiang, X.W. Sun, G.Q. Lo, D.L. Kwong, J.X. Wang, Improved dye-sensitized solar cells with a ZnO-nanoflower photoanode, *Appl. Phys. Lett.* 90 (2007) 263501.
- [94] Y.F. Hsu, Y.Y. Xi, C.T. Yip, A.B. Djurišić, W.K. Chan, Dye-sensitized solar cells using ZnO tetrapods, *J. Appl. Phys.* 103 (2008) 083114.
- [95] A. Le Viet, R. Jose, M.V. Reddy, B.V.R. Chowdari, S. Ramakrishna, Nb<sub>2</sub>O<sub>5</sub> photoelectrodes for dye-sensitized solar cells: Choice of the polymorph, *J. Phys. Chem. C.* 114 (2010) 21795–21800.
- [96] H. Zheng, Y. Tachibana, K. Kalantar-zadeh, Dye-sensitized solar cells based on WO<sub>3</sub>, *Langmuir.* 26 (2010) 19148–19152.

- [97] B. Tan, E. Toman, Y. Li, Y. Wu, Zinc stannate ( $Zn_2SnO_4$ ) dye-sensitized solar cells, *J. Am. Chem. Soc.* 129 (2007) 4162–4163.
- [98] A. Kumar, R. Jose, K. Fujihara, J. Wang, S. Ramakrishna, Structural and optical properties of electrospun  $TiO_2$  nanofibers, *Chem. Mater.* 19 (2007) 6536–6542.
- [99] JC Jamieson, Bart Olinger, F Dacheille, PY Simons, R Roy. Pressure temperature studies of anatase, brookite rutile and  $TiO_2$  (ii): A discussion, University of Chicago 1969, Available at: [http://www.minsocam.org/ammin/AM54/AM54\\_1477.pdf](http://www.minsocam.org/ammin/AM54/AM54_1477.pdf)
- [100] S.J. Smith, R. Stevens, S. Liu, G. Li, A. Navrotsky, J. Boerio-Goates, B.F. Woodfield, Heat capacities and thermodynamic functions of  $TiO_2$  anatase and rutile: Analysis of phase stability, *Am. Mineral.* 94 (2009) 236–243.
- [101] C.N. Sao, Dye-sensitized solar cells based on perylene derivatives, PhD Thesis, University of Kassel (Germany), 2009, Available at: <https://kobra.bibliothek.uni-kassel.de/bitstream/urn:nbn:de:hebis:34-2009110330833/3/Noumissing-Thesis.pdf>
- [102] A. Di Paola, M. Bellardita, L. Palmisano, Brookite, the Least Known  $TiO_2$  Photocatalyst, *Catalysts.* 3 (2013) 36–73.
- [103] T. Ma, T. Kida, M. Akiyama, K. Inoue, S. Tsunematsu, K. Yao, H. Noma, E. Abe, Preparation and properties of nanostructured  $TiO_2$  electrode by a polymer organic-medium screen-printing technique, *Electrochem. Commun.* 5 (2003) 369–372.
- [104] R. Knödler, J. Sopka, F. Harbach, H.W. Grünling, Photoelectrochemical cells based on dye sensitized colloidal  $TiO_2$  layers, *Sol. Energy Mater. Sol. Cells.* 30 (1993) 277–281.
- [105] H.-Y. Chen, D.-B. Kuang, C.-Y. Su, Hierarchically micro/nanostructured photoanode materials for dye-sensitized solar cells, *J. Mater. Chem.* 22 (2012) 15475–15489.

- [106] T.P. Chou, Q. Zhang, B. Russo, G.E. Fryxell, G. Cao, Titania particle size effect on the overall performance of dye-sensitized solar cells, *J. Phys. Chem. C*. 111 (2007) 6296–6302.
- [107] P. Wang, S.M. Zakeeruddin, J.-E. Moser, M. Grätzel, A new ionic liquid electrolyte enhances the conversion efficiency of dye-sensitized solar cells, *J. Phys. Chem. B*. 107 (2003) 13280–13285.
- [108] D. Kuang, S. Ito, B. Wenger, C. Klein, J.-E. Moser, R. Humphry-Baker, S.M. Zakeeruddin, M. Grätzel, High molar extinction coefficient heteroleptic ruthenium complexes for thin film dye-sensitized solar cells, *J. Am. Chem. Soc.* 128 (2006) 4146–4154.
- [109] M.K. Nazeeruddin, F. De Angelis, S. Fantacci, A. Selloni, G. Viscardi, P. Liska, S. Ito, B. Takeru, M. Grätzel, Combined experimental and DFT-TDDFT computational study of photoelectrochemical cell ruthenium sensitizers, *J. Am. Chem. Soc.* 127 (2005) 16835–16847.
- [110] S. Ito, P. Chen, P. Comte, M.K. Nazeeruddin, P. Liska, P. Péchy, M. Grätzel, Fabrication of screen-printing pastes from TiO<sub>2</sub> powders for dye-sensitised solar cells, *Prog. Photovolt. Res. Appl.* 15 (2007) 603–612.
- [111] S. Hore, C. Vetter, R. Kern, H. Smit, A. Hinsch, Influence of scattering layers on efficiency of dye-sensitized solar cells, *Sol. Energy Mater. Sol. Cells*. 90 (2006) 1176–1188.
- [112] Q. Zhang, T.P. Chou, B. Russo, S.A. Jenekhe, G. Cao, Aggregation of ZnO nanocrystallites for high conversion efficiency in dye-sensitized solar cells, *Angew. Chem. Int. Ed Engl.* 47 (2008) 2402–2406.
- [113] Y.-F. Wang, J.-W. Li, Y.-F. Hou, X.-Y. Yu, C.-Y. Su, D.-B. Kuang, Hierarchical tin oxide octahedra for highly efficient dye-sensitized solar cells, *Chem. Eur. J.* 16 (2010) 8620 – 8625.

- [114] J. Bisquert, A. Zaban, M. Greenshtein, I. Mora-Seró, Determination of rate constants for charge transfer and the distribution of semiconductor and electrolyte electronic energy levels in dye-sensitized solar cells by open-circuit photovoltage decay method, *J. Am. Chem. Soc.* 126 (2004) 13550–13559.
- [115] M. Law, L.E. Greene, J.C. Johnson, R. Saykally, P. Yang, Nanowire dye-sensitized solar cells, *Nat. Mater.* 4 (2005) 455–459.
- [116] G. K. Mor, K Shankar, M Paulose, O. K. Varghese, and C. A. Grimes, Use of highly-ordered TiO<sub>2</sub> nanotube arrays in dye-sensitized solar cells, *Nano Lett.* 6 (2006) 215–218.
- [117] J.R. Jennings, A. Ghicov, L.M. Peter, P. Schmuki, A.B. Walker, Dye-sensitized solar cells based on oriented TiO<sub>2</sub> nanotube arrays: Transport, trapping, and transfer of electrons, *J. Am. Chem. Soc.* 130 (2008) 13364–13372.
- [118] T.P. Chou, Q. Zhang, G.E. Fryxell, G.Z. Cao, Hierarchically structured ZnO film for dye-sensitized solar cells with enhanced energy conversion efficiency, *Adv. Mater.* 19 (2007) 2588–2592.
- [119] Q. Zhang, T.P. Chou, B. Russo, S.A. Jenekhe, G. Cao, Polydisperse Aggregates of ZnO Nanocrystallites: A method for energy-conversion-efficiency enhancement in dye-sensitized solar cells, *Adv. Funct. Mater.* 18 (2008) 1654–1660.
- [120] Y. Bai, H. Yu, Z. Li, R. Amal, G.Q. (Max) Lu, L. Wang, In situ growth of a ZnO nanowire network within a TiO<sub>2</sub> nanoparticle film for enhanced dye-sensitized solar cell performance, *Adv. Mater.* 24 (2012) 5850–5856.
- [121] K.T. Dembele, G.S. Selopal, R. Milan, C. Trudeau, D. Benetti, A. Soudi, M.M. Natile, G. Sberveglieri, S. Cloutier, I. Concina, F. Rosei, A. Vomiero, Graphene below the percolation threshold in TiO<sub>2</sub> for dye-sensitized solar cells, *J. Mater. Chem. A.* 3 (2015) 2580–2588.

- [122] T. Sawatsuk, A. Chindaduang, C. Sae-kung, S. Pratontep, G. Tumcharern, Dye-sensitized solar cells based on TiO<sub>2</sub>-MWCNTs composite electrodes: Performance improvement and their mechanisms, *Diam. Relat. Mater.* 18 (2009) 524–527.
- [123] K.T. Dembele, R. Nechache, L. Nikolova, A. Vomiero, C. Santato, S. Licoccia, F. Rosei, Effect of multi-walled carbon nanotubes on the stability of dye sensitized solar cells, *J. Power Sources.* 233 (2013) 93–97.
- [124] C.-Y. Yen, Y.-F. Lin, S.-H. Liao, C.-C. Weng, C.-C. Huang, Y.-H. Hsiao, C.-C.M. Ma, M.-C. Chang, H. Shao, M.-C. Tsai, C.-K. Hsieh, C.-H. Tsai, F.-B. Weng, Preparation and properties of a carbon nanotube-based nanocomposite photoanode for dye-sensitized solar cells, *Nanotechnology.* 19 (2008) 375305.
- [125] J. Durantini, P.P. Boix, M. Gervaldo, G.M. Morales, L. Otero, J. Bisquert, E.M. Barea, Photocurrent enhancement in dye-sensitized photovoltaic devices with titania–graphene composite electrodes, *J. Electroanal. Chem.* 683 (2012) 43–46.
- [126] N. Yang, J. Zhai, D. Wang, Y. Chen, L. Jiang, Two-dimensional graphene bridges enhanced photoinduced charge transport in dye-sensitized solar cells, *ACS Nano.* 4 (2010) 887–894.
- [127] X Liu, J Fang, Y Liu, T Lin, Progress in nanostructured photoanodes for dye-sensitized solar cells, *Front. Mater. Sci.* 10 (2016) 225–237.
- [128] M. Liu, J. Yang, S. Feng, H. Zhu, J. Zhang, G. Li, J. Peng, Composite photoanodes of Zn<sub>2</sub>SnO<sub>4</sub> nanoparticles modified SnO<sub>2</sub> hierarchical microspheres for dye-sensitized solar cells, *Mater. Lett.* 76 (2012) 215–218.
- [129] A. Kay, M. Grätzel, Dye-sensitized core–shell nanocrystals: Improved efficiency of mesoporous tin oxide electrodes coated with a thin layer of an insulating oxide, *Chem. Mater.* 14 (2002) 2930–2935.

- [130] M. Shimura, K. Shakushiro, Y. Shimura, Photo-electrochemical solar cells with a SnO<sub>2</sub>-liquid junction sensitized with highly concentrated dyes, *J. Appl. Electrochem.* 16 (1986) 683–692.
- [131] K. Itoh, M. Nakao, K. Honda, Influence of donor density of semiconductor substrate on quantum yield of dye-sensitized photocurrent in the rhodamine B/SnO<sub>2</sub> system, *J. Electroanal. Chem. Interfacial Electrochem.* 178 (1984) 329–332.
- [132] Q. Wali, A. Fakharuddin, R. Jose, Tin oxide as a photoanode for dye-sensitised solar cells: Current progress and future challenges, *J. Power Sources.* 293 (2015) 1039–1052.
- [133] E. Hendry, F. Wang, J. Shan, T.F. Heinz, M. Bonn, Electron transport in TiO<sub>2</sub> probed by THz time-domain spectroscopy, *Phys. Rev. B.* 69 (2004) 081101.
- [134] M. Zúkalová, A. Zúkal, L. Kavan, M.K. Nazeeruddin, P. Liska, M. Grätzel, Organized mesoporous TiO<sub>2</sub> films exhibiting greatly enhanced performance in dye-sensitized solar cells, *Nano Lett.* 5 (2005) 1789–1792.
- [135] P. Tiwana, P. Docampo, M.B. Johnston, H.J. Snaith, L.M. Herz, Electron mobility and injection dynamics in mesoporous ZnO, SnO<sub>2</sub>, and TiO<sub>2</sub> films used in dye-sensitized solar cells, *ACS Nano.* 5 (2011) 5158–5166.
- [136] E. Hendry, M. Koeberg, B. O'Regan, M. Bonn, Local field effects on electron transport in nanostructured TiO<sub>2</sub> revealed by terahertz spectroscopy, *Nano Lett.* 6 (2006) 755–759.
- [137] J. Robertson, Electronic structure of SnS<sub>2</sub>, SnSe<sub>2</sub>, CdI<sub>2</sub> and PbI<sub>2</sub>, *J. Phys. C Solid State Phys.* 12 (1979) 4753.
- [138] K.J. Button, C.G. Fonstad, W. Dreybrodt, Determination of the electron masses in stannic oxide by submillimeter cyclotron resonance, *Phys. Rev. B.* 4 (1971) 4539–4542.

- [139] R. Summitt, N.F. Borrelli, Infrared absorption in single crystal stannic oxide, *J. Phys. Chem. Solids.* 26 (1965) 921–925.
- [140] C. Kormann, D.W. Bahnemann, M.R. Hoffmann, Preparation and characterization of quantum-size titanium dioxide, *J. Phys. Chem.* 92 (1988) 5196–5201.
- [141] K. Tennakone, P.K.M. Bandaranayake, P.V.V. Jayaweera, A. Konno, G.R.R.A. Kumara, Dye-sensitized composite semiconductor nanostructures, *Phys. E Low-Dimens. Syst. Nanostructures.* 14 (2002) 190–196.
- [142] R.G. Breckenridge, W.R. Hosler, Electrical properties of titanium dioxide semiconductors, *Phys. Rev.* 91 (1953) 793–802.
- [143] K. Tennakone, P.V.V. Jayaweera, P.K.M. Bandaranayake, Dye-sensitized photoelectrochemical and solid-state solar cells: charge separation, transport and recombination mechanisms, *J. Photochem. Photobiol. Chem.* 158 (2003) 125–130.
- [144] S. Gubbala, H.B. Russell, H. Shah, B. Deb, J. Jasinski, H. Rypkema, M.K. Sunkara, Surface properties of SnO<sub>2</sub> nanowires for enhanced performance with dye-sensitized solar cells, *Energy Environ. Sci.* 2 (2009) 1302–1309.
- [145] S. Dutta, A review on production, storage of hydrogen and its utilization as an energy resource, *J. Ind. Eng. Chem.* 20 (2014) 1148–1156.
- [146] D.T. Boyles, *Bio-energy: technology, thermodynamics, and costs*, E. Horwood ;, Chichester, West Sussex :, 1984.
- [147] Introduction to hydrogen technology, Wiley.Com, Available at: <https://www.wiley.com/en-ca/Introduction+to+Hydrogen+Technology+p9780471779858>.

- [148] G Collodi, F Wheeler, Hydrogen production via steam reforming with CO<sub>2</sub> capture-semantic scholar, Available at: <http://paper/Hydrogen-Production-via-Steam-Reforming-with-CO-2-Wheeler/4bce0493c6937d4a8e5a844e75e51d5471182a04>.
- [149] N. Muradov, 17 - Low-carbon production of hydrogen from fossil fuels, in: *Compend. Hydrog. Energy*, Woodhead Publishing, Oxford, (2015) 489–522.
- [150] S. Koumi Ngoh, D. Njomo, An overview of hydrogen gas production from solar energy, *Renew. Sustain. Energy Rev.* 16 (2012) 6782–6792.
- [151] S.Z. Baykara, Hydrogen production by direct solar thermal decomposition of water, possibilities for improvement of process efficiency, *Int. J. Hydrog. Energy.* 14 (2004) 1451–1458.
- [152] Z. Wang, R.R. Roberts, G.F. Naterer, K.S. Gabriel, Comparison of thermochemical, electrolytic, photoelectrolytic and photochemical solar-to-hydrogen production technologies, *Int. J. Hydrog. Energy.* 37 (2012) 16287–16301.
- [153] P. Haueter, T. Seitz, A. Steinfeld, A new high-flux solar furnace for high-temperature thermochemical research, *J. Sol. Energy Eng.* 121 (1999) 77–80.
- [154] D. Riveros-Rosas, J. Herrera-Vázquez, C.A. Pérez-Rábago, C.A. Arancibia-Bulnes, S. Vázquez-Montiel, M. Sánchez-González, F. Granados-Agustín, O.A. Jaramillo, C.A. Estrada, Optical design of a high radiative flux solar furnace for Mexico, *Sol. Energy.* 84 (2010) 792–800.
- [155] A. Fujishima, K. Honda, Electrochemical photolysis of water at a semiconductor electrode, *Nature.* 238 (1972) 37–38.
- [156] X. Chen, S. Shen, L. Guo, S.S. Mao, Semiconductor-based photocatalytic hydrogen generation, *Chem. Rev.* 110 (2010) 6503–6570.

- [157] Q. Ding, B. Song, P. Xu, S. Jin, Efficient Electrocatalytic and photoelectrochemical hydrogen generation using MoS<sub>2</sub> and related compounds, *Chem.* 1 (2016) 699–726.
- [158] R. Abe, Recent progress on photocatalytic and photoelectrochemical water splitting under visible light irradiation, *J. Photochem. Photobiol. C Photochem. Rev.* 11 (2010) 179–209.
- [159] L. Jin, B. AlOtaibi, D. Benetti, S. Li, H. Zhao, Z. Mi, A. Vomiero, F. Rosei, Near-infrared colloidal quantum dots for efficient and durable photoelectrochemical solar-driven hydrogen production, *Adv. Sci.* 3 (2016) 1-7.
- [160] R. Adhikari, L. Jin, F. Navarro-Pardo, D. Benetti, B. AlOtaibi, S. Vanka, H. Zhao, Z. Mi, A. Vomiero, F. Rosei, High efficiency, Pt-free photoelectrochemical cells for solar hydrogen generation based on “giant” quantum dots, *Nano Energy.* 27 (2016) 265–274.
- [161] S.K. Pathak, A. Abate, P. Ruckdeschel, B. Roose, K.C. Gödel, Y. Vaynzof, A. Santhala, S.-I. Watanabe, D.J. Hollman, N. Noel, A. Sepe, U. Wiesner, R. Friend, H.J. Snaith, U. Steiner, Performance and stability enhancement of dye-sensitized and perovskite solar cells by Al doping of TiO<sub>2</sub>, *Adv. Funct. Mater.* 24 (2014) 6046–6055.
- [162] A.N.M. Green, E. Palomares, S.A. Haque, J.M. Kroon, J.R. Durrant, Charge transport versus recombination in dye-sensitized solar cells employing nanocrystalline TiO<sub>2</sub> and SnO<sub>2</sub> films, *J. Phys. Chem. B.* 109 (2005) 12525–12533.
- [163] J. Qian, P. Liu, Y. Xiao, Y. Jiang, Y. Cao, X. Ai, H. Yang, TiO<sub>2</sub>-coated multilayered SnO<sub>2</sub> hollow microspheres for dye-sensitized solar cells, *Adv. Mater.* 21 (n.d.) 3663–3667.
- [164] K. Zhu, E.A. Schiff, N.-G. Park, J. van de Lagemaat, A.J. Frank, Determining the locus for photocarrier recombination in dye-sensitized solar cells, *Appl. Phys. Lett.* 80 (2002) 685–687.

- [165] F. Fabregat-Santiago, J. Bisquert, G. Garcia-Belmonte, G. Boschloo, A. Hagfeldt, Influence of electrolyte in transport and recombination in dye-sensitized solar cells studied by impedance spectroscopy, *Sol. Energy Mater. Sol. Cells*. 87 (2005) 117–131.
- [166] Y.J. Kim, K.H. Kim, P. Kang, H.J. Kim, Y.S. Choi, W.I. Lee, Effect of layer-by-layer assembled SnO<sub>2</sub> interfacial layers in photovoltaic properties of dye-sensitized solar cells, *Langmuir*. 28 (2012) 10620–10626.
- [167] Q. Wang, S. Ito, M. Grätzel, F. Fabregat-Santiago, I. Mora-Seró, J. Bisquert, T. Bessho, H. Imai, Characteristics of high efficiency dye-sensitized solar cells, *J. Phys. Chem. B*. 110 (2006) 25210–25221.
- [168] F. Fabregat-Santiago, G. Garcia-Belmonte, I. Mora-Seró, J. Bisquert, Characterization of nanostructured hybrid and organic solar cells by impedance spectroscopy, *Phys. Chem. Chem. Phys.* 13 (2011) 9083–9118.
- [169] S. Ito, P. Liska, P. Comte, R. Charvet, P. Péchy, U. Bach, L. Schmidt-Mende, S.M. Zakeeruddin, A. Kay, M.K. Nazeeruddin, M. Grätzel, Control of dark current in photoelectrochemical (TiO<sub>2</sub>/I<sup>-</sup>-I<sub>3</sub><sup>-</sup>) and dye-sensitized solar cells, *Chem. Commun.* 0 (2005) 4351–4353.
- [170] S. Gubbala, V. Chakrapani, V. Kumar, M.K. Sunkara, Band-edge engineered hybrid structures for dye-sensitized solar cells based on SnO<sub>2</sub> nanowires, *Adv. Funct. Mater.* 18 (2008) 2411–2418.
- [171] H.J. Snaith, C. Ducati, SnO<sub>2</sub>-Based dye-sensitized hybrid solar cells exhibiting near unity absorbed photon-to-electron conversion efficiency, *Nano Lett.* 10 (2010) 1259–1265.
- [172] L. Zhaoyue, P. Kai, Z. Qinglin, L. Min, J. Ruokun, L. Qiang, W. Dejun, B. Yubai, L. Tiejin, The performances of the mercurochrome-sensitized composite semiconductor

- photoelectrochemical cells based on  $\text{TiO}_2/\text{SnO}_2$  and  $\text{ZnO}/\text{SnO}_2$  composites, *Thin Solid Films*. 468 (2004) 291–297.
- [173] D. Gust, T.A. Moore, A.L. Moore, Mimicking photosynthetic solar energy transduction, *Acc. Chem. Res.* 34 (2001) 40–48.
- [174] K.T. Dembele, G.S. Selopal, C. Soldano, R. Nechache, J.C. Rimada, I. Concina, G. Sberveglieri, F. Rosei, A. Vomiero, Hybrid carbon nanotubes– $\text{TiO}_2$  photoanodes for high efficiency dye-sensitized solar cells, *J. Phys. Chem. C*. 117 (2013) 14510–14517.
- [175] R. van de Krol, Y. Liang, J. Schoonman, Solar hydrogen production with nanostructured metal oxides, *J. Mater. Chem.* 18 (2008) 2311–2320.
- [176] G. Shang, J. Wu, S. Tang, M. Huang, Z. Lan, Y. Li, J. Zhao, X. Zhang, Preparation of hierarchical tin oxide microspheres and their application in dye-sensitized solar cells, *J. Mater. Chem.* 22 (2012) 25335–25339.
- [177] L. Xd, Z. Zm, C. Ll, L. Zp, C. Jl, N. W, X. Eq, W. B, Cadmium sulfide quantum dots sensitized tin dioxide-titanium dioxide heterojunction for efficient photoelectrochemical hydrogen production, *J. Power Sources*. 269 (2014) 866–872.
- [178] Z. Zhang, C. Gao, Z. Wu, W. Han, Y. Wang, W. Fu, X. Li, E. Xie, Toward efficient photoelectrochemical water-splitting by using screw-like  $\text{SnO}_2$  nanostructures as photoanode after being decorated with CdS quantum dots, *Nano Energy*. 19 (2016) 318–327.
- [179] J. Yu, Y. Wang, W. Xiao, Enhanced photoelectrocatalytic performance of  $\text{SnO}_2/\text{TiO}_2$  rutile composite films, *J. Mater. Chem. A*. 1 (2013) 10727–10735.

- [180] P. Docampo, J.M. Ball, M. Darwich, G.E. Eperon, H.J. Snaith, Efficient organometal trihalide perovskite planar-heterojunction solar cells on flexible polymer substrates, *Nat. Commun.* 4 (2013) 1-6.
- [181] P.M. Sommeling, B.C. O'Regan, R.R. Haswell, H.J.P. Smit, N.J. Bakker, J.J.T. Smits, J.M. Kroon, J.A.M. van Roosmalen, Influence of a  $\text{TiCl}_4$  post-treatment on nanocrystalline  $\text{TiO}_2$  films in dye-sensitized solar cells, *J. Phys. Chem. B.* 110 (2006) 19191–19197.
- [182] B.O. Dabbousi, J. Rodriguez-Viejo, F.V. Mikulec, J.R. Heine, H. Mattoussi, R. Ober, K.F. Jensen, M.G. Bawendi, (CdSe)ZnS Core-shell quantum dots: synthesis and characterization of a size series of highly luminescent nanocrystallites, *J. Phys. Chem. B.* 101 (1997) 9463–9475.
- [183] Y. Ghosh, B.D. Mangum, J.L. Casson, D.J. Williams, H. Htoon, J.A. Hollingsworth, New Insights into the Complexities of Shell Growth and the Strong Influence of Particle Volume in Nonblinking “Giant” Core/Shell Nanocrystal Quantum Dots, *J. Am. Chem. Soc.* 134 (2012) 9634–9643.
- [184] L. Jin, H. Zhao, D. Ma, A. Vomiero, F. Rosei, Dynamics of semiconducting nanocrystal uptake into mesoporous  $\text{TiO}_2$  thick films by electrophoretic deposition, *J. Mater. Chem. A.* 3 (2014) 847–856.
- [185] X-Ray powder diffraction spectrometer - image and chemical analysis laboratory | Montana State University, Available at: <http://www.physics.montana.edu/ical/instrumentation/xrd.html>.
- [186] FTIR and UV-vis accessories, ATR Specular and diffuse reflectance, integrating spheres, microscopes and transmission, Available at: [http://www.piketech.com/Catalog Downloads.html](http://www.piketech.com/CatalogDownloads.html).

- [187] A. Escobedo Morales, E. Sánchez Mora, U. Pal, Use of diffuse reflectance spectroscopy for optical characterization of un-supported nanostructures, *Rev. Mex. Fis. Suppl.* 53 (2007) 18–22.
- [188] H. Bubert, J.C. Rivière, W.S.M. Werner, X-Ray photoelectron spectroscopy (XPS), in: *Surf. Thin Film Anal.*, Wiley-Blackwell, (2011) 7–41.
- [189] Shodhganga : a reservoir of Indian theses @ INFLIBNET, Available at: <http://shodhganga.inflibnet.ac.in/>.
- [190] H. McDaniel, N. Fuke, N.S. Makarov, J.M. Pietryga, V.I. Klimov, An integrated approach to realizing high-performance liquid-junction quantum dot sensitized solar cells, *Nat. Commun.* 4 (2013) 1-10.
- [191] What is Transient Spectroscopy? Available at: <http://www.andor.com/learning-academy/transient-spectroscopy-an-introduction-to-pump-probe-spectroscopy>.
- [192] S. Sarker, A.J.S. Ahammad, H.W. Seo, D.M. Kim, Electrochemical impedance spectra of dye-sensitized solar cells: fundamentals and spreadsheet calculation, *Int. J. Photoenergy.* (2014) 1-17.
- [193] R. Trevisan, P. Rodenas, V. Gonzalez-Pedro, C. Sima, R.S. Sanchez, E.M. Barea, I. Mora-Sero, F. Fabregat-Santiago, S. Gimenez, Harnessing infrared photons for photoelectrochemical hydrogen generation. A PbS quantum dot based “Quasi-artificial leaf,” *J. Phys. Chem. Lett.* 4 (2013) 141–146.

# Appendix: Résumé

## L'introduction

Tout autour du monde, motivé par la pollution de l'environnement, l'augmentation de la demande énergétique et de la disponibilité limitée des sources d'énergie traditionnelle telles que le charbon, le pétrole et les combustibles fossiles, La prise de conscience concernant les sources d'énergie renouvelable a augmenté considérablement. Au cours des cinq dernières décennies, la demande d'énergie dans le monde a augmenté très rapidement la consommation mondiale d'énergie passant ainsi du simple au double. [1] Pour répondre à la demande croissante d'énergie, tout en minimisant les dommages fait à l'environnement, nous devons utiliser des sources d'énergie propre, durable et renouvelable. [7] Parmi toutes les sources d'énergie renouvelable disponibles, l'énergie solaire est la plus abondante. Le soleil émet de l'énergie à un taux colossal de  $3,8 \times 10^{23}$  kW, [13] et la terre, étant située à environ 150 millions de km du soleil, en intercepte près de  $1,8 \times 10^{14}$  kW. [13] Le phénomène de transformer la lumière en énergie électrique a été initialement observé en 1839 par le scientifique français Alexandre Edmond Becquerel. Il a observé que l'exposition à la lumière d'une électrode en platine et une en chlorure d'argent dans un électrolyte produisait une petite quantité de courant électrique. [15] La première cellule solaire a été mise au point par les laboratoires Bell en 1954, mettant en œuvre une jonction p-n de silicium, qui a atteint un rendement d'environ 6%. [37] La technologie PV peut être catégorisée en trois générations. La première génération de photovoltaïque repose principalement sur le silicium cristallin. Bien que le silicium soit abondamment présent dans la nature, la purification et la fabrication de silicium sans défaut consomment beaucoup d'énergie, ce qui augmente le coût par énergie produite. [39] Bien que cette classe de cellules solaires puisse atteindre un rendement élevé, proche de la limite de Shockley-Queisser, [28] les coûts de production élevés exigent de travailler avec une nouvelle technologie

plus rentable. La deuxième génération de photovoltaïques constitue principalement des technologies à couches minces telles que le cadmium tellure (CdTe), le cuivre indium gallium séléniure (CIGS) et le silicium amorphe [40] fabriqués sur des substrats en verre ou en céramique, ce qui est moins chers, réduisant ainsi considérablement les coûts de production. En revanche, l'efficacité de puissance de conversion (PCE) de ces photovoltaïques est relativement faible. [39] La troisième génération a été introduite pour combiner efficacement les avantages des deux premiers générations de photovoltaïques. [41,42] Les technologies photovoltaïques de troisième génération utilisent des technologies émergentes telles que les cellules solaires à pigment photosensible (DSSC) et les cellules photovoltaïques à pérovskite, [43,44] dont les excitons photogénérés et le transport de charges sont réalisée séparément dans des semi-conducteurs de pureté inférieure, réduisant ainsi leurs coûts de production. Les cellules photovoltaïques à pigment photosensible sont une technologie photovoltaïque de troisième génération de perspectives prometteuses qui peuvent surpasser le rendement des cellules photovoltaïques traditionnelles dans des conditions de faible éclairage intérieure ou en lumière solaire diffuse et est moins dépendant de l'angle d'incidence de la lumière (AOI) que les cellules solaires conventionnelles. [52-54]

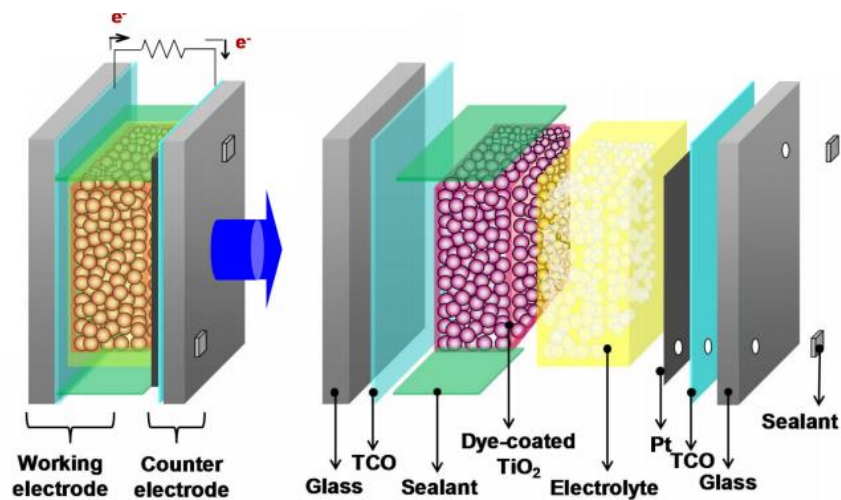


Figure A1: Diagramme schématique [58] d'un DSSC typique, les composants individuels sont montrés en détails à droite

Un DSSC typique est construit par un substrat d'oxyde conducteur transparent, un film mince de semi-conducteur mésoporeux à large bande interdite (également appelé photoanode), un photosensibilisateur (des molécules de colorant adsorbées sur la photoanode mésoporeuse), un électrolyte en couple redox, et enfin une contre-électrode (CE) pour compléter la cellule. La photoanode est le composant le plus important d'un DSSC, qui joue un rôle crucial dans la maximisation du PCE d'un DSSC. La photoanode nécessite une grande surface pour pouvoir ancrer une grande quantité de molécules de colorant et ainsi générer suffisamment de photoélectrons pour contribuer à la densité de photocourant et donc augmenter le PCE global du dispositif. [50,64] La bande de conduction (CB) du matériau photoanode doit être énergétiquement à une position légèrement inférieure à la plus basse orbitale moléculaire inoccupée (LUMO) du colorant pour minimiser les pertes potentielles énergétiques. [60] La photoanode doit également posséder une grande mobilité d'électrons pour assurer un transport d'électrons efficace puisque le transport de charge dans un DSSC se produit via un procédé de diffusion lente caractérisée par des pièges à électrons. Les DSSCs basé sur des photoanodes de  $\text{TiO}_2$  ont atteint les rendements les plus élevés à ce jour, essentiellement en raison de la faible surtension par rapport aux colorants couramment utilisés et du rapport surface / volume élevé.

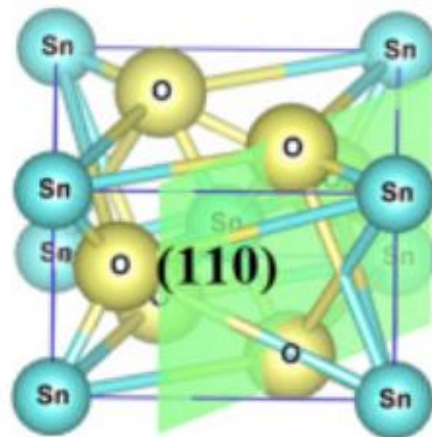


Figure A2: Schéma de la structure cristalline rutile tétragonale de  $\text{SnO}_2$  [130], plan cristallin (110) représenté en vert.

Le chargement supérieur de colorant dans l'anatase TiO<sub>2</sub> et ZnO est le résultat du point isoélectrique élevé de TiO<sub>2</sub> (pH 6-7) et ZnO (pH ~ 9) par rapport au point isoélectrique faible de SnO<sub>2</sub> (pH 4-5). Ceci facilite une densité de photocourant plus élevée dans TiO<sub>2</sub> et ZnO. [128,129] Cependant, le SnO<sub>2</sub> a été utilisé dans la sensibilisation des colorants depuis le début des années 1980. [130-132] Comme le transport de charge dans le DSSC est attribuable par la diffusion, la mobilité électronique est l'une des caractéristiques clés qui définit l'efficacité de la percolation des électrons.

L'une des propriétés les plus attrayantes de SnO<sub>2</sub> est la grande mobilité des électrons par rapport aux autres semi-conducteurs largement utilisés dans les DSSCs. La mobilité des électrons ( $\mu_e$ ) de SnO<sub>2</sub> est de  $\sim 250 \text{ cm}^2 \text{ V}^{-1} \text{ s}^{-1}$  pour les monocristaux et de  $\sim 150 \text{ cm}^2 \text{ V}^{-1} \text{ s}^{-1}$  pour les nanostructures, ce qui est de plusieurs ordres de grandeur supérieur à TiO<sub>2</sub>, le choix alternative préféré, qui a une mobilité d'électrons  $\sim 1 \text{ cm}^2 \text{ V}^{-1} \text{ s}^{-1}$  en monocristaux et  $\sim 10^{-5} \text{ cm}^2 \text{ V}^{-1} \text{ s}^{-1}$  en nanostructures. [132-136] La mobilité d'électrons peut être estimée par  $\mu_e = e \frac{\tau_s}{m_e}$ , où  $e$  est la charge électronique,  $\tau_s$  est la fréquence de collision et  $m_e$  est la masse effective. [132] La mobilité d'électrons élevée de SnO<sub>2</sub> est obtenue grâce à sa faible masse effective,  $m_e \sim 0,17-0,30 m_0$  [137-139] alors que dans le cas du TiO<sub>2</sub> la masse effective élevée  $\sim 1-50 m_0$  [140-143] limite la mobilité d'électrons. Le diagramme schématique de la structure cristalline rutile tétragonale de SnO<sub>2</sub> est démontré sur la Fig. A2. Dans la structure cristalline de SnO<sub>2</sub>, chaque atome de Sn est placé au centre d'un octaèdre entouré de six atomes d'oxygène. [132, 144] Les paramètres de maille de la structure rutile sont  $a = b = 4,737 \text{ \AA}$ ,  $c = 3,18 \text{ \AA}$ . Le plan cristallin (110) avec un espacement interplanaire,  $d_{110} = 3,33470 \text{ \AA}$ , est représenté sur la Fig. A2, qui a le pic le plus proéminent de SnO<sub>2</sub> rutile tétragonal. Dans notre thèse, des dispositifs avec structure rutile SnO<sub>2</sub> ont été largement étudiés.

L'hydrogène est une ressource énergétique non carbonée [145] qui a le potentiel de remplacer les combustibles fossiles qui produisent le gaz à effet de serre car le seul sous-produit de sa combustion est l'eau. De plus, l'hydrogène a une énergie spécifique (énergie par unité de poids) meilleure que toutes autres sources d'énergie chimique [146] et conduit à la recherche d'une économie entraînée par l'hydrogène. Dans l'industrie, la production de masse d'hydrogène est habituellement effectuée par le reformage à la vapeur du méthane ou du gaz naturel, qui est actuellement le plus rentable. [147] Ce processus implique une réaction endothermique, atteignant des températures supérieures à 1000 °C. Cette réaction divise les molécules de méthane en présence de vapeur et le monoxyde de carbone (CO) et les molécules de H<sub>2</sub> sont alors formées. L'inconvénient majeur de la fabrication industrielle actuelle de H<sub>2</sub> est qu'elle dépend des combustibles fossiles. Le reformage à la vapeur du méthane, l'un des plus propres procédés de génération de H<sub>2</sub>, produit environ 10 kg de CO<sub>2</sub> par kg de H<sub>2</sub>. La production de H<sub>2</sub> à partir de l'énergie solaire est considérée comme la solution ultime pour l'énergie durable [151] car elle n'émet pas de gaz à effet de serre et elle utilise les deux ressources les plus abondantes et les plus facilement disponibles: la lumière et l'eau. En 1972, les scientifiques Fujishima et Honda ont construit une cellule photoélectrochimique [155] qui décomposait l'eau en hydrogène et en oxygène. Le TiO<sub>2</sub> a été utilisé comme photoanode et le platine, comme la cathode, a été immergé dans l'eau. Dans leur travail de pionnier, ils ont observé que lorsqu'une photoanode de TiO<sub>2</sub> était éclairée par la lumière ultraviolette (UV), un dégagement d'oxygène se produisait à la photoanode de TiO<sub>2</sub> et de H<sub>2</sub> à la cathode. Depuis lors, des efforts considérables ont été réalisés pour générer de l'hydrogène en mettant en œuvre des cellules PEC en utilisant des semi-conducteurs à large bande interdite. Les semi-conducteurs à large bande interdite comme le TiO<sub>2</sub> sont exceptionnellement performants dans les systèmes PEC en raison de leur excellente stabilité contre

la photocorrosion, mais un inconvénient majeur est qu'ils ne peuvent absorber que le rayonnement UV. Les points quantiques (QD) qui possèdent des propriétés optiques programmables selon leur taille, et peuvent étendre l'absorption des semi-conducteurs à large bande interdite au spectre visible et au proche infrarouge. Puisque les photoanodes sensibilisées par QD peuvent élargir la gamme d'absorption des semi-conducteurs à large bande, des rendements de génération de H<sub>2</sub> plus élevés peuvent être obtenus. [159,160] Bien que les cellules PEC sensibilisées QD aient été largement étudiées pour leur excellente efficacité en génération H<sub>2</sub>, la recherche d'un matériau photoanode hautement stable pour les cellules PEC à base de QD est toujours en cours. En effet, la faible stabilité des cellules PEC à base de QD provient principalement de la formation de pièges profonds induits par les UV [161] dans les oxydes métalliques tels que TiO<sub>2</sub>, qui favorisent la formation de trous excessifs dans TiO<sub>2</sub>. Ces trous agissent comme centres de recombinaison non radiatifs qui contribuent largement au processus de photooxydation des QD. Dans cette thèse, nous présentons de nouvelles photoanodes SnO<sub>2</sub>-TiO<sub>2</sub> / graphène pour résoudre ce problème.

### **Les objectifs**

Cette thèse est divisée en deux parties avec deux objectifs correspondants :

#### **Partie I : Fabrication et caractérisation des DSSC avec une nouvelle photoanode à hétérostructure**

Dans les DSSC, les films minces mésoporeux de nanoparticules de TiO<sub>2</sub> ont été largement utilisés comme matériau de photoanode en raison de ses vitesses d'injection d'électrons très rapides de l'état excité du colorant dans la bande de conduction des nanoparticules de TiO<sub>2</sub>. Cependant, en raison de la mobilité limitée des électrons dans le TiO<sub>2</sub>, les taux de recombinaison élevés des électrons conduisent à une dégradation de PCE. D'un autre côté, le SnO<sub>2</sub> est un matériau oxyde prometteur en raison de sa plus grande mobilité électronique et de sa grande bande interdite (3,8

eV). La mobilité pour le SnO<sub>2</sub> monocristallin et nanostructuré est supérieure d'un ordre de grandeur à celle du TiO<sub>2</sub> monocristallin. Cependant, en raison d'une cinétique de recombinaison électronique plus rapide et d'une densité de piégeage plus faible dans SnO<sub>2</sub>, résultant d'un décalage positif de 300 mV de la bande de conduction par rapport au TiO<sub>2</sub>, il en résulte une augmentation du courant d'obscurité [162,163] En outre, SnO<sub>2</sub> a un point isoélectrique inférieur (IEP, à pH 4-5) par rapport à l'anatase TiO<sub>2</sub> (IEP à pH 6-7), [129] ce qui conduit à une adsorption de colorant plus faible avec des groupes carboxyle acides, [163] en diminuant la densité optique de la photoanode et sa capacité à absorber le rayonnement solaire.

Le verre d'oxyde d'étain dopé au fluor (FTO) dans les DSSC peut directement entrer en contact avec l'électrolyte liquide, car la photoanode mésoporeuse ne peut recouvrir uniformément toute la surface FTO. À l'interface de FTO et de l'électrolyte liquide, la recombinaison de charge d'interface limite la collection d'électrons et affecte le PCE. [164-168] La modification de l'interface FTO/électrolyte joue un rôle clé dans le renforcement des performances du DSSC en supprimant la recombinaison des électrons du FTO vers les électrolytes. Une approche d'une telle modification d'interface consiste à ajouter une couche de blocage d'oxyde métallique compact sur FTO qui inhiberait le transport d'électrons de retour de FTO vers l'électrolyte. [167] En outre, des hétérojonctions à base de SnO<sub>2</sub>-TiO<sub>2</sub> peuvent être considérées pour atténuer le problème de la mobilité à faible électron dans le cas du TiO<sub>2</sub> et de la recombinaison d'électrons rapides dans le cas de SnO<sub>2</sub>. En fait, le bord de la bande de conduction de SnO<sub>2</sub> est à une position plus basse que TiO<sub>2</sub>, de sorte que les électrons injectés du colorant au TiO<sub>2</sub> peuvent être injectés efficacement dans SnO<sub>2</sub>, qui à son tour a également une plus grande mobilité. En conséquence, la conductivité électronique globale du système peut être améliorée. [170] Les hétérojonctions SnO<sub>2</sub>-TiO<sub>2</sub> créent une structure de bande en cascade lorsqu'elles sont stratifiées avec le colorant N719. [171,172] Le

transport d'électrons à plusieurs étages dans une structure de bande en cascade augmente la durée de vie du porteur et réduit la recombinaison de charge. [173] De plus, une couche mince de passivation de  $\text{TiO}_2$  à la surface des nanoparticules de  $\text{SnO}_2$  peut réduire la recombinaison des électrons de la photoanode  $\text{SnO}_2$  vers l'électrolyte, qui est l'un des facteurs déterminants des mauvaises performances des cellules solaires  $\text{SnO}_2$ .

Pour traiter les problèmes de recombinaison mentionnés ci-dessus dans une photoanode mésoporeuse  $\text{SnO}_2$  DSSC, et acquérir plus de compréhension sur les DSSC fabriqués avec photoanode  $\text{SnO}_2$ , je prévois de mettre en œuvre une photoanode  $\text{SnO}_2$  modifiée, dans laquelle le concept d'injection électronique efficace est poursuivi dans un  $\text{SnO}_2$ - Hétérojonction de  $\text{TiO}_2$ , pour former une structure de bande en cascade en modifiant la photoanode de  $\text{SnO}_2$  avec une solution de précurseur  $\text{TiCl}_4$  ou  $\text{TiO}_x$ , et en traitant les substrats de FTO avec les mêmes solutions de précurseur pour former une couche de blocage. De plus, les électrons photogénérés dans la photoanode d'un DSSC doivent traverser le réseau de particules semi-conductrices et rencontrer ainsi d'innombrables joints de grains pendant le transit, ce qui les rendent sujet à recombinaison avec les trous présents dans l'électrolyte. Ainsi, l'ajout d'une petite quantité de nanotubes de carbone à parois multiples (MWCNT) et de graphène à l'anode peut créer un réseau de percolation tridimensionnel (3D) hautement conducteur, en agissant comme des voies de guidage de charges. [121,174]

Par conséquent, les objectifs de la partie I sont les suivants :

1. Réalisation d'une couche de blocage sur des substrats FTO / verre et une couche de passivation sur la photoanode mésoporeuse  $\text{SnO}_2$  avec une solution de précurseur  $\text{TiO}_x$  et  $\text{TiCl}_4$ , pour inhiber le processus de recombinaison des trous d'électrons, créant ainsi une hétérojonction  $\text{SnO}_2$ - $\text{TiO}_2$ .

2. Etude du rôle de la solution précurseur  $\text{TiCl}_4$  et  $\text{TiO}_x$  sur la structure mésoporeuse  $\text{SnO}_2$  de la photoanode, et comprendre l'effet combiné de la couche de blocage et de la couche de passivation sur la performance photovoltaïque des dispositifs.
3. Étude de la performance photovoltaïque des DSSC de photoanodes  $\text{SnO}_2\text{-TiO}_2$  avec l'introduction de microplatelets de graphène et son rôle dans l'amélioration des propriétés de transfert de charge dans la photoanode.
4. Étude de l'effet de l'introduction de microplatelets de graphène dans la stabilité à long terme des paramètres fonctionnels du DSSC.

## **Partie II : Etude d'une nouvelle photoanode à hétérostructure pour une génération de $\text{H}_2$ à base de PEC**

L'hydrogène ( $\text{H}_2$ ) a la plus forte teneur en énergie par unité de poids [146] par rapport aux autres combustibles gazeux connus. Bien que  $\text{H}_2$  soit considéré comme un combustible propre puisqu'il ne restitue, comme produit de réaction lors de l'oxydation, que de l'eau [175], mais actuellement, la production à grande échelle de  $\text{H}_2$  repose principalement sur l'extraction d'hydrocarbures tels que le méthane utilisant des combustibles fossiles. La production d'hydrogène à partir d'eau en utilisant des cellules photoélectrochimiques (PEC) utilisant l'énergie solaire est une approche très intéressante. Les cellules PEC qui utilisent généralement des semi-conducteurs à bande large comme photoanodes peuvent être davantage sensibilisées par des points quantiques (QD) pour étendre leur spectre d'absorption, améliorant ainsi leur efficacité de génération de  $\text{H}_2$ . [159,160] Bien que les cellules PEC sensibilisées par QD aient été largement étudiées pour leur efficacité considérable dans la production de  $\text{H}_2$ , la stabilité reste toujours une préoccupation majeure. Une faible stabilité dans les cellules PEC à base de QD colloïdales nous pousse à explorer un matériau photoanode hautement stable. En raison de

ses propriétés photocatalytiques fascinantes, l'anatase  $\text{TiO}_2$  est principalement exploitée pour la fabrication de la photoanode dans une cellule PEC. Cependant, une bande interdite plus large (3,6 eV) de  $\text{SnO}_2$  par rapport à l'anatase  $\text{TiO}_2$  (3,2 eV) crée moins de trous oxydatifs dans la bande de valence sous éclairage ultraviolet (UV),[176] Ceci peut jouer un rôle crucial dans l'amélioration à long terme stabilité des cellules PEC. Jusqu'à présent, le  $\text{SnO}_2$  a été beaucoup moins étudié pour les applications de séparation d'eau PEC, principalement parce que ces minima de bande de conduction sont inférieurs au potentiel de réduction de l'eau[177], et qu'il présente un taux de séparation d'excitons limité.[178] D'un autre côté, le  $\text{TiO}_2$  présente un alignement favorable de la bande pour la séparation de l'eau, mais la dégradation des UV est un revers. Pour relever ces défis, nous avons conçu une hétérojonction  $\text{SnO}_2\text{-TiO}_2$ , afin d'intégrer les avantages de  $\text{SnO}_2$  et de  $\text{TiO}_2$ , à savoir le bord supérieur de la bande de conduction de  $\text{TiO}_2$  et la stabilité élevée et la mobilité électronique exceptionnelle de  $\text{SnO}_2$ . En outre, un alignement de bande de type II dans le cas de l'hétérojonction  $\text{SnO}_2\text{-TiO}_2$  favorise le transport et la séparation des charges, ce qui peut améliorer les performances des cellules PEC.[177,179]

Par conséquent, les objectifs de la partie II sont les suivants :

1. Fabrication et mise en œuvre de photoanode  $\text{SnO}_2\text{-TiO}_2$ /graphène dans des cellules PEC pour une application de génération de  $\text{H}_2$ .
2. Étude de la cinétique de transfert de charges dans la photoanode avec des caractérisations telles que la photoluminescence transitoire et la spectroscopie d'absorption ultrarapide.
3. Étude des performances et de la stabilité de notre photoanode hétérostructurée dans les cellules PEC.

## Résultats : Partie I : Propriétés photovoltaïques améliorées dans les cellules solaires sensibilisées aux colorants par traitement de surface des photoanodes SnO<sub>2</sub>

Dans cette partie, nous rapportons la fabrication et la caractérisation de cellules solaires à colorant (DSSC) à base de particules d'oxyde d'étain (SnO<sub>2</sub>) de taille moyenne ~ 20 nm. Des substrats en verre conducteurs d'oxyde d'étain dopé au fluor (FTO) ont été traités avec des solutions de précurseurs de TiO<sub>x</sub> ou de TiCl<sub>4</sub> pour créer une couche de blocage avant la coulée sur bande de l'anode mésoporeuse de SnO<sub>2</sub>.

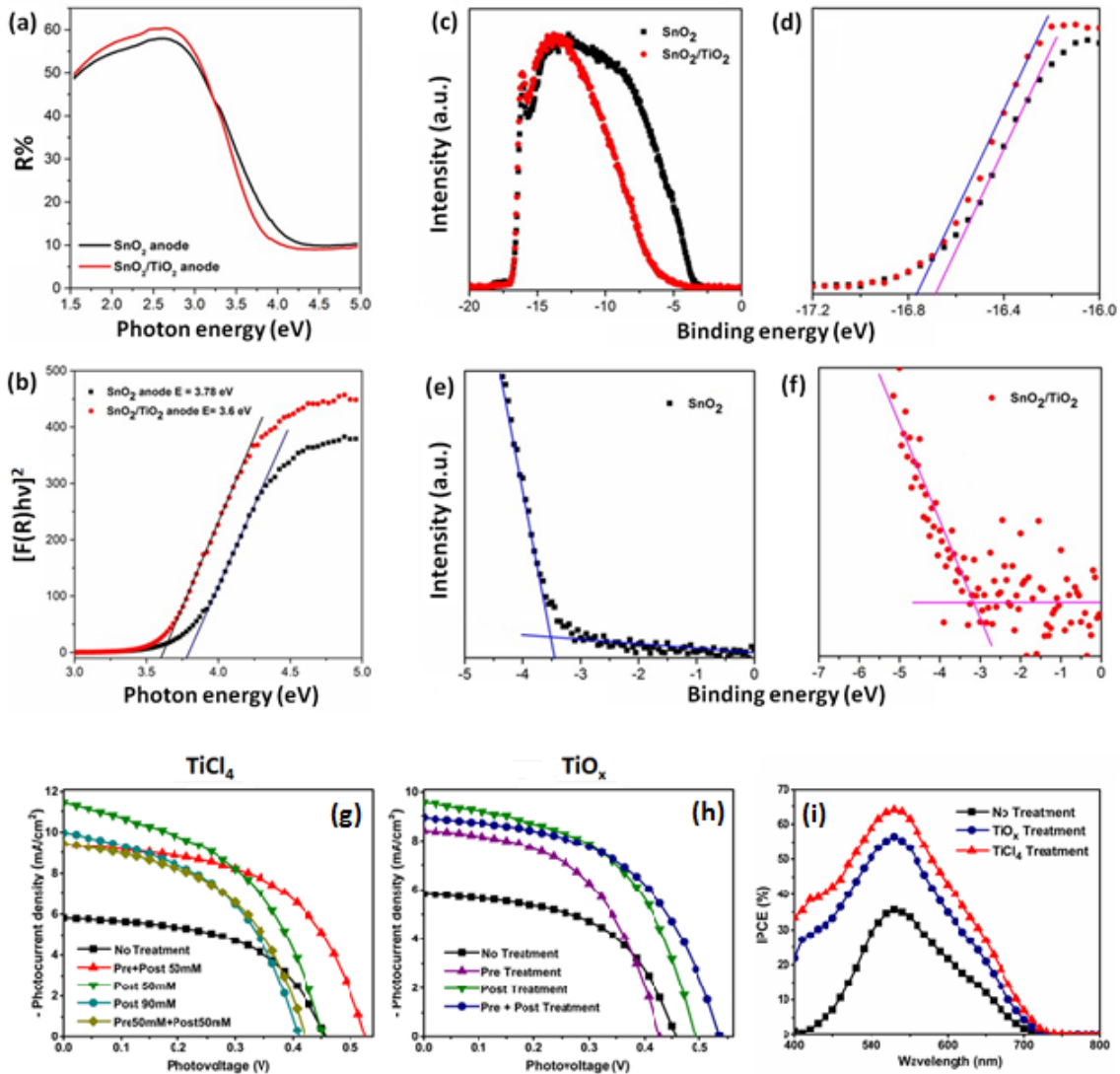


Figure A3: (a) Les spectres de réflectance diffuse en fonction de l'énergie des photons pour l'anode SnO<sub>2</sub> et l'anode SnO<sub>2</sub> après le post-traitement TiO<sub>x</sub>; (b) les spectres transformés de Kubelka-Munk pour l'anode SnO<sub>2</sub> et l'anode SnO<sub>2</sub>

après traitement; (c) UPS complet de SnO<sub>2</sub> et anodes de SnO<sub>2</sub> traitées; (d) vue agrandie de la coupure d'énergie de liaison élevée (niveau de Fermi) et (e, f) coupure d'énergie de liaison faible (bord VB) des anodes SnO<sub>2</sub>. (g) les caractéristiques photocourant de photocourant (J-V) photocourant des DSSC à base de nanoparticules de SnO<sub>2</sub>, sous 1 illumination solaire, obtenues à partir du pré- et post-traitement de différentes concentrations de précurseur de TiCl<sub>4</sub>; (h) les caractéristiques J-V obtenues à partir du pré-traitement et du post-traitement du précurseur de TiO<sub>x</sub>; (i) Dépendance de l'IPCE absolu des cellules solaires avec des électrodes de SnO<sub>2</sub> nanocristallines sensibilisées au colorant modifiées par traitement TiO<sub>x</sub> et TiCl<sub>4</sub>.

De plus, les photoélectrodes SnO<sub>2</sub> ont été traitées avec les mêmes solutions de précurseurs pour déposer une couche de passivation de TiO<sub>2</sub> recouvrant les particules de SnO<sub>2</sub>. La couche de blocage inhibe le transport des électrons vers l'électrolyte, qui sont collectés par le FTO, tandis que la passivation de la couche mésoporeuse de SnO<sub>2</sub> bloque la voie de réaction inverse des électrons photo-injectés de l'anode semi-conductrice à l'électrolyte. Nous avons constaté que la modification améliore le courant de court-circuit, la tension en circuit ouvert et le facteur de remplissage, conduisant à une augmentation de près de deux fois l'efficacité de conversion de puissance, de 1,48% sans traitement, à 2,85% avec TiCl<sub>4</sub>. L'amélioration de la tension en circuit ouvert a été rendue possible grâce à la modification de l'alignement de bande électronique en raison de la recombinaison de charge réduite. L'effet de l'interconnexion des nanoparticules d'électrode fournit un meilleur chemin pour le flux d'électrons et joue un rôle majeur dans l'amélioration du courant de court-circuit du dispositif. La performance photovoltaïque supérieure des DSSC assemblés avec la photoanode modifiée est attribuée à une durée de vie accrue des électrons et à la suppression de la recombinaison électronique à dans l'électrolyte, confirmée par spectroscopie d'impédance électrochimique (EIS) réalisée à l'obscurité. Ces résultats indiquent que la modification de l'anode FTO et SnO<sub>2</sub> par l'oxyde de titane via l'approche du précurseur TiO<sub>x</sub> ou TiCl<sub>4</sub> peut jouer un rôle majeur dans la maximisation de PCE.

Les résultats extraits de cette partie sont présentés dans la publication [90]:

[91]: K. Basu, D. Benetti, H. Zhao, L. Jin, F. Vetrone, A. Vomiero and F. Rosei, *Sci. Rep.*, 2016, **6**, 23312, 1-10.

**Partie I: Photoanodes Hybrides de Graphène et d'Oxyde de Métal pour Cellule Solaire Sensible et Efficace et Stable**

Dans une photoanode mésoporeuse, les électrons doivent rencontrer une quantité considérable de joints de grains, cela augmente la probabilité de recombinaison avec les trous présents dans l'électrolyte.

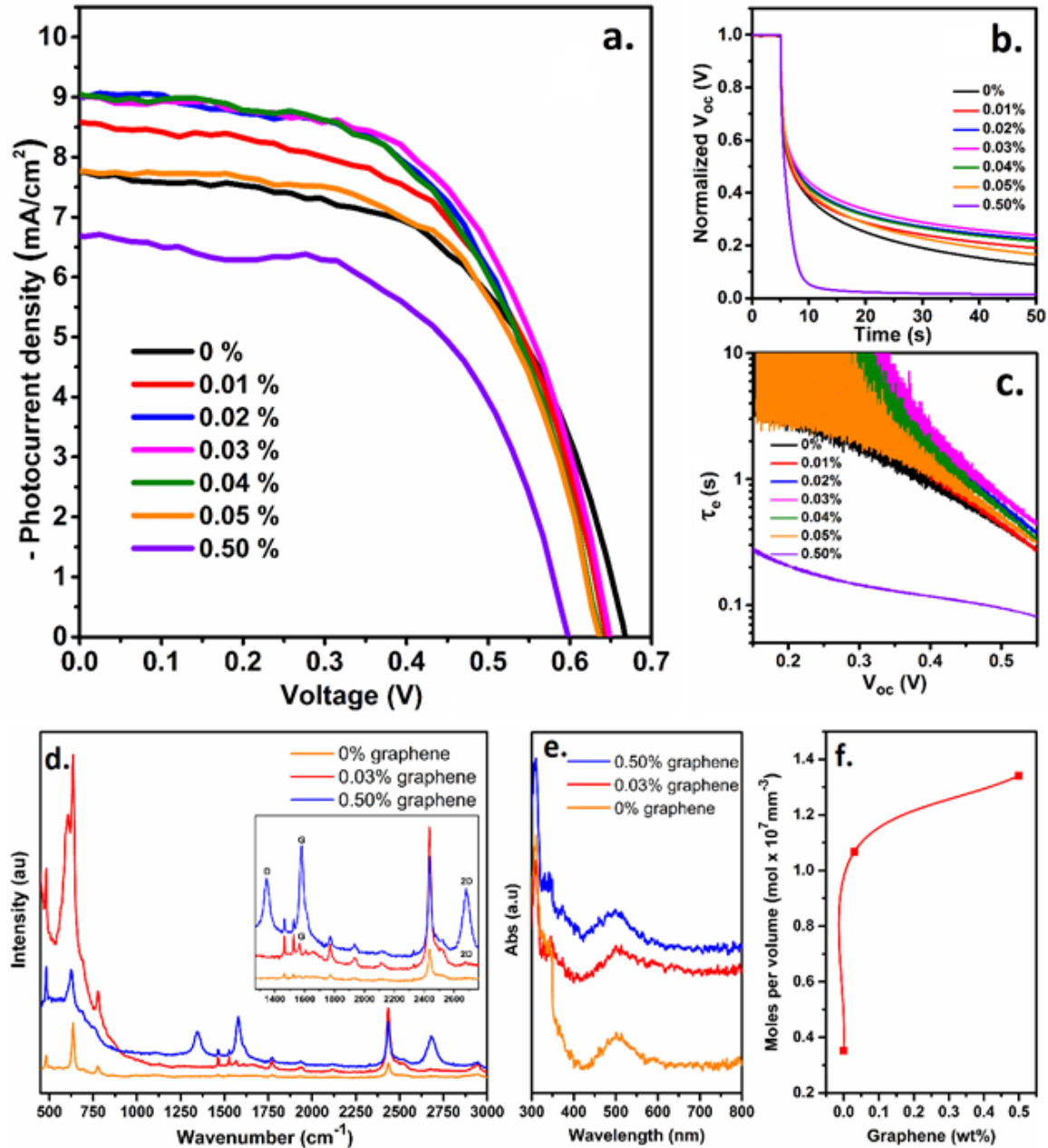


Figure A4: (a) Courbes J-V de dispositifs avec différentes concentrations de microplatelets de graphène dans la photoanode  $\text{SnO}_2\text{-TiO}_2$  sous un seul éclairage solaire (AM1.5G,  $100 \text{ mW}/\text{cm}^2$ ); (b) Courbes de décroissance de

tension de photovoltage ( $V_{oc}$ ) à circuit ouvert transitoire normalisées des dispositifs correspondants; (c) Valeurs de durée de vie des électrons calculées à partir de la dynamique de désintégration de  $V_{oc}$ . (d) les spectres Raman pour la photoanode nue et avec 0,03% et 0,50% de microplatelets de graphène; (e, f) Mesure du chargement de colorant pour une photoanode nue et avec 0,03% et 0,50% de microplatelets de graphène.

Pour pallier ce problème, des nanomatériaux de carbone à charge dirigée peuvent être introduits.

Dans ce travail, nous rapportons l'effet de l'incorporation de microplatelets de graphène dans une photoanode mésoporeuse  $\text{SnO}_2\text{-TiO}_2$  pour augmenter l'efficacité et la stabilité à long terme des DSSC. Les DSSC ont été fabriqués en introduisant différentes concentrations de microplatelets de graphène (jusqu'à 0,50% en poids) dans le réseau mésoporeux  $\text{SnO}_2\text{-TiO}_2$  en utilisant une technique de racle rapide et de grande surface. A une concentration optimisée de 0,03% en poids de microplatelets de graphène, PCE la plus élevée de 3,37% a été atteinte, soit environ 16% de plus que pour les DSSC à base de photoanode  $\text{SnO}_2\text{-TiO}_2$ . Cette amélioration du PCE peut être attribuée à une augmentation de la durée de vie des électrons et à une réduction de la recombinaison de charge dans les photoanodes  $\text{SnO}_2\text{-TiO}_2$  / graphène, comme le prouvent la désintégration transitoire de photovoltage et la spectroscopie d'impédance. De plus, les mesures de stabilité à long terme des DSSC ont été enregistrées pendant 200 heures d'éclairage continu sous une lumière solaire simulée (AM 1,5G). Notre étude a démontré que l'addition de microplatelets de graphène entraîne une stabilité supérieure des DSSC, où la chute de PCE était de seulement 8%, tandis qu'une chute brutale de 30% dans PCE était observée dans le cas du DSSC basé sur des photoanodes  $\text{SnO}_2\text{-TiO}_2$ . Ces résultats indiquent que l'architecture  $\text{SnO}_2\text{-TiO}_2$ / graphène est une photoanode prometteuse pour des cellules solaires efficaces et stables, telles que les DSSC et d'autres dispositifs optoélectroniques.

Les résultats extraits de cette partie sont présentés dans la publication, être soumis.

## Partie II: Cellules photoélectrochimiques hautement stables pour la production d'hydrogène à l'aide de photoanodes hétérotropes SnO<sub>2</sub>-TiO<sub>2</sub> / Points quantiques

La séparation photoélectrochimique (PEC) de l'eau mettant en œuvre des points quantiques colloïdaux (QD) en tant que sensibilisateurs est une approche prometteuse pour la génération d'hydrogène (H<sub>2</sub>) en raison des propriétés optiques accordables en taille de QD.

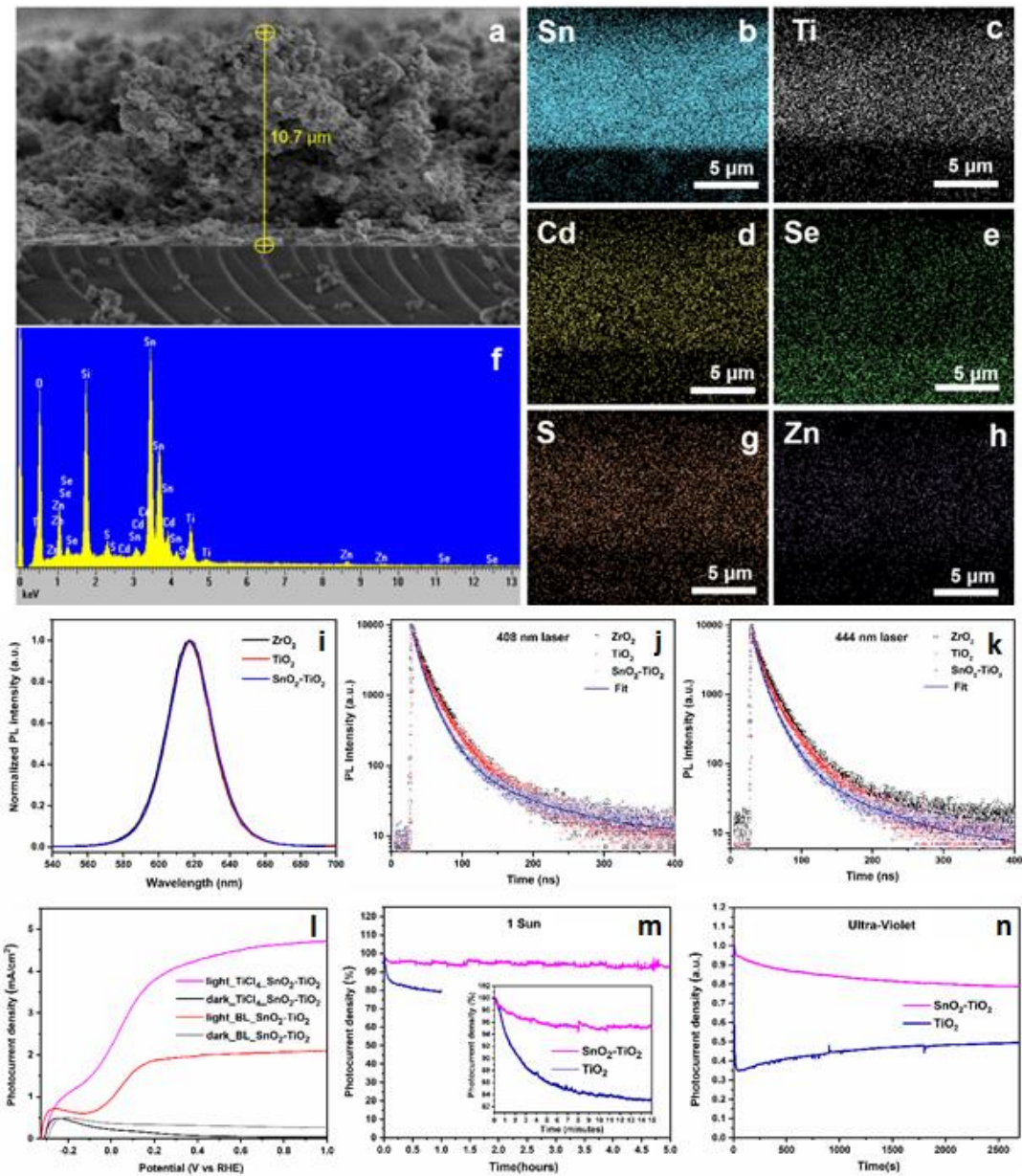


Figure A5: Image en coupe transversale au MEB de notre photoanode composite après la sensibilisation QD "géante" CdSe / CdS. (b) Cartes EDS de tous les éléments incluant (b) Sn, (c) Ti, (d) Cd, (e) Se, (g) S et (h) Zn (f) spectre EDS

du composite SnO<sub>2</sub>-TiO<sub>2</sub> confirmant la présence de ses éléments constitutifs. (i) Spectres PL de QD "géantes" CdSe / CdS dans différentes photoanodes. (j) Dynamique de décroissance de PL pour différentes anodes sensibilisées avec des QD "géantes" CdSe / CdS sous une excitation laser de 408 nm. (k) décroissances PL pour différentes anodes sensibilisées avec des QD "géantes" CdSe / CdS sous la longueur d'onde d'excitation,  $\lambda = 444$  nm. (l) Densité photocourant en fonction de la tension appliquée (vs RHE) pour différentes configurations de SnO<sub>2</sub>-TiO<sub>2</sub> et core / shell QD dans l'obscurité et sous 1 soleil AM 1.5G illumination (100 mW / cm<sup>2</sup>) avec TiO<sub>2</sub> commercial (BL) et TiCl<sub>4</sub> couche de blocage. (m) Essai de stabilité de longue durée de 5 h pour 0,6 V (vs RHE) pour SnO<sub>2</sub>-TiO<sub>2</sub> et 1 h pour photoanode TiO<sub>2</sub> sous 1 illumination solaire en utilisant un filtre AM 1,5G. Les 15 premières minutes de la stabilité de longue durée sont montrées dans l'encart. (n) Stabilité de la photoanode SnO<sub>2</sub>-TiO<sub>2</sub> et TiO<sub>2</sub> sous éclairage UV.

Cependant, le défi de stabilité à long terme des QD n'est toujours pas résolu. Ici, nous présentons un dispositif PEC à base de QD hautement stable pour la génération de H<sub>2</sub> en utilisant une photoanode basée sur une hétérostructure SnO<sub>2</sub>-TiO<sub>2</sub>, sensibilisée par des QD CdSe / CdS / shell épais. Cette architecture photoanode hybride conduit à une densité de photocourant saturée appréciable de  $\sim 4,7$  mA / cm<sup>2</sup>, en conservant  $\sim 96\%$  de sa densité de courant initiale après deux heures, et en maintenant  $\sim 93\%$  après cinq heures d'irradiation continue sous AM 1,5G (100 mW /cm<sup>2</sup>) spectre solaire simulé. Les mesures de photoluminescence transitoire (PL) montrent que la photoanode SnO<sub>2</sub>-TiO<sub>2</sub> hétérostructurée présente un transfert d'électrons plus rapide par rapport à la photoanode TiO<sub>2</sub> nue. Le taux de transfert d'électrons inférieur dans la photoanode TiO<sub>2</sub> peut être attribué à la cinétique des électrons lents dans le régime ultraviolet, révélée par la spectroscopie d'absorption transitoire ultrarapide. Des microplatelets de graphène ont ensuite été introduits dans la photoanode hétérostructurée, ce qui a augmenté la densité de photocourant à  $\sim 5,6$  mA/cm<sup>2</sup>. Nos résultats démontrent que photoanode hétérostructuré SnO<sub>2</sub>-TiO<sub>2</sub> détient un potentiel important pour le développement de cellules PEC hautement stables.

Les résultats de cette publication sont publiés dans la publication, accepté pour publication à Nanoscale.